High Resolution Laser Spectroscopy of Supersonic Jet-cooled Molecules

Thesis by

Brian William Keelan

In Partial Fulfillment of the Requirements
for the Degree of
Doctor of Philosophy

California Institute of Technology
Pasadena, California

1987
(submitted 3 June 1986)

Acknowledgments

I would like to thank my research advisor, Ahmed Zewail, for four years of guidance and financial support, and acknowledge the substantial contributions made by the coauthors of papers from which five of my thesis chapters are derived: Ch. 4 - Jack Syage, John Shepanski, and Ahmed Zewail [*Proceedings of the International Conference on Lasers 1983* (STS Press, McLean, Virginia, 1985), p. 718]; Ch. 5 - John Shepanski and Ahmed Zewail [*Chem. Phys. Letts. 103*, 9 (1983)]; Ch. 6 - Ahmed Zewail [*J. Phys. Chem. 89*, 4939 (1985)]; Ch. 7 - Ahmed Zewail [*J. Chem. Phys. 82*, 3011 (1985)]; and Ch. 8 - Lawrence Peng and Ahmed Zewail [to be published]. Support for these studies came from National Science Foundation grants CHE-8211356 and DMR-8105034, and from an Atlantic Richfield Company Summer Fellowship in 1984.

Jack Syage and John Shepanski constructed the pulsed valve assembly and the original crystal autotracking system, respectively, as well as contributing to other aspects of the experimental apparatus. Peter Felker introduced me to the technique of rotational band contour analysis, performed the time-resolved measurements on diphenylbutadiene with Lutfur Khundkar, and discussed many of the anthracene experiments with me. Lawrence Peng assisted in the stilbene study, and David Semmes worked closely with us in obtaining temporal data for the deuterated anthracenes project. I thank Robert Birge, William Goddard III, and Vincent McKoy for helpful discussions.

All of the members of the Zewail research group have at one time or another offered advice on experimental and other problems, for which I am grateful. The members of the machine and mechanical shops (Tony Stark, Ray Garcia, Guy Duremburg, Delmer Dill, Jim Olson, Jim Gangwer, and the late William Scheulke) have spent countless hours teaching me machining techniques and helping me in the design and construction of a variety of equipment, for which I

cannot thank them adequately. Tom Dunn of the electronics shop built the second crystal autotracking system, helped in the design and construction of electronic circuitry, and on several occasions fixed equipment in record times during critical periods, for which I am greatly indebted. Tina Wood, our secretary, helped with numerous logistical aspects of our papers, and Adria McMillan introduced me to word processing, which proved to be invaluable in the production of this thesis.

Finally, I want to thank all my friends for their moral support during my graduate career; especially my parents, who encouraged me and kept me from starving on a graduate stipend, Jim and Ellen Strauss, with whom I have travelled all over the southwestern US, and whose friendship has helped me through many trying times, and my fiancée Eileen, whose love, affection, and sense of humor have helped me survive the latter portion of my graduate career more or less intact.

ABSTRACT

The phenomenon of intramolecular vibrational redistribution (IVR) is currently of significant theoretical and practical interest. Consideration of a simple model raises several important questions about the coupling mechanisms responsible for IVR. A review of recent work indicates that these questions are best addressed using complimentary high resolution spectral and temporal experiments, as have been reported elsewhere for only two large molecules. Thus, a tunable laser - free jet apparatus capable of producing fluorescence excitation, dispersed fluorescence, and rotational band contour spectra was constructed and is described in detail herein. High resolution spectral data obtained using this apparatus is presented for five molecules for which complimentary temporal data is now available: stilbene, diphenylbutadiene, anthracene–h_{10}, anthracene–$9d_1$, and anthracene–d_{10}. Analysis of the spectral data yields information about coupling mechanisms which is relevant to the questions proposed initially. The results obtained support the following conclusions for these molecules: (1) anharmonic coupling predominates at ranges of ≈ 1 - 10 cm^{-1}, but Coriolis coupling may also be important at shorter ranges; (2) molecular symmetry influences coupling by limiting the number of nearby levels with which a given level may interact; and (3) coupling is more extensive at higher vibrational densities of states due to the increased number of levels of the appropriate symmetry lying within the effective coupling range of a given level.

Table of Contents

RESEARCH REPORT

Introduction

Chapter 1

The phenomenon of intramolecular vibrational redistribution (IVR) is currently of great theoretical and practical interest. It may be introduced using an example of laser-selective chemistry. Consider a molecule containing a bond at which reaction enhancement is desired. It is often possible, *via* laser excitation, to deposit one or more quanta of energy exclusively into this bond. This may effectively lower the activation energy for reaction of the bond. However, enhanced reactivity will only result if the energy deposited in the bond remains localized there long enough for reaction to occur.

Delocalization of energy from one vibrational state to other approximately isoenergetic vibrational states (which may correspond to considerably different nuclear motions) is termed vibrational redistribution. In condensed phases this is a very facile process, since small amounts of energy may be exchanged between the molecule and its surroundings, relaxing the isoenergetic restriction. Under isolated molecule (collisionless) conditions, however, the isoenergetic requirement must be stringently obeyed. Thus the strictly intramolecular process, IVR, should be particularly amenable to experimental and theoretical study. An understanding of IVR is desirable from both a practical standpoint, insofar as it is relevant to laser selective chemistry, and from a theoretical viewpoint, as it is a highly fundamental process occurring in a well-defined system (an isolated molecule excited by a coherent pulse of minimal duration and bandwidth).

IVR would not occur at all in a perfectly harmonic molecule in which vibrational motion were fully decoupled, since the normal modes of a molecule diagonalize a quadratic potential Hamiltonian. In real molecules, anharmonicity (terms higher than quadratic in the potential), vibration-rotation (Coriolis) coupling, or electronic state interactions may induce IVR. Thus the usual model for IVR (see Fig. 1) involves the interaction of a zero order vibronic state $|s>$, which may be directly excited from an initial ground state $|g>$ (i.e. $<g|\mu|s> \neq 0$), with N zero order 'bath' states $\{|l>\}$, which cannot be directly excited ($<g|\mu|l> = 0$). These zero order states mix to form molecular eigenstates, but as a laser pulse with a coherence width spanning these eigenstates can be used to prepare $|s>$ initially, it is appropriate to describe the dynamical process of IVR in terms of these zero order states.

IVR is induced by one or more of the perturbations V already mentioned, since $<s|V|l> \neq 0$. The forward ($|s> \rightarrow \{|l>\}$) and reverse ($\{|l>\} \rightarrow |s>$) rate constants, k_{IVR} and k_{rev}, respectively, are related by $k_{rev} = k_{IVR}/N$. In the intermediate case, N is small, and reversible IVR occurs. In the statistical case, N is sufficiently large that k_{rev} is negligible, and dissipative IVR results. If $|s>$ and $\{|l>\}$ are in an excited electronic state, then it may be possible to monitor the emission from these states in the frequency and/or time domains. Spectrally, emission from $|s>$ normally consists of sharp structure, while emission from $\{|l>\}$ approaches a broad continuum as N increases. Temporally, fluorescence decays are found to be modulated by quantum beats in the intermediate case, and to be biexponential in the statistical case. These manifestations of IVR are discussed in greater detail in Ch. 2.

Within the framework of this model, several questions concerning the process of IVR may be posed: (1) What type of coupling is actually responsible for IVR in specific cases? (2) What are typical magnitudes of the coupling strength $<V>$ (= $<s|V|l>$) and coupling range ΔE? (3) Does molecular symmetry influence coupling efficiency? (4) What is the effect of the vibrational density of states ρ_{vib} on coupling efficiency? As discussed in the following chapter, the elucidation of these questions requires complimentary high resolution spectral and temporal data, as has been obtained for only two large molecules other than those investigated in this thesis. I herein describe primarily high resolution free jet spectral studies which, in conjunction with previous or concurrent temporal studies, provide insight on the questions posed above.

This thesis is arranged as follows: In Ch. 2, several recent, definitive studies on IVR are discussed in detail to illustrate the current approaches to, and understanding of, IVR in large molecules. In Ch. 3, the technique of rotational band contour analysis, used extensively in later chapters, is documented and exemplified. In Ch. 4, our high resolution laser and pulsed free jet apparatus and its operation are exhaustively described. Some of the advantages of high resolution free jet experiments are delineated in this chapter. In Chs. 5 and 6 studies of two diphenylpolyenes, diphenylbutadiene and stilbene, are presented. The high resolution spectral data for stilbene compliments previous temporal data. Both spectral and temporal data are provided for the next higher analog, diphenylbutadiene, allowing comparison with stilbene to probe the effect of size (ρ_{vib}) on IVR. In Chs. 7 - 8, thorough, systematic spectral studies of anthracene and two deuterated anthracenes are reported; these studies compliment previous and concurrent temporal studies, respectively. The three anthracenes provide an analogous series for elucidating the effects of symmetry and density of states on IVR. Finally, in Ch. 9, the principal conclusions of the thesis are summarized.

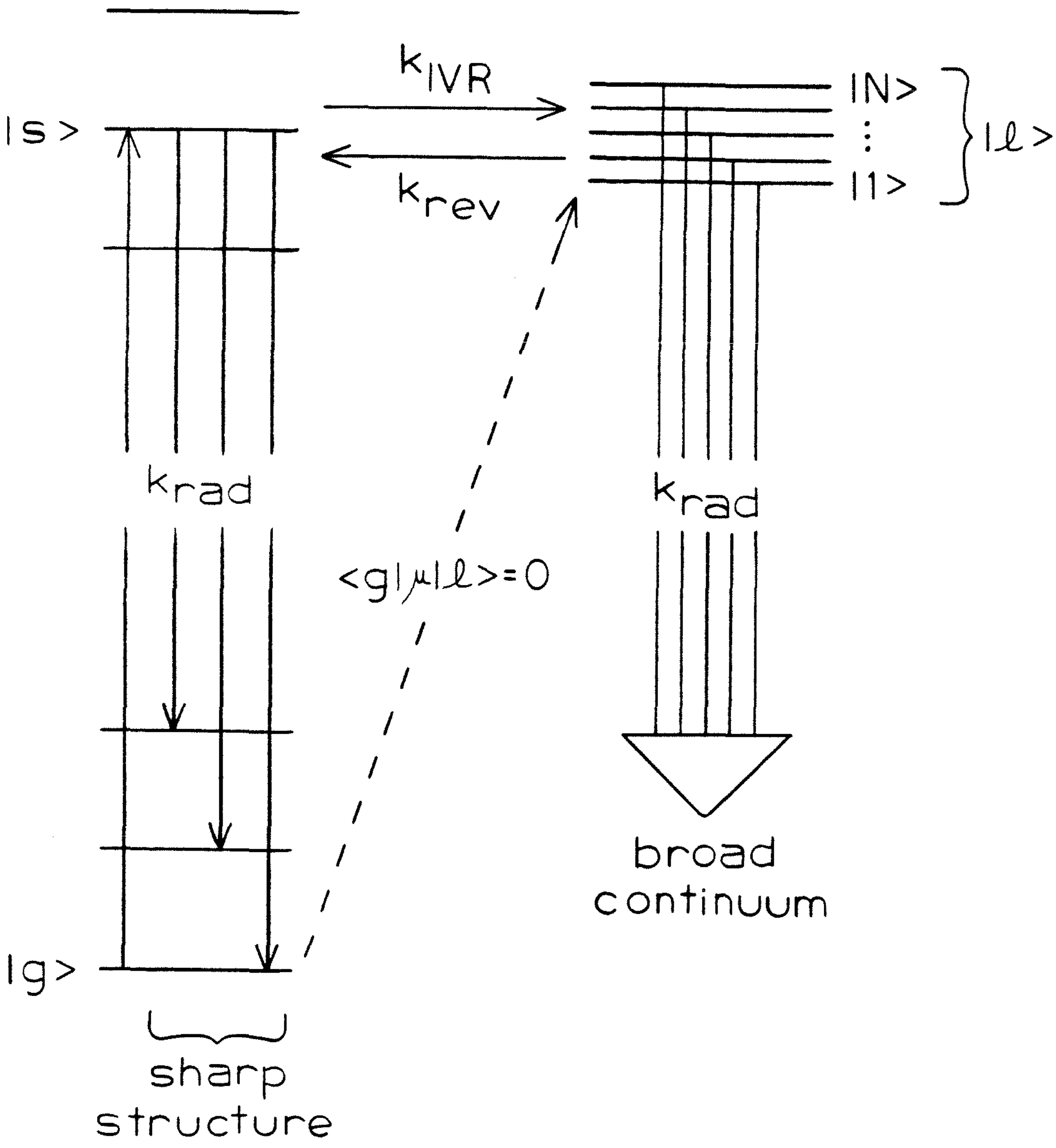
k_{IVR}
k_{rev}
|s>
|N>
⋮
|1>
|ℓ>
k_{rad}
k_{rad}
<g|μ|ℓ>=0
broad continuum
|g>
sharp structure

Fig. 1

Recent Work on IVR in Large Molecules

Chapter 2

In the past decade, there has been considerable progress both experimentally and theoretically in the study of IVR in large molecules. These advances, and the resultant current understanding of this phenomenon, are clearly expounded in two definitive series of papers published in 1985-6 [1-9]. Parmenter and coworkers have studied the temporal evolution of paradifluorobenzene (pDFB) S_1 emission, using the fluorescence quenching technique. They experimentally demonstrate that the dynamic process of IVR (as opposed to the static process of state mixing) occurs in this molecule, and then discuss appropriate theoretical descriptions of this system. Felker, Zewail, and Lambert have studied the temporal and spectral characteristics of the S_1 emission from anthracene and stilbene in supersonic molecular beams. They relate the time and frequency domain behaviors to the different types of IVR, and provide a thorough analysis of the phenomenon of frequency modulations (quantum beats). These two studies are described in detail below.

In the pDFB experiments, frequency-resolved emission (= dispersed fluorescence) spectra were obtained at a variety of oxygen pressures. Oxygen deactivated pDFB S_1 at about one-third the hard sphere collision rate. Thus, after a dozen or so mean collision times, there was essentially no fluorescence, biasing the emission character towards short times. By increasing oxygen pressure to 31 ktorr, fluorescence was limited to about 10 psec, the temporal resolution of the method. At high pressures, a significant enhancement of sharp (unrelaxed) structure relative to broad (relaxed) continuum was observed. The enhanced sharp structure was found to be essentially identical with the resonance emission expected from $|s>$. This fact conclusively identifies the source of the broad continuum as a dynamic process rather than a static state mixing.

To allow quantitative analysis, each emission spectrum was partitioned into sharp structure and broad continuum, and the ratio of the areas was determined. For each level studied, the dependence of this ratio on the fluorescence time scale was reproduced by a kinetic model. Corrections were included for thermal inhomogeneous broadening and collisionally induced vibrational redistribution. The fitting procedure for the kinetic model yielded the forward rate constant k_{IVR} and the number of coupled states N for each level (recall that this determines the reverse rate constant also: k_{rev} = k_{IVR}/N). Radiationless transition theory was then used to calculate the coupling matrix element $<V>$, the coherence width ΔE, and the effective density of coupled states, ρ_{eff}.

Eleven levels in pDFB in the region 1615 - 3310 cm^{-1} were characterized, yielding the following ranges of values: k_{IVR} = 15 - 300 psec; N = 1 - 17 (below 2500 cm^{-1}); $<V>$ = 0.01 - 0.1 cm^{-1}; ΔE = 0.02 - 0.3 cm^{-1}; and ρ_{eff} = 3.2 - 40 /cm^{-1}. Above 2500 cm^{-1}, the statistical limit ($N > 30$) was found to apply, in agreement with the nature of the unquenched emission spectrum (almost no sharp structure above S_1 + 2500 cm^{-1}). For comparison, it was deduced from spectral experiments that: (1) the broad continuum appeared to result from the superimposed fluorescence of $N \approx 10^2 - 10^3$ states; (2) there is significant anharmonic coupling between states separated by up to tens of cm^{-1}, implying similar magnitude $<V>$ and ΔE values; (3) for the four lower energy levels studied, ρ_{eff} exceeds ρ_{vib} for a single symmetry type (only states of the same symmetry type can couple anharmonically).

These discrepancies were explained by the following hypotheses: (1) dynamical experiments probe only those coupled states lying within the coherence width of the excitation source, while spectral experiments can probe coupled states which are more widely separated; (2) in addition to anharmonic coupling, Coriolis coupling is of importance in pDFB (this reduces the symmetry restriction on state coupling). However, as the authors state, more detailed comparisons are needed between high resolution spectral and temporal studies to confirm and clarify these hypotheses.

An ancillary result of interest from this work was that combination bands involving ν_{30} (the in-phase, out-of-plane CCF bend), which is the lowest frequency fundamental (122 cm^{-1}), had especially large intramolecular and collisionally induced vibrational redistribution rates, apparently due to anomalously large $<V>$ values. This is one of the best documented cases of mode selectivity in a large molecule.

The three emission types (sharp structure only, mixed sharp structure and broad continuum, and broad continuum only), which are associated with three regimes of IVR (absent, restricted, and dissipative) also correspond to three fluorescence decay behaviors (single exponential, modulated exponential, and biexponential), as shown in the anthracene and stilbene studies. Quantum beats result from periodic IVR among a small number of levels, and so are definitive evidence for restricted IVR. For a two-level system, in-phase bands (a type) may be thought of as arising from the $|s>$ level, while out-of-phase bands are due to emission from the $|l>$ level. The differing phase behavior may be rationalized in terms of the energy content of these two levels. When the energy is localized in $|s>$ at time t = 0 (the excitation event), the modulation of the emission will be at a maximum for an in-phase band, and at a minimum for an out-of-phase band. At some later time t = $\tau/2$, where τ is the beat period or recurrence time, the in-phase emission will be at a minimum and the out-of-phase at a maximum, corresponding to the energy having migrated to $|l>$. Thus the beat period provides the time scale of IVR.

Multilevel systems are more complicated; N level systems (this includes the $|s>$ level, unlike in Parmenter *et al.*) have N possible types of emission bands, each with different phase behaviors. The number of interacting levels is a measure of the extent or type of IVR, with N = 2 - 10 corresponding to the intermediate case (compare to $N < 30$ in Parmenter *et al.*). From the beat frequencies and modulation depths, ΔE and the magnitude of $<V>$, respectively, may be determined. To a crude approximation, $\rho_{eff} = N/\Delta E_{max}$.

In anthracene, quantum beats were found at all five intense levels in the range 1380 - 1514 cm^{-1}, corresponding to ρ_{vib} = 25 - 40 /cm^{-1} (all symmetry types). This is more restricted than the 10 - 2000 /cm^{-1} for pDFB (same point group), but recall that a larger range of N was considered to be indicative of the intermediate case in that molecule. At S_1 + 1380 cm^{-1}, there are 3 coupled levels in 8.4 GHz suggesting $\rho_{eff} \approx 11$ /cm^{-1}. This is significantly larger than the 3.3 /cm^{-1} per symmetry type, but smaller than the 13 /cm^{-1} per 4 symmetry types (Coriolis coupling allowed), just as in pDFB. Values found for $<V>$ and ΔE were 0.01 - 0.14 cm^{-1} and 0.03 - 0.36 cm^{-1}, respectively, comparable to pDFB. Dissipative IVR was confirmed at S_1 + 1792 cm^{-1} by the observation of a biexponential decay with $N \approx 15$ and $\tau = 22$ psec. Biexponential decays result from a rapid dephasing due to IVR and a slower radiative process.

Similar results were also obtained for the lower symmetry, less rigid stilbene molecule. Modulation depths were not as great as those in anthracene, and beats were not as ubiquitous in the intermediate region, 789 - 1170 cm^{-1}. In this region ρ_{vib} = 10 - 50 /cm^{-1}, similar to anthracene (depending upon the point group of stilbene, this should be divided by 2 or 4 for anharmonic coupling only, or by 1 or 2 for Coriolis coupling also). Dissipative IVR was documented at several levels above 1237 cm^{-1} (including mode selective effects).

Rotational effects were found to be important in accelerating the decay rate of the quantum beat modulation envelope relative to the underlying single exponential decay. This was attributed to the dependence of the excited state rotational constants on vibrational motion, which leads to a more rapid loss of coherence than if the rotational constants were invariant during IVR. This effect is enhanced at higher rotational temperatures, as expected, and is reflected by an increase in Fourier transform component widths.

The studies discussed in this chapter emphasize the importance of complimentary high resolution spectral and temporal data in the further elucidation of the phenomenon of IVR in large molecules. According to Parmenter ***et al.*** [5], excluding the molecules studied in this thesis, such complimentary data is available only for pDFB and pyrazine [10,11]. I herein present high resolution spectral data which compliments the data available for anthracene and stilbene, as well as similar data for two deuterated anthracenes and diphenylbutadiene, which have been concurrently studied in the time domain.

REFERENCES

[1] D. L. Catlett, Jr., K. W. Holtzclaw, D. Krajnovich, D. B. Moss, and C. S. Parmenter, *J. Phys. Chem.* *89*, 1577 (1985).

[2] R. A. Coveleskie, D. A. Dolson, and C. S. Parmenter, *J. Phys. Chem.* *89*, 645 (1986).

[3] R. A. Coveleskie, D. A. Dolson, and C. S. Parmenter, *J. Phys. Chem.* *89*, 655 (1986).

[4] K. W. Holtzclaw and C. S. Parmenter, *J. Chem. Phys.* *84*, 1099 (1986).

[5] D. A. Dolson, K. W. Holtzclaw, D. B. Moss, and C. S. Parmenter, *J. Chem. Phys.* *84*, 1119 (1986).

[6] P. M. Felker and A. H. Zewail, *J. Chem. Phys.* *82*, 2961 (1985).

[7] P. M. Felker and A. H. Zewail, *J. Chem. Phys.* *82*, 2975 (1985).

[8] P. M. Felker and A. H. Zewail, *J. Chem. Phys.* *82*, 2994 (1985).

[9] P. M. Felker, W. R. Lambert, and A. H. Zewail, *J. Chem. Phys.* *82*, 3003 (1985).

[10] P. M. Felker, W. R. Lambert, and A. H. Zewail, *Chem. Phys. Letts.* *89*, 309 (1982).

[11] B. J. van der Meer, H. T. Jonkman, J. Kommandeur, W. L. Meerts, and W. A. Majewski, *Chem. Phys. Letts.* *92*, 565 (1982).

Rotational Band Contour Analysis

Chapter 3

Rotational Band Contour Analysis

ABSTRACT

The use of a rotational band contour program to simulate experimental profiles is discussed in detail. Explicit examples of calculations of rotational constants and nuclear statistical weights are given for four anthracenes.

I. INTRODUCTION

In order to simulate rotational band contours, one must: (1) calculate the rotational constants of the molecule in question, (2) calculate the nuclear statistical weights of the different rotational symmetries, and (3) properly enter these and other data into the Rotational Band Contour Analysis (RBCA) program [1]. Topics (1) - (3) are considered in turn below, using anthracene–h_{10}, anthracene–9d_1, anthracene–d_{10}, and anthracene–9Me as examples.

II. CALCULATION OF ROTATIONAL CONSTANTS

The moment of inertia about an axis associated with coordinate q is:

$$I_q = \sum_i m_i q_i^2 \tag{1}$$

The rotational axes of a molecule (x, y, z) are three mutually orthogonal axes passing through the center of mass (CM) of the molecule with corresponding moments of inertia which are local extrema. The rotational constants (A, B, and C) of the molecule are given by

$$A, B, C = h / 8\pi^2 c \, I_{x,y,z} \tag{2}$$

where I have chosen the conventions $A > B > C$ and $I_x < I_y < I_z$. If A - C are in cm^{-1} and I_{x-z} are in amu$-$pm^2, then $h / 8\pi^2 c = 168600$.

The structure of anthracene$-$h$_{10}$ (point group symmetry D_{2h}) is shown in Fig. 1. The C-H bond lengths (d_0) were all taken to be 108 pm, a typical value for aromatic C-H bonds [2]; the angles labelled γ were assumed to be 120°. The skeletal parameters, i.e., the five C-C bond lengths (d_{1-5}) and the two C-C-C bond angles (α, β), were obtained from a gas phase electron diffraction study [3]. These parameters in total uniquely determine the geometry of anthracene$-$h$_{10}$. In order to calculate I_{x-z}, we need the (x, y, z) triplets for the atomic positions labelled 1 - 7 in Fig. 1. As anthracene$-$h$_{10}$ is planar, $Z_{1-7} = 0$. Thus:

$$I_x = \sum_i m_i (y_i^2 + z_i^2) = \sum_i m_i y_i^2 \tag{3}$$

$$I_y = \sum_i m_i (x_i^2 + z_i^2) = \sum_i m_i x_i^2 \tag{4}$$

$$I_z = \sum_i m_i (x_i^2 + y_i^2) = I_x + I_y \tag{5}$$

The latter result is simply the perpendicular axis theorem.

Determining the x and y coordinates of 1 - 7 is an exercise in trigonometry; the results are presented in Table I. In Table II, the effective masses at each of the positions 1 - 7 is tabulated for the isotopic anthracenes. As an example, there are 4 carbons with mass 12 each at position 1 or its equivalent in D_{2h}, so $m_1 = 4 \times 12 = 48$. Similar considerations yield the rest of the entries in Table II. Application of Eqs. (3) - (5) and then Eq. (2) gives the final anthracene$-$h$_{10}$ rotational constant entries in Table III.

The deuterated anthracenes can reasonably be taken to have the same geometry as anthracene$-$h$_{10}$, so the atomic positions need not be recalculated; only the effective masses change. In anthracene$-$d$_{10}$, which is still D_{2h} in symmetry, the masses at positions 3, 5, amd 7 are doubled; note that the heavier atoms result in larger moments of inertia and thus smaller rotational constants.

Anthracene$-$9d$_1$ is slightly more complicated, as it is C_{2v} in symmetry rather than D_{2h}. The CM is no longer coincident with the geometrical center of the molecule; it has shifted along the y-axis towards the heavier substituent (deuterium). The best way to approach this problem is to calculate the moments of inertia as for the other isotopes (i.e. about the geometrical center) and then transform the result to the true CM using the parallel axis theorem, which states that

$$I_{CM} = I_{par} - MR^2 \tag{6}$$

where I_{CM} is the moment of inertia about an axis through the CM, I_{par} is the moment of inertia about some parallel axis, R is the separation of the two parallel axes, and $M = \sum_i m_i$. To calculate R, we use the definition of the CM:

$$\bar{r}_{CM} = \sum_i m_i \bar{r}_i / M \tag{7}$$

If we use the geometrical origin as our origin, all the contributions to $\bar{r}_{CM}$ cancel except the y contributions of the deuterium and its analogous proton; thus:

$$y_{CM} = [(2)(y_3) + (1)(-y_3)]/M \tag{8}$$

Substituting (8) in (6), the parallel axis theorem, yields

$$I_{CM} = I_{par} - y_3^2/M \tag{9}$$

The transformation is applied to both I_x and I_z; I_y is the same as in anthracene–h$_{10}$ since the substituent lies along the y-axis.

The case of anthracene–9Me is more complicated still. We start by assuming tetrahedral geometry of the methyl group (δ = 109.5°) and use tabulated bond lengths for C–CH$_3$ from toluene (153 pm = d_6) and for CC–H$_3$ (110 pm = d_7) [2]. We assume that the methyl group is a free rotor, which is probably a good approximation and would lead to negligible error even if it were a poor approximation. The three hydrogens may now be thought of as a ring of radius s (see Fig. 2). The moment of inertia of the ring about the y-axis is $3s^2$ by inspection, thus:

$$I_y(\text{anthracene–9Me}) = I_y(\text{anthracene–h}_{10}) + 3s^2 \tag{10}$$

The sum of the moments of inertia about the x' and z' axes (in the plane of the ring) are equal by symmetry and must sum to $3s^2$ by the perpendicular axis theorem, so each is equal to $3s^2/2$.

We now calculate the contributions to the moments of inertia about the anthracene geometrical center, then transform as in the anthracene–9d$_1$ example. The contributions are the same about the x and z axes:

$$I_{par} = I(\text{anthracene–h}_{10}) - 1y_3^2 + 12y_8^2 + 3s^2/2 + 3(y_8+l)^2 \tag{11}$$

In Eq. (11), we started with I(anthracene–h$_{10}$), took away a hydrogen, added the methyl carbon (note $y_8 = y_2 + d_6$), and finally added the contribution of the hydrogen ring (which consisted of two terms: $3s^2/2$ about x' or z' and $3(y_8+l)^2$ to transform back to x or z using the parallel axis theorem). The new CM lies on the y-axis; its Y-coordinate is given by:

$$y_{CM} = [12y_8 - 1y_3 + 3(y_8+l)]/M \tag{12}$$

Using Eq. (12) in (6), the parallel axis theorem, yields:

$$I_{CM} = I_{par} - (15y_8 - y_3 + 3l)^2/M \tag{13}$$

for both I_x and I_y. Application of Eqs. (10), (11), and (13) provides the values of the rotational constants given for anthracene–9Me in Table III.

III. CALCULATION OF NUCLEAR STATISTICAL WEIGHTS

When there are identical fermions in a molecule which may be interchanged through rotational symmetry operations, the Pauli exclusion principle causes different rotational symmetries to have different statistical weights [4]. Since anthracene–d_{10} has no fermions, the statistical weights are all unity, but the other three anthracenes do have identical fermions (protons). Statistical weights may be calculated using group theoretical character anaylsis, as explained below.

In anthracene–h_{10} there are three types of protons, labelled A, B, and C in Fig. 1. Note that the 4 H_B and 4 H_C transform identically under the rotational symmetry operations, but that the 2 H_A transform differently. Anthracene–h_{10} belongs to point group D_{2h}, the rotational subgroup of which is D_2; its character table is shown in Table IV. We first write down the possible spin functions for the different sets of equivalent fermions, and sort them out according to how they transform with respect to the rotational operations of D_2. As an example, consider the 2 H_A. There are $2^2 = 4$ spin functions: ++, --, +-, and -+. Clearly, ++ and -- transform identically, as do +- and -+. Thus the spin functions may be represented by 2 ++ and 2 +-. Now ++ is totally symmetric and is transformed into itself ($\chi = 1$) by all four elements of D_2. Referring to Table IV, we see that ++ = A, since $\chi = 1$ for each element for A. In contrast, +- is transformed into itself under E and C_{2y}, but is changed to -+ ($\chi = 0$) under C_{2x} and C_{2z} (see Fig. 1). Inspection of Table IV reveals that the appropriate linear combination is 2 +- = $A + B_2$. The results of character analysis are shown in Tables V and VI for the H_A and H_B. The only new aspect of treating the H_B is that one must use a *consistent* scheme for numbering the protons.

The total irreducible representation decomposition is obtained by summing the weighted contributions from each of the representative spin functions. For example, $H_A = (2A) + (A + B_2) = 3A + B_2$. As stated earlier, $H_B = H_C$, so we can now calculate the total decomposition, $H_{tot} = H_A H_B H_C = H_A H_B^2$. Note that one multiplies the irreducible representations just like polynomials, and then uses the group element multiplication rules. For example, $(B_1+B_2)^2 = B_1B_1 + B_1B_2 + B_2B_1 + B_2B_2 = A + B_3 + B_3 + A = 2(A + B_3)$. The results for the polynomial expansion $H_A H_B^2$ is $H_{tot} = 288A + 256B_2 + 240(B_1 + B_3)$. Note that the sum of the polynomial coefficients is 2^{10} as required for 10 fermions with 2 possible spin states each. The coefficients of the irreducible representations are their relative nuclear statistical weights. In the RBCA program, statistical weights are entered in the form a.bc, so convenient values for anthracene–h_{10} are: sw(B_1) = sw(B_3) = 1.00, sw(A) = 288/240 = 1.20, and sw(B_2) = 256/240 = 1.07.

Anthracene–9d_1 and anthracene–9Me are treated in the same fashion since the methyl protons are not interchangeable by a rotational operation of C_2, the rotational subgroup of C_{2v}. There are now 4 pairs of equivalent fermions (labelled 1 - 4 in the diagram accompanying Table VII); each pair transforms identically. Character analysis (see Table VII) yields $H_{pair} = 3A + B$, so $H_{tot} = H_{pair}^4 = 136A + 120B$. Note that 136 + 120 = 256 = 2^8. Statistical weights for program data entry would be sw(B) = 1.00 and sw(A) = 136/120 = 1.13. The fact that the statistical weights are very close for each rotational symmetry in each of these molecules is not surprising, as each has a number of identical fermion sets, and the coefficients of polynomial expansions containing high powers tend to average out.

IV. RBCA PROGRAM DATA ENTRY

To produce a simulation, two programs, RBCA.EXE and PL.EXE are used. Two input files are required, MOL and PLT. During this process a number of temporary files are created and these must be renamed, deleted, etc. I use the command file RBCA.COM listed in Table VIII (type "b4 rbca" to execute). Plotting is done by the ZETA plotter. The command sequence plots one simulation at a time, and at the end of a run, the most recent plotting data (PL.DAT) and the log file (RBCA.LOG) remain in the user's directory. If the program does not run correctly, the cause of the problem can be found in the log file. If the plotter malfunctions, one can use the direct command "PLOT PL.DAT" to generate another copy.

Note that while the most recent version of MOL is deleted after use, the PLT file is retained. This is because the parameters in PLT do not usually change from one simulation to the next, while those of MOL change almost every time. If one or more parameters in PLT are to be changed, edit PLT and then purge PLT, leaving the single working version. MOL.;n is edited before each simulation run, generating MOL.;n+1; this is deleted after the run, so that one edits MOL.;n again to produce the working data file. In the event that one wishes to change the basic editing file MOL.;n, edit it, then purge (leaving the new MOL.;n+1), then reedit or copy to produce the working data file MOL,;n+2. The point of these manipulations is to avoid the confusion that can result from the accumulation of used files; it can sometimes be difficult to figure out exactly which files were used in a given run.

The relatively infrequently changed plotting data file PLT has the structure given in Table IX. For a two-photon experiment, special polarization codes are required (see existing documentation). For one-photon experiments, polarization is either 2 (linear) or 5 (circular). If absolute cm^{-1} rather than relative

cm^{-1} are desired for the plot abcissa, enter the band origin for the reference energy. The scale factor is arbitrary. Note which data are entered as integers and which as real numbers (use a decimal point) -- these conventions must be followed.

Finally, let us consider the more complicated MOL file, which contains the molecular information. A sample file, for the anthracene$-h_{10}$ origin in neon, is given in Table X. The cutoff intensity must be small enough that decreasing it significantly results in no change in the tails of the contour. The symmetry is 1 for a transition which is vibronically polarized along the *A* axis (that axis about which the moment of inertia is smallest), 2 for B-polarized, and 3 for C-polarized (moment of inertia largest). The number of photons and symmetry values are entered on the same line, separated by a space. The distortion constants are entered on 6 sequential lines; these constants are usually unknown (except for very small molecules), and so are usually set equal to zero. Calculation of ground state rotational constants has been discussed in detail in § II; excited state constants are usually slightly smaller (≈ 1 %) because excited states usually have weaker, longer bonds and thus larger moments of inertia. Minimum J and K values are normally zero, and maximum J and K values are normally equal. The latter values must be large enough that a significant increase in them does not change the shape of the tails of the simulation (they are usually kept as small as possible to minimize computer time). These values increase roughly as the square root of the temperature. Although an increment of 1 in the J values is the logical choice, the program runs faster if larger increments are used. The increment must be small enough that decreasing it significantly does not change the contour shape. Clearly, if individual rotational lines are resolved, an increment of 1 will be required.

The statistical weights, discussed in § III, are entered on one line, separated by spaces, in the format a.bc. Determination of the proper order of entry of the weights is complicated (see existing documentation). The method is as follows: Consider the J = 2 levels for an asymmetric rotor [4a]. A level is termed E if K is even, and O if K is odd. Note that $K = K_c$ for a prolate top, like the anthracenes, but $K = K_a$ for an oblate rotor. If $K_a + K_c = 2$, then the level is +; when $K_a + K_c = 3$, it is -. Thus we find that for the four lowest levels, the designations are $\tau = -2$, E+; $\tau = -1$, O-; $\tau = 0$, O+; $\tau = 1$, E-.

Now we must obtain the rotational symmetries which correspond to these same levels. This can be done by considering the rotational wavefunctions themselves, or referring to symmetry diagrams, as in Herzberg [4]. The latter approach for the C_{2v} anthracenes [4b] yields: $\tau = -2$, A; $\tau = -1$, B; $\tau = 0$, A; $\tau = 1$, B (initial vibronic levels in the free jet are normally totally symmetric). Thus we establish the correspondence E+ = A, O- = B, O+ = A, E- = B. Data entry into the program is in the order E+, O+, O-, E+, so the statistical weights should be entered in the order *AABB*.

For D_{2h} anthracene–h_{10}, we have the result $\tau = -2$, A; $\tau = -1$, B_1; $\tau = 0$, B_2; $\tau = 1$, B_3 [4c]. Thus we establish the correspondence E+ = A, O- = B_1, O+ = B_2, E- = B_3. Data entry would then be $AB_2B_1B_3$. The statistical weights for the four anthracenes, listed in the order of data entry, are given in Table XI. Note that if individual rotational lines are not resolved and/or statistical weights are very similar for the different rotational symmetries, the effect of the weights on the simulation will be very small.

The parameters which are normally varied to reproduce experimental contours are the temperature and the excited state rotational constants. The width of a contour increases approximately as the square root of the temperature, so temperature is fitted by comparing full-widths at half-maxima of experimental and simulated contours, or by comparing their P-R branch separations (the latter is more reproducible, and yields smaller estimates of the temperature; apparently there is not a true Boltzmann equilibrium in the free jet). Decreasing the excited state rotational constants (all three by the same amount to simplify the fitting procedure) relative to the ground state constants decreases the intensity of the P branch relative to the R branch and changes the shape of each of the branches. The former dependence is easier to quantify and so is used to compare experimental and simulated contours. Fitting is done by trial and error in each case; see Chs. 6-8 for examples of results.

REFERENCES

[1] H. Selzle, W. E. Howard, and E. W. Schlag, *Rotational Band Contour Program*, from Technische Universitat Munchen.

[2] R. C Weast (ed.), *Handbook of Chemistry and Physics*, 55th ed. (Cleveland: CRC Press, 1974), p. F-200.

[3] B. N Cyvin and S. J. Cyvin, *J. Phys. Chem. 73*, 1430 (1969).

[4] G. Herzberg, Molecular Spectra and Molecular Structure, Vol III, Infrared and Raman Spectra of Polyatomic Molecules (New York: Van Nostrand, 1945), (a) p. 45; (b) p. 463, Fig. 144; (c) p. 464.

Table I

X and Y Coordinates of Atomic Positions in Anthracene*

Position #	X-Coordinate	Y-Coordinate
1	$d_3\cos[(\pi-\alpha)/2]$	$d_5/2$
2	0	$Y_1+d_3\sin[(\pi-\alpha)/2]$
3	0	Y_2+d_0
4	$X_1+d_2\cos[(\pi-\beta)/2]$	$Y_1+d_2\sin[(\pi-\beta)/2]$
5	$X_4-d_0\sin[\gamma+\beta/2]$	$Y_4-d_0\cos[\gamma+\beta/2]$
6	$X_1+(d_2+d_1)\cos[(\pi-\beta)/2]$	$Y_1+(d_2-d_1)\sin[(\pi-\beta)/2]$
7	$X_6+d_0\sin[\gamma-\beta/2]$	$Y_6+d_0\cos[\gamma-\beta/2]$

* See Fig. 1 for definitions of positions, lengths, and angles.

Table II

Effective Masses (amu) at Atomic Positions in Three Anthracenes*

Position #	Anthracene-h_{10}	Anthracene-$9d_1$	Anthracene-d_{10}
1	48	48	48
2	24	24	24
3	2	3	4
4	48	48	48
5	4	4	8
6	48	48	48
7	4	4	8

* See Fig. 1 for position # definitions.

Table III

Rotational Constants (cm^{-1}) of Four Anthracenes

Molecule	A	B	C
Anthracene-h_{10}	0.07000	0.01520	0.01249
Anthracene-9d_1	0.06824	0.01520	0.01243
Anthracene-d_{10}	0.05915	0.01385	0.01122
Anthracene-9Me	0.04647	0.01516	0.01146

Table IV

Character Table for D_2, the Rotational Subgroup of D_{2h}

	E	C_{2z}	C_{2y}	C_{2x}
A	1	1	1	1
B_1	1	1	-1	-1
B_2	1	-1	1	-1
B_3	1	-1	-1	1

Table V

Character Analysis for Anthracene–h_{10} Spin Functions

	E	C_{2z}	C_{2y}	C_{2x}
		H_A*		
2 ++	1	1	1	1
2 +-	1	0	1	0
		H_B**		
2 ++++	1	1	1	1
8 +++-	1	0	0	0
2 ++--	1	0	1	0
2 +-+-	1	0	0	1
2 +--+	1	1	0	0

---

[*] See Fig. 1 for definition of proton types.

[**] Arrangement of H_B with respect to the x and y axes shown below (z is out-of-plane):

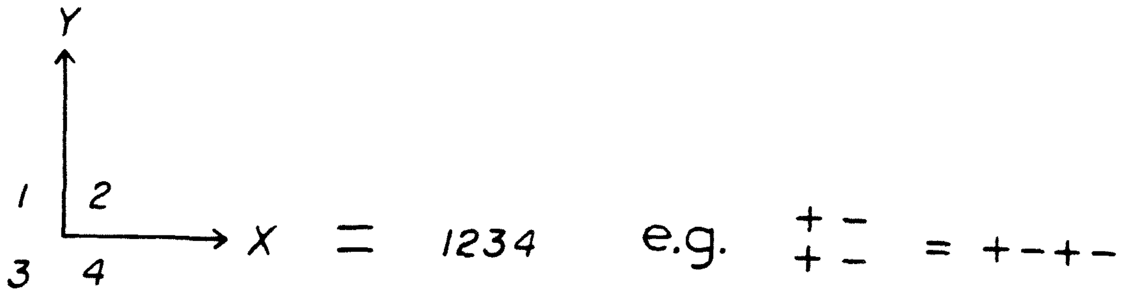

Table VI

Anthracene–h_{10} Spin Function Irreducible Representations.

Spin Functions*	Irreducible Representations
	H_A**
2 ++	$2A$
2 +-	$A+B_2$
Σ	$3A+B_2$
	H_B
2 ++++	$2A$
8 +++-	$2(A+B_1+B_2+B_3)$
2 ++--	$A+B_2$
2 +-+-	$A+B_3$
2 +--+	$A+B_1$
Σ	$7A+3(B_1+B_2+B_3)$

* See Table V for spin function definitions.

** See Fig. 1 for definition of proton types.

Table VII

Group Theoretical Analysis of Spin Functions of C_{2v} Anthracenes

Character Table for C_2, the Rotational Subgroup of C_{2v}

	E	C_{2y}
A	1	1
B	1	-1

Character Analysis of Spin Functions

	E	C_{2y}
2 ++	1	1
2 +-	1	0

Decompositions of Spin Functions into Irreducible Representations

2 ++	$2A$
2 +-	$A+B$
Σ	$3A+B$

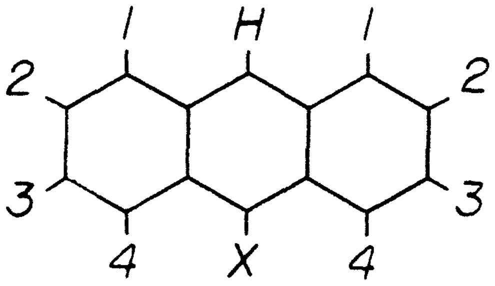

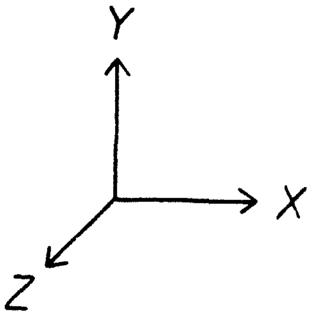

Table VIII

Command File for RBCA

```
REN MOL ANT01.DAT;1
COPY PLT PREPLT.DAT;1
RUN RBCA
PURGE RBCA.LOG
DELETE FOR022.DAT;1
DELETE FOR021.DAT;1
REN FOR023.DAT;1 FOR23.DAT;1
RUN PL
DELETE FOR23.DAT;1
REN FOR009.DAT PL.DAT
PURGE PL.DAT
PLOT PL.DAT
DELETE ANT01.DAT;1
DELETE PREPLT.DAT;1
END
STOP
```

Table IX

Plotting Data File PLT

Parameter	Value
number of photons	1
resolution (cm^{-1})	0.1
high-energy plot limit (cm^{-1})	5.
low-energy plot limit (cm^{-1})	-5.
reference energy for plot origin (cm^{-1})	0.
polarization	2
scale	1.

Table X

Molecular Data File MOL

Parameter	Value
cutoff intensity	0.5
band origin (cm^{-1})	27695.
number of photons; symmetry	1 2
ground state distortion constant DJ	0.
ground state distortion constant DK	0.
ground state distortion constant DJK	0.
excited state distortion constant DJ*	0.
excited state distortion constant DK*	0.
excited state distortion constant DJK*	0.
ground state rotational constant A (cm^{-1})	0.07000
ground state rotational constant B (cm^{-1})	0.01249
ground state rotational constant C (cm^{-1})	0.01520
excited state rotational constant A^* (cm^{-1})	0.06930
excited state rotational constant B^* (cm^{-1})	0.01505
excited state rotational constant C^* (cm^{-1})	0.01237
minimum J value	0
maximum J value	30
J value increment	1
minimum K value	0
maximum K value	30
minimum energy relative to band origin (cm^{-1})	-5.
maximum energy relative to band origin (cm^{-1})	+5.
temperature (K)	5.
excitation bandwidth(cm^{-1})	0.05
statistical weights	1.20 1.07 1.00 1.00

Table XI

Statistical Weights for Four Anthracenes*

Molecule	Symmetries*	sw(1)	sw(2)	sw(3)	sw(4)
Anthracene–h_{10}	$AB_2B_1B_3$	1.20	1.07	1.00	1.00
Anthracene–$9d_1$	$AABB$	1.13	1.13	1.00	1.00
Anthracene–d_{10}	$AB_2B_1B_3$	1.00	1.00	1.00	1.00
Anthracene–9Me	$AABB$	1.13	1.13	1.00	1.00

* Listed in order of data entry into RBCA data file MOL.

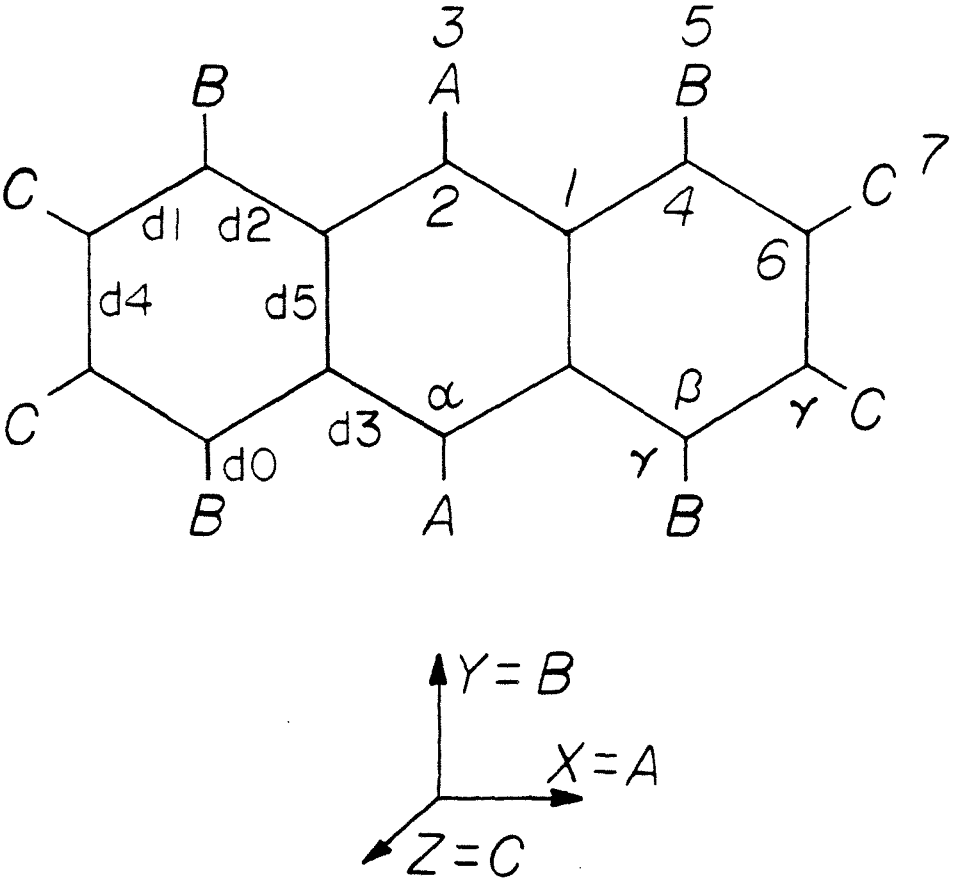

d_0 = 108 pm

d_1 = 136.8 pm

d_2 = 143.6 pm

d_3 = 139.9 pm

d_4 = 141.9 pm

d_5 = 142.8 pm

α = 120.93°

β = 120.22°

γ = 120°

Fig. 1

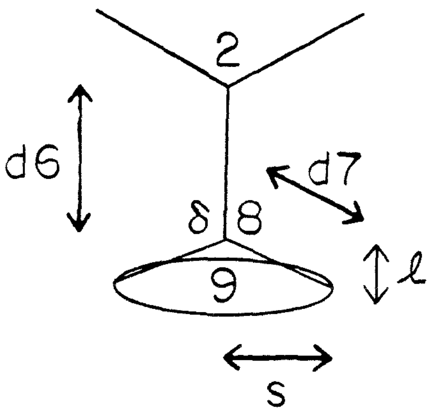

$\delta = 109.7°$

$d_6 = 153$ pm

$d_7 = 110$ pm

$m_8 = 12$

m_9 (ring) $= 3$

$$S = d_7 \sin(\pi - \delta)$$

$$\ell = d_7 \cos(\pi - \delta)$$

Fig. 2

Description of High Resolution Laser / Supersonic Free Jet Apparatus

Chapter 4

Description of High Resolution Laser / Supersonic Free Jet Apparatus

ABSTRACT

An apparatus consisting of a tunable near UV laser system, a pulsed free jet, detection optics and electronics, and a computer data acquisition and analysis system is thoroughly described. Broad-band fluorescence excitation (resolution = 0.7 cm^{-1}, scan range ≈ 2000 cm^{-1}), narrow-band fluorescence excitation (resolution = 0.07 - 0.10 cm^{-1}, scan range ≈ 20 cm^{-1}), and energy-resolved emission (= dispersed fluorescence) experiments may be accomplished using this apparatus. Practical aspects of the operation of the system and procedures for optimization of performance are discussed in detail.

I. INTRODUCTION

Supersonic free jets are an ideal medium in which to study excited state molecules for a variety of reasons, e.g., (1) the molecules are isolated, so the effect of collisions and environment need not be considered (i.e., the only important processes are *intra*molecular); (2) low rotational temperatures reduce rotational envelope widths, reducing overlap of nearby vibronic levels; (3) low vibrational temperatures result in only the vibrationless level of the ground electronic state (v'' = 0 for all vibrational degrees of freedom) being appreciably populated, so that there are no hot bands or sequence bands; and (4) the greatly simplified absorption resulting from (1) - (3) allow single vibronic levels to be probed with narrow-band laser excitation sources.

In order to study dynamical processes in excited state molecules, it is first necessary to fully characterize the nature of the excited state, especially with respect to vibrational structure. Three types of experiments are especially useful in this context. First, broad-band fluorescence excitation spectra probe the overall vibronic structure of excited states, yielding excited state vibrational frequencies and Franck-Condon overlap factors. In such an experiment, the total emission is monitored while the exciting energy is scanned. If the quantum yield is unity, the excitation spectrum is thus equivalent to an absorption spectrum. The latter, however, is much more difficult to accomplish in a free jet. Second, narrow-band fluorescence spectra are similar to the broad-band analog except that the resolution is much higher and the scan ranges are much smaller. They are useful for resolving gross rotational structure (P, Q, R branches) of molecules with very small rotational constants and resolving overlapping vibronic levels. These experiments can yield such information as vibrational symmetry, spectral purity, and even estimates of coupling matrix elements between nearby vibronic levels. Third, energy-resolved emission (=

dispersed fluorescence) spectra allow determination of ground state vibrational frequencies and Franck-Condon overlap factors, as well as probing vibrational redistribution on the time scale of fluorescence. These experiments are conducted by setting the excitation source to an energy where there is intensity in the excitation spectrum, and resolving and scanning the emission with a monochromator.

Using these three types of experiments, the vibronic structure of excited states in isolated molecules may be thoroughly characterized, in preparation for dynamical studies. Indeed, these frequency-domain experiments may be modified and extended to provide critical information on dynamical processes which complements temporal domain data (see e.g. Ch. 7). The very low densities of molecules in supersonic free jets require powerful UV sources and sensitive detection systems. Herein is described a practical apparatus for accomplishing all three types of experiments in a routine manner.

It should be noted that the system is somewhat more versatile than is indicated in this paper. The two-photon excitation spestroscopy of diphenylbutadiene has been investigated by removing the UV generating optics [1]. By scanning the boxcar gates, time-resolved fluorescence decays have been obtained [2]. Finally, addition of a differentially-pumped electron-multiplier to the vacuum chamber has allowed ionization detection in pump-probe experiments [3].

II. THE SUPERSONIC FREE JET

A. Hardware

There are a number of advantages of pulsed supersonic jet expansions over continuous jets, most of which are related to the reduced pumping requirements. Higher backing pressures and larger apertures may be used in pulsed systems, which improves cooling and results in higher densities of the sample molecules. Sample consumption is minimal in pulsed systems.

Our free jet is one of the most compact in use today. The 4" diameter chamber is pumped down to below 100 μtorr (valve closed) by a 4" diffusion pump. The chamber is equipped with two pairs of mutually orthogonal opposing portals which are in turn orthogonal to the jet axis. One pair is used for the detection system and viewing of the nozzle arrangement; the other pair for transmission of the UV laser beam.

In Fig. 1 a simplified diagram of the pulsed valve assembly is presented. Initially the spring seals the pin against the aperture and the magnetic core is in contact with the front o-ring. When the solenoid is actuated, the magnetic core is accelerated backward. Before contacting the lip of the pin, the core has attained nearly final velocity, hence when contact is made, the aperture is opened with a very short rise time. After current has ceased to flow through the solenoid, the core contacts the back o-ring, which reverses the direction of its motion. The assembly is returned to its initial configuration by the spring, resealing the aperture. The aperture seat is made out of aluminum, the pin out of a hard plastic, Vespel.

The diameter of the pinhole may be reduced from the 750 μm bore size by inserting apertures designed for electron microscopy. The pulsed valve is capable of operating at repetition rates in excess of 50 Hz, however, we are limited to 20 Hz by the laser system. Gas pulse widths are typically 300 μs, although pulses widths below 200 μs have been produced. Under normal running conditions (10 Hz, 50 psi Ne, and 300 μm aperture), the ambient pressure in the chamber is ≈ 200 μtorr. The accessibility of the sample holder allows rapid sample refills and convenient cleaning.

The valve assembly may be heated as high as 475 K. The temperature is monitored by two chromel-alumel thermocouples, one located at the sample holder and one away from the sample to detect any thermal gradients (in practice the readings differ by only a few K). Two 40 W cartridge heaters are controlled by a digital monitor which utilizes the thermocouple readings in a feedback loop. The set point temperature is stable to better than a K.

The entire valve assembly is mounted on a vacuum-sealed x-y-z translatable mount to allow adjustment of the laser to nozzle distance and optimization of alignment for excitation and detection.

B. Electronics

The electronics controlling the actuation of the solenoid and the triggering of the laser were built in our laboratory. The control box is essentially a dual pulse generator. The two pulsed outputs may be adjusted independently for pulse duration and pulse delay (both 5μs - 5 ms) from a reference trigger, either internal or external. The repetition rate may be set from 0.1 - 50 Hz. These quantities, as well as total number of pulses, may all be displayed on a digital readout with a variable sampling time.

The valve electronics are triggered by a TTL pulse derived from the CMOS oscillator synchronous output of the Nd^{3+}:YAG laser. The delayed TTL pulse generated by the valve electronics is (1) used to trigger all other electronics in the apparatus, and (2) passed through an optoisolator and then amplified to drive the pulsed valve. A diagram of the pulsed amplifier circuitry is given in Fig. 1. A DC power supply is used to charge large capacitors which are then rapidly discharged by a series of transistors. The high peak power pulse (100 V, ≈ 100 A) actuates the low inductance solenoid in the valve. The MJ10002 and MJ10100 high power switching transistors provide the major current amplification. The 2N2222 boosts the current of the optoisolated TTL pulse to an acceptable level for the MJ10002.

High-speed circuits protect against the backlash induced by the magnetic core returning to its initial position. A fast diode (ECG506) and a 135 VAC source, rectified with a capacitor and 1N4005 diode, generates a 200 VDC clamp on the reverse voltage. If the reverse voltage does exceed this value, the diode becomes reverse biased, passes current, and thereby prevents excessive voltage from being applied to the MJ10100. Additional protection is offered by the V250LA20A varistor. The MJ10002 and MJ10100 power transistors and the 50 Ω, 50 W resistor assembly (two parallel 100 Ω, 25 W elements) are mounted on heat sinks. A fan and vent provide circulation of air over all the components.

III. THE LASER SYSTEM

Laser tunability is most readily achieved in the visible region, using organic dyes. Tunable UV can then be generated by frequency-doubling the tunable visible. There are commercially available dyes which, when pumped at 532 nm, yield efficient lasing action in the region 540 - 740 nm. This gives a UV range of 270 - 370 nm, which is appropriate for studying systems with low-lying excited states, as in conjugated molecules.

Our pump laser, a Quanta-Ray Nd^{3+}:YAG (repitition rate to 20 Hz, pulse duration 7 ns, pulse energy 280 mJ) yields 80 mJ/pulse of 532 nm green after frequency-doubling. This is effected by passing the infrared beam through a KDP crystal cut to the proper phase-matching angle. KDP is preferable to $LiIO_3$ due to its much higher damage threshold. The crystal mount may be rotated about three mutually orthogonal axes to enable fine tuning of the orientation. The phase-matching angle is very sensitive to temperature changes, which can produce substantial long term power fluctuations. It is necessary to separate the 75 % of the 1064 nm which is not frequency-doubled from the 532 nm before dye-pumping. This is effected by a series of two high-damage-threshold 45° dichroic mirrors which transmit 1064 nm but reflect 532 nm. These are mounted in x-y mounts to facilitate alignment of the beam into our Quanta-Ray pulsed dye laser (PDL). The ≈ 2 W (at 10 Hz) of infrared passing through the first dichroic is dumped into a 10 cm water cell encased in a protective box just outside the PDL.

The PDL cavity is bounded by a computer-controlled grating and an output mirror (see Fig. 2). In addition to the transversely-pumped oscillator dye cell, the cavity contains a removable solid quartz etalon and a beam expander. These, with the grating, are contained within a sealed box which can be pressurized from 0 - 2.4 atmospheres absolute. Since the wavelength of electromagnetic radiation depends upon the index of refraction of the medium, the lasing wavelength may be varied by changing the pressure of the cavity. This topic is considered in detail in § IV. A full scan over the available pressure range with nitrogen results in a scan about 10 cm^{-1} long in the visible (20 cm^{-1} in the UV). This is appropriate for investigating rotational structure of vibronic transitions, and resolving overlapping vibronic transitions separated by a cm^{-1} or more. Pressure-tuning is done with the etalon in place, which reduces the laser linewidth from 0.5 cm^{-1} to 0.05 - 0.07 cm^{-1}. This line narrowing is accompanied by a substantial loss of cavity gain, which causes a 75 % power decrease at the highest visible powers (25 mJ/pulse) and complete loss of lasing at low visible powers (below about 7 mJ/pulse).

Since the etalon angle must be readjusted for wavelength changes exceeding about 0.5 nm, it is removed for broad-band scanning, in which the laser grating angle is varied. A microcomputer is used to control a stepping motor which scans the dye laser grating. Primitive commands sent from the keyboard of the microcomputer are used to program a CY500 stepping motor controller. This device is a specialized peripheral control chip that generates four square wave signals, the frequencies and relative phases of which determine the stepping motor rate and direction. The CY500 output must be amplified prior to driving the stepping motor. A stepping motor step corresponds to an increment of 0.005 nm on the PDL (at grating order 5). Broad-band scan ranges are limited by dye efficiency; with DCM we have achieved scan ranges in excess of 2000 cm^{-1}.

The oscillator output is amplified in one or two stages by an optional transversely-pumped preamplifier and a transversely- or longitudinally-pumped amplifier. With the etalon removed, pulse energies of up to 25 mJ may be obtained. Frequency-doubling of the visible, discussed in § V, yields up to a few mJ/pulse of UV. Frequency-doubling is expected to reduce the pulse duration by $\approx 2^{1/2}$, and increase the bandwidth (energy) by the same factor, so calculated UV pulse duration and linewidth are 5 ns and 0.7 cm^{-1} (etalon removed) or 0.07 - 0.1 cm^{-1} (etalon in), respectively.

IV. PRESSURE-TUNING

The wavelength of electromagnetic radiation in a medium varies with the index of refraction of the medium as follows:

$$n\lambda(n) = \lambda_{vac} = hc/\varepsilon \tag{1}$$

A grating in the laser cavity sets a restriction on λ *within* the cavity. If the allowed wavelength in a cavity with index of refraction n is λ_{res}, then

$$\varepsilon = hc/n\lambda_{res} = \varepsilon_{res}/n \tag{2}$$

The index of refraction of a gas is related to its pressure in the following manner [4]:

$$P = P_0(n^2 - 1)/(n^2 + 2) \tag{3}$$

where the characteristic pressure can be expressed conveniently in terms of the index of refraction at one atmosphere (atm), n_{atm}:

$$P_0 = (n_{atm}^2 + 2)/(n_{atm}^2 - 1) \tag{4}$$

P_0 is in atm. Inverting (3) and substituting (2) into the result yields the working equation:

$$\varepsilon = \varepsilon_0[(1 - P/P_0)/(1 + P/P_0)]^{1/2} \tag{5}$$

Using (4) and (5), one can calculate the output energy as a function of cavity pressure, since P_0 can be calculated from the atmospheric index of refraction of a gas, which is a commonly tabulated value. Since $n \approx 1$, $P \ll P_0$, so (4) and (5) can be greatly simplified by using polynomial expansions and retaining only leading terms. Together these yield the intuitively pleasing result:

$$\varepsilon - \varepsilon_0 = \varepsilon_0 P(n_{atm} - 1) \tag{6}$$

For nitrogen, $n_{atm} - 1 \approx 3x10^{-4}$. For a full pressure scan (0 - 2.4 atm), at 15,000 cm^{-1}, this corresponds to an energy scan of 10.8 cm^{-1}. In the UV this translates to 21.6 cm^{-1} at 30,000 cm^{-1}. This is reasonable for scanning single levels or clusters of nearby or overlapping levels. Larger scan ranges can be achieved by using a gas with a higher index of refraction.

Now that the dependence of energy on pressure is known, it is necessary to study the dependence of pressure on time in a pressure scan. A gas leaking from a high-pressure reservoir (which has a constant pressure through the use of a regulator) through a small orifice (e.g. a needle valve opening) into a fixed volume (in this case the laser cavity) will, under certain conditions, have a net flow rate proportional to the pressure differential across the orifice, i.e.,

$$dP/dt = k(P_{res} - P) \tag{7}$$

where P is the cavity pressure. Using separation of variables and integrating,

$$P_{res} - P(t) = (P_{res} - P_i)e^{-kt} \tag{8}$$

where P_i is the initial cavity pressure. Since P_{res} and P_i can be measured directly, if the final pressure P_f and scan time are noted, then k may be determined. In practice, the time is not noted, since data points are collected at equal time intervals, so point number and time are equivalent. If N is the number of data points,

$$k = N^{-1}\ln[(P_{res} - P_i)/(P_{res} - P_f)] \tag{9}$$

At high reservoir pressures, the flow rate (dP/dt) approaches a constant, i.e., the pressure varies linearly with time. Unfortunately, it is not experimentally feasible to use high enough reservoir pressures to render the nonlinearities negligible, because needle valves operate unpredictably at such high pressures. Needle valves do appear to operate reproducibly for $P_{res} \leq 200$ psi; the largest allowable cavity pressure is 35 psi. The resulting nonlinearity is slight, but still must be corrected by using (8) and (9) rather than assuming a constant flow rate. It should be noted that a slight improvement in linearity results from treating P_{res} as a calculated parameter rather than measuring it (the calculated value is normally within 25 % of the measured value). P_{res} can be calculted by measuring the time (dt) required to scan a given pressure interval (dP) at average pressure P_j. If this is done for two P_j (which should be separated as widely as feasible), (7) yields:

$$t_2/t_1 = (P_{res} - P_1)/(P_{res} - P_2) \tag{10}$$

which rearranges to:

$$P_{res} = (P_2 t_2 - P_1 t_1)/(t_2 - t_1) \tag{11}$$

V. FREQUENCY-DOUBLING

A. Optics

The PDL output beam is steered by two antireflection-coated 90° turning prisms into a simple two-lens telescope which reduces the beam diameter by a factor of ≈ 3. This increases the light intensity by nearly an order of magnitude, with a corresponding increase in frequency-doubling efficiency. The beam divergence is increased by the reduction factor, preventing the use of even higher reduction factors.

The light is then doubled by one of two interchangeable KDP crystals (cut for different wavelength regions) with up to ≈ 10 % efficiency. The effective phase-matching angle of the crystal can be varied by tilting the crystal. A fixed angle will typically frequency-double wavelengths spanning only a few nm in the UV, but tilting the crystal can result in a tuning range of ≈ 100 nm. This, however, introduces a variable displacement in the beam path which would necessitate frequent realignment of the optics if not corrected. To eliminate this displacement we have constructed a compensator, using a liquid cell with the same index of refraction and path length as the KDP crystal assembly. The crystal and cell are mounted on counter-rotating wheels which may be disengaged for initial synchronization. The liquid cell has quartz windows and is filled with CCl_4 . We have found the liquid cell superior to a solid quartz compensating element both in terms of UV transmission and beam quality.

The beam is then directed to one of two high-damage-threshold 45° dichroic mirrors which transmit visible output but reflect UV. The two dichroics, which cover different wavelength regions, are attached to a translating stage, and can be interchanged without affecting the alignment of the system. The dichroics are mounted in x-y mounts, facilitating steering of the beam into the vacuum chamber.

The entire optics assembly described above is covered by a removable 2.5 optical-density plexiglas box to reduce scattered light. When the laser is operating, it is possible to distinguish each optical component but no intense light escapes. As plexiglas with 2.5 optical density is available only by special order in bulk, the plexiglas for this application was fabricated by laminating three 1/8 " thick sheets of 12 % transmitting gray with (1,2)-dichloroethane. An entrance port was drilled out for PDL input; because of its location, escape of scattered light from this port is minimal. The exit port is a removable UV bandpass filter (Schott UG-11) which eliminates the small amount of visible reflected by the dichroic mirror.

B. Feedback Loop

The process of frequency-doubling requires a condition of index matching of fundamental and second harmonic waves in a birefringent crystal [5]. For a given wavelength this occurs when the fundamental ray is incident at a specific angle, termed the phase-matching angle, from the relevant crystal axis. The phase-matching angle is wavelength dependent, so as the PDL grating is scanned, the KDP crystal angle must be continuously readjusted. This is the most difficult aspect of generating broad-band tunable UV.

When the doubling crystal is set exactly to the phase-matching angle, the UV ray propagates on the same axis as the visible ray. Small deviations from the phase-matching angle (a few tenths of a degree) produce a marked decrease in frequency-doubling efficiency. This is accompanied by an angular divergence of the harmonic ray from the fundamental axis. As the visible wavelength is scanned away from the wavelength corresponding to the crystal angle, the UV ray displacement (about 1 mm per meter of path length) is used to activate a feedback circuit, which corrects the angle of the crystal. The sensitivity of the circuit is sufficient to prevent any significant decrease in UV intensity at normal laser scan rates. This circuit allows continuous scanning of the entire wavelength range of a dye with only minor adjustment of optics.

A block diagram of the feedback circuit is presented in Fig. 3. During initial system adjustment, the UV beam is centered between two matched photodiodes so that they generate equal currents (the diameter of the UV beam is slightly greater than the distance between photodiodes). Any shift in the UV beam position produces a difference in photocurrents, which is used to activate the feedback loop.

Photocurrents generated by a laser pulse are converted to voltages and held by peak detector circuits. These circuits, like others in the feedback system, are described in Ref. 6. The two peak detectors are reset before each laser pulse so that they sample shot-to-shot changes in the UV beam position. The output voltage of each detector is sent to three circuits designated as cw/ccw, |diff|, and sum in Fig. 3. The first of these is a comparator that determines which photodiode produces the largest current. This is used to determine whether the stepping motor needs to turn clockwise or counterclockwise in order to correct the crystal angle. The latter two circuits take the sum, V_s , and absolute value of the difference, V_d , between the two peak-detector voltages, respectively.

V_s and V_d are used in a rate-selecting circuit to determine how rapidly the stepping motor should move. V_s is dropped in steps by a series of resistors. Each divided voltage is compared to V_d . If $V_d < 0.15\ V_s$ the motor is stationary as this indicates nearly perfect adjustment of the crystal. If $0.15\ V_s < V_d < 0.40\ V_s$ or $0.40\ V_s < V_d < 0.70\ V_s$, the motor adjusts the crystal angle at a stepping rate of 10 or 33 Hz, respectively. We have found that when UV intensity is low, shot-to-shot fluctuations in the beam introduce spatial inhomogeneities that can disrupt the tracking of the feedback system. For this reason the rate-selecting circuit disables the motor when $V_d > 0.70\ V_s$.

The output of the rate selector is sent to a latch that prevents the motor from stepping during the reset sequence, as circuit noise during this interval was found to produce spurious stepping. The timing of the reset sequence is illustrated at the bottom of Fig. 3. A pulse synchronized with the laser triggers a delay timer. At the end of its period the delay circuit activates two other timed pulses, designated as reset and hold. The first clears the peak detectors and prepares them to sample the next laser pulse. The second activates the latch and prevents stepping motor movement. Between the trailing edges of the reset and hold pulses there is a "timing window" during which the next laser pulse occurs. The position of the timing window is adjusted to the laser frequency using a potentiometer in the delay timer circuit. In rapidly-pulsed or continuous laser systems, the two peak detectors could be replaced by time-averaging circuits and the timing circuits eliminated.

Rate and direction information are conveyed to a CY500 stepping motor control chip (see § III). The crystal angle may also be adjusted manually in single step increments or at stepping rates of 10, 33 and 100 Hz. The motor used to turn the KDP crystal is geared down so that one motor step changes the crystal's orientation by 0.03°, allowing sufficiently fine adjustment of the angle to achieve high frequency-doubling efficiency.

VI. SIGNAL DETECTION, PROCESSING, AND DATA ANALYSIS

A. UV Manipulation and Monitoring

The UV beam propagates from the laser table to a second steel table and passes through two angled quartz windows acting as 10 % beamsplitters. One beamsplitter directs light to a 1P28 photomultiplier tube (PMT), which is used to monitor the UV intensity. The output of this PMT is used by the boxcar integrator to normalize the fluorescence signal. This eliminates two potential sources of error in the signal: shot-to-shot variation in the laser power, and variation of dye efficiency with wavelength in an excitation scan. Before reaching the PMT, the UV beam is attenuated by one to several orders of magnitude to avoid saturation.

The other beamsplitter directs light onto an x-y adjustable aluminum-coated mirror which is used to accurately align the beam between two matched photodiodes, the active surfaces of which are ≈ 3 mm apart. If the UV beam angle changes slightly, one photodiode will receive more UV than the other; this serves as the basis for a feedback system, described in § IVB, which continuously adjusts the KDP crystal angle as the PDL grating is scanned.

The UV which passes through both beamsplitters is reflected upward by an antireflection-coated 90° turning prism, passes through the molecular beam chamber, and is terminated on a fluorescent card to allow visual monitoring of the UV intensity and beam quality. In the vacuum chamber the laser beam intersects the free jet, excites the molecules under study, and causes them to fluoresce.

B. Signal Detection

The fluorescence emission is collected by an f/1.4 lens mounted in the vacuum chamber, and imaged into an optics housing configured to collect either total or resolved emission (see Fig. 4). A field lens collimates light collected by the f/1.4 lens which would be lost by divergence in a two-lens system [7]. Only light originating from the 5 mm diameter excitation region is detected, which strongly discriminates against scattered laser light. All lenses and mirrors shown in Fig. 4 are translatable and adjustable in both directions in-plane to facilitate initial alignment and adjustment of focal planes.

After passing through the field lens, the fluorescence emission either (1) is filtered to remove scattered laser light (with a cutoff filter) and stray visible light (with a UV bandpass filter), and focussed onto the PMT aperture; or (2) is steered by a kinematic mirror, focussed onto the monochromator slit, resolved, and propagated to the PMT aperture. Filtering of the emission is unnecessary when the emission is resolved, since the unwanted wavelengths are removed by the grating. Our Spex f/6.8, 0.5 meter monochromator has a dispersion of 0.8 nm/mm and is controlled by a dedicated microcomputer. The two kinematic mirror arrangements (for total detection or resolved emission) may be interchanged in about 4 minutes, allowing flexibility in arranging experiment sequences.

C. Signal Processing and Data Analysis

The output of the EMI 6256B PMT is fed into the boxcar integrator A-channel. As indicated above, the output of a PMT, monitoring laser pulse intensity, is fed into the boxcar B-channel. The fluorescence signal is then normalized by using the A/B ratio mode of the gated integrator. An oscilloscope is used to display the A and B boxcar inputs, and two voltage meters and a strip chart recorder monitor the integrated A/B output. The A/B output voltage of the boxcar is fed into a variable gain circuit and then into a voltage-to-frequency converter. A counting circuit digitizes the frequency output. The count is read by the microcomputer and reset each time the PDL grating is stepped. The digitized voltage is sent to the main computer where it is stored on floppy disk, using programs DE (narrow-band excitation) or DS (broad-band excitation, resolved emission).

Subsequent to storage on floppy disk, data can be plotted and analyzed when convenient. Plots of intensity *vs.* wavelength, absolute energy, or relative energy can be generated for broad-band excitation and resolved emission spectra (program PS). Also, tabulations of peak positions (in the above three units and laser wavelength units) and peak intensities (crudely corrected for baseline) with varying sensitivity and resolution can be generated for these spectra (program LS). These convenient tabulations are accurate for isolated levels, but overlapping level intensities and positions should be determined manually from narrow-band excitation scans. An important use of such tabulations is the rapid location of specific levels for narrow-band excitation scans; they are also useful in preparing tables of vibronic levels for the literature. Narrow-band excitation scans are always plotted against relative energy (program PE), and multiple recorded data files may be signal-averaged together when the signal or laser power is very small and fluctuating (program SE).

VII. PRACTICAL ASPECTS OF THE APPARATUS

There are a number of routine procedures for optimization of performance, some which are required occasionally, others which are required many times each day. As the development and understanding of these procedures is accomplished only through considerable practical experience with the apparatus, they are reported below for the benefit of others using this system or other similar systems.

A. Laser System Adjustments

The infrared frequency-doubling crystal phase-matching angle is very dependent on temperature, and so must be readjusted regularly until temperature equilibrium is reached. This typically requires 3 - 4 hours. Fortunately, it is normally only necessary to adjust one rotational degree of freedom to obtain efficient doubling, and modification of the assembly has made it possible to do this without removing the cover (which completely upsets temperature equilibrium). With practice, the crystal angle can be optimized by looking at the green reflection off the first dichroic mirror (it should be a round, evenly illuminated doughnut), but it is safer to monitor the UV power using the B-channel option on the boxcar integrator, and a digital voltage display (recall that the signal is sent to the boxcar A-channel, and the laser intensity to the B-channel; for spectra one uses the A/B option, but A or B can be integrated instead with a simple setting change). This adjustment must be made every half-hour or so until the crystal is equilibrated, and afterwards only occasionally.

When the etalon is in place in the dye laser cavity, its angle will require readjustment every time the grating angle, i.e., wavelength is changed. Furthermore, there appears to be a temperature equilibration process for the etalon which can take 4 - 5 hours. Thus, even if the grating angle is not changed, the etalon angle may need to be adjusted every half-hour or hour as convenient. The dependence of laser power on etalon angle is roughly sinusoidal except that the peak amplitudes decrease slowly going either direction from some optimal peak. To find the appropriate angle, one must start at the end of the travel and sample the peak amplitudes until a maximum is found. This should be done monitoring the boxcar B-channel, though approximate location of the sinusoidal peaks can be effected by eye by placing a fluorescent business card in the UV beam. Once the maximum amplitude peak is found for one wavelength, it may be assumed that the same peak will be appropriate for other nearby wavelengths (within 5 - 10 nm), greatly simplifying the optimization procedure.

B. UV Alignment and Quality

The alignment of the UV beam into the vacuum chamber is critical and must be readjusted regularly (due to temperature equilibration of the dye solutions and optical components, which causes visible and UV beam drift). The optimal alignment for total and resolved emission is slightly different, the latter being at larger laser to nozzle distance (hereafter X). . The best way to align the beam initially is to monitor signal (A/B) and vary the two degrees of freedom on the visible/UV dichroic mirror (which can be accessed through a hole in the plexiglas optics box). The signal would vary with X^{-2} in the absence of detection efficiency effects, but the optical system limits the region from which emission is detected. Thus it is advisable to directly measure X after such an alignment (by sticking a ruler into the chamber) to be certain that X/D (D = pinhole diameter) is sufficiently large (at least 15 - 20). Once the initial alignment is accomplished, a fluorescent card can be marked with an x and placed above the laser port (this does not contribute measurably to detected laser scatter). Subsequently, as long as the visible/UV dichroic is not translated and the UV turning prism not adjusted in any way, one need only adjust the UV alignment so that the beam strikes the x. (As mentioned earlier, there will be a ≈ 2 mm shift upon changing the detection configuration). This also allows convenient visual monitoring of the UV for other optimization procedures.

UV beam quality and doubling conversion efficiency are significantly affected by alignment of the telescope preceeding the doubling crystal. The visible beam should be centered on *all* optics, especially the telescope lenses. Since the lenses are dispersive, the focal lengths of the two lenses must be rematched each time the wavelength is changed significantly (about 5 nm or more). This may be done by monitoring the UV for beam quality on a fluorescent card and adjusting the lens separation with the translational mount.

C. Manipulation of the Visible Frequency-Doubling Crystal

For emission and narrow-band excitation spectra, the visible doubling crystal angle is manually adjusted and then remains fixed during the scan (this can lead to a factor of two change in laser power with pressure-tuning, but this is corrected by signal normalization with respect to laser power). This is easily done using the manual controls on the feedback loop electronics. The crystal may be roughly positioned with 10 Hz stepping by monitoring the UV on a fluorescent card; fine adjustment must be made in the single step mode with B-channel monitoring (with a great deal of practice this can be done more rapidly by eye). Note that a single crystal step can make a noticeable difference in power and beam quality.

The alignment of, and choice of settings for, the doubling crystal feedback loop electronics is nontrivial. Since there is some UV beam drift in very long scans (longer than 5 nm), it is necessary to stop during long scans periodically and realign the UV beam. Since long scans often sample the low-efficiency regions of dye curves, additional difficulties may arise at the beginning and/or end of some long scans. Given that long scans (i.e. full broad-band excitation scans) are usually done only a few times for a given molecule, the recommended procedure is to *manually* adjust the crystal under these circumstances. An alert experimentalist can manually adjust the crystal angle more accurately and smoothly than can the feedback loop. The procedure is as follows: After initially setting of the crystal angle, the scan is started. As the grating is scanned, the symmetric UV spot on the fluorescent card above the vacuum chamber exit port will grow asymmetric and will start to drift above the x. The single step button is then pressed, which should either restore or worsen the beam symmetry and position. If the latter occurs, the stepping direction is switched and the single step button hit twice (this button receives a lot of use and, if worn, may have to be pushed several times to cause a crystal step). Hereafter, whenever the UV deviates far enough from the x (1 - 2 mm), the crystal is stepped (the stepping direction will not have to be changed again). At some point in the scan it may become evident that the best beam quality no longer occurs when the beam is centered on the x. This is remedied by slightly overcompensating the crystal angle to allow time to reach the visible/UV dichroic, then quickly adjusting the dichroic when the beam quality is best so that it is once again centered on the x. A typical interval between steps would be about 20 sec.

For shorter, repetitive scans, use of the feedback loop becomes practical. The alignment, UV power, and electronic settings are all critical when using this system. Invariant settings are parity = 1, COMMON ANODE on the remote photodiode unit, and, apparently, GAIN = 1. Preliminary studies suggest the following optimization procedure: (1) adjust visible doubling crystal manually at center of scan range to produce high quality UV beam; (2) display DIODE MONITORS output on oscilloscope and align UV beam (using x-y mirror adjustments) so that the two signals are equal (this should correspond to the UV being centered between the two photodiodes); (3) attenuate the UV until the HI and RANGE LED's are alternately flashing at ≈ 2 Hz; and (4) set photodiode gain (black knob on remote unit) so that the photodiode signals (on oscilloscope) are ≈ 5 V. The photodiode gain should not need to be reset unless there is a large change in UV wavelength. The LOCK LEVEL adjusts the sensitivity of the device; at higher levels it will correct the crystal angle at smaller deviations from optimal alignment. Instability of the tracking results from too high a setting (typical settings are 1 - 3). Note that with practice, one can align the UV visually by monitoring the CCW, CW, and BALANCE LED's. At optimal alignment, BALANCE will be lit almost continuously, while CCW and CW will alternately flash at ≈ 2 Hz.

D. Locating Absorption and Emission Peaks

It is often desirable to determine the magnitude of a signal in order to determine appropriate scan parameters or to test system performance. This requires properly tuning the excitation energy and, in the case of resolved detection, properly setting the detection conditions. For broad-band excitation, one normally knows the laser setting from the computer generated tabulations to ± 1 LWU (laser wavelength unit; see § VII G). There is often a slight offset, < 2 LWU, which is nearly constant within a single scan. Thus one need only proceed to a setting slightly larger than that expected and then manually decrease the setting in small increments (0.5 LWU), monitoring the signal A/B, until the transition is found. Note the laser wavelength dial is only calibrated when the setting is decreasing. Over this small range the doubling crystal angle need not be adjusted, simplifying the procedure.

The procedure for narrow-band excitation is slower since there is an equilibration lag time (5 - 10 sec) associated with changing the pressure of the laser cavity. The recommended procedure is to expand small volumes of reservoir pressure gas into the cavity and thus increment the pressure in small steps (0.05 atm), allowing time for reequilibration of the laser cavity before the next expansion. Since peak positions are usually known to ± 0.3 atm, finding a peak in this manner rarely takes more than a minute or two. This can be sped up further by first estimating the peak position from a very fast (15 sec) pressure scan and then using the incremental procedure over a narrower range. Fast scans should be done by pumping down the cavity rather than pressurizing it, since then overpressurization cannot result. This means that the estimated peak position, if uncorrected, will be at too low a pressure due to equilibration lag.

Finally, to set detection conditions properly when resolving the emission, one usually opens the slits up all the way and optimizes the signal in other respects first, then narrows the slits to the desired value, and sets the controller for a short scan across the expected peak (which should be able to be estimated to ± 0.2 nm). The digital wavelength display can be monitored at the same time as A/B; there is, of course, a response lag of a few boxcar time constants, so the scan should not be too rapid. If no signal can be found, it only takes ten minutes to revert to total detection, locate the signal, and reconvert to resolved detection (unless something is seriously wrong).

E. Pulsed Valve Adjustments and Cleaning

The valve pulse characteristics are markedly different at 20 °C, 100 °C, and 180 °C. Once the valve has equilibrated in temperature (15 - 30 minutes at the final temperature), preliminary adjustments can be made, but these may have to be modified once or twice more before operation stabilizes. The three parameters which are routinely adjusted are the transistor voltage (normally 100 V but can be turned up to 105 V to increase gas flow), the electrical pulse duration to the solenoid (typically 500 - 700 μsec, but can go to 1000 μsec to increase gas flow), and the pulse delay relative to the laser (variable, but usually 1500 - 2000 μsec). The gas flow is usually considered appropriate when, with nitrogen carrier gas, the difference between the chamber pressure with the valve on and off is 100 - 400 μtorr. Once the transistor voltage and pulse duration have been adjusted, the pulse delay may need to be readjusted. To do this, watch the oscilliscope signal (A-channel) trace as the delay is varied (the trace will move since the scope is triggered off the delayed pulse). The delay should be set to produce the largest signal unless the signal becomes erratic. After this procedure, the boxcar gate delays will need to be reset, which can be crudely done visually with the scope and then finely adjusted using the boxcar voltage output. The gate delays are essentially identical for the A-and B-channels.

The procedure for cleaning out the valve is standardized, but a few notes on bakeout procedure are in order. Once nearly all of a sample has been removed by washing with solvents, the remainder can be removed by running the valve at its maximum operating temperature (200 °C) at 50 Hz repitition rate for 24 - 48 hours (the chamber should be pumped by the mechanical pump during this process). Use of a proxy spring and pin are recommended for this harsh procedure. Then a small amount of the next compound to be studied (or a substitute) is added and signal is optimized, which allows a scan of the previous sample origin to test for remaining impurities. If impurity is detected, the process is repeated (including solvent washing so that the new sample is not decomposed).

F. Performance Tests

The performance of the system can be tested in a number of ways. The most important things to confirm are:(1) that UV power is good; (2) that the signal level is appropriate; (3) that the signal is steady and not fluctuating unreasonably; (4) that there is no saturation (either molecular or detector); (5) that rotational and/or vibrational cooling is adequate. This points are considered in turn below.

The simplest way to measure UV power is to note the B-channel voltage at a particular laser PMT bias at a strong absorption (with etalon in, usually). This should be reproducible from day to day, and varies predictably with wavelength. At the same strong absorption, the A/B voltage at particular laser and fluorescence PMT biases should be noted, along with relevant experimental parameters. This may also be compared from day to day. In this way a change in performance will be immediately apparent. To test signal stability, optimize the signal at the reference absorption or elsewhere, and follow A/B on the strip chart recorder for five minutes or so. Allowing for slow drift, when performing optimally all fluctuations should be within 5 % of the mean voltage value. The best test for detecting saturation is to check the A/B voltage, then insert a low absorbance neutral density filter or equivalent into the UV beam and note the change in the A/B voltage. The filter should change the UV intensity significantly (tens of %). The filter must be placed on the laser side of the laser PMT beamsplitter so that the input to the A- and B-channels is reduced equally. If there is insignificant saturation, there will be little change in A/B (± 5 %); an increase in A/B indicates molecular saturation (or conceivably saturation of the fluorescence PMT); a decrease in A/B indicates laser PMT saturation (a common problem). Vibrational cooling can be evaluated by studying the excitation spectrum near the electronic origin; sequence bands and occasional hot bands will be observed if cooling is inadequate. Increasing the laser to nozzle distance should alleviate this problem. Rotational cooling can be optimized by varying the laser to nozzle distance and obtaining rotational contours of an isolated line. The linewidth, which varies roughly as $T_{rot}^{1/2}$, should asymptotically decrease as the laser to nozzle distance is increased.

G. Signal Averaging Through Boxcar Integration

There is one general criterion for determining the appropriate boxcar integration time constant τ: it should be roughly one-half the time required to scan across one resolution unit. If it is less, then full use is not made of signal averaging. If it is more, the dynamic response range drops below $e^2 \approx 7.4$, and the resolution rapidly becomes limited by τ rather than by the laser linewidth or monochromator slit width. Occasionally this is done intentionally to increase signal averaging when a preliminary scan reveals no fine structure.

The resolution of a monochromator is equal to the slit width times the dispersion; when divided by the scan rate, this yields the time required to scan across one resolution unit, which is halved to obtain τ. The Spex dispersion is 0.8 nm/mm = $(1250\ \mu\text{m} / \text{nm})^{-1}$, so:

$$\tau = \text{slit}/[2500 \times \text{rate}] \tag{12}$$

Note that τ is in seconds (throughout this section); rate is nm/sec, slit width is in μm. The rate is programmed directly into the Compudrive microcomputer. In practice, one usually sets the slitwidth to give the desired resolution, then either (1) sets the scan rate to make a reasonable scan time and calculates the appropriate τ; or (2) sets τ to give a steady A/B voltage and calculates the allowed scan rate. Note that signal magnitude varies proportionally with slit width; signal to noise should vary with the square root of the same at low signal levels, although experimentally the dependence seems much more dramatic.

For pressure-tuning scans, we use Eq. (6) in § IV. Plugging in P = 0 and P = 2 atm, and subtracting the two resulting relations, yields:

$$\Delta\varepsilon_2 = 2\,\varepsilon_0(n_{atm} - 1) \tag{13}$$

where $\Delta\varepsilon_2$ is the laser energy difference between P = 0 and P = 2 atm (this is usually termed a full scan, even though P_{max} = 2.4 atm). Energy units throughout this section are cm^{-1}. If nitrogen is used, $n_{atm} - 1 \approx 3\text{x}10^{-4}$. If we now define t_2 to be the time required to scan from P = 0 to P = 2 atm, then the scan rate is just $\Delta\varepsilon_2/t_2$. Thus:

$$\tau = \text{res x } t_2/[12\text{x}10^{-4} \text{ x } \varepsilon_0] \tag{14}$$

where res is the laser linewidth. In practice, one first selects an energy in the middle of the region being studied, and then guesses the laser bandwidth (≈ 0.05 cm^{-1} at 540 nm, 0.07 cm^{-1} at 740 nm) or measures it with a Fabry-Perot analyzer (this will not work with dyes prone to amplified spontaneous emission). The constant in the above equation (cast in the form $\tau = t_2/k$) can then be calculated, and its value will not vary enough over the study region to justify recalculation. As an example, in the far red (15,000 cm^{-1}), the UV linewidth is estimated to be $0.07 \text{ x } 2^{1/2} = 0.10$ cm^{-1} (see § III), and ε_0 (UV) will be 30,000 cm^{-1}. Thus $\tau = t_2/360$; variation of ± 1000 cm^{-1} in the UV changes the constant by only ± 3 %.

Given the difficulty of adjusting the needle valve in the pressure-tuning manifold, scan rate is varied by changing the backing pressure (but not exceeding 200 psi; see § IV) until $\tau \approx 2$ sec, a convenient value. If additional signal averaging is required, multiple scans can be taken and averaged by the computer program SE, which works best with sequential scans. It is important to determine the offset values for each spectrum independently, relative to a reference scan, when using this program (otherwise artifactual structure may be enhanced). Averaging N scans seems to work better than increasing τ by a factor of N, although in theory both methods should increase signal to noise by

$N^{1/2}$.

To derive the τ relation for broad-band excitation, it is necessary to discuss laser wavelength units (LWU), which are defined as the product of the visible wavelength in angstroms and the grating order (these are sometimes denoted by A-O's for angstrom-orders). To obtain the excitation wavelength, LWU must be divided by the product of the grating order and harmonic (visible = 1, UV = 2). This product is termed the effective grating order (EGO). The following relations thus hold:

$$\lambda(\text{nm}) = \text{LWU}/[10 \text{ x EGO}] \tag{15}$$

$$\varepsilon = \text{EGO x } 10^8/\text{LWU} \tag{16}$$

$$|d\varepsilon/d\text{LWU}| = \text{EGO x } 10^8/\text{LWU}^2 \tag{17}$$

The absolute derivative in Eq. (17) is the energy interval per LWU, which will appear in the τ relation. One grating step corresponds to ≈ 1/4 (0.24) LWU and also corresponds to one data point, since the Rockwell microcomputer controls both data acquisition and the grating stepper motor. Values of data acquisition rate (DAR, in points/sec) depend upon the F number programmed into the Rockwell. We can now write an expression for τ:

$$\tau = \text{res}/[2 \text{ x DAR x } (1/4 \text{ LWU/point}) \text{ x } |d\varepsilon/d\text{LWU}|] \tag{18}$$

Using Eq. (17) and assuming a UV resolution of 0.7 cm^{-1} (0.5 cm^{-1} for visible), we obtain the more practical:

$$\tau = \text{LWU}^2/[6.8\text{x}10^7 \text{ x EGO x DAR}] \tag{19}$$

Plugging extreme values of LWU and EGO into (19), one finds that the ratio LWU^2/EGO varies by only 20 % about a mean value. Thus the most practical form of the τ relation uses a mean value for this parameter:

$$\tau \approx 1.34 \,/\, \mathrm{DAR}\ (\pm 20\ \%) \tag{20}$$

The unimportance of this variation is apparent when one notes that the ratio of two τ's per resolution unit scan time is somewhat arbitrary.

H. Optogalvanic Calibration

The procedure for obtaining optogalvanic calibration data is standardized, but use of this information to correct spectral data is not as simple as one might expect. Broad-band excitation spectra are often broken down into several short, overlapping scans (due to variation in intensity). These scans may have different offsets (due to slight instability in the stepping motor when supposedly at rest), which must be accounted for. The best way to do this is to first obtain a printout (program L) of the data in the file containing the origin. Choose the LWU offset such that $\Delta\nu$ is zero for the origin. Then find a reference line that will appear in the next short, overlapping scan, and note its absolute frequency ν_{ref}. Using the *same* LWU offset, print out the data for this second scan, and note the relative frequency (vibrational energy) of the reference line, $\Delta\nu_{ref}$. This allows calculation of the effective origin position in LWU for the second scan:

$$\mathrm{LWU}^0_{eff}(2) = \mathrm{EGO} \times 10^8 / [\nu_{ref1} - \Delta\nu_{ref1}(2)] \tag{21}$$

The parenthetical numbers refer to the scan number, and ref1 is the first reference line. Now find a reference line contained in both the second and third scans, and calculate the absolute energy it *would* have had if the offset were the same as in the first (origin) scan:

$$\nu_{ref2} = \nu_{ref2}(2) - \nu_{ref1}(2) + \nu_{ref1}(1) \tag{22}$$

Now use ν_{ref2} just like ν_{ref1} in Eq. (21). This iteration procedure will remove the offsets in a consistent manner. Once the LWU^0_{eff} are determined for each scan, then each line in each scan can be properly optogalvanically corrected. The correction is applied to the tabulated LWU, and the vibrational energy then obtained from:

$$\Delta\nu(\text{corr}) = \text{EGO} \times 10^{8} / [\text{LWU}(\text{corr}) - \text{LWU}^{0}_{\text{eff}}(\text{corr})] \qquad (23)$$

Note that $\text{LWU}^{0}_{\text{eff}}$ must be corrected using the proper optogalvanic data (that near the origin), which may be different from the correction applied to other spectral data. Corrections are conveniently made on a programmable calculator.

REFERENCES

[1] J. F. Shepanski, B. W. Keelan, and A. H. Zewail, *Chem. Phys. Letts.* 103, 9 (1983).

[2] J. A. Syage, P. M. Felker, and A. H. Zewail, *J. Chem. Phys. 81*, 2233 (1984).

[3] (a) J. W. Perry, N. F. Scherer, and A. H. Zewail, *Chem. Phys. Letts. 103*, 1 (1983); (b) N. F. Scherer, J. F. Shepanski, and A. H. Zewail, *J. Chem. Phys 81*, 2181 (1984).

[4] R. Wallenstein and T. W. Hansch, *Appl. Opt. 13*, 1625 (1974).

[5] A. Yariv, *Quantum Electronics* (New York: Wiley) 1976, Ch. 16.

[6] P. Horowitz and W. Hill, *The Art of Electronics* (Cambridge: Cambridge University Press) 1980, Ch. 3.

[7] M. V. Klein, *Optics* (New York: Wiley) 1970, Ch. 3, pp. 111 - 116.

FIGURE CAPTIONS

Figure 1: Analog switching circuitry and pulsed valve schematic. A capacitor bank is charged by a DC power supply and then discharged through a series of transistors upon triggering. The amplified pulse activates the valve solenoid, accelerating the magnetic core, and in turn lifting the pin. The core motion is reversed by the back o-ring, and the pin is restored to its initial position by the spring. The resulting gas pulse is typically 300 μs long. For simplicity, the thermocouples and cartridge heaters are not shown. See § II.

Figure 2: Schematic of pulsed dye laser cavity, showing output mirror, transversely-pumped oscillator dye cell, solid quartz etalon, beam-expanding telescope, and computer-controlled grating. The latter three components are contained within a sealed box which may be pressurized from 0 - 2.4 atm. If pressure is varied over this range using nitrogen, the lasing energy can be shifted ≈ 10 cm^{-1} due to the change in cavity index of refraction. See § III, IV.

Figure 3: Frequency-doubling feedback circuitry. During a laser pulse, the photocurrents generated by two matched photodiodes are monitored by two peak detectors. The fractional difference (absolute difference divided by sum) of the peak values is used to determine the rate of change of the doubling crystal angle, while the relative sizes of the peak values are used to determine the direction of angular change. The peak detectors are reset just prior to the next laser pulse. The stepping motor is disabled during the resetting of the peak detectors and the laser pulse to avoid spurious stepping instructions resulting from noise. See § V.

Figure 4: Schematic of signal detection and processing system. Fluorescence emission is collected by an f/1.4 lens and passes through a field lens for collima-

tion. Depending upon the placement of two kinematic mirrors, either total emission (except that absorbed by a laser cutoff filter) is focussed onto the photomultiplier tube (PMT), or the emission is focussed into an f/6.8 monochromator (dispersion 0.8 nm/mm) and resolved before passing to the PMT. The kinematic mirror placement can be changed from one configuration to the other in about 4 minutes. A boxcar integrator divides the fluorescence signal by the signal from another PMT, which monitors the UV laser power, on a shot-by-shot basis. The power-normalized signal is integrated, averaged, converted to a digital signal by a voltage-to-frequency converter, and sent to a computer. The data can then be reduced, analyzed, plotted, and stored on floppy disk. See § VI.

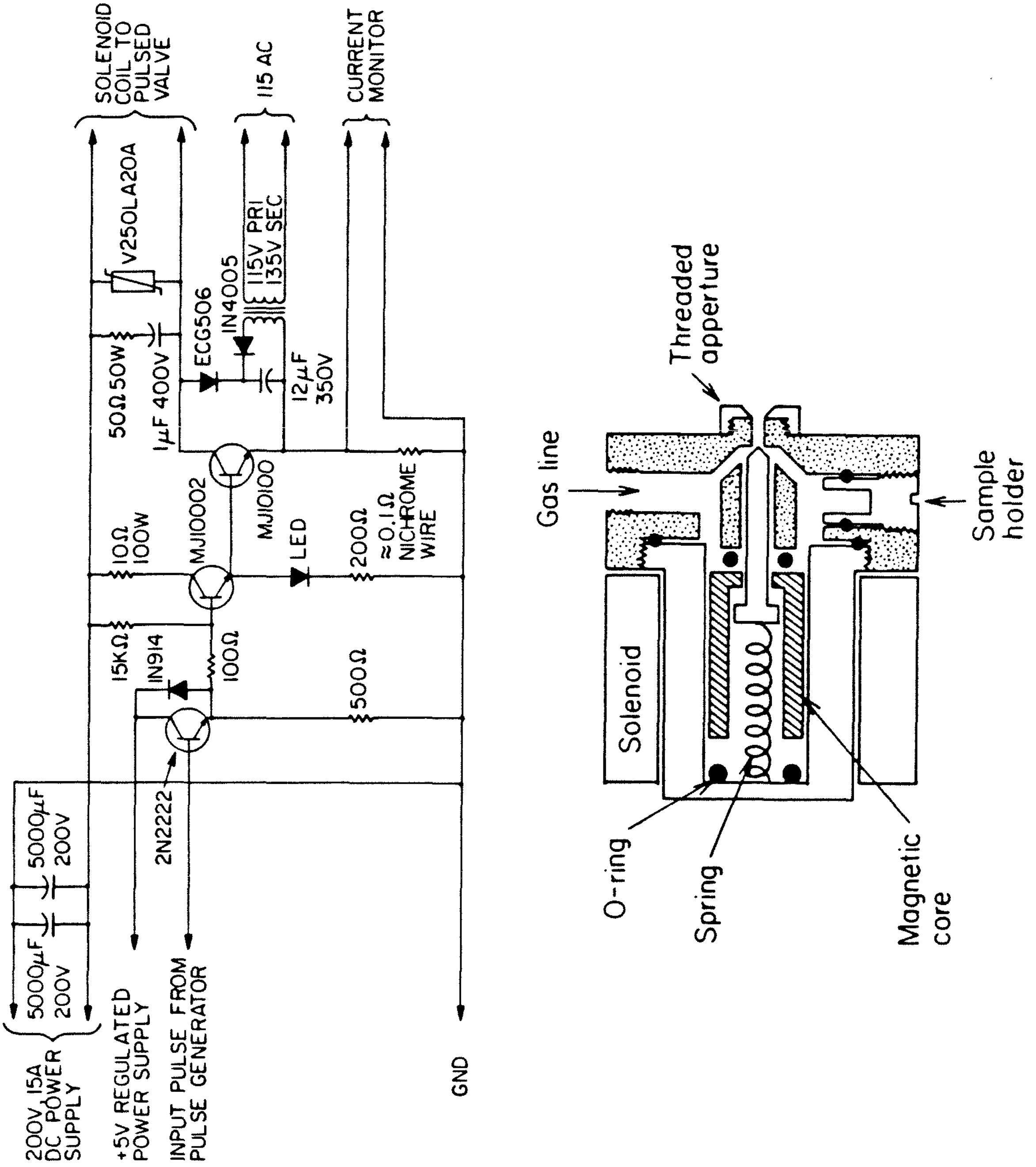
200V, 15A DC POWER SUPPLY
5000μF 200V
5000μF 200V
+5V REGULATED POWER SUPPLY
INPUT PULSE FROM PULSE GENERATOR
2N2222
15KΩ
IN914
100Ω
500Ω
10Ω 100W
MJ10002
MJ10100
LED
200Ω
≈0.1Ω NICHROME WIRE
50Ω 50W
1μF 400V
ECG506
IN4005
12μF 350V
115V PRI 135V SEC
V250LA20A
SOLENOID COIL TO PULSED VALVE
115 AC
CURRENT MONITOR
GND
Gas line
Threaded appertures
Sample holder
Solenoid
O-ring
Spring
Magnetic core

Figure 1

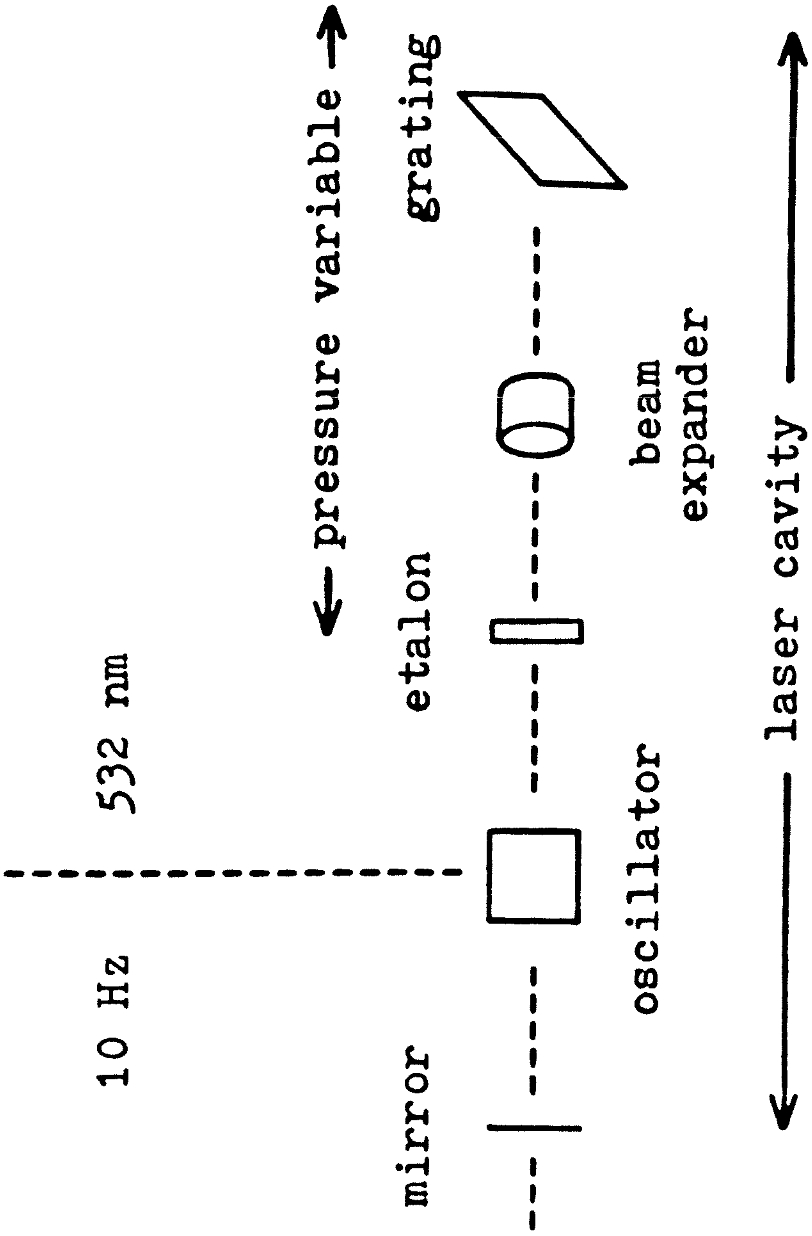
10 Hz
532 nm
pressure variable
mirror
etalon
grating
oscillator
beam
expander
laser cavity

Figure 2

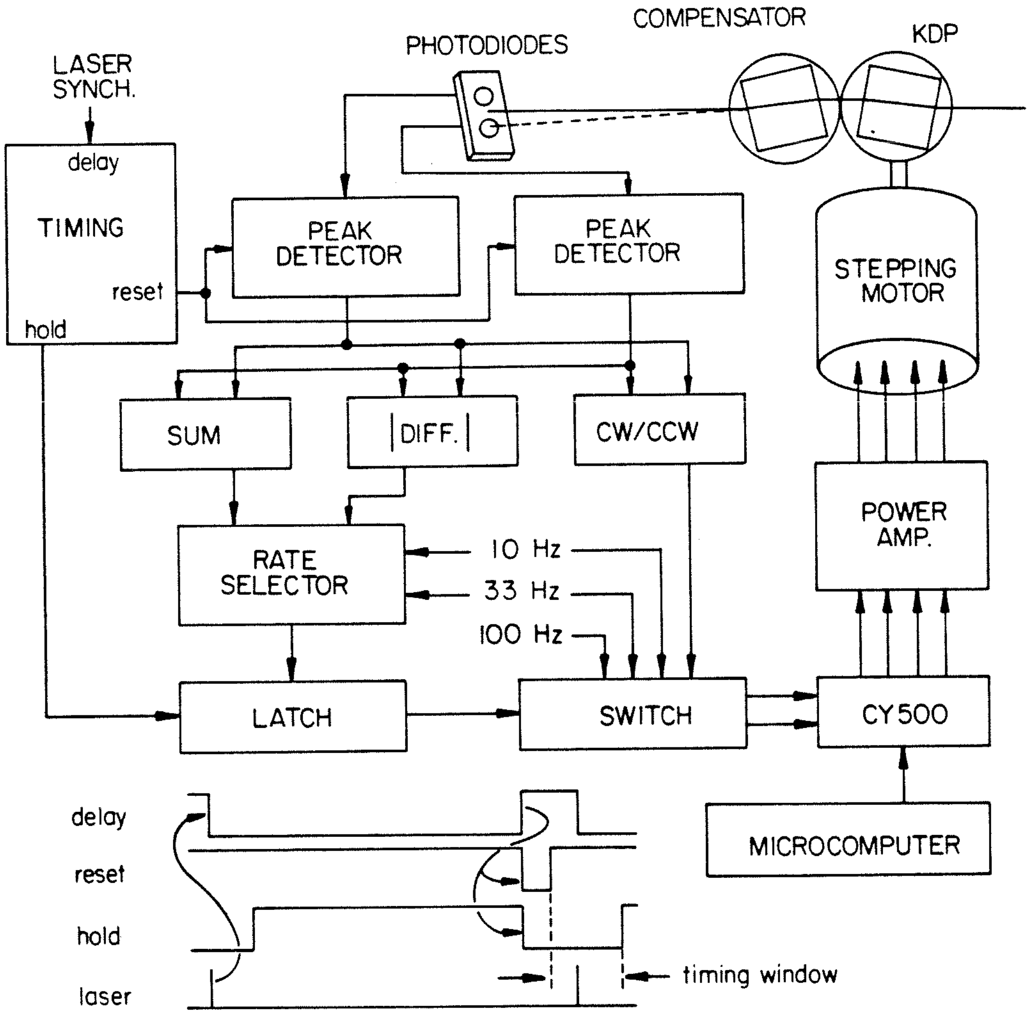
COMPENSATOR
KDP
PHOTODIODES
LASER SYNCH.
delay
TIMING
reset
hold
PEAK DETECTOR
PEAK DETECTOR
STEPPING MOTOR
SUM
|DIFF.|
CW/CCW
POWER AMP.
RATE SELECTOR
10 Hz
33 Hz
100 Hz
LATCH
SWITCH
CY500
MICROCOMPUTER
delay
reset
hold
laser
timing window

Figure 3

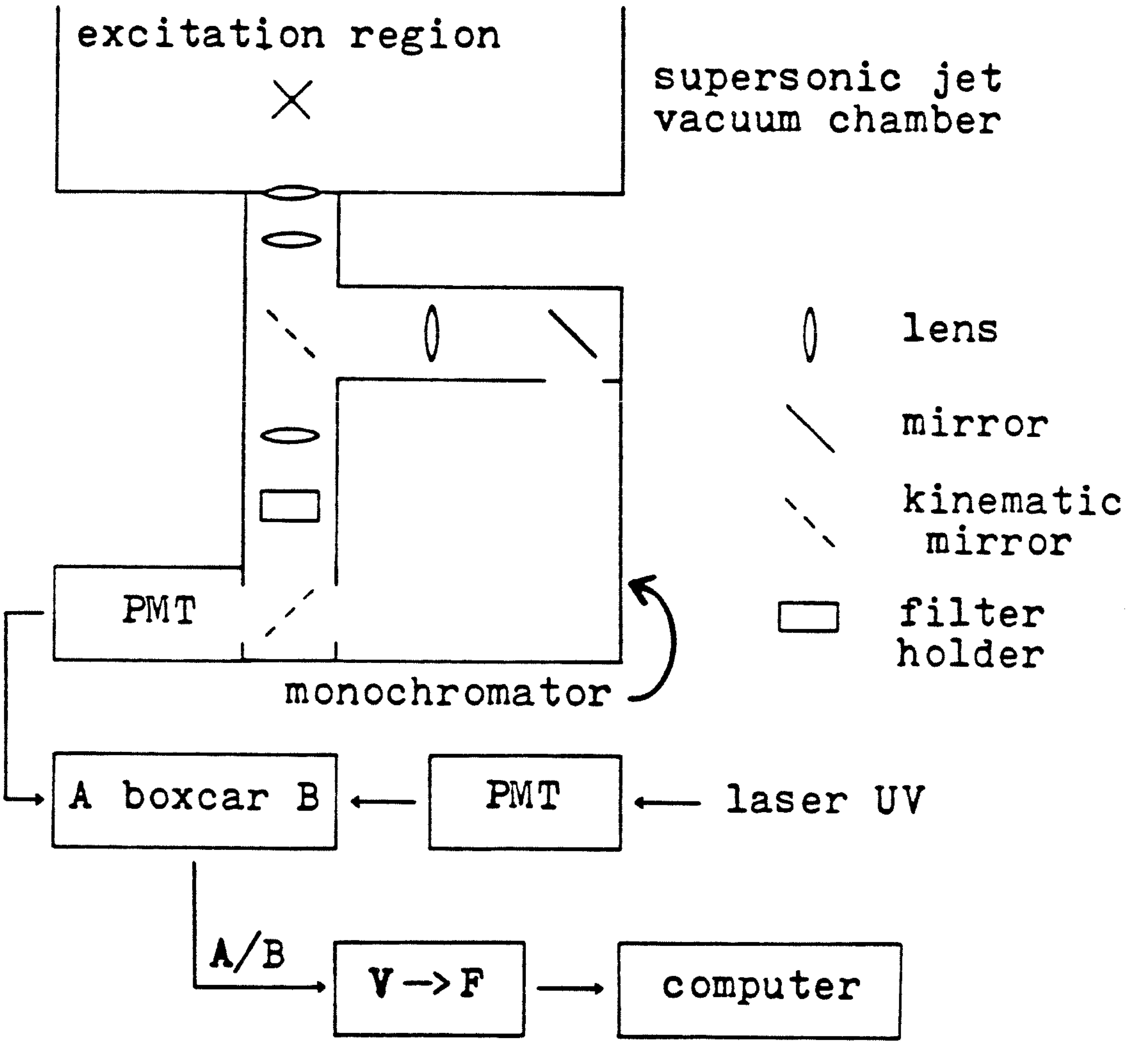
excitation region
supersonic jet vacuum chamber
lens
mirror
kinematic mirror
filter holder
PMT
monochromator
A boxcar B
PMT
laser UV
A/B
V -> F
computer

Figure 4

Diphenylbutadiene in Supersonic Jets:
Spectroscopy and Picosecond Dynamics

Chapter 5

Diphenylbutadiene in Supersonic Jets:

Spectroscopy and Picosecond Dynamics

ABSTRACT

The picosecond dynamics and one- and two-photon excitation of jet-cooled diphenylbutadiene are reported. An A_g^* state is found to lie below the dipole allowed B_u^* state. Isomerization and/or other nonradiative processes are important above a threshold of 1050 cm^{-1} excess energy. Results are compared with those previously obtained for stilbene.

I. INTRODUCTION

Recently, the spectra and *trans–cis* photoisomerization dynamics of stilbene have been reported by Syage *et al.* using a picosecond-jet technique [1]. The stilbene molecules were cooled by supersonic jet expansion and excited with picosecond laser pulses. The low-frequency modes and barrier height for isomerization ($\approx$ 1200 cm^{-1}) were obtained in this study. Here, we wish to extend this work to the next higher member of the all-*trans* α,ω-diphenylpolyenes ($C_6H_5-(C_2H_2)_n-C_6H_5$), diphenylbutadiene (hereafter DPB).

Fully conjugated linear polyenes have been of considerable spectroscopic interest, as they provide simple yet rigorous tests of molecular bonding theories, and have important derivatives that are critical in such processes as vision. In particular, a great deal of effort has been focussed on aromatically-substituted species, which fluoresce strongly and so may be studied readily by a variety of spectroscopic techniques. The simplest spectroscopic properties of these molecules were elucidated decades ago [2]; more recently, attempts have been made to expain various anomalies in terms of the nature of the excited state [3].

These molecules possess an A_g ground state (assuming C_{2h} symmetry), and low-lying B_u^* and A_g^* excited states of roughly comparable energy. In the dipole approximation these states are one- and two-photon allowed, respectively. The energy and oscillator strength of the $B_u^* \leftarrow A_g$ transition decreases and increases, respectively, with increasing chain length. The relative energy of the B_u^* state is very sensitive to the molecular environment, whereas that of the A_g^* is less so; hence the ordering and separation of the excited states is strongly dependent on solvent. This has profound effects on the spectroscopy of these species, as the A_g^* state may be involved in the processes of fluorescence and photoisomerization to *cis* forms [3,4]. The ordering of the excited states has been reliably determined for stilbene and some of the longer chain species but there is still controversy over the ordering in DPB, which may arise from solvent effects masking the actual ordering in the isolated molecule. In longer chain species the A_g^* state is more stabilized relative to the B_u^* state, with near degeneracy occuring for DPB in EPA glass at 77 K [5].

In this paper, we investigate the ordering, separation, and interaction of the A_g^* and B_u^* states of isolated, jet-cooled DPB, and explore the effects of these properties on the decay processes which occur following picosecond laser excitation. We compare the results obtained for DPB with those of stilbene in order to elucidate the mechanisms of isomerization and other nonradiative decays. We also compare our findings with those of Heimbrook *et al.* [6], who very recently reported a vibronic analysis of the one-photon excitation and fluorescence spectra of DPB in a molecular beam. Finally, a preliminary two-photon excitation spectrum is presented.

II. EXPERIMENTAL

DPB (Aldrich, 98%) was recrystallized from methanol; purity was confirmed by melting point and thin layer chromatography. The excitation spectra were obtained using a pulsed molecular beam apparatus [7] (see also Ch. 4), while dispersed and picosecond time-resolved fluorescence were measured on a continuous-flow molecular beam system [8]. The gas-phase absorption spectrum was obtained using a Cary 17 spectrophotometer and a heated quartz cell at 80° C.

Experimental parameters for the pulsed molecular beam systems are as follows. Spectra were taken using 50 psi carrier gas at 140° C following a cooling optimization procedure. The laser to nozzle distance was estimated to be 12 mm, and the pinhole diameter was 0.3 mm, so X/D ≈ 40. The dyes used were methanolic LDS698 and DCM for lower and higher energies, respectively. Scattered laser light and stray room light were separated from the fluorescence by cutoff (Schott GG-375 or GG-395) and UV bandpass (Schott UG-11 or Corning 7-51) filters, respectively.

The excitation source for the continuous-flow molecular beam consisted of a mode-locked argon ion laser pumping a cavity-dumped dye laser. The output was frequency doubled using $LiIO_3$, providing UV pulses with 15 ps and 3 cm^{-1} temporal and spectral pulsewidths, respectively. The sample was expanded through a 0.1 mm aperture at 140° C with a backing pressure of 30 psi He, and passed through the excitation beam 4 mm from the nozzle (X/D ≈ 40). Ambient chamber pressure was 100 μtorr. The dispersed emission was measured by a fast photomultiplier and recorded on an MCA. Fluorescence decays were measured using time-correlated, single-photon counting at the peak emission wavelength (380 nm). Data were transferred to a laboratory computer for storage and analysis.

Frequencies reported were calibrated optogalvanically using an Fe-Ne lamp.

III. RESULTS AND DISCUSSION

A. One-Photon Excitation Spectra

In Figure 1, the excitation spectrum of DPB in a supersonic jet is presented. There are several notable features of this spectrum. First, the spectrum is atypical in its intensity distribution. Second, both the density of bands and their apparent widths increase with increasing excess energy, leading to a somewhat congested spectrum above 30600 cm^{-1}. Finally, there is a rapid dropoff in intensity of the excitation spectrum above 30700 cm^{-1}.

The low energy portion of the excitation spectrum is shown in Figure 2. The lowest energy band is located at 29657 cm^{-1}. If this is taken to be the energy reference point (though it is not necessarily the 0-0 transition, as discussed later), then the prominent bands in the uncongested portion of the spectrum are at excess energies of 134, 238, 372 (238+134), 397, 460, 504 (238+2x134), 529 (397+134), and 582 cm^{-1}. The bands at 134 and 238 cm^{-1} will be assigned as fundamentals below.

The dropoff in intensity of the excitation spectrum above 30700 cm^{-1} can be caused by either a decrease in the absorption cross-section, or the appearance of an efficient nonradiative decay channel. The gas phase absorption at 80°C, depicted in the inset of Figure 1, clearly shows that the absorption is increasing in this region. This indicates that nonradiative decay, which includes isomerization, becomes competitive with emission at these energies. This is further confirmed by the picosecond experiments detailed below.

B. Decay Rates vs. Excess Energy

We have measured the excited state decay rate as a function of energy by exciting modes between 0 and 1823 cm^{-1} excess energy. These rates are plotted as a function of excess energy in Figure 3. There are several interesting aspects to this plot. First, lifetimes up to 1050 cm^{-1} are much longer than anticipated for an allowed electric dipole transition, as discussed below. The lifetimes decrease from 63 ns at 0 cm^{-1} to 31 ns at 1039 cm^{-1}. Second, the lifetimes at very low excess energies fluctuate considerably and so appear to be mode-selective. Third, above 1050 cm^{-1}, the lifetimes decrease rapidly; at 1823 cm^{-1} the lifetime is only 426 ps. Finally, the decay rate of DPB at high excess energies increases more rapidly with increasing excess energy than does that of stilbene.

Considering that (1) allowed electric dipole transitions typically have associated lifetimes of a few nanoseconds, (2) stilbene has a lifetime of 2.7 ns at the origin in the jet [1], and (3) the lifetime of DPB in cyclohexane at room temperature is 1.8 ns [9], the lifetime of DPB would be expected to be a few nanoseconds at low excess energy if the state involved were similarly electric dipole allowed. As the lifetime is actually tens of nanoseconds, it appears that the radiative decay from low energy states is only partially allowed. This would result if a dipole forbidden A_g^* state were coupled to a dipole allowed state, e.g.,the nearby B_u^* state.

C. Two-Photon Excitation and the A_g^* Origin

In order to test for the presence of a low-lying A_g^* state, we attempted to detect fluorescence resulting from two-photon (red) excitation of DPB in order to contrast it with the one-photon (UV) excitation. Two bands were observed at 14811.5 and 14878.5 cm^{-1}, corresponding to one-photon excitation at 29623 and 29757 cm^{-1}. Due to the low intensity of these bands, we could not determine their power dependence. Null scans proved that the signal arose from the DPB sample, and not from the system or external contaminants. The possibility of a trace impurity in the DPB sample cannot be completely ruled out; however, the separation between the bands (134 cm^{-1}) corresponds exactly to the most ubiquitous interval in the one-photon excitation spectrum. These bands are shifted 34 cm^{-1} from the lowest energy pair of bands in the one-photon spectrum.

D. Vibronic Analysis

The prediction of an a_g fundamental at 158 cm^{-1} [10] is consistent with the assignment of the 134 cm^{-1} mode as an a_g fundamental. A low-frequency torsional mode of a_u symmetry is predicted at 33 cm^{-1} [10], the value of the shift between the one-photon and two-photon bands. Vibronic coupling of the A_g^* state to a dipole allowed A_u^* state would produce a partially allowed one-photon vibronic state. Such Herzberg-Teller vibronic coupling is to be expected in a molecule with nearby electronic states [11]. There is an A_u^* state in butadiene only $\approx$ 5000 cm^{-1} above the B_u^* state [12] in DPB it is expected that this Rydberg state will be of even lower energy.

The first intense band in the spectrum is at 238 cm^{-1} excess energy, and it has an intense counterpart at 238+134=372 cm^{-1}. These bands differ from the bands at 0 and 134 cm^{-1} in several important respects. First, the 238 and 372 cm^{-1} bands are approximately three times as intense as the 0 and 134 cm^{-1} bands. Second, the lifetimes of the 238 and 372 cm^{-1} bands are 53 and 48 ns, whereas those of the 0 and 134 cm^{-1} bands are 63 and 61 ns, respectively. Finally, the dispersed fluorescence spectra obtained by exciting at 0 and 238 cm^{-1} are significantly different. Since the B_u^* state is only slightly higher in energy than the A_g^* state, a relatively intense Herzberg-Teller false origin is expected due to coupling between these two electronic states by a b_u vibration. The above observations are therefore consistent with the 0 and 238 cm^{-1} bands being false origins of the A_u^* state caused by vibronic coupling through a_u (34 cm^{-1}) and b_u (238+34=272 cm^{-1}) vibrations, respectively [13].

This conclusion differs from that of Heimbrook *et al.* [6]. We assign two important bands in the one-photon excitation spectrum as Herzberg-Teller false origins. Although Heimbrook *et. al.* agree on the assignment of the second false origin, they interpret the first false origin as the true A_g^* origin and ascribe its appearance to static or rotationally-induced distortion. As discussed above, our two-photon origin is clearly lower in energy than the first one-photon origin, indicating the false nature of the latter. Hence distortion is not required to explain the data.

Finally, note that the complexity of the excitation spectrum at higher excess energies indicates that accurate mode assignment in this region would require a full understanding of the vibronic interactions present.

E. Isomerization and Other Nonradiative Decay Channels

The ordering of the states is crucial in determining lifetime behaviors of stilbene and DPB. In stilbene, B_u^* lies below A_g^*; S_0, S_1, and S_2 have minima, minima, and maxima, respectively, at $\vartheta=0°$. As the ethylenic bond is twisted (as would occur when the molecule undergoes torsional excitation), there is an avoided crossing of the S_1 and S_2 potential curves (depicted schematically in Figure 3, Ref. 1). This creates a potential barrier which prevents molecules of low excess energy from accessing large torsional angles. Molecules with excess energy greater than the barrier height can access large torsional angles, where a nonradiative decay to an S_0 maximum is possible. Consequently, the barrier height represents an isomerization threshold [1].

Since the A_g^* state in DPB is below the B_u^* state, a potential energy diagram similar to that of the longer diphenylpolyenes [4] is the best choice for illustrative purposes (see Figure 4), although it may not be a perfect description of DPB. Again, a barrier results from an avoided curve crossing, but unlike the case of stilbene, the allowed state is higher in energy, and the lower state is accessable only through vibronic coupling. Hence, distinct behaviors might be predicted for different energy regions: (1) below the A_g^* barrier, there should be relatively weak fluorescence, due to vibronic coupling, and slow nonradiative decay, in part via barrier tunneling; (2) above the A_g^* barrier, isomerization and/or other nonradiative processes should become more important, as larger torsional angles may be accessed. If this picture is correct, the isomerization threshold would be ≈ 1050 cm^{-1}, which is close to that found for stilbene in the jet (≈ 1200 cm^{-1}) [1]. The value for DPB in solution is 1650 ± 150 cm^{-1} [14]. (However, it should be noted that the ordering and separation of the A_g^* and B_u^* states is different in these cases.) Clearly this places a lower bound of 1050 cm^{-1} on the separation of the A_g^* and B_u^* states in isolated DPB molecules. Finally, it is reasonable to conclude that the more rapid increase of decay rate with increasing energy in DPB reflects its larger size and hence its more rapidly increasing density of states.

IV. CONCLUSIONS

Our principal results for jet-cooled diphenylbutadiene are as follows:

(1) The A_g^* state is below the B_u^* state as determined by two-photon band positions, one-photon excitation spectrum intensities, and fluorescence lifetimes. The A_g^* state is Herzberg-Teller vibronically coupled to nearby electronic states, resulting in two false origins in the one-photon excitation spectrum. This is deduced from comparison of the one-photon and two-photon excitation spectra and correlation of mode-dependent lifetimes and dispersed fluorescence spectra.

(2) Measurement of decay rate *vs.* excess energy indicates the presence of a 1050 cm^{-1} threshold for isomerization and/or other nonradiative processes, close to that of stilbene in the jet. Above this threshold, the decay rate increases more rapidly in DPB than in stilbene, reflecting the larger size and more rapidly increasing density of states of DPB.

REFERENCES

[1] J. A. Syage, Wm. R. Lambert, P. M. Felker, A. H. Zewail, and R. M. Hochstrasser, *Chem. Phys. Letts. 88*, 266 (1982).

[2] J. Dale, *Acta Chem. Scand. 11*, 971 (1957).

[3] B. S. Hudson and B. E. Kohler, *J. Chem. Phys. 59*, 4948 (1973); W. A. Yee, J. S. Horowitz, R. A. Goldbeck, C. M. Einertz, and D. S. Kliger, *J. Phys. Chem. 87*, 380 (1983), and references therein.

[4] J. B. Birks, G. N. R. Tripathi, and M. D. Lumb, *Chem. Phys. 33*, 185 (1978).

[5] J. A. Bennett and R. R. Birge, *J. Chem. Phys. 73*, 4234 (1980).

[6] L. A. Heimbrook, B. E. Kohler, and T. A. Spiglanin, *Proc. Natl. Acad. Sci. USA 80*, 4580 (1983).

[7] B. W. Keelan, J. A. Syage, J. F. Shepanski, and A. H. Zewail, *Proceedings of the International Conference on Lasers 1983*, San Francisco, California, Society of Optical and Quantum Electronics (STS Press, McLean, Virginia, 1985), p. 718.

[8] Wm. R. Lambert, P. M. Felker, and A. H. Zewail, *J. Chem. Phys. 81*, 2217 (1984).

[9] J. B. Birks and D. J. Dyson, *Proc. R. Soc. London Ser. A 275*, 135 (1963).

[10] B. M. Pierce and R. R. Birge, *J. Phys. Chem. 86*, 2651 (1982).

[11] G. Herzberg, *Molecular Spectra and Molecular Structure*, Vol. III, Electronic Spectra and Electronic Structure of Polyatomic Molecules (Van Nostrand Reinhold Co., New York, 1966), pp. 66-8, 137-41.

[12] M. A. C. Nascimento and Wm. A. Goddard III, *Chem. Phys.* *53*, 251 (1980).

[13] A b_u mode predicted at 351 cm^{-1} [10] likely corresponds to the 272 cm^{-1} mode observed experimentally. This difference, like that between the predicted 157 cm^{-1} and observed 134 cm^{-1}, is probably due to the near degeneracy of the lowest lying states which, in general, reduces the frequency of the active modes of the lowest state. We considered the possibility that the b_u mode predicted at 53 cm^{-1} [10] is responsible for the 0 cm^{-1} excess energy false origin. However, the magnitude of the frequency shift (36 %) is much greater than that of the 272 cm^{-1} b_u mode (23 %) or the 134 cm^{-1} mode (17 %).

[14] S. P. Velsko and G. R. Fleming, *J. Chem. Phys.* *76*, 3553 (1982).

FIGURE CAPTIONS

Figure 1: One-photon excitation spectrum of DPB in a supersonic jet, normalized for laser intensity. Inset shows gas-phase absorption at 80 °C; note that the emission in the jet becomes undetectable at energies where the gas-phase absorption is still strong.

Figure 2: Comparison of one-photon and two-photon excitation signals (see text). The lower trace is a high resolution one-photon excitation scan of the lowest energy bands observed. The upper trace shows the two-photon excitation signal plotted as a function of twice the excitation energy. Note that the two two-photon bands are displaced 34 cm^{-1} to the red of the two lowest energy bands observed in the one-photon spectrum.

Figure 3: Excited state decay rates of DPB (circles) as a function of excess vibrational energy, measured relative to the lowest energy band in the one-photon excitation spectrum (see text). Compared to stilbene (triangles), DPB has longer lifetimes at low excess energy, and the more rapid increase of decay rate at high excess energy. The inset shows the common logarithms of the decay rates *vs.* excess energy, which accentuates the presence of a 1050 cm^{-1} threshold, indicated by an arrow.

Figure 4: An illustrative potential energy diagram for DPB. The avoided crossing of the A_g^* and B_u^* curves results in a barrier to rotation (of height Δ) about either of the ethylenic bonds in the A_g^* state.

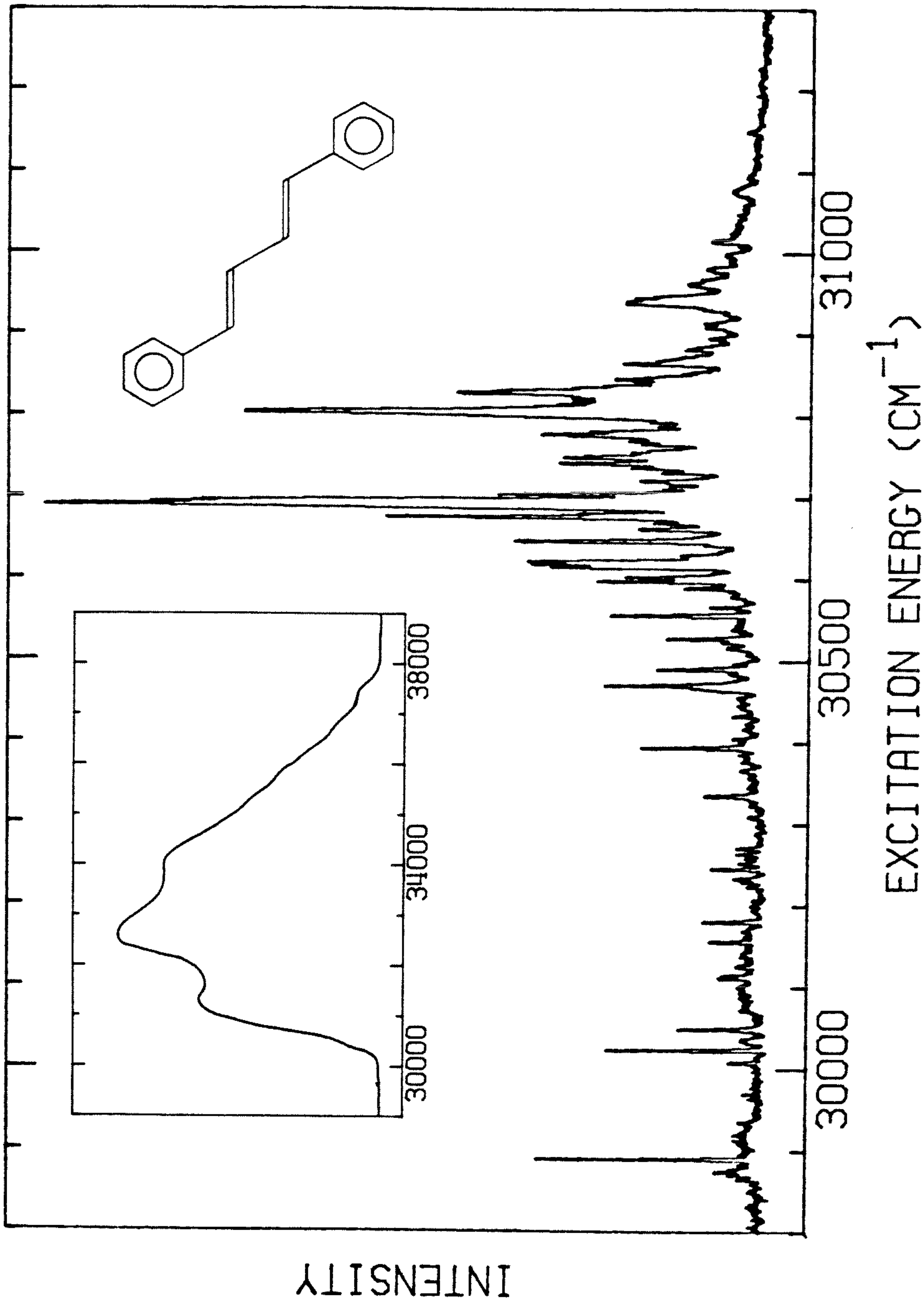
INTENSITY
EXCITATION ENERGY (CM^{-1})
30000
30500
31000
30000
34000
38000

Figure 1

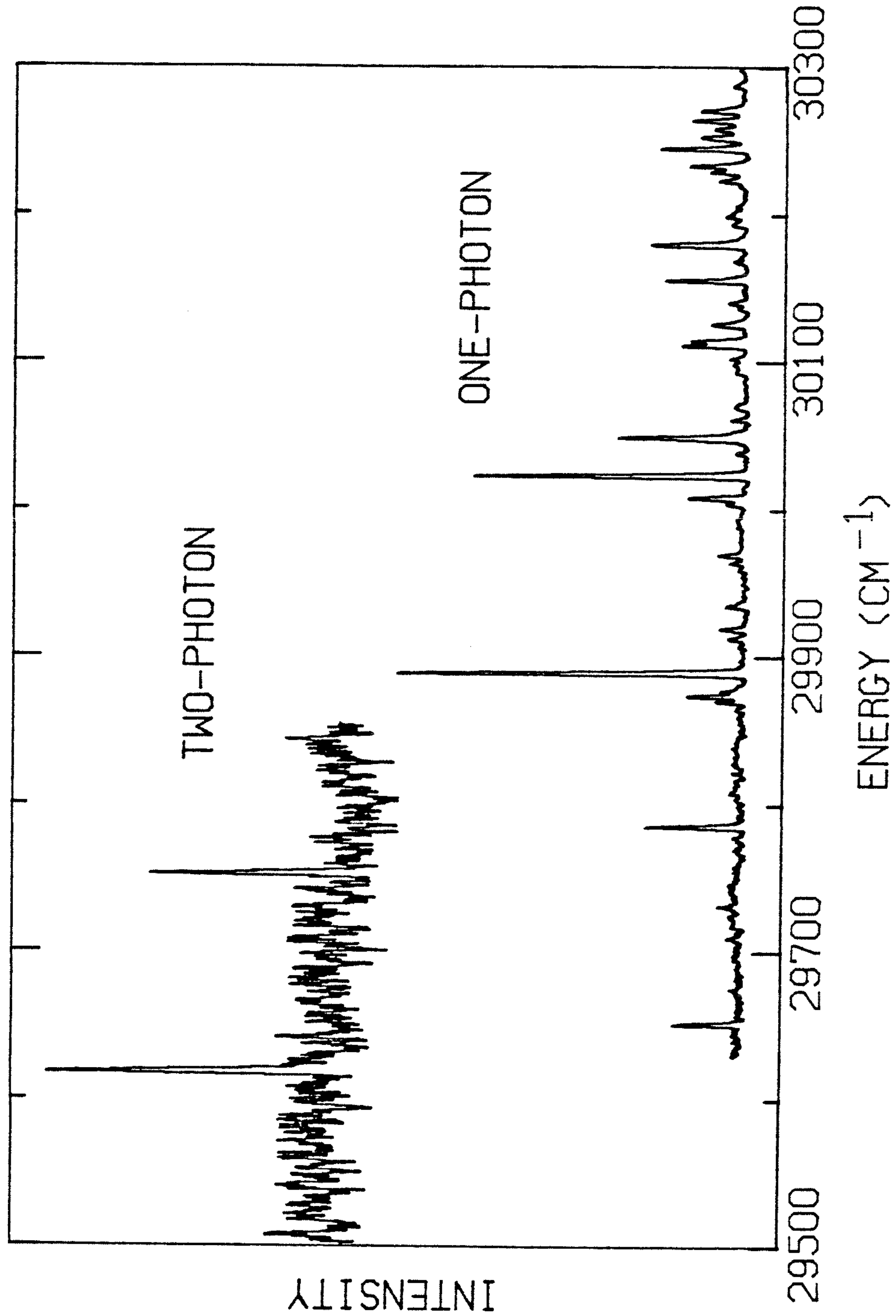
INTENSITY
ENERGY (CM^{-1})
29500
29700
29900
30100
30300
TWO-PHOTON
ONE-PHOTON

Figure 2

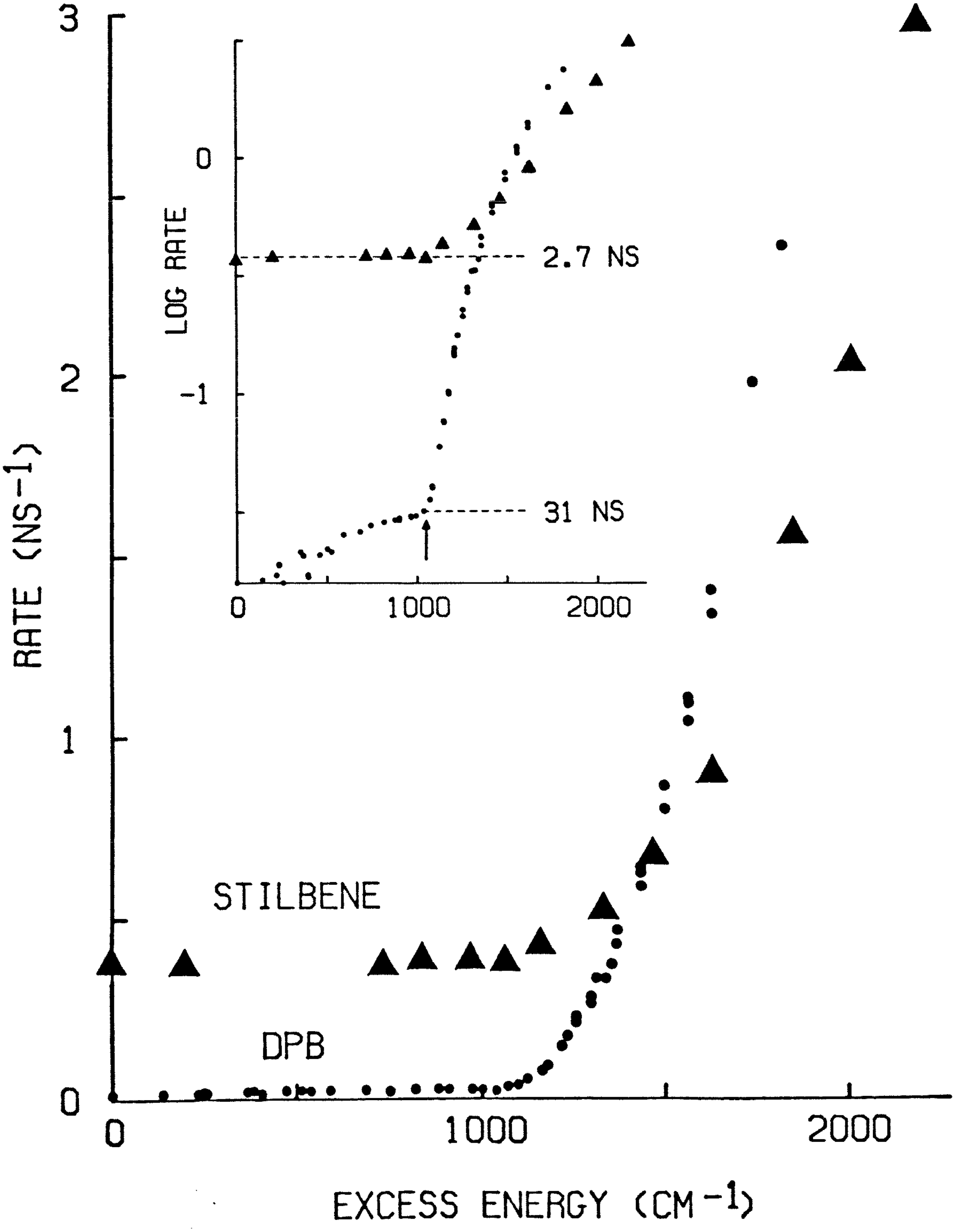
3
2
1
0
RATE (NS-1)
0
1000
2000
EXCESS ENERGY (CM-1)
STILBENE
DPB
LOG RATE
0
-1
2.7 NS
31 NS
0
1000
2000

Figure 3

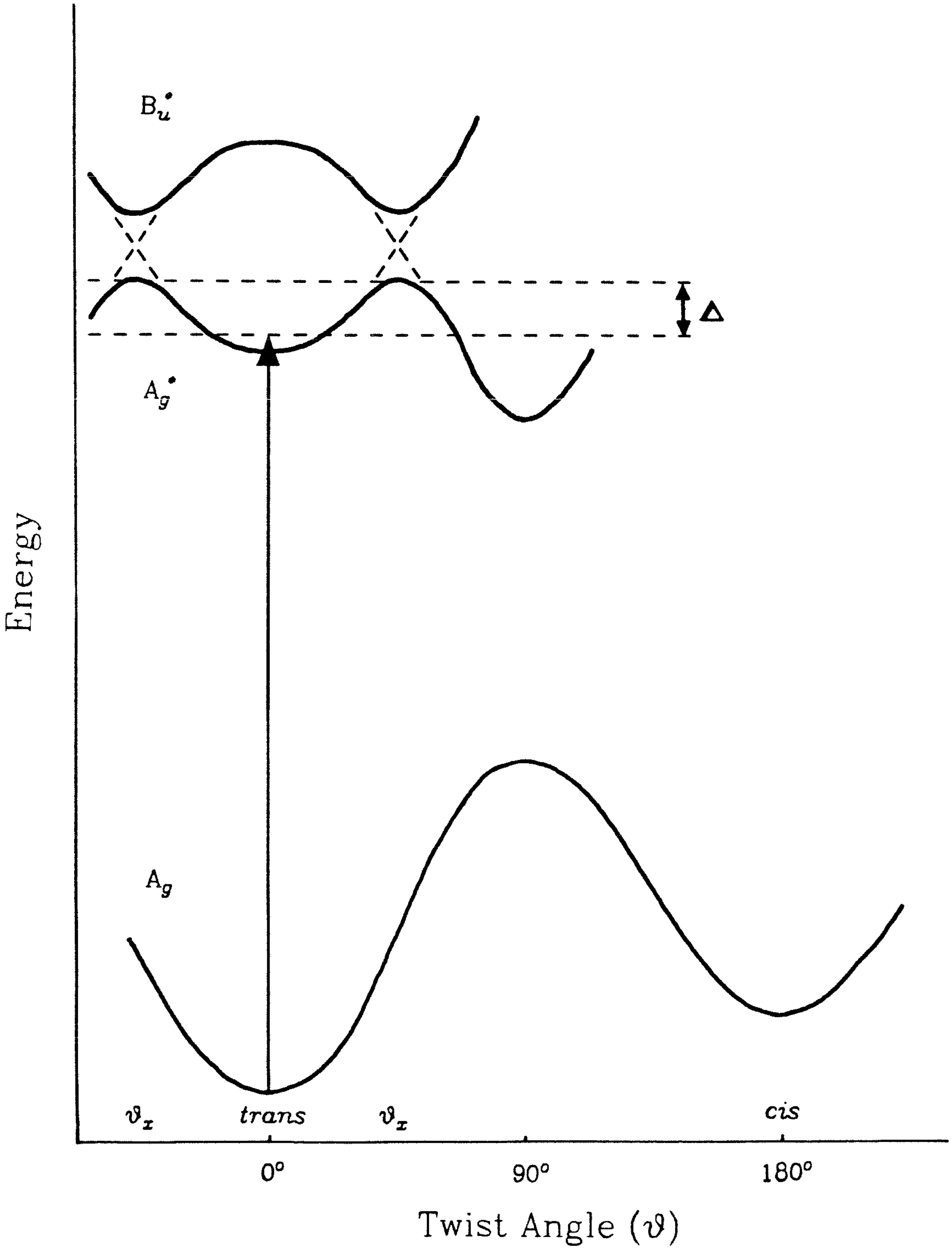

B_u^*
A_g^*
Δ
A_g
Energy
ϑ_x
trans
ϑ_x
cis
0°
90°
180°
Twist Angle (ϑ)

Figure 4

Rotational Band Contour Studies of Single Vibronic Levels in Jet-cooled Stilbene

Chapter 6

Rotational Band Contour Studies of Single Vibronic Levels in Jet-cooled Stilbene

ABSTRACT

The rotational band contours of approximately 40 vibrational levels in the first excited singlet state (S_1) of supersonic jet-cooled stilbene are obtained and analyzed using computer simulations. No substantial differences are found in contour shapes of different levels, which is attributed to low symmetry and/or extensive torsional motion. Approximately 35 levels are studied by frequency-resolving their emission, but no dependence of contour shape on detection conditions (specific mode detected, relaxed *vs.* unrelaxed emission) is observed. The use of selective detection to resolve overlapping levels in excited states is discussed qualitatively and quantitatively, with excellent agreement between experiment and theory. Finally, high-resolution (0.05 cm^{-1}) maps of the two known regions in S_1 exhibiting evidence of dissipative intramolecular vibrational redistribution (IVR) are presented to clarify the level structure involved.

I. INTRODUCTION

We have recently used rotational band contour analysis with frequency-resolved detection to analyze symmetries of, and interactions between, vibrational levels in anthracene S_1 [1]. Studies of high-symmetry molecules by complementary narrow-band excitation and resolved detection have yielded information on Fermi resonances [1], IVR [1-4], Coriolis perturbations [5], and rotational structure [6,7]. Narrow-band excitation has also been used to obtain sub-Doppler resolution spectra of rotational envelopes, allowing elucidation of coupling mechanisms in the channel three region of benzene [8,9].

In this paper, we extend the methods of our anthracene work [1] to stilbene (*trans*-1,2-diphenylethylene). Our group has studied the dynamics [10-13] and spectroscopy [14] of this molecule in supersonic jets to characterize the processes of photoisomerization and IVR in the isolated molecule. Rotational band contour analysis can potentially contribute to the understanding of these phenomena by (1) providing symmetry assignments for the vibrational levels in S_1; (2) clarifying level structure in regions with overlapping transitions; and (3) providing frequency domain data which is complementary to temporal data. The latter allows assessment of the spectral manifestations of the decay character (exponential, quantum beat modulated, or biexponential).

Approximately 40 levels in stilbene S_1 in the 0 - 1350 cm^{-1} vibrational energy region are studied herein. Unlike the case of anthracene, no differences are found in the contour shapes of the different levels. This is attributed to the lower symmetry and/or lesser rigidity of stilbene compared to anthracene. High-resolution (0.05 cm^{-1}) maps of different levels are analyzed with respect to time-resolved data, demonstrating the difficulty of inferring temporal behavior from frequency domain data.

II. EXPERIMENTAL

Our experimental system, except for the pressure-tuning apparatus, has previously been described in detail in the literature [15]; a full description may be found in Chapter 4. The dyes used in this study were twice-normal concentration R640 (R = rhodamine) in methanol (0 - 600 cm^{-1}), normal concentration R640 in ethanol (600 - 950 cm^{-1}), and 20 % normal concentration R640 in normal concentration methanolic R590 (950 - 1350 cm^{-1}). Energy transfer was very efficient in the latter case [16], and the dye mixture could probably have been used at lower energies than stated, perhaps eliminating the need for the ethanolic dye solution. Excitation scans were obtained at a 353 K sample temperature, contours and dispersed fluorescence spectra at 383 K. Carrier gas backing pressure (neon or nitrogen) was 50 psi throughout. The laser to nozzle distance and pinhole diameter were 12 mm and 0.5 mm, respectively, so X/D = 24. Doubling the laser-to-nozzle distance had no effect on the excitation spectrum near the origin, indicating optimal cooling at X = 12 mm. When the fluorescence emission was not dispersed with a monochromator, it was passed through a Schott WG-345 cutoff filter to remove scattered laser light and a Schott UG-11 UV bandpass filter to remove stray visible light. Pressure-tuning was done with nitrogen, which gives a full scan range of $\approx$ 23 cm^{-1} at the electronic origin (310.2 nm).

III. RESULTS AND DISCUSSION

A. Preliminary Considerations

In the gas phase, electron diffraction data indicates that stilbene is non-planar, with the phenyl groups rotated approximately 30° in opposite senses, resulting in C_2 symmetry [17]. Supporting evidence is provided by photoelectron spectroscopy [18] and Raman spectroscopy of melts [19]. Nonetheless, it is convenient to use C_{2h} (planar) symmetry designations which correlate to C_2 designations by dropping u and g subscripts.

We take the long in-plane axis to be the x-axis, the short in-plane axis to be y, and the out-of-plane axis to be z. With this convention, the ground electronic state (S_0) is A_g and the first excited singlet state (S_1) B_u. The transition is $\pi \rightarrow \pi^*$, and is polarized along the long x-axis, as indicated by a single-crystal absorption study [20] and theoretical calculations [21]. However, as B_u transforms like both x and y in C_{2h}, there is no symmetry restriction on the orientation of the transition moment within the molecular (x-y) plane.

From the vibrationless level of S_0, the only level appreciably populated in the molecular beam, $A_g a_g \rightarrow B_u a_g$ transitions (capital letters denote electronic symmetries, small letters vibrational symmetries) are fully (dipole and Franck-Condon) allowed, and are expected to predominate in the excitation and emission spectra. As only the vibrational symmetry in S_1 varies in excitation, transitions may unambiguously be denoted by their S_1 vibrational symmetry, a_g in this case. As A_u transforms like z in C_{2h}, b_g vibrations potentially might arise from Herzberg-Teller vibronic coupling [22] to the A_u states ≈ 23000 cm^{-1} away [21]. Vibronic coupling is responsible for the unusual excitation spectrum of diphenylbutadiene, the next higher polyene analog [23]. With reduced C_2 symmetry in stilbene, a_u ($\rightarrow a$) vibrations become Franck-Condon-allowed, and are termed out-of-plane vibrations, as they are induced by the nonplanarity of the molecule. The transition moment, however, would still lie in-plane, as B transforms like x and y in C_2.

Using the gas-phase electron diffraction data for stilbene (C_2 symmetry, phenyl groups rotated 30°) [17], we have calculated the rotational constants of stilbene to be A = 0.08927 cm^{-1} (x-axis), B = 0.00863 cm^{-1} (y-axis), and C = 0.00821 cm^{-1} (z-axis). Stilbene is close to a prolate symmetric top, with an asymmetry parameter [24] of κ = -0.9896. Stilbene corresponds most closely to "Case 10" (2C/B = 1.90, 1-C/A-C/B = -0.0433) in the comprehensive survey of rotational band contour shapes in asymmetric tops by Ueda and Shimanouchi [25].

Stilbene in C_{2h} (or C_2) has six pairs of equivalent fermions (protons) giving a total of 2^{12} = 4096 spin states. Since the pairs transform identically, character analysis need only be performed for one pair. The 2^2 = 4 spin functions for a pair decompose into irreducible representations as follows: $\Gamma_{pair} = 3A_g + B_u$. Raising this to the sixth power for the six equivalent pairs, $\Gamma_{tot} = 2080A_g + 2016B_u$. The coefficients of the irreducible representations are their statistical weights; note 2080 + 2016 = 4096 = 2^{12}. Due to the appreciable number of fermions present in this molecule, it is not surprising that the statistical weights for the two symmetries are very close.

It should be emphasized that the above analyses neglect the dynamic nature of the molecular symmetry. Consideration of the effect of large amplitude torsional motion requires permutation group analysis [26], which is beyond the scope of this work.

Finally, in this paper, transitions and vibrational levels are denoted by A_n^m, where A is the mode number, and n and m are the number of quanta of mode A in the ground and excited states, respectively. Mode numbering and frequencies follow the previous work from this laboratory [14].

B. Analysis of Rotational Band Contour Shapes

The rotational band contours of approximately 40 levels in S_1 below 1350 cm^{-1} vibrational energy were obtained detecting total emission. No substantial differences were observed in the contour shapes of different levels, although some minor differences were noted. In particular, the P-R branch ratios were somewhat variable from level to level. The contours of a typical level (S_1 + 987 cm^{-1}) in neon and nitrogen are shown at the top of Fig. 1.

We employed a well-documented Fortran program [27] to simulate the experimental contours, using the rotational constants and statistical weights given above. Sufficiently large J values were included in the simulation so that an appreciable increase in the J values included had no effect on the shape of the simulated contour. A resolution of 0.1 cm^{-1} (twice the laser bandwidth) was used, as this was found to be the best value for anthracene simulations employing the same apparatus and conditions [1]. Distortion was assumed to be negligible in both S_0 and S_1; although, as discussed above, this may not be the case. In order to reduce the number of adjustable parameters, the rotational constants in S_1 were assumed to differ from those in S_0 by a multiplicative factor only. This multiplicative factor and the temperature were the only two adjustable parameters. The polarization was assumed to be along the long A-axis, as discussed previously.

The temperature was varied to match the P-R branch separation of the experimental contours, then the multiplicative factor varied to match the P-R branch relative intensities. The temperatures for neon and nitrogen were 3 K and 10 K respectively, consistent with the better cooling efficiency of neon. These values are similar to those obtained for anthracene, 2-3 K for neon and

8-15 K for nitrogen.

The relative magnitudes of the rotational constants in S_0 and S_1 had a strong effect on the relative P-R branch intensities. A 1 % increase in the rotational constants in S_1 relative to S_0 yielded a substantially better fit than no increase or a 2 % increase. The best simulations are shown in the middle of the figure.

Using the above parameters, simulated contours for B-axis and C-axis contours at 10 K were also generated, and are shown at the bottom of Fig. 1. Given the lack of symmetry restriction on the in-plane polarization, hybrid bands with contours intermediate between A- and B-axis simulations may occur. This could partly account for the widths of the experimental contours being greater than those of the simulations, as the B-axis simulation is quite broad. *No* experimental contours resemble the C-axis simulation, indicating that Herzberg-Teller vibronic coupling is negligible in stilbene S_1.

In anthracene, where x, y, and z belong to different irreducible representations, two distinct types of contours with orthogonal polarizations (one induced by vibronic coupling) were readily distinguished experimentally [1]. Also, the anthracene contours had very distinct and reproducible P-(Q)-R structures. The contrasting behavior in stilbene is apparently due to the lack of symmetry restrictions on polarization in the molecular plane and/or its torsional nonrigidity.

C. Effect of Detection Conditions on Rotational Band Contours

In anthracene, dependence of the rotational band contour shape on detection conditions has been demonstrated [1,28]. After excitation to S_1 + 1380 cm^{-1}, detection at S_0 + 1460 cm^{-1} yielded a "typical" contour. Detection at S_0 + 389 cm^{-1}, where quantum beats had been observed [12], produced a contour with a much greater P-R branch separation, corresponding to a suppression of low J values. Approximately 35 levels in stilbene S_1, including 12 of 13 levels exhibiting unusual temporal behavior (quantum beats or fast decays), were studied using resolved detection. Despite considerable effort, no convincing contour shape dependence on detection conditions could be documented.

A typical resolved detection study is depicted in Fig. 2. Emission from the S_1 + 789 cm^{-1} level ($23^1 25^1$) is shown in the top half of the figure. The emission consists of sharp structure superimposed on a broad (redistributed) background, which is typical of intermediate vibrational energies. At lower energies sharp structure predominates, while at higher energies the emission is nearly continuous. This continuous (relaxed) emission results from IVR and spectral congestion [29], and hence is favored at higher vibrational energies, where the density of states is greater [11]. The unusual intensity distribution of this spectrum has been explained by Franck-Condon analysis [14]; note especially the absence of a 25^1_1 transition. Delocalization of the ethylenic π electrons upon excitation causes a large geometry change, which results in virtually complete destructive interference between the 25^1 and 25_1 level wavefunctions. If there were no geometry change upon excitation, strongly constructive interference between these wavefunctions would result in a strong 25^1_1 transition.

Detection of total emission yields contour A in the lower half of the figure. Resolved detection of sharp emission only (labelled B above), broad emission only (C), or sharp emission due to another transition (D) produces contours B, C, and D. These four contours are identical within experimental reproducibility. The slight obscuring of P-R structure with resolved detection relative to total detection is due to the greatly reduced signal when the emission is resolved. Hence there is no apparent mode dependence (compare B and D) or structural dependence (compare B or D to C). Since the total emission is a superposition of sharp and broad emission, it follows that the total emission contour should be identical with the resolved detection contours, as it is experimentally. Although the observation of detection dependence may be hampered in stilbene by its nonrigidity or low symmetry, as discussed earlier, it still would appear that observation of detection dependence requires rather special conditions.

D. Examples of Selective Detection Enhancement of Overlapping Levels in S_1

It is often the case that two or more overlapping levels in an excited state, which are not strongly coupled, will have substantially different emission (dispersed fluorescence) spectra. In this case, the differences in emission can be exploited to better resolve the overlapping levels. A representative example of this method, which we refer to as selective detection enhancement, is depicted in Fig. 3.

First, an excitation profile is obtained collecting total emission (contour A above). This shows overlapping levels at S_1 + 590/592 cm^{-1} (previously listed as 590.7 and 592.1 cm^{-1} [14]), corresponding to 23^1 and 25^3_0 respectively. Narrow-band (0.05 cm^{-1}) excitation of 590 and 592 cm^{-1} yields emission spectra 1 and 2 (below), respectively. These spectra are well structured, composed of sharp structure with little broad background emission.

If, instead of collecting total emission, only a specified range of emission is detected, then the excitation profile is expected to change. For example, at position D (below), the emission from 592 cm^{-1} is substantial, while that from 590 cm^{-1} is negligible, so detection at D produces a strong enhancement of 592 cm^{-1} in the excitation profile (contour D, above). Analagously, at position C the 590 cm^{-1} emission is much stronger than 592 cm^{-1}, so 590 cm^{-1} is enhanced in contour C. Emission at B due to 590 and 592 cm^{-1} is of comparable magnitude, thus little enhancement is observed in contour B relative to the total emission contour A.

This method of selective detection is quite useful for resolving overlapping levels, and can be especially helpful when trying to obtain contour shapes for each level to allow assignment of symmetries [1]. The effectiveness of the method depends upon the levels having differences in emission profiles. This is illustrated by two additional examples of selective detection, shown in Fig. 4 (S_1 + 389/391 cm^{-1}) and Fig. 5 (S_1 + 425/427 cm^{-1}). As the emission becomes more similar in the series Figs. 3, 4, and 5, the achievable enhancement decreases correspondingly.

E. Prediction of Effect of Selective Detection from Emission Spectra

Fluorescence excitation and dispersed fluorescence spectra probe the *same* fundamental molecular process: absorption of a photon at $\nu_{exc} \pm \Delta\nu_{exc}$ followed by emission of a photon at $\nu_{\text{det}} \pm \Delta\nu_{\text{det}}$. The probability of this process occurring can be determined from either spectrum (provided there are no saturation effects), and the same result should be obtained. In the former case, the detector is set to collect emission in the range $\nu_{\text{det}} \pm \Delta\nu_{\text{det}}$, and an excitation spectrum including the range $\nu_{exc} \pm \Delta\nu_{exc}$ is taken. The area under the excitation profile within the limits $\nu_{exc} \pm \Delta\nu_{exc}$ is proportional to the probability of the specified process. In the latter case, molecules are excited by a fixed source spanning the range $\nu_{exc} \pm \Delta\nu_{exc}$, and a dispersed fluorescence spectrum including the range $\nu_{\text{det}} \pm \Delta\nu_{\text{det}}$ is taken. The area under the dispersed fluorescence profile within the limits $\nu_{\text{det}} \pm \Delta\nu_{\text{det}}$ is then proportional to the probability of the same specified process. Thus,

$$k_{ex}A_{ex} = k_{df}A_{df} \tag{1}$$

where A_{ex} and A_{df} are the areas under the excitation and dispersed fluorescence profiles, and k_{ex} and k_{df} are the constants of proportionality. These constants of proportionality depend only upon experimental parameters; if these are held constant, then different spectra may be quantitatively compared. Then, for a second process (different $\nu_{exc} \pm \Delta\nu_{exc}$, $\nu_{det} \pm \Delta\nu_{det}$, or both),

$$k_{ex}A'_{ex} = k_{df}A'_{df} \tag{2}$$

Now Eqs. (1) and (2) may be combined into the more useful form

$$A_{ex}/A'_{ex} = A_{df}/A'_{df} \tag{3}$$

Note that no reference has been made to level structure, coupling, etc. in either S_0 or S_1; this result is independent of these considerations.

The relevance of these observations to the present case of selective detection is as follows: one need only obtain the calibrated dispersed fluorescence spectrum of each of N levels in S_1 to predict the relative intensities of the N levels in *any* resolved detection excitation spectrum. The area ratios in the excitation spectrum will, by Eq. (3), be identical to the area ratios in the dispersed fluorescence spectra.

From a practical standpoint, several complications arise. The emission profile of the excitation source (e.g. gain profile of a laser) and the sensitivity profile of the detector (e.g. the slit profile of a monochromator) must be convoluted into the area measurements. More seriously, obtaining a dispersed fluorescence spectrum of *one* level is difficult if it is overlapping other levels (precisely when the technique of selective detection is most useful). Eq. (3) still holds -- it is independent of level structure, coupling, etc. -- but its use becomes more complicated. The most general approach to this problem is to obtain dispersed fluorescence spectra at regular intervals, and assemble the excitation profile in a piecewise manner. Unfortunately, this usually requires many more than N dispersed fluorescence spectra. When practical, it is preferable to obtain N dispersed fluorescence spectra in which a relatively "pure" portion of each contour is excited, so that emission from the level of interest is enhanced relative to emission from overlapping levels. In the case of two overlapping levels, this is readily accomplished by exciting the low-energy side of the lower energy contour and the high-energy side of the higher energy contour.

In addition to enhancement for the purpose of resolution, this selective detection scheme has been utilized to estimate anharmonic coupling strengths in anthracene [1]. As the coupling strength increases, the emission profiles of the uncoupled levels are effectively "mixed" and so become more similar. The result is that there is no detection range for which complete enhancement can be obtained; the maximum achievable enhancement provides a measure of the coupling strength.

F. Quantitative Analysis of Selective Detection: S_1 + 590/592 cm^{-1}

The S_1 + 590/592 cm^{-1} system may be used to demonstrate the agreement between experiment and Eq. (3). The results of the analysis of this system are summarized in Table I.

We assumed the slit profile of the monochromator to be rectangular in the calculation of the emission ratio, a good approximation at the large slit widths (1.5 mm) employed here. Since contour shape has been found to be independent of detection conditions (Sec. IIIC), we measured the *total* area under each contour, rather than the convoluted area under the excitation profile, to determine the excitation ratio. Overlapping contours were deconvoluted by eye; areas were measured by cutting and weighing.

Despite the potential errors already discussed, the simplifying assumptions made, and the difficulty of deconvoluting overlapping contours by eye, the excitation and emission ratios are remarkably similar for most detection energies. The discrepancies at very high ratios (205, 323, and 428 cm^{-1}) are undoubtedly due to small absolute errors in the measurement of the area of the repressed contour, which produce large relative errors in the excitation ratio. The discrepancy at 1633 cm^{-1} has no obvious explanation. The remaining nine levels have ratios in close agreement. The last column gives the common logarithm of the ratio of the emission and excitation ratios, which should be zero. The average value of this column for all values is -0.008, and for the nine more reasonable values is +0.021, corresponding to 2 and 5 % deviations from Eq. (3), respectively.

G. Characterization of Regions Exhibiting IVR

At high vibrational energies, some levels in stilbene S_1 exhibit biexponential decays with fast component lifetimes on the order of tens of picoseconds, compared to slow component (radiative decay) lifetimes of several nanoseconds. The fast decay has been convincingly shown in fluorescence [12,30] and multiphoton ionization [13,31] studies to be a real-time manifestation of dissipative IVR. Levels exhibiting this behavior are 1237, 1241, 1246, 1249, and 1332 cm^{-1}. Given the importance of this behavior, it is desirable to obtain high resolution maps of these regions to characterize the exact level structures.

The 1234 - 1256 and 1328 - 1336 cm^{-1} regions are shown in Fig. 6 (top and bottom, respectively). Taking the most intense band in the 1234-1256 cm^{-1} region to be 1249.3 cm^{-1} as reported previously [14], the other levels are at 1237.0, 1241.2, 1242.8, 1245.6, and approximately 1252.4 cm^{-1}. There also is a high-energy shoulder on 1237.0 cm^{-1} ($\approx$ 1237.7 cm^{-1}), and low-energy shoulders on 1241.2 cm^{-1} ($\approx$ 1240.6 cm^{-1}) and 1249.3 cm^{-1} ($\approx$ 1248.8 cm^{-1}). The 1242.8 and 1252.4 cm^{-1} levels and the three shoulders have not been reported previously. The structure of this spectrum is highly reproducible, even with the greatly reduced resolved detection signal (trace B).

The 1332.4 cm^{-1} band reported previously is flanked by two less intense, unreported bands at approximately 1330.8 and 1334.0 cm^{-1}. Total detection (C) and resolved detection (D) contours are very similar. Although this structure is vaguely remniscent of the C-axis contour simulation shown in Fig. 1, several observations preclude this being a C-axis vibration. The Q-branch of the simulation is very narrow (< 0.2 cm^{-1} FWHM = full-width at half-maximum), whereas the center portion of the 1332 cm^{-1} complex is much broader (> 1.0 cm^{-1} FWHM). In addition, the nitrogen contour (not shown) is different in its shape, as expected when the P-R branch separations of overlapping contours are changed (increased going from neon to nitrogen). Although the FWHM of C- and B-axis simulations increases with increasing temperature, the appearance of these contours is relatively independent of temperature in the range of consideration.

The high density of optically active levels in S_1 at energies where dissipative IVR occurs is evident from these high resolution spectra, and is clearly a manifestation of the roughly exponential increase in density of states with respect to vibrational energy. The additional torsional nonrigidity above the photoisomerization threshold may also relax symmetry restrictions on optical activity.

The difficulty of inferring temporal behavior from frequency domain data is evident from these spectra. The FWHM of S_1 + 1246 cm^{-1} (selected as it has no apparent overlapping transitions) is 1.6 cm^{-1}. The S_1 + 987 cm^{-1} level (Fig. 1) has a 1.1 cm^{-1} FWHM contour in neon, and the contour shape is nearly identical with that of S_1 + 1246 cm^{-1}. From the frequency domain data, it is not possible to infer that S_1 + 987 cm^{-1} exhibits quantum beats, while S_1 + 1246 cm^{-1} decays biexponentially.

Spectral analysis of IVR in low symmetry, nonrigid molecules is hampered by spectral congestion, which is severe even in supersonic jets (Fig. 6). Torsional dynamics must be properly accounted for to fully understand rotational-vibrational coupling and IVR in these molecules.

REFERENCES

[1] B. W. Keelan and A. H. Zewail, *J. Chem. Phys. 82*, 3011 (1985).

[2] J. A. Syage, P. M. Felker, D. H. Semmes, F. Al Adel, and A. H. Zewail, *J. Chem. Phys. 82*, 2896 (1985).

[3] M. Fujii, T. Ebata, N. Mikami, M. Ito, S. H. Kable, W. D. Lawrance, T. B. Parsons, and A. E. W. Knight, *J. Phys. Chem. 88*, 2937 (1984).

[4] B. Fourmann, C. Jouvet, A. Tramer, J. M. Le Bars, and Ph. Millie, *Chem. Phys. 92*, 25 (1985).

[5] See, e.g., E. C. Apel and E. K. C. Lee, *J. Phys. Chem. 88*, 1283 (1984).

[6] See, e.g. C. S. Parmenter and B. F. Rordorf, *Chem. Phys. 27*, 1 (1978).

[7] B. F. Rordorf and C. S. Parmeter, *J. Mol. Spectrosc. 69*, 365 (1978).

[8] E. Riedle, H. J. Neusser, and E. W. Schlag, *J. Phys. Chem. 86*, 4847 (1982).

[9] E. Riedle and H. J. Neusser, *J. Chem. Phys. 80*, 4686 (1984).

[10] J. A. Syage, W. R. Lambert, P. M. Felker, A. H. Zewail, and R. M. Hochstrasser, *Chem. Phys. Letts. 88*, 266 (1982).

[11] J. A. Syage, P. M. Felker, and A. H. Zewail, *J. Chem. Phys. 81*, 4706 (1984).

[12] P. M. Felker, W. R. Lambert, and A. H. Zewail, *J. Chem. Phys. 82*, 3003 (1985).

[13] N. F. Scherer, J. F. Shepanski, and A. H. Zewail, *J. Chem. Phys. 81*, 2181 (1984).

[14] J. A. Syage, P. M. Felker, and A. H. Zewail, *J. Chem. Phys. 81*, 4685 (1984).

[15] B. W. Keelan, J. A. Syage, J. F. Shepanski, and A. H. Zewail, *Proceedings of the International Conference on Lasers 1983*, San Francisco, California, Society of Optical and Quantum Electronics (STS Press, McLean, Virginia, 1985), p. 718.

[16] R. E. Drullinger, *Opt. Commun. 39*, 263 (1981).

[17] M. Traetteberg, E. B. Fransten, F. C. Mijlhoff, and A. Hoekstra, *J. Mol. Struct. 26*, 57 (1975).

[18] T. Kobayashi, H. Suzuki, and K. Ogawa, *Bull. Chem. Soc. Japan 55*, 1734 (1982).

[19] A. Bree and M. Edelson, *Chem. Phys. 51*, 77 (1980).

[20] R. H. Dyck and D. S. McClure, *J. Chem. Phys. 36*, 2326 (1962).

[21] G. Hohlneicher and B. Dick, *J. Photochem. 27*, 215 (1984) and references therein.

[22] G. Herzberg, *Molecular Spectra and Molecular Structure*, Vol. III, Electronic Spectra and Electronic Structure of Polyatomic Molecules (Van Nostrand Reinhold Co., New York, 1966), pp. 66-8, 137-41.

[23] J. F. Shepanski, B. W. Keelan, and A. H. Zewail, *Chem. Phys. Letts. 103*, 9 (1983).

[24] G. Herzberg, *Molecular Spectra and Molecular Structure*, Vol. II, Infrared and Raman Spectra (Van Nostrand Reinhold Co., New York, 1945), p. 47.

[25] T. Ueda and T. Shimanouchi, *J. Mol. Spectrosc.* *28*, 350 (1968).

[26] P. R. Bunker, *Molecular Symmetry and Spectroscopy* (Academic Press, New York, 1979) pp. 344-72.

[27] H. Selzle, W. E. Howard, and E. W. Schlag, Rotational Band Contour Program, from Technische Universitat Munchen.

[28] W. R. Lambert, P. M. Felker, and A. H. Zewail, *J. Chem. Phys.* *81*, 2217 (1984).

[29] A. H. Zewail, *Ber. Bunsenges. Phys. Chem.* *89*, 264 (1985).

[30] P. M. Felker and A. H. Zewail, *J. Phys. Chem.* *88*, 6106 (1984).

[31] N. F. Scherer, J. W. Perry, F. E. Doany, and A. H. Zewail, *J. Phys. Chem* *89*, 894 (1985).

Table I

Dependence of intensities of overlapping transitions (S_1 + 590/592 cm^{-1}) upon detection conditions.

Detection Energy [note a]	Emission from 25^3 (592 cm^{-1})	Emission from 23^1 (590 cm^{-1})	Excitation Ratio [note b]	Emission Ratio [note c]	log Ratio Deviation [note d]
205	25^3_1	208 cm^{-1}	13.16	6.747	-0.290
323	$25^3_1\ 36^0_1$		15.71	9.117	-0.236
428	25^3_2		9.697	4.786	-0.307
616	25^3_3	23^1_1	0.854	0.938	+0.041
719	$25^3_3 36^0_1$	$23^1_1 36^0_1$	0.857	1.237	+0.159
812	25^3_4	$23^1_1 25^0_1$	0.479	0.480	+0.001
1016	25^3_5	$23^1_1 25^0_2$	0.861	0.976	+0.054
1218	25^3_6	$23^1_1 25^0_3$	2.056	1.781	-0.062
1427	25^3_7	$23^1_1 25^0_4$	2.831	2.946	+0.017
1633	25^3_8	$23^1_1 25^0_5$	0.865	2.279	+0.532
1826	25^3_9	$23^1_1 25^0_6$	2.547	2.507	-0.007
2244	2240 cm^{-1}	2270 cm^{-1}	1.037	1.068	+0.013
2458		2473 cm^{-1}	0.840	0.794	-0.024

[a] cm^{-1} at center of detection region; range approximately ± 60 cm^{-1}.

[b] ratio of area of S_1 + 592 cm^{-1} contour to that of S_1 + 590 cm^{-1}.

[c] ratio of area of emission in S_1 + 592 cm^{-1} dispersed fluorescence spectrum, within detection limits, to that of S_1 + 590 cm^{-1}.

[d] common logarithm of emission area ratio (previous column) divided by contour area ratio (next-to-previous column); theoretically should be zero.

FIGURE CAPTIONS

Figure 1: Experimental rotational band contours of a typical level (S_1 + 987 cm^{-1}) in neon and nitrogen carrier gases, compared to computer simulations of transitions along the A-, B-, and C-axes. Although the low symmetry of stilbene does not restrict the possible transition moment orientations to the rotational axes, single-crystal absorption data [20] and theoretical calculations [21] indicate that the electronic transition moment lies along the long (A) axis. Temperature was varied to match the A-axis simulation P-R branch separations to the experimental contours, yielding estimated temperatures of 3 K and 10 K for neon and nitrogen respectively. B- and C-axis simulations for 3 K are slightly narrower than those shown for 10 K, but otherwise are similar in appearance. A 1% increase in rotational constants in S_1 relative to S_0 best reproduced the P-R branch relative intensities. Quantum beats have previously been observed in the emission from the S_1 + 987 cm^{-1} level.

Figure 2: Dispersed fluorescence spectrum (top) and rotational band contours (bottom) of the S_1 + 789 cm^{-1} level ($23^1 25^1$) in neon. In Figs. 2 - 5, the dispersed fluorescence spectra zeroes are at the excitation energies. In contour A, total emission is detected; in B, the sharp $23^1_1 25^1_0$ emission (labelled B below); in C, the broad background emission at S_0 + 705 - 955 cm^{-1}; and in D, the sharp $23^1_0 25^1_2$ emission. The contour shapes are essentially independent of the type of structure detected (compare B and C) and the specific mode detected (compare B and D). Thus, as expected, detecting total emission (trace A) yields a contour identical to that obtained with resolved detection. The absence of a sharp transition at C has been shown by Franck-Condon analysis to be due to a large geometry change upon excitation [14].

Figure 3: Rotational band contours (top) and dispersed fluorescence spectra (bottom) of the S_1 + 590/592 cm^{-1} levels in neon. Trace A shows the contour for the two levels when the total emission is detected. Narrow-band excitation of S_1 + 590 cm^{-1} and S_1 + 592 cm^{-1} (labelled 1 and 2 above, respectively) yields dispersed fluorescence spectra 1 and 2 (bottom). The differences in emission structure may be exploited to selectively enhance either of the levels in S_1. Resolved detection of emission at B, C, and D (bottom) yields contours B, C, and D (top). These demonstrate weak enhancement (B), strong enhancement of S_1 + 590 cm^{-1} (C), and very strong enhancement of S_1 + 592 cm^{-1} (D). A quantitative discussion is given in the text.

Figure 4: Rotational band contours (top) and dispersed fluorescence spectra (bottom) of S_1 + 389/391 cm^{-1} levels in neon. Detection of total emission yields contour A, showing overlapping levels in S_1. Narrow-band excitation of 389 cm^{-1} (labelled 1 at top) and 391 cm^{-1} (labelled 2) produces dispersed fluorescence spectra 1 and 2 (bottom). Selective detection of emission can better resolve the two levels in S_1. Detection of emission at B and C (bottom) yields contours B and C (top), where 391 cm^{-1} and 389 cm^{-1}, respectively, have been enhanced.

Figure 5: Rotational band contours (top) and dispersed fluorescence spectra (bottom) of S_1 + 425/427 cm^{-1} levels in neon, arranged as in Figure 4, demonstrating selective detection enhancement of overlapping levels in S_1. The congested emission of S_1 + 427 cm^{-1} results in less effective enhancement than the sparser, more structured emission of the S_1 + 590/592 cm^{-1} and S_1 + 389/391 cm^{-1} systems (compare to Figs. 3 and 4, respectively).

Figure 6: High resolution maps of the S_1 + 1234 - 1256 cm^{-1} (top) and S_1 + 1328 - 1336 cm^{-1} regions (bottom). The energy zeroes are S_1 + 1240 cm^{-1} and S_1 + 1332 cm^{-1} respectively. The upper traces of each pair (A and C) were obtained

by collecting total emission, the lower (B and D) by detecting only near the peaks of the structureless emission profiles (S_1 + 1240 cm^{-1}: S_0 + 1550 ± 120 cm^{-1}; S_1 + 1332 cm^{-1}: S_0 + 1720 ± 120 cm^{-1}). These regions have previously been observed to display very fast decays, which represent real-time observation of dissipative IVR.

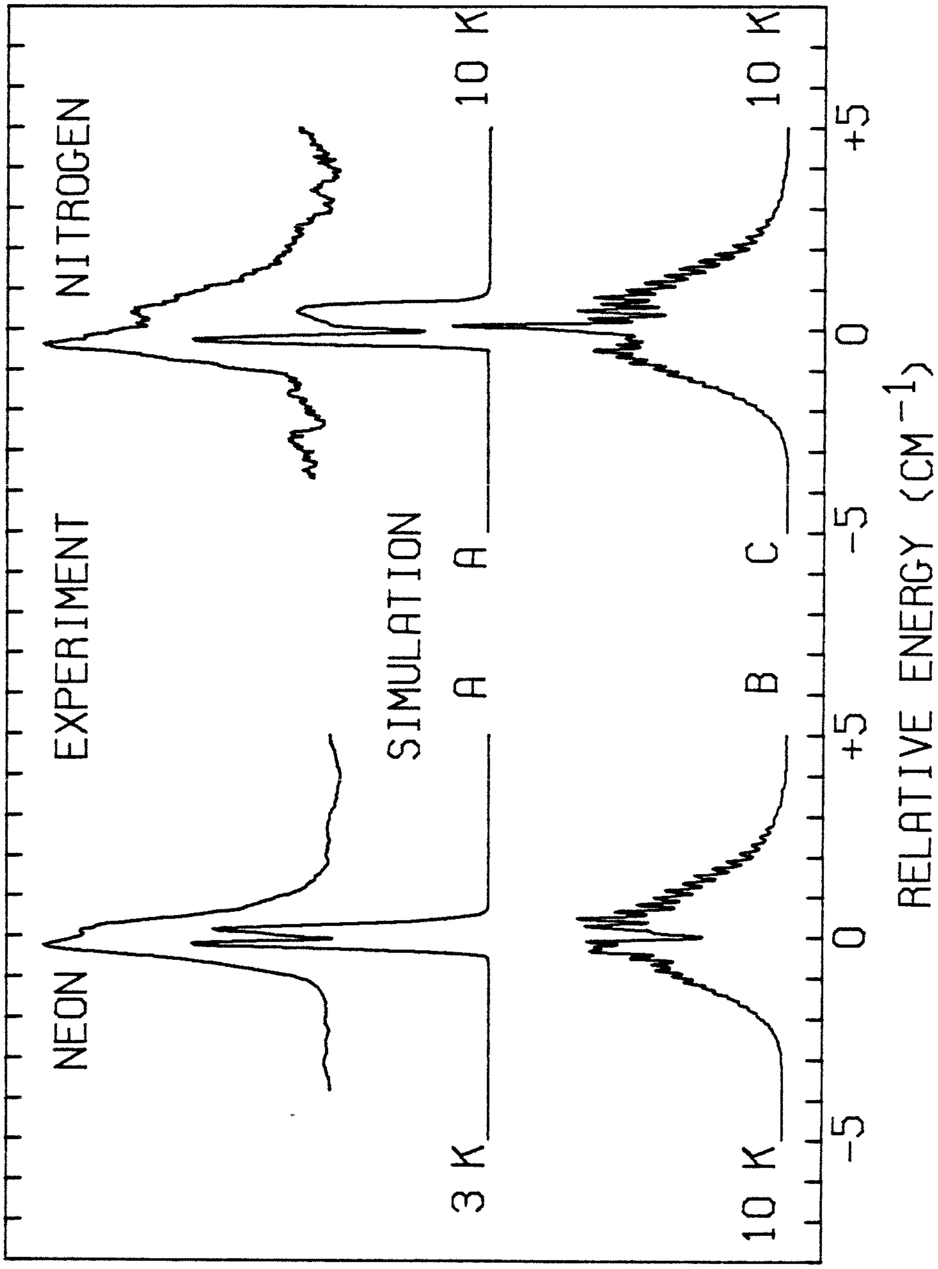
NEON
EXPERIMENT
NITROGEN
SIMULATION
3 K
A
A
10 K
10 K
B
C
10 K
-5
0
+5
-5
0
+5
RELATIVE ENERGY (CM^{-1})

Figure 1

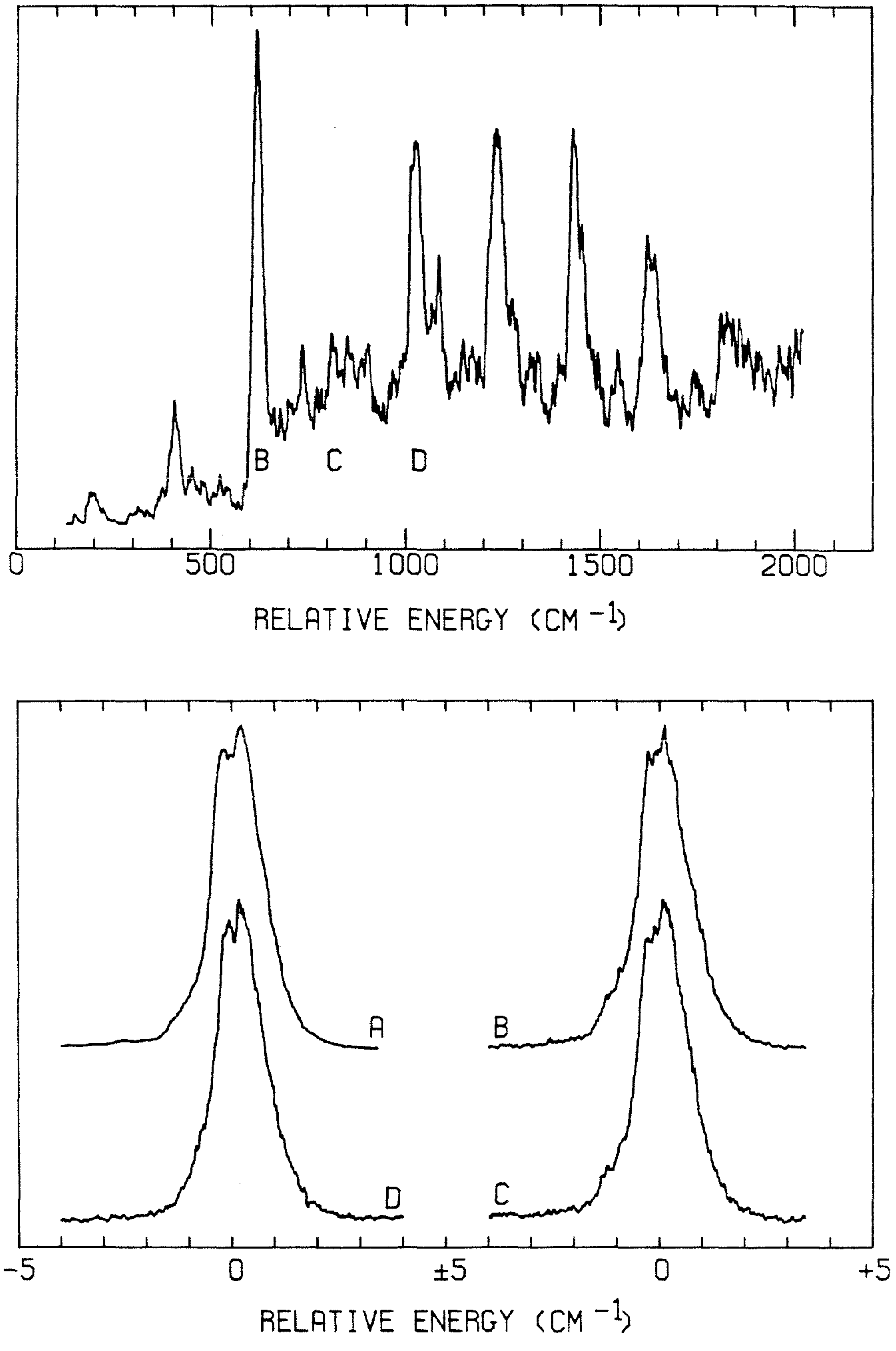
B
C
D
0
500
1000
1500
2000
RELATIVE ENERGY (CM $^{-1}$)
A
B
D
C
-5
0
±5
0
+5
RELATIVE ENERGY (CM $^{-1}$)

Figure 2

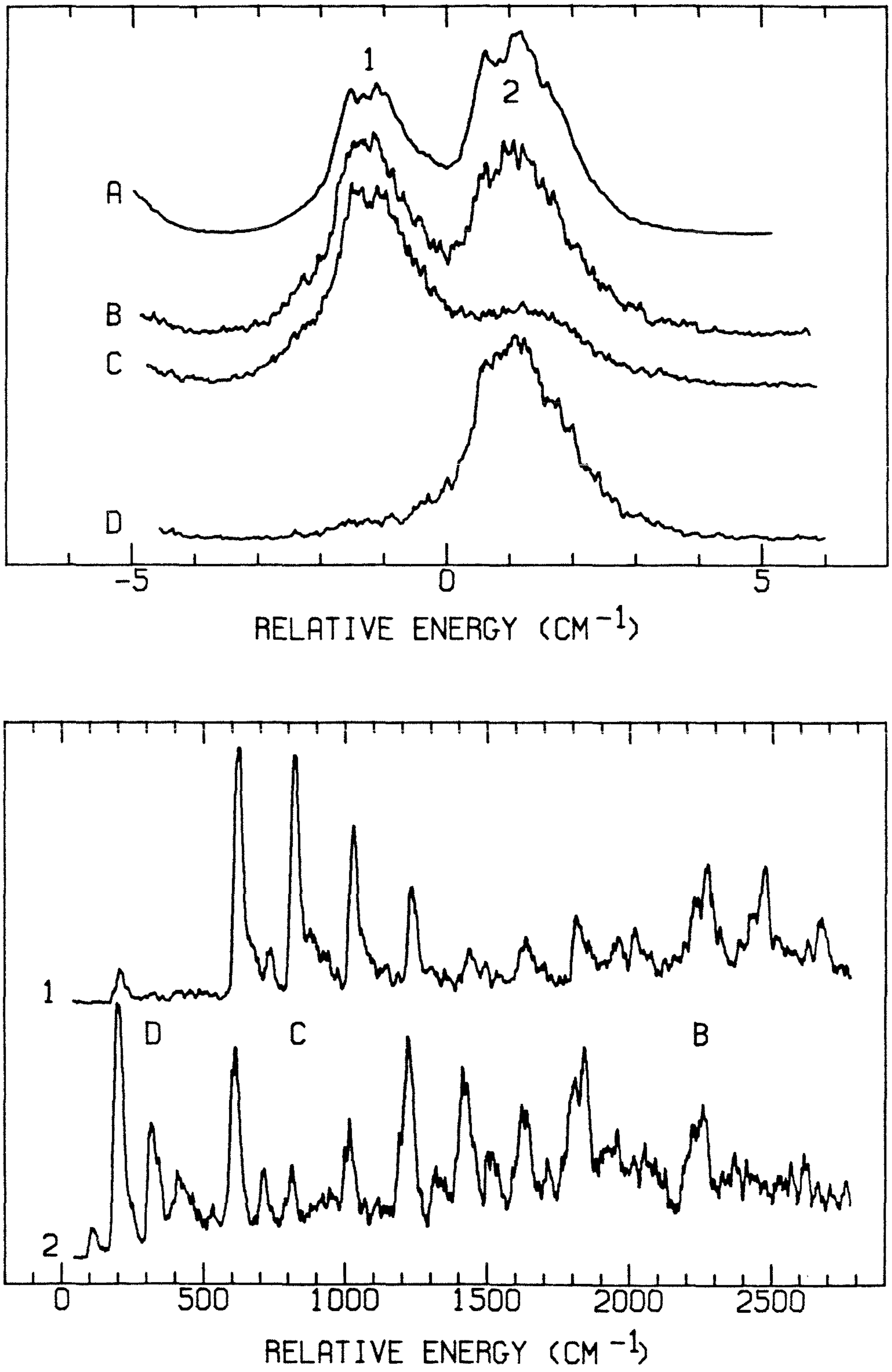
1
2
A
B
C
D
-5
0
5
RELATIVE ENERGY (CM^{-1})
1
D
C
B
2
0
500
1000
1500
2000
2500
RELATIVE ENERGY (CM^{-1})

Figure 3

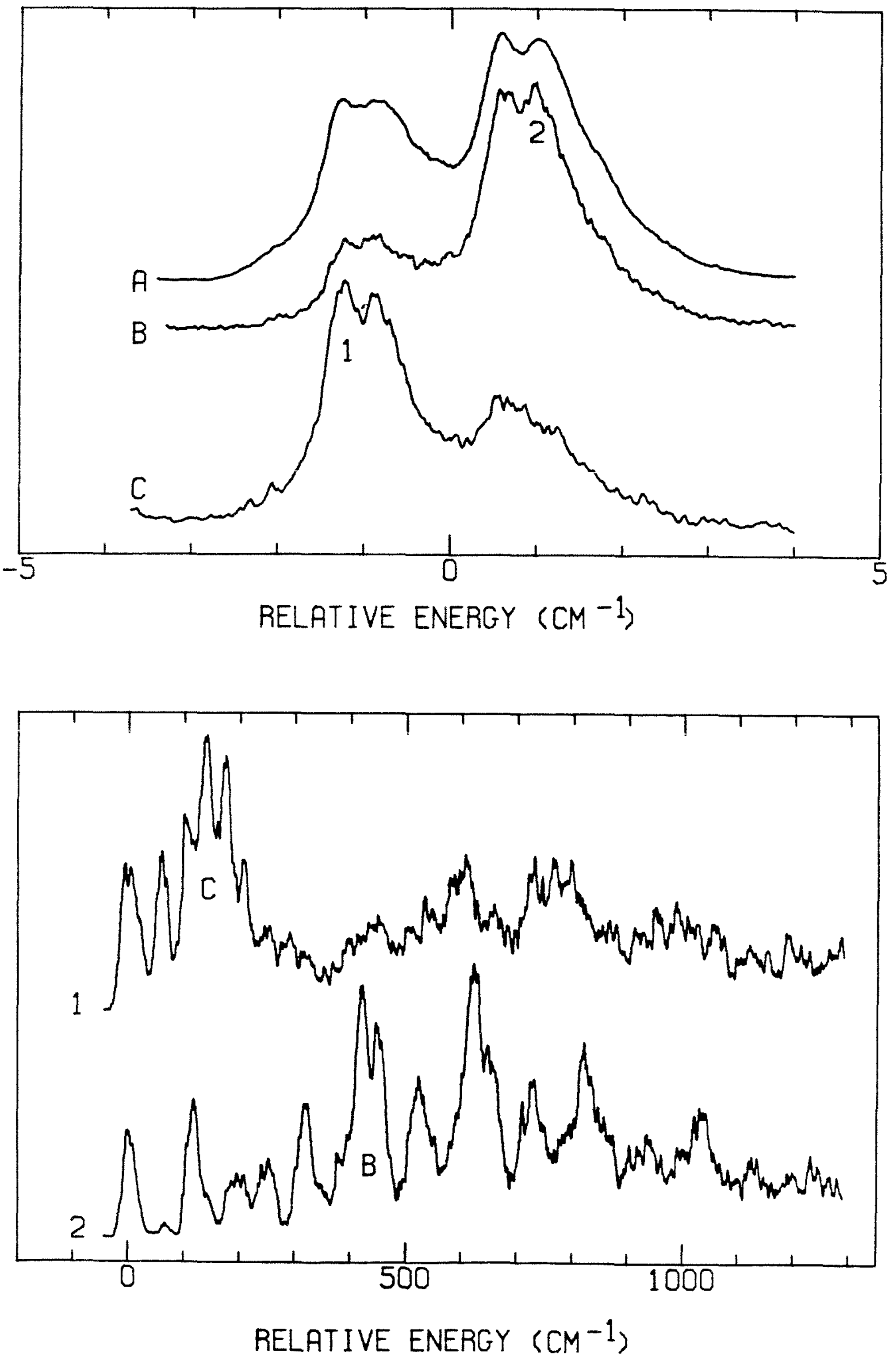
A
B
C
1
2
-5
0
5
RELATIVE ENERGY (CM^{-1})
C
B
1
2
0
500
1000
RELATIVE ENERGY (CM^{-1})

Figure 4

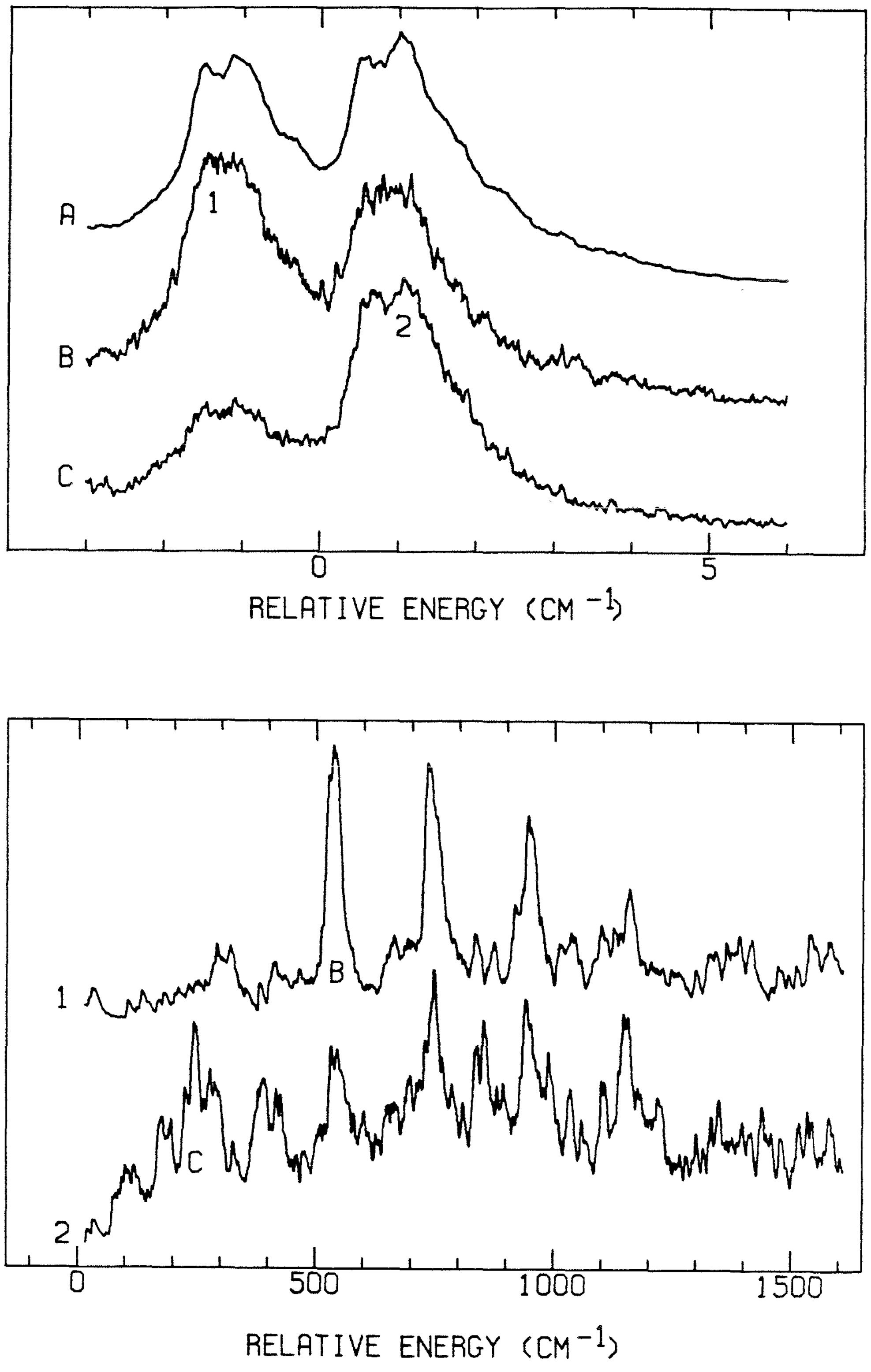
A
B
C
1
2
0
5
RELATIVE ENERGY (CM $^{-1}$)
1
2
B
C
0
500
1000
1500
RELATIVE ENERGY (CM $^{-1}$)

Figure 5

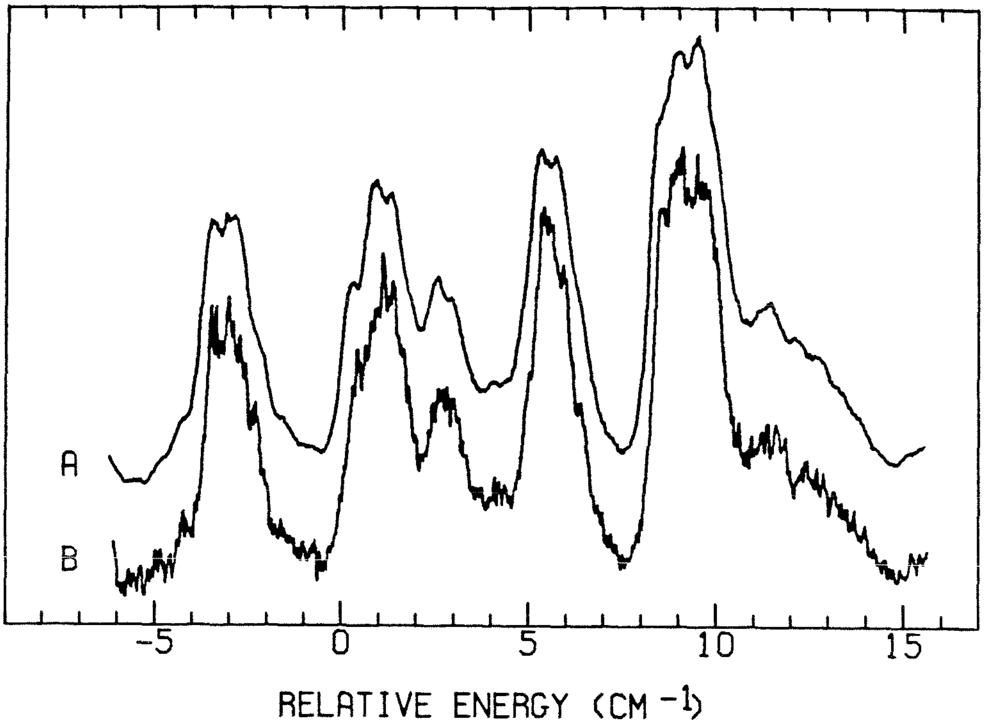

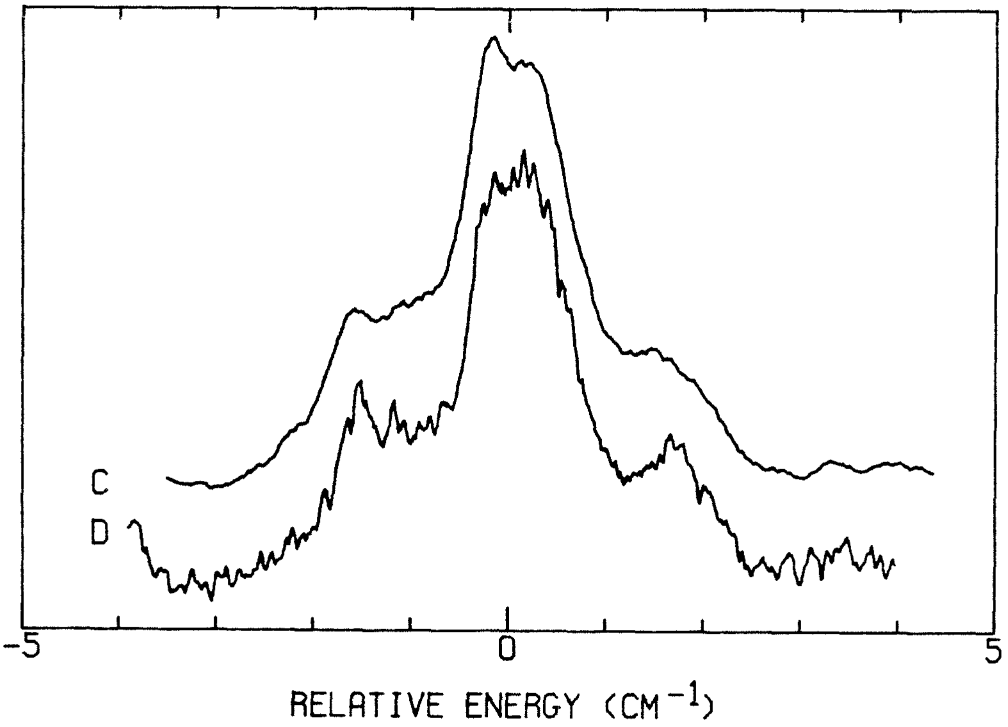

Figure 6

Rotational Band Contour Analysis of Symmetries and Interactions of Vibrational Levels in Anthracene S_1

Chapter 7

Rotational Band Contour Analysis of Symmetries and Interactions of Vibrational Levels in Anthracene S_1

ABSTRACT

Over 50 of the more intense transitions in the S_1 excitation spectrum (0-2000 cm^{-1} of vibrational energy) of supersonic jet-cooled anthracene are investigated using rotational band contour analysis, including computer simulations. This allows unambiguous assignment of the vibrational symmetries of all levels below 1100 cm^{-1} and many levels at higher energies, some of which were unassigned previously. Using complementary narrow-band excitation and energy-resolved detection techniques, a Fermi resonance at 755 cm^{-1} is thoroughly investigated to obtain the energy separation of the unperturbed states and the magnitude of the coupling matrix element. Levels which showed restricted or dissipative intramolecular vibrational redistribution in time-resolved experiments (1380, 1420, and 1792 cm^{-1}) are also studied.

I. INTRODUCTION

Anthracene has recently been studied quite extensively in supersonic jets. The excitation spectrum of S_1 and the fluorescence from the S_1 origin to S_0 has been studied for anthracene and some of its deuterated analogs [1]; the fluorescence spectra and lifetimes of different S_1 vibrational levels have been obtained [2]; quantum beats have been observed following excitation to S_1+1380 cm^{-1} [3,4] and S_1+1420 cm^{-1} [4,5]; and a fast decay component associated with intramolecular vibrational redistribution (IVR) has been observed for excitation to S_1+1792 cm^{-1} [6]. To fully characterize the dynamics of this molecule, it is necessary to study the interactions between different vibrational levels, especially at higher vibrational energies, where the greater density of states increases the likelihood of interactions.

Rotational band contour shapes can vary markedly with vibronic symmetry [7], which can be useful in the assignment of vibrational symmetries. Recently, several groups have employed complementary narrow-band excitation and energy-resolved detection experiments to study Coriolis perturbations [8] and IVR [9]. Extremely narrow-band excitation has been used to obtain sub-Doppler resolution spectra of rotational envelopes, allowing elucidation of coupling mechanisms in the channel three region of benzene [10].

In this paper, we use rotational band contour analysis to assign vibrational symmetries in anthracene, and complementary narrow-band excitation and energy-resolved detection experiments to probe interactions among S_1 vibrational levels.

II. EXPERIMENTAL

Our experimental system, except for the pressure-tuning apparatus, has previously been described in detail [11]; a full description may be found in Ch. 4. The dye used in this study was methanolic LDS698, which was very weak at both the low and high-energy extremes. Excitation scans were obtained at 415 K, contours and dispersed fluorescence spectra at 450 K. Carrier gas backing pressure (neon or nitrogen) was 50 psi throughout. The laser-to-nozzle distance and pinhole diameter were 12 mm and 0.5 mm, respectively, so X/D = 24. Doubling the laser to nozzle distance had no effect on the excitation spectrum near the origin, indicating optimal cooling at X = 12 mm. When the fluorescence emission was not dispersed with a monochromator, it was passed through a Schott GG-395 cutoff filter to remove scattered laser light, and a Schott UG-11 bandpass filter to remove stray visible light. Pressure-tuning was done with nitrogen, which gives a full scan range of 20 cm^{-1} at 360 nm.

III. RESULTS AND DISCUSSION

A. Excitation Spectra

The excitation spectrum of the first excited state of anthracene (S_1) in neon is shown in Figure 1. This spectrum agrees well with the previously published jet spectrum [1]. The excitation spectrum in nitrogen (not shown) has greater linewidths than in neon, and transitions associated with anthracene-nitrogen complexes are present. These observations are consistent with neon providing better rotational cooling than nitrogen.

As expected, the excitation spectrum becomes more complicated at higher vibrational energies. At low energies (0-600 cm^{-1}) the modes are well isolated, at intermediate energies (600-1300 cm^{-1}) the mode density increases and overlapping transitions are present, and at high energies (1300-2000 cm^{-1}) the transitions are so closely spaced as to form several regions of nearly continuous absorption within the resolution of the spectrum (0.5 cm^{-1}). The increasing complexity of the excited state vibrational structure with increasing energy is manifested in both the rotational band contours and in the dispersed fluorescence spectra, as discussed in subsequent sections.

B. Symmetries and Simulations

A survey of the rotational band contours of all but the weakest bands in the excitation spectrum yielded interesting information concerning transition symmetries and interactions. The positions, which conform to the previous study where applicable [1], and intensities of the bands studied are summarized in Table 1.

At relatively low energies (0-1100 cm^{-1}), all but one of the 17 transitions studied clearly belonged to one of two well-defined contour types. The single exception, 755 cm^{-1}, is discussed in detail later. The prevalent contour type (13 transitions) exhibited well-separated P and R branches (average 0.6 cm^{-1} in neon, 1.4 cm^{-1} in nitrogen) but no Q-branch (see the left side of Figure 2). The rarer contour type, depicted on the right side of Figure 2, showed a strong Q-branch and was comparatively narrower (P and R branch separation average 0.5 cm^{-1} in neon, 1.2 cm^{-1} in nitrogen).

The ground electronic state of anthracene is A_g in symmetry. Assuming anthracene is planar, it has D_{2h} symmetry; the x, y, and z axes transform like B_{3u}, B_{2u}, and B_{1u} respectively. Our axis convention is explained in Appendix 1. The S_1 state is B_{2u}, and there is a relatively low-lying B_{3u} state, approximately 13,600 cm-1 above the B_{2u} state [12], which has a large oscillator strength to the ground state. There are no known low-lying B_{1u} states. Thus, we would expect the strongest transitions in the S_1 excitation spectrum to correspond to the fully dipole-allowed $A_g a_g \rightarrow B_{2u} a_g$ (here capital letters denote electronic symmetries and small letters vibrational symmetries). Given the small intensities of the hot bands in the excitation spectrum, it is reasonable to neglect initial states other than the lowest energy a_g. Thus we may denote these transitions by the excited state vibrational symmetry a_g. In addition, some less intense transitions in the excitation spectrum may result from Herzberg-Teller coupling to the B_{3u} state [13]; these false origins would be attributable to b_{1g} vibrations ($B_{2u} x B_{3u} = b_{1g}$), and would have vibronic transition moments along the x axis.

On this basis alone, we may speculate that the prevalent contour type is associated with a_g vibrations, and the rarer type with b_{1g} vibrations. This supposition is further strengthened by the fact that the lowest energy transition (excluding hot bands and complexes), if a 0_0^0 transition, must be of a_g vibrational symmetry, and this band experimentally does indeed exhibit the prevalent type of contour. We shall hereafter refer to these two types of contours as a_g and b_{1g} contours, after the vibrations that characterize them.

In order to further substantiate these assignments, we generated computer simulations of rotational band contours using a well-documented Fortran program [14]. We assumed that there is no distortion in either the S_0 or S_1 states. The S_0 rotational constants and the rotational symmetry statistical weights are summarized in Appendix I. Sufficiently large J values were included in the calculations so that a substantial increase in the allowed J values resulted in no significant change in the calculated contour. A resolution of 0.1 cm^{-1}, twice the laser bandwidth, best reproduced the experimental contours. The fitting parameters were the temperature and the S_1 rotational constants. Varying the temperature primarily affected the separation of the P and R branches and the overall width of the contours, while varying the S_1 rotational constants primarily affected the relative intensities of the P and R branches. Consequently, to obtain a reasonable fit, we first varied the S_1 rotational constants to reproduce the P and R branch relative intensities, and then varied the temperature to match the P and R branch separation.

Although the relative intensity of the P and R branches is quite sensitive to the S_1 rotational constants, it was expedient to reduce the three degrees of freedom to a single degree of freedom by assuming that the S_1 rotational constants differed from the S_0 rotational constants only by a multiplicative factor. With this assumption, it was found that a 1% reduction in the S_1 constants relative to the S_0 constants reproduced the P and R branch relative intensities very well, substantially better than no reduction or 2% reduction.

Using these S_1 constants, the temperature was fit independently for the a_g and b_{1g} contours for each carrier gas. As the temperatures for the different vibrational symmetries would be expected to be the same, this provides a measure of the uncertainty of the fit. The simulations and experimental contours are contrasted in Figure 2. The rotational temperatures for neon (2 K for b_{1g}, 3 K for a_g) are in better agreement than those for nitrogen (8 K for b_{1g}, 15 K for a_g). Clearly neon cools rotations more efficiently than nitrogen.

The temperature, S_1 rotational constants, and resolution values chosen had no effect on the general appearance (e. g., presence or absence of a Q-branch) of the contours of the two symmetries except, of course, that at low resolution all fine structure was lost, and that at very high resolution individual rotational lines became discernable. Thus, the remarkably good agreement between the simulations and the experimental contours confirms the a_g and b_{1g} assignments. It is worth noting that calculated b_{3g} contours (not shown) exhibited a Q-branch but were very broad; no such contours were observed experimentally, as expected.

At higher energies (1100-2000 cm^{-1}), many of the contours were relatively structureless or appeared to be superpositions of two or more simple contours; many of these transitions could not be unambiguously assigned a symmetry. The assignments made using rotational contour analysis are summarized in Table 1, where they are compared with the assignments and implied symmetries of the previous work [1].

The complexity of many of the contours at higher energies parallels the trend noted in the excitation spectrum. This increased complexity is no doubt largely due to the density of states, which increases approximately exponentially with energy. The density of states in anthracene S_1 is about $1/cm^{-1}$ at 750 cm^{-1}, $25/cm^{-1}$ at 1400 cm^{-1}, and $120/cm^{-1}$ at 1800 cm^{-1} [6].

We now separately discuss each vibrational level which was studied by complementary narrow-band excitation and energy-resolved detection experiments.

C. 755 cm^{-1} (a_g:ν_{10})

The only band below 1100 cm^{-1} in energy which is not a simple a_g or b_{1g} contour type is the 755 cm^{-1} level. Referring to Figure 3, trace A, the contour obtained when total fluorescence is detected appears to be a superposition of two a_g contours, separated by 2.0 cm^{-1}. In order to determine the amount of interaction between the two levels (hereafter 754 and 756 cm^{-1}), we obtained dispersed fluorescence spectra for excitation on the blue side of 756 cm^{-1} and the red side of 754 cm^{-1}. Comparing these, it is clear that the band labelled B (835 cm^{-1}) is associated with the 754 cm^{-1} band, and that labelled A (755 cm^{-1}) with the 756 cm^{-1} band.

Although these levels are well separated in the ground state, they are quasidegenerate in the excited state. To quantify their interaction, we obtained contours detecting only the 755 or 835 cm^{-1} bands. Note that as the 754 and 756 cm^{-1} contours overlap substantially, it is not feasible, even with narrow-band excitation, to excite one level exclusively. In contrast, the 755 and 835 cm^{-1} levels are well isolated in the dispersed fluorescence spectrum, so one of the levels can be detected exclusively. Hence, if there is no interaction between the 754 and 756 cm^{-1} levels, detection of one band in the dispersed fluorescence spectrum should yield only one of the two contours. If there is an interaction between the two levels in the excited state, then even if a single band is detected, both contours will be observed, although one of the contours will be more intense. The relative intensities of the contours provide a measure of the strength of interaction between the levels, as discussed in Appendix II.

In Figure 3, the contours B and C in the top box result from single-band detection of 835 and 755 cm^{-1} levels respectively; note that the spectra are essentially "mirror images" of each other (see Appendix II). The more intense level is 2.7 times as intense as the less intense level. Using Eqs. (3, 4, and 14 or

15), Appendix II, the coupling matrix element is estimated to be 0.89 cm^{-1}, and the zero-order energy spacing is found to be 0.92 cm^{-1}, which is reasonable as the eigenstates are 2.0 cm^{-1} apart, and the unperturbed states are expected to repel each other.

This calculated matrix element is somewhat larger than the matrix elements found for states exhibiting IVR-related phase-shifted quantum beats, 0.01-0.30 cm^{-1} [6]. Further evidence of matrix elements on the order of cm^{-1} can be found in the high resolution excitation spectrum of the 1505-1517 cm^{-1} region, shown in Figure 4. The four transitions (1506, 1508, 1514, and 1516 cm^{-1}) all have b_{1g} symmetry (although there is an intense transition of unknown symmetry on the low-energy side of the 1514 cm^{-1} transition). It is very unlikely that there would be four optically-active zero-order modes of the same symmetry (especially the rarer b_{1g} symmetry) this close together in energy, suggesting that only one of the zero order modes is optically active, and that the other modes are coupled to it through Fermi resonance. This would imply the existence of matrix elements on the order of one to several cm^{-1}.

D. 1380 cm^{-1} (a_g:ν_6)

This is one of two bands (the other being discussed in the next section) where quantum beats have been especially well documented in anthracene S_1 [3,4]. Consequently, studying interactions between these modes and other nearby or overlapping modes is of considerable interest.

Detection of the total fluorescence yields an essentially structureless rotational band contour (not shown), but wide-band detection (1375-1555 cm^{-1}) reveals a slight a_g type splitting and a red shoulder, as shown in Figure 5, trace A. Clearly, multiple transitions are involved, but the symmetries cannot be unambiguously determined without more highly-resolved detection. Exciting the red shoulder and scanning the emission produces the dispersed fluorescence trace 1 (lower box), while exciting on the blue side of the contour yields trace 2. Comparing these spectra, it is clear that the bands between 1475 and 1520 cm^{-1} are significantly more intense in trace 1, and therefore are associated with the red shoulder in trace A. Detecting one of these bands (B) and taking a rotational contour results in trace B (top), clearly showing an a_g type contour centered at 1379 cm^{-1}, as well as residual 1380 cm^{-1}. Detecting only band C at 1460 cm^{-1} (bottom) and obtaining a rotational contour yields trace C (top), exhibiting an a_g type contour centered at 1380 cm^{-1}. We may therefore conclude that there are two overlapping bands at 1379 and 1380 cm^{-1}, with the latter substantially more intense. Despite the difference in intensities, the 1379 cm^{-1} band obscures the P-R branch gap and contributes a red shoulder to the wide-band detection contour (trace A), as well as greatly complicating the dispersed fluorescence spectrum. Because the 1379 and 1380 cm^{-1} bands are of dissimilar intensities, and because the dispersed fluorescence bands are not well isolated, estimation of a matrix element is not feasible.

To help confirm results from a previous study [3], rotational contours for bands in the dispersed fluorescence spectrum which do (389 cm^{-1}; "beating") and do not (1460 cm^{-1}; "non-beating") display quantum beats were obtained in both neon and nitrogen. The neon spectra are shown in Figure 6. The non-beating contour is typical in its P-R branch separation; the beating transition has a much larger P-R branch separation (1.5 vs. 0.5 cm^{-1}). The same trend is shown in the nitrogen spectra. Clearly, lower J values are suppressed in the beating band, suggesting a strongly J-dependent coupling between the states. Coriolis coupling is stronger at higher J values, consistent with these results, but anharmonicity cannot be ruled out, as the energy gap may become very small for a range of higher J values, increasing the interaction strength.

E. 1420 cm^{-1} (a$_g$:ν_5)

As indicated earlier, quantum beats have previously been observed for certain lines in the dispersed fluorescence spectrum of 1420 cm^{-1} [4,5]. The rotational contour obtained when total fluorescence is detected is shown in trace A of Figure 7. The main band at 1420 cm^{-1} is a_g in symmetry; there are several overlapping transitions to the red. Exciting at 1418 cm^{-1}, trace 1 (bottom) is obtained; exciting at 1420 cm^{-1} produces trace 2. These dispersed fluorescence spectra differ in a number of minor respects,but two obvious differences are the appearance of the band labelled B at 1081 cm^{-1} (bottom) when 1420 cm^{-1} excitation is used and the appearance of the band labelled C at 1750 cm^{-1} when 1418 cm^{-1} excitation is used. If only band B is detected, trace B (top) results; red components at 1414 cm^{-1} and 1418 cm^{-1} are prominent, but the 1420 cm^{-1} mode is very weak. In contrast, if only band C is detected (trace C), the 1420 cm^{-1} mode appears with no discernable red bands. The C band, which exhibits phase-shifted quantum beats, can unambiguously be associated with the main 1420 cm^{-1} mode.

F. 1792 cm^{-1} (a$_g$)

The 1792 cm^{-1} band is of interest because it shows a very rapid decay associated with dissipative IVR in time-resolved studies. Hence the characterization of this band and the assignment of its symmetry are desirable. The contour of 1792 cm^{-1} in neon is shown in Figure 8. Although clearly an a_g level, the P-R branch gap is not as well defined as in a typical a_g contour, e. g. 766 cm^{-1}, shown at the bottom of the figure. There appears to be a slight wing on the red side of the contour, and a weak band is present near 1795 cm^{-1}. The 1792 cm^{-1} band is a combination of 1409 cm^{-1}, shown in the middle of the figure, and 385

cm^{-1}, an a_g mode which figures prominently in combination bands in the excitation spectrum. The 1409 cm^{-1} contour is complicated; it is likely composed of two overlapping a_g bands (the R branch of the lower energy band partially coincident with the P branch of the higher energy band, producing three "branches" in the total contour). Since the 385 cm^{-1} mode is a_g in symmetry, the 1409 cm^{-1} band must contain at least one a_g component, as 1792 cm^{-1} is a_g. The complexity of the 1409 cm^{-1} band typifies many of the higher energy contours.

G. Correlation of Results with Time-resolved Studies

It is instructive to correlate the spectral features observed at different energies in this study with the phenomena observed in time-resolved studies at comparable energies.

At lower energies (0-1100 cm^{-1}), we observe a sparse spectrum, composed almost exclusively of well-isolated lines which correspond to fundamentals. Dispersed fluorescence spectra in this region are also composed of discrete lines, with little relaxed emission present [2]. In time-resolved studies, single-exponential decays without modulation are observed [6]. Quantum beats are not observed for the 755 cm^{-1} Fermi resonance pair because the resultant beats would be at too high a frequency to be resolved.

At intermediate energies (1100-1600 cm^{-1}), overlapping transitions are frequent. Dispersed fluorescence spectra show both relaxed and unrelaxed emission [2]. Quantum beats are observed from several levels [3,4,5] (1380 and 1420 cm^{-1}), the symmetries of which have clearly been shown to be a_g in this study. This is a region characterized by restricted IVR.

At high excess energies (1600-2000 cm^{-1}), the intensities of the transitions, many of which are combination bands, are rapidly decreasing, which is consistent with the presence of a nonradiative decay process [2]. The transitions tend to be broad, and the contours rarely correspond to typical a_g or b_{1g} types, suggesting that few levels are well isolated. Dispersed fluorescence spectra are very congested, with almost no unrelaxed emission [2]. A fast decay associated with dissipative IVR is observed for excitation to 1792 cm^{-1} [6], which is definitively assigned as an a_g level in this study.

Finally, this study has shown that many of the bands at higher energies (those with contours which do not match the a_g or b_{1g} types) are considerably inhomogeneously broadened (e.g. 1409 cm^{-1} in Figure 7). The lifetimes of such transitions will be substantially underestimated if calculated from the linewidths. This emphasizes the importance of time-resolved experiments in complementing studies such as this one.

APPENDIX I: Rotational Analysis of Anthracene

Our axis convention for anthracene is depicted in Fig. 9. The moments of inertia are ordered $I_x<I_y<I_z$, so using the convention of the rotational constants being ordered A>B>C, the x, y, and z axes may be referred to as the a, b, and c axes, respectively. Using structural data [15], the ground-state rotational constants of anthracene have been calculated to be A = 0.07184 cm^{-1}, B = 0.01512 cm^{-1}, and C = 0.01249 cm^{-1} [16]. Anthracene is close to a prolate symmetric top, with an asymmetry parameter κ = -0.911 [17]. Anthracene corresponds most closely to "Case 8" (2C/B = 1.67, 1-C/A-C/B = -0.01) in the comprehensive survey of rotational band contour shapes in asymmetric tops by Ueda and Shimanouchi [7].

Anthracene has one set of two (labelled 1 in diagram) and two sets of four (labelled 2 and 3) identical fermions (protons) for a total of 2^{10} = 1024 spin states. The two sets of four transform identically, so only one set need be analyzed. Performing character analysis on sets 1 and 2, using the symmetry operations of the rotational subgroup D_2, the spin functions decompose into the irreducible representations as follows [18]:

$$\Gamma_1 = 3A + B_2$$
$$\Gamma_2 = 7A + 3(B_1 + B_2 + B_3)$$

Recalling that $\Gamma_2 = \Gamma_3$, the total spin function decomposition is given by:

$$\Gamma_{tot} = \Gamma_1\Gamma_2\Gamma_3 = 288A + 240(B_1 + B_3) + 256B_2$$

where the coefficients of the rotational symmetries are their statistical weights.

Due to the appreciable number of fermions present in this molecule, it is not surprising that the statistical weights are very close for the different rotational symmetries.

APPENDIX II: Excitation and dispersed fluorescence spectra of two vibrational levels in Fermi resonance

When two vibrational levels of the same symmetry accidentally are nearly degenerate, the levels are said to be in Fermi resonance, and interact through the anharmonic portion of the potential energy function. The interaction produces eigenstates which are farther apart than the zero order states, i.e., the states repel each other. We shall utilize the level structure shown in Fig. 10 throughout this analysis. We assume that the ground-state vibrational levels are well isolated, and that it is the excited-state vibrational levels which are interacting. If we denote the zero-order states by $|\varphi_a^*\rangle$ and $|\varphi_b^*\rangle$, and the eigenstates by $|\psi_+^*\rangle$ and $|\psi_-^*\rangle$ (the asterisks indicating excited state levels), then:

$$|\psi_+^*\rangle = \cos\vartheta\ |\varphi_a^*\rangle + \sin\vartheta\ |\varphi_b^*\rangle \qquad (1)$$

$$|\psi_-^*\rangle = \sin\vartheta\ |\varphi_a^*\rangle - \cos\vartheta\ |\varphi_b^*\rangle \qquad (2)$$

We have taken $|\varphi_a^*\rangle$ and $|\psi_+^*\rangle$ to be the higher energy zero order state and eigenstate respectively, implying that $V>0$ and $0<\vartheta<\pi/4$.

The two-level system may be solved in closed form [19]. Diagonalizing the Hamiltonian yields the relation:

$$\Delta_\psi^2 = \Delta_\varphi^2 + 4V^2 \qquad (3)$$

where Δ_φ is the energy difference between the zero-order states, Δ_ψ is the energy difference between the eigenstates, and V is the real matrix element coupling the zero-order states. Solution of the eigenvalue-eigenvector equation for either eigenvalue gives the relation:

$$\tan(2\vartheta) = 2V/\Delta_\varphi \qquad (4)$$

These two equations allow the calculation of the zero-order energy separation and coupling matrix element from the observed eigenstate energy separation and ϑ; the latter may be deduced from the relative intensities of the eigenstates under selected detection conditions once assumptions are made concerning the oscillator strengths of each of the possible transitions.

Let us now assume, as shown in the level structure diagram, that there is oscillator strength only between an excited-state level and its own ground-state level, i. e.

$$<\varphi_b^*|\mu|\varphi_b> \neq 0 \neq <\varphi_a^*|\mu|\varphi_a> \tag{5}$$

$$<\varphi_b^*|\mu|\varphi_a> = 0 = <\varphi_a^*|\mu|\varphi_b> \tag{6}$$

Here the oscillator strength includes both the electronic dipole matrix element and the associated Franck-Condon factors. This is a reasonable assumption since the ground-state levels are well isolated. It is now necessary to make assumptions about the oscillator strengths for absorption. Two "limiting" cases illustrate the different behavior possible:

Case 1: One zero order state with all the absorption strength

Let us select $|\varphi_a^*>$ to have all the absorption strength and detect only transitions to one of the ground state levels, e. g. $|\varphi_a>$. If we take an excitation scan with sufficient resolution to resolve $|\psi_+^*>$ and $|\psi_-^*>$, then from Eqs. (1,2) we find the intensity ratio of $|\psi_+^*>$ and $|\psi_-^*>$ to vary as follows:

$$(I_\pm)_a = c^2 \,|<\psi_0|\mu|\psi_\pm^*>|^2|<\psi_\pm^*|\mu|\varphi_a>|^2 \tag{7}$$

$$(I_+/\,I_-)_a = cot^4\vartheta \tag{8}$$

If instead we detected only the emission to $|\varphi_b>$, we would obtain:

$$(I_+/\,I_-)_b = 1 \tag{9}$$

If instead of detecting emission to a single level, we detect all emission, assuming the quantum yields for the eigenstates are comparable, we are essentially taking an absorption spectrum. Therefore, the intensity ratio will depend only on the absorption oscillator strengths:

$$(I_+/I_-)_{tot} = cot^2\vartheta \tag{10}$$

Case II: Two zero order states with equal absorption strength

If the two zero order states both have absorption strength, then there are interference terms in the absorption strengths of the eigenstates. Using Eqs. (1,2), we obtain

$$(I_+/I_-)_a = \frac{1 + \sin 2\vartheta}{1 - \sin 2\vartheta}\, cot^2\vartheta \tag{11}$$

$$(I_+/I_-)_b = \frac{1 + \sin 2\vartheta}{1 - \sin 2\vartheta}\, \tan^2\vartheta \tag{12}$$

$$(I_+/I_-)_{tot} = \frac{1 + \sin 2\vartheta}{1 - \sin 2\vartheta} \tag{13}$$

Note that the intensity ratios for single level detection are reciprocals, so the spectra will be "mirror images".

Inspection of Figure 3 shows that there are three experimental observations of importance with respect to the intensity ratios: (1) the intensity ratio with total detection is close to unity; (2) the intensity ratios with single level detection are not zero or unity for either level; and (3) the intensity ratios with single level detection are reciprocals for the two detection levels, i. e. the spectra are "mirror images". Case I is ruled out by observation (2), as well as observations (1) and (3) except for $\vartheta = \pi/4$ (strong coupling). Case II is ruled out by observation (1) except for $\vartheta = 0$ (no coupling), when it is ruled out by observation (2).

It is simple to construct a model which satisfies observations (1-3) by modifying Case II slightly, since it satisfies observations (2-3). Instead of specifying that the zero-order states have equal absorption stengths, the eigenstates are assumed to have equal absorption strengths, automatically satisfying observation (1). This corresponds to a particular set of unequal but nonzero absorption strengths for the zero-order levels, and so is intermediate between Cases I and II. The intensity ratios for single level detection are now:

$$(I_+/I_-)_a = cot^2\vartheta \tag{14}$$

$$(I_+/I_-)_b = \tan^2\vartheta \tag{15}$$

This allows the determination of ϑ from the experimentally observed intensity ratios in the single level detection contours.

Although the situation of eigenstates with equal absorption strength could occur "accidentally", another plausible explanation is that this is not a two level system, but a multilevel system. This is supported by the fact that no 835 cm^{-1} interval is observed in the emission from 0^0. If this were the case, both of the zero order levels could lack absorption strength, but the eigenstates could gain intensity through mixing with a third zero-order level with substantial absorption strength. If the mixing coefficients of the third level were the same in the two eigenstates, then the apparent absorption strengths would be the same. It is possible that the nearby, intense a_g level at 766 cm^{-1} corresponds to the third level carrying the absorption strength. Regardless of how many levels are involved, the 754 and 756 cm^{-1} levels clearly show spectral manifestations of Fermi resonance.

REFERENCES

[1] W. R. Lambert, P. M. Felker, J. A. Syage, and A. H. Zewail, *J. Chem. Phys. 81*, 2195 (1984).

[2] W. R. Lambert, P. M. Felker and A. H. Zewail, *J. Chem. Phys. 81*, 2209 (1984).

[3] W. R. Lambert, P. M. Felker, and A. H. Zewail, *J. Chem. Phys. 81*, 2217 (1984).

[4] P. M. Felker and A. H. Zewail, *Phys. Rev. Letts. 53*, 501 (1984).

[5] P. M. Felker and A. H. Zewail, *Chem. Phys. Letts. 102*, 113 (1983).

[6] P. M. Felker and A. H. Zewail, *Chem. Phys. Letts. 108*, 303 (1984).

[7] T. Ueda and T. Shimanouchi, *J. Mol. Spectrosc. 28*, 350 (1968).

[8] See, e.g. E. C. Apel and E. K. C. Lee, *J. Phys. Chem. 88*, 1283 (1984).

[9] See, e.g. (a) M. Fujii, T. Ebata, N. Mikami, M. Ito, S. Kable, W. Lawrance, T. Parsons, and A. Knight, *J. Phys. Chem. 88*, 2937 (1984); (b) B. Fourmann, C. Jouvet, A. Tramer, J. M. Lebars, and Ph. Millie, *Chem. Phys. 92*, 25 (1985).

[10] (a) E. Riedle, H. J. Neusser, and E. W. Schlag, *J. Phys. Chem. 86*, 4847 (1982); (b) E. Riedle and H. J. Neusser, *J. Chem. Phys. 80*, 4686 (1984).

[11] B. W. Keelan, J. A. Syage, J. F. Shepanski, and A. H. Zewail, *Proceedings of the International Conference on Lasers 1983*, San Francisco CA, Society for Optical and Quantum Electronics (STS Press, McLean VA, 1985), p. 718.

[12] See, e.g. S. Fischer and E. Lim, *Chem. Phys. Letts. 26*, 312 (1974), and references therein.

[13] G. Herzberg, *Molecular Spectra and Molecular Structure*, Vol. III, Electronic

Spectra and Electronic Structure of Polyatomic Molecules (Van Nostrand Reinhold Co., New York, 1966), pp. 66-8, 137-41.

[14] H. Selzle, W. E. Howard, and E. W. Schlag, *Rotational Band Contour Program* from Technische Universitat Munchen.

[15] B. N. Cyvin and S. J. Cyvin, *J. Phys. Chem.* *73*, 1430 (1969).

[16] W. R. Lambert, Ph. D. thesis, California Institute of Technology, 1982, p. 150.

[17] G. Herzberg, *Molecular Spectra and Molecular Structure*, Vol. II, Infrared and Raman Spectra (Van Nostrand Reinhold Co., New York, 1945), p. 47.

[18] E. B. Wilson, Jr., *J. Chem. Phys.* *3*, 276 (1935).

[19] G. Herzberg, *Molecular Spectra and Molecular Structure*, Vol. II, Infrared and Raman Spectra (Van Nostrand Reinhold Co., New York, 1945), pp. 215-7.

Table I

Symmetry assignments of anthracene S_1 vibrational levels from rotational band contour analysis

Energy [cm^{-1}]	Intensity [/10000]	Assignment [Ref. 1]	Symmetry [Ref. 1]	Symmetry [this work]
0	10000	0^0_0	a_g	a_g
209	17	-	b_{3g}?	a_g
232	74	$\overline{11}^1_0$	b_{1g}	b_{1g}
385	1351	12^1_0	a_g	a_g
390	45	2*209?	a_g?	a_g
473	19	$\overline{10}^1_0$	b_{1g}	a_g
541	71	$\overline{11}^2_0$	a_g	a_g
583	24	11^1_0	a_g	a_g
748	19	?	?	a_g
755	45	10^1_0	a_g	$2a_g$
766	91	12^2_0	a_g	a_g
889	22	$\overline{9}^1_0$	b_{1g}	b_{1g}
895	8	-	-	b_{1g}
905	9	-	-	a_g
1019	24	9^1_0	a_g	a_g
1042	21	?	?	a_g
1094	14	?	?	a_g
1142	7	-	-	a_g

Table I (cont.)

Energy [cm^{-1}]	Intensity [/10000]	Assignment [Ref. 1]	Symmetry [Ref. 1]	Symmetry [this work]
1146	19	-	-	?
1158	8	-	-	a_g
1168	56	$7/8^1_0$	a_g	$2a_g$
1184	15	$\bar{7}^1_0$	b_{1g}	?
1291	19	?	?	a_g
1380	139	6^1_0	a_g	$2a_g$[a]
1389	27	?	?	a_g
1409	80	$\bar{5}^1_0$	b_{1g}	$2a_g$?
1414	13	-	-	?
1418	35	-	-	?
1420	73	5^1_0	a_g	a_g
1501	103	4^1_0	a_g	?
1506	20	-	-	b_{1g}
1508	24	-	-	b_{1g}
1514	56	$\bar{4}^1_0$	b_{1g}	$b_{1g}+$[b]
1516	24	-	-	b_{1g}
1543	6	-	-	?
1545	8	-	-	?
1548	9	-	-	a_g
1550	14	$7/8^1_0\ 12^1_0$	a_g	?

Table I (cont.)

Energy [cm^{-1}]	Intensity [/10000]	Assignment [Ref. 1]	Symmetry [Ref. 1]	Symmetry [this work]
1635	25	$\bar{3}^1_0$?	b_{1g}?	a_g +[b]
1640	9	-	-	?
1767	23	$6^1_0\ 12^1_0$	a_g	?
1771	11	-	-	?
1773	13	-	-	?
1792	28	$\bar{5}^1_0\ 12^1_0$	b_{1g}	a_g
1795	5	-	-	a_g?
1798	5	-	-	?
1801	14	$5^1_0\ 12^1_0$	a_g	?
1883	4	-	-	?
1885	12	-	-	?
1890	4	-	-	?
1895	4	-	-	?
1897	4	-	-	?

[a] assignment possible only with resolved detection

[b] + indicates the presence of at least one strong overlapping transition

FIGURE CAPTIONS

Figure 1: Fluorescence excitation spectrum of the first excited state (S_1) of anthracene at 50 psi of neon. Conditions for each of the figures are as described in the experimental section. The energy scale is relative to the 0_0^0 transition (27695 cm^{-1}). The normalized spectrum has been plotted on three scales (-50 - 190 cm^{-1}, x1; 200 - 420 cm^{-1}, x10; 430 - 2000 cm^{-1}, x100) to better depict the less intense transitions.

Figure 2: Experimental (E) and computer-simulated (S) rotational band contours for a_g and b_{1g} vibrations in neon and nitrogen. The a_g band is the 0_0^0 transition, and the b_{1g} band is the 232 cm^{-1} mode. The excited state rotational constants were reduced 1% in energy from the ground state values to match the experimentally observed P and R branch relative intensities. Temperatures were varied to reproduce the P and R branch peak separations. The temperatures used were: a_g(Ne) = 3 K; b_{1g}(Ne) = 2 K; a_g(N_2) = 15 K; b_{1g}(N_2) = 8 K. As expected, nitrogen does not cool rotations as well as neon. Note the presence of Q-branches in, and the narrowness of, the b_{1g} profiles, readily distinguishing them from the a_g profiles.

Figure 3: Rotational band contours (top) and dispersed fluorescence spectra (bottom) of the 755 cm^{-1} complex in Ne. The energy zeroes are S_1 + 755 cm^{-1}. Total detection of the fluorescence yields trace A, showing two overlapping a_g modes. Exciting at positions 1 and 2 (top) and scanning the detection energy produces traces 1 and 2 (bottom) respectively. Recording the excitation profile while detecting only bands B and C (bottom) results in traces B and C (top) respectively. The well separated ground state modes at 755 cm^{-1} (C) and 835 cm^{-1} (B) are in Fermi resonance in the excited state (756 and 754 cm^{-1} respectively).

Figure 4: Rotational band contours of 1506, 1508, 1514, and 1516 cm^{-1} transitions in neon. Due to the length of the scan, the energy axis is not linear; the four transition energies are noted in the figure. The energy zero is S_1+1514 cm^{-1}. The four transitions are all clearly b_{1g} in symmetry, although a second intense component of unknown symmetry is present on the low energy side of the 1514 cm^{-1} transition. The 1506, 1508, and 1516 cm^{-1} modes are probably in Fermi resonance with the strong 1514 cm^{-1} mode, as discussed in the text.

Figure 5: Rotational band contours (top) and dispersed fluorescence spectra (bottom) of the 1380 cm^{-1} complex in neon. The energy zeroes are S_1 + 1380 cm^{-1}. Wide-band (1375-1555 cm^{-1}) detection of the fluorescence yields trace A. Traces B and C (top) result from detection of only bands B and C (1460 cm^{-1}). Excitation at positions 1 and 2 (top) produce the dispersed fluorescence traces 1 and 2 (bottom). The lower energy excited-state a_g component (1379 cm^{-1}) is much less intense than the main a_g component (1380 cm^{-1}), but nonetheless obscures the P-R branch gap and contributes a red shoulder to the wide-band contour, as well as complicating the dispersed fluorescence spectrum.

Figure 6: Rotational contours for the 1380 cm^{-1} band under two different detection conditions. Detection at 1460 cm^{-1}, where no quantum beats have been observed, produces "normal" contours. Detection at 389 cm^{-1}, where quantum beats do occur, results in unusual contours with greatly increased P-R branch separations; this corresponds to a suppression of low J values.

Figure 7: Rotational band contours (top) and dispersed fluorescence spectra (bottom) of the 1420 cm^{-1} complex in neon. The energy zeroes are S_1 + 1420 cm^{-1}. Detecting total fluorescence yields trace A with the main 1420 cm^{-1} a_g component and several overlapping lower energy components of uncertain symmetries. Traces B and C (top) result from detecting only bands B (1081 cm^{-1})

and C (1750 cm^{-1}) respectively. Excitation at positions 1 and 2 (top) produces dispersed fluorescence traces 1 and 2 respectively. Phase-shifted quantum beats have been observed for the C band.

Figure 8: Rotational contours for 1792, 1409, and 766 cm^{-1} in neon. The 1792 cm^{-1} mode is a combination of the 1409 and 385 cm^{-1} modes, the latter being observed in combination with many bands in the excitation spectrum. Although the 1792 cm^{-1} mode is clearly a_g in symmetry, comparison with 766 cm^{-1}, a typical a_g contour, shows that 1792 cm^{-1} is broader and has somewhat obscured P and R branches.

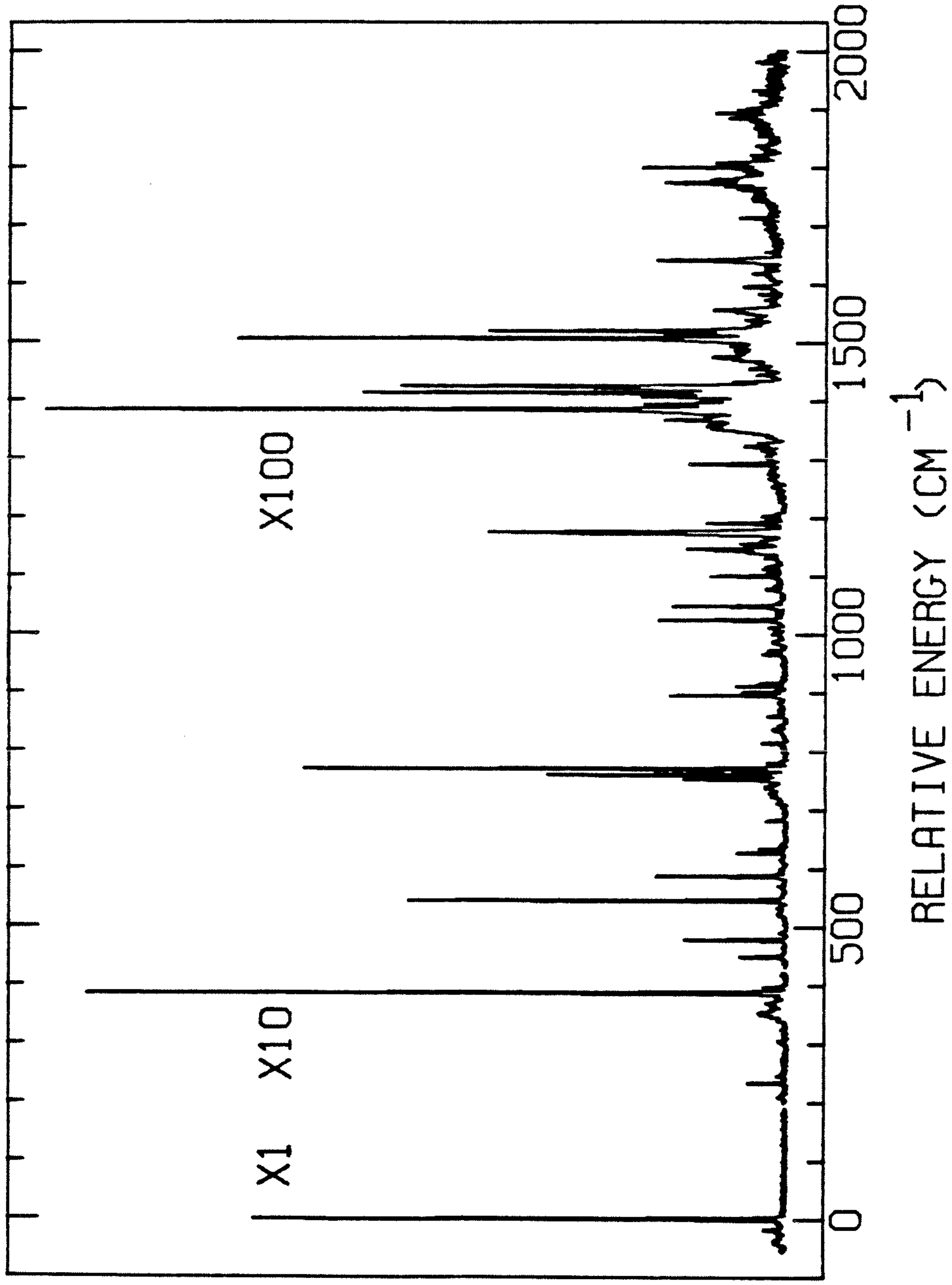

Figure 1

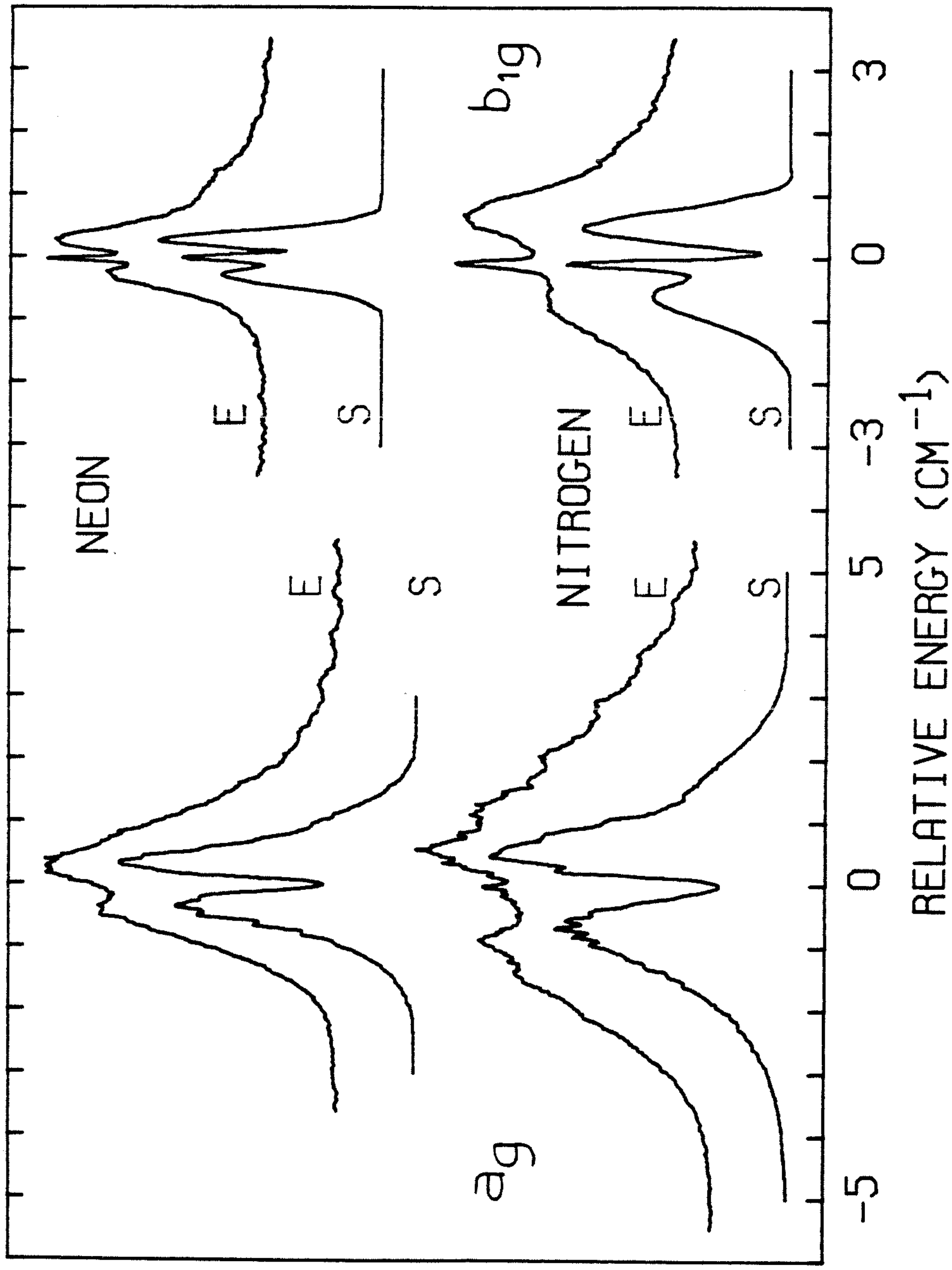

Figure 2

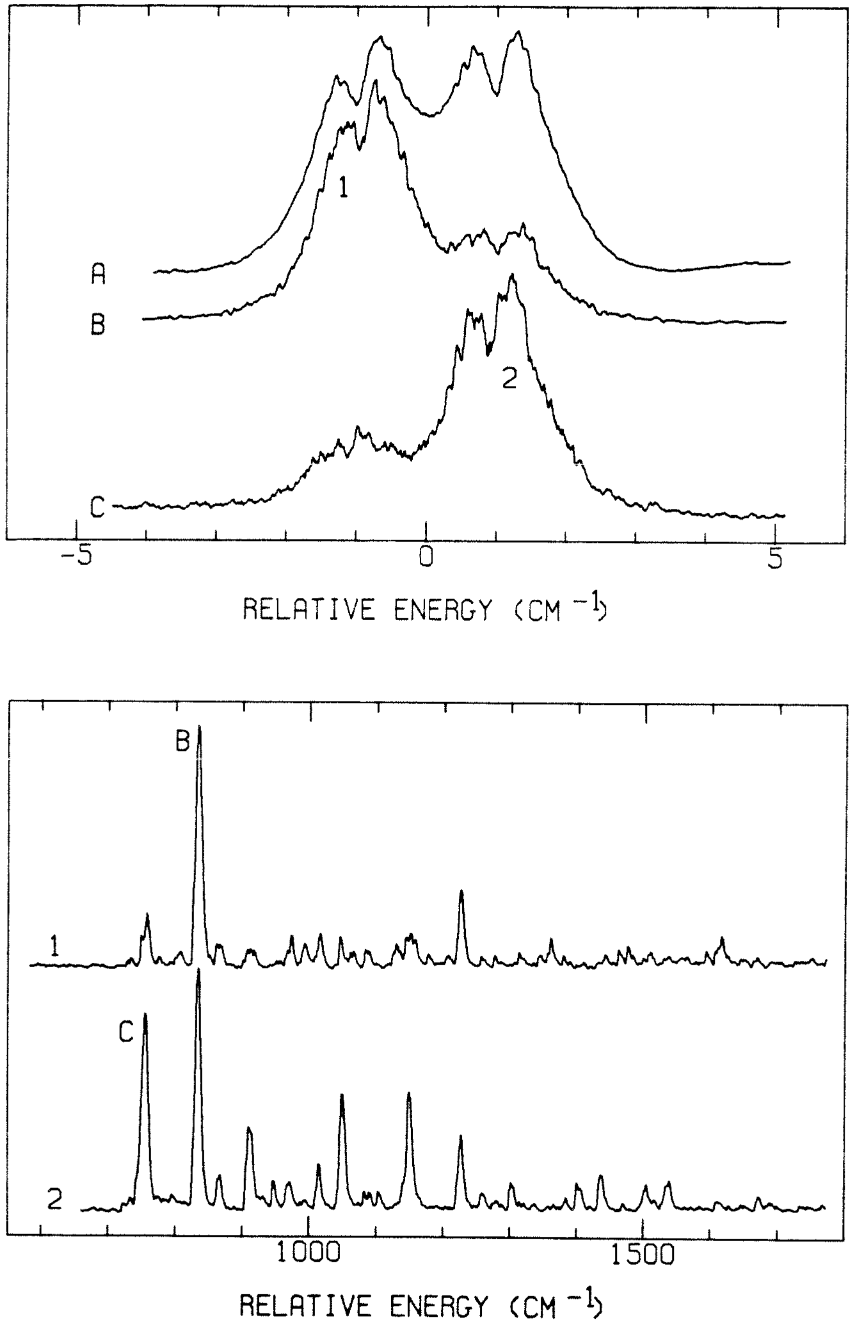
A
B
C
1
2
-5
0
5
RELATIVE ENERGY (CM^{-1})
B
C
1
2
1000
1500
RELATIVE ENERGY (CM^{-1})

Figure 3

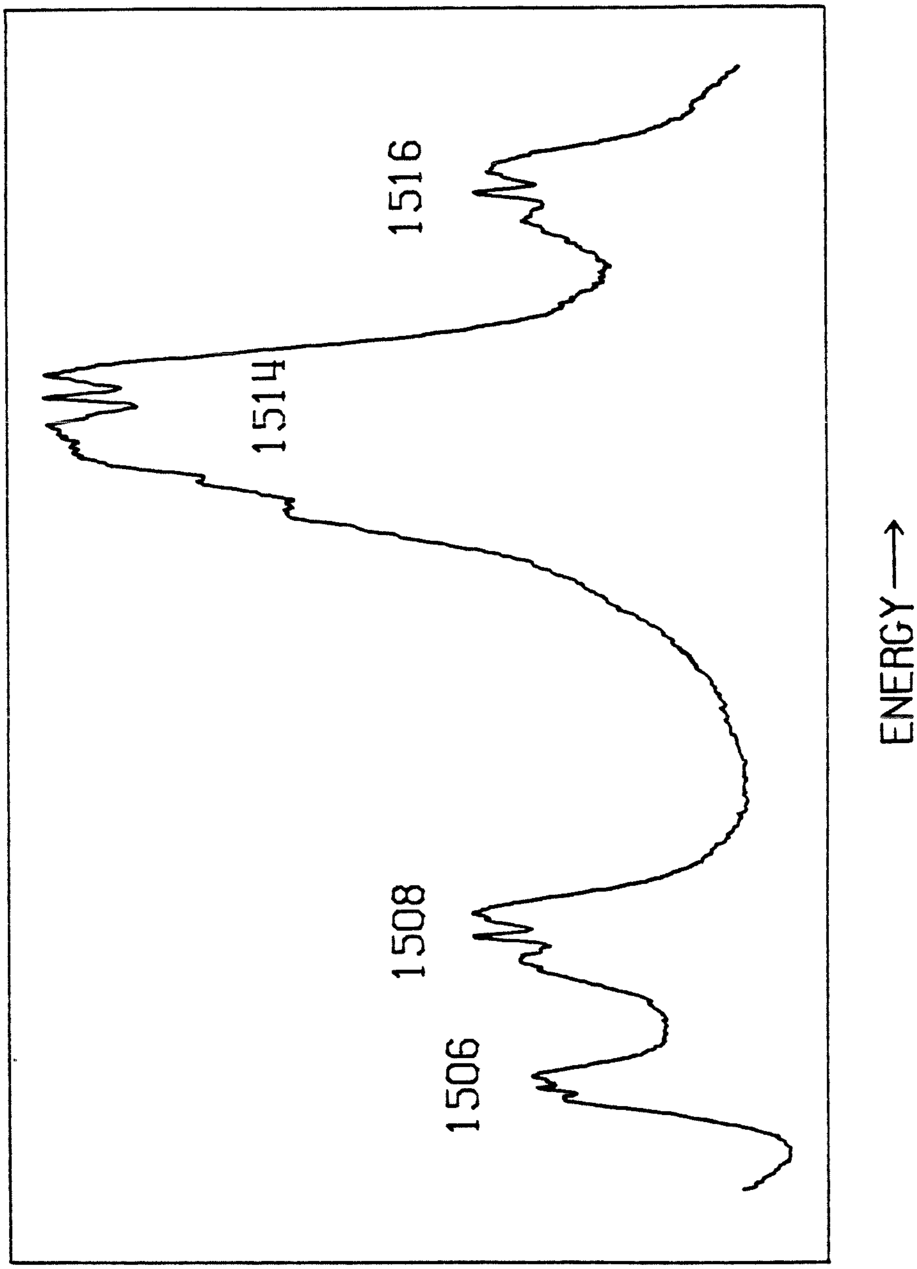

Figure 4

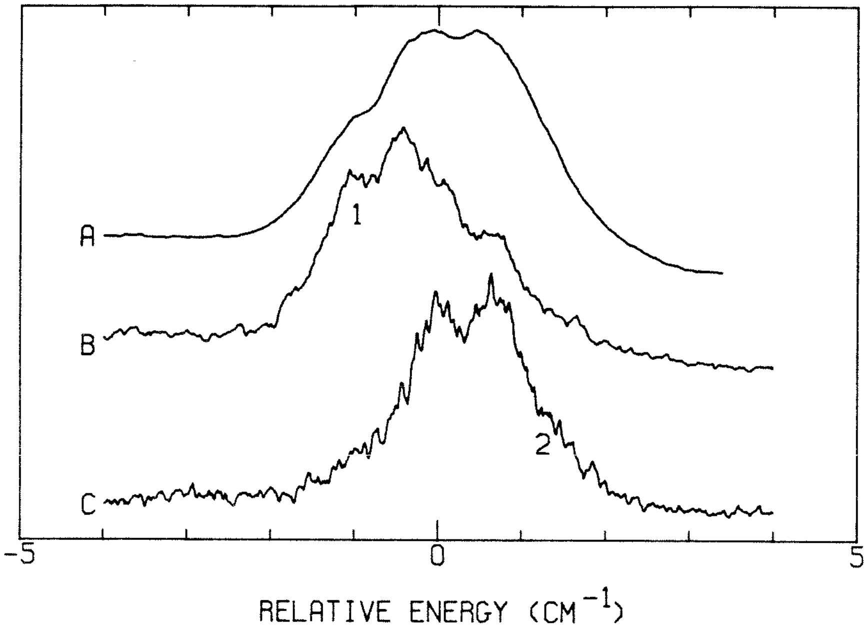
A
B
C
1
2
-5
0
5
RELATIVE ENERGY (CM^{-1})

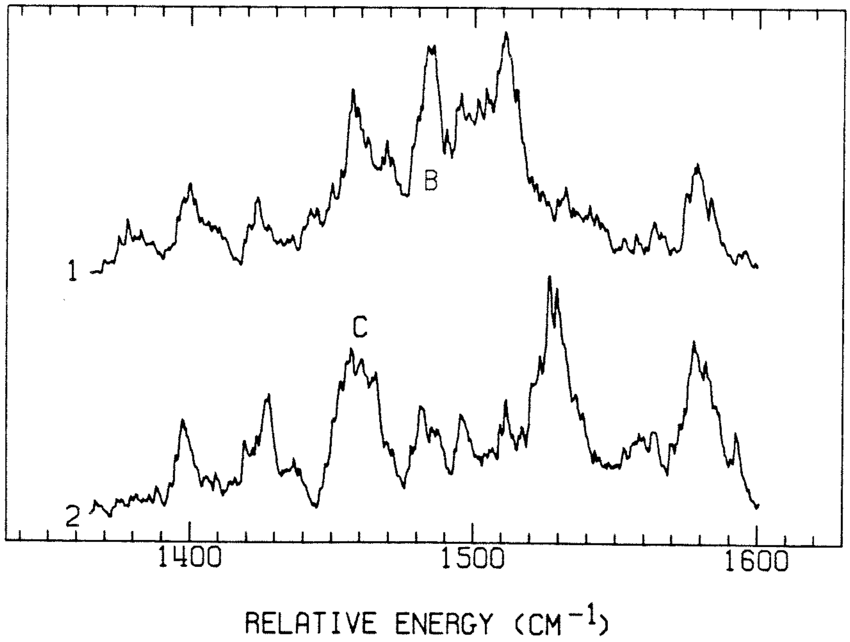
1
2
B
C
1400
1500
1600
RELATIVE ENERGY (CM^{-1})

Figure 5

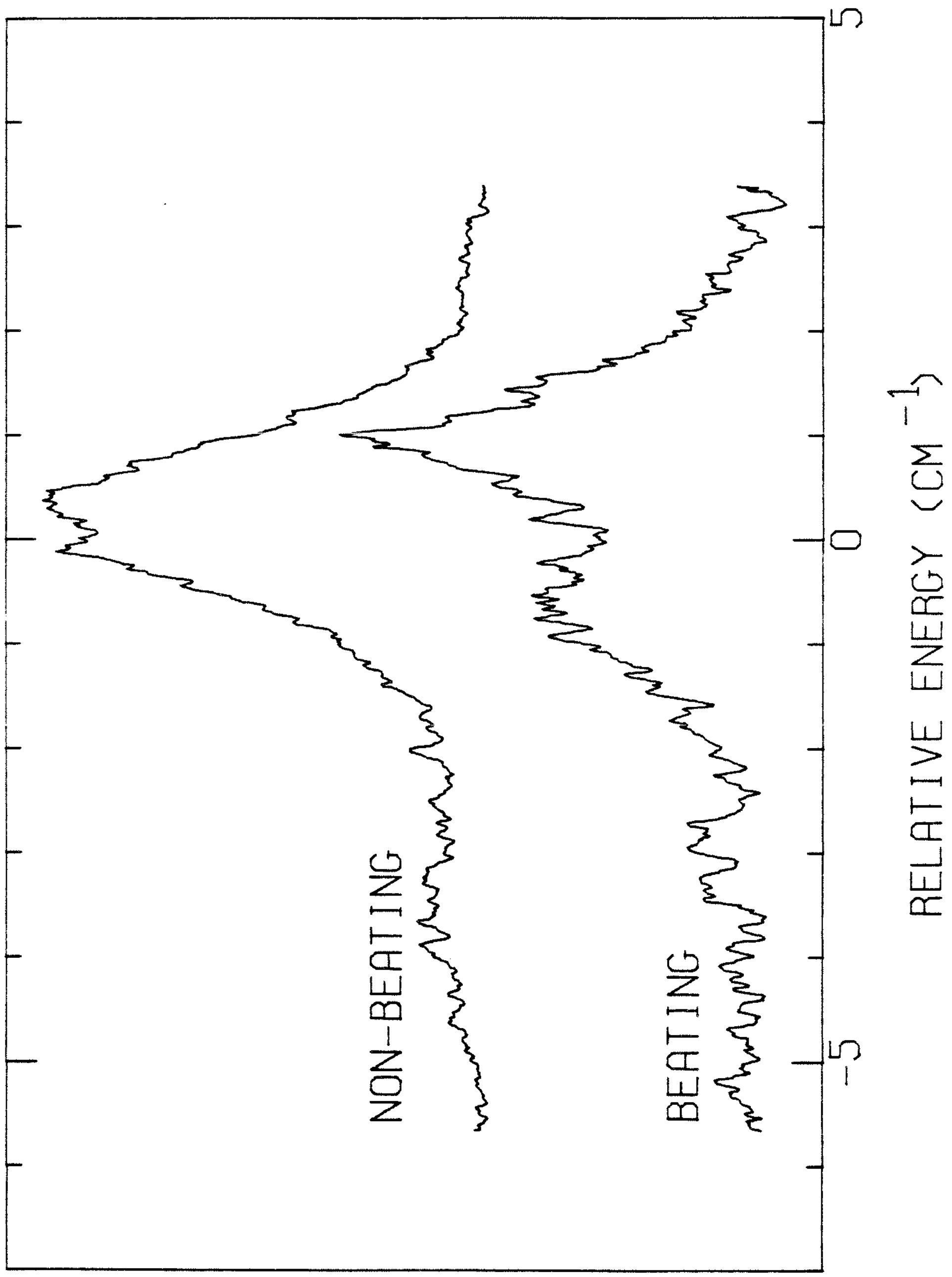

Figure 6

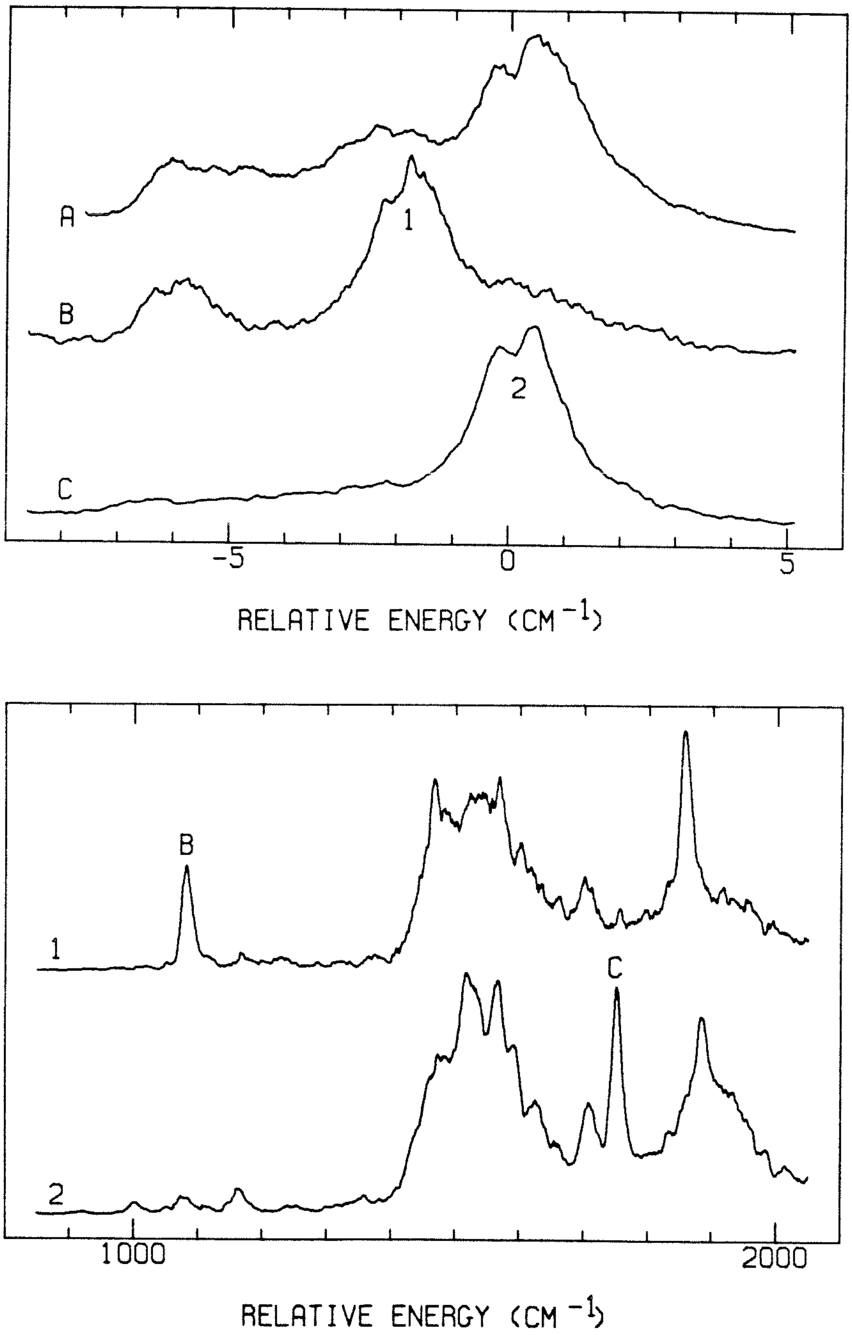
A
B
1
C
2
-5
0
5
RELATIVE ENERGY (CM^{-1})
B
1
C
2
1000
2000
RELATIVE ENERGY (CM^{-1})

Figure 7

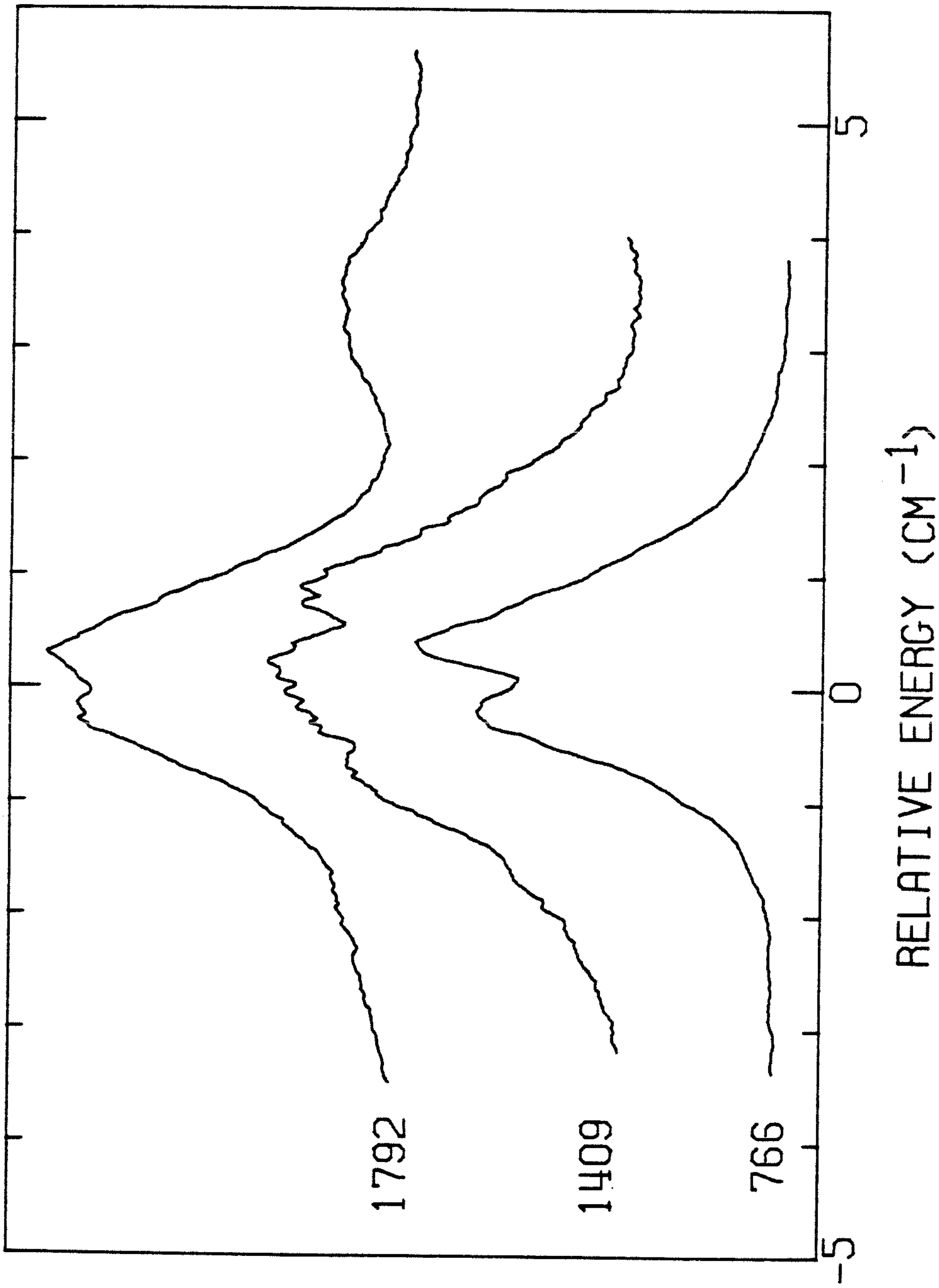

Figure 8

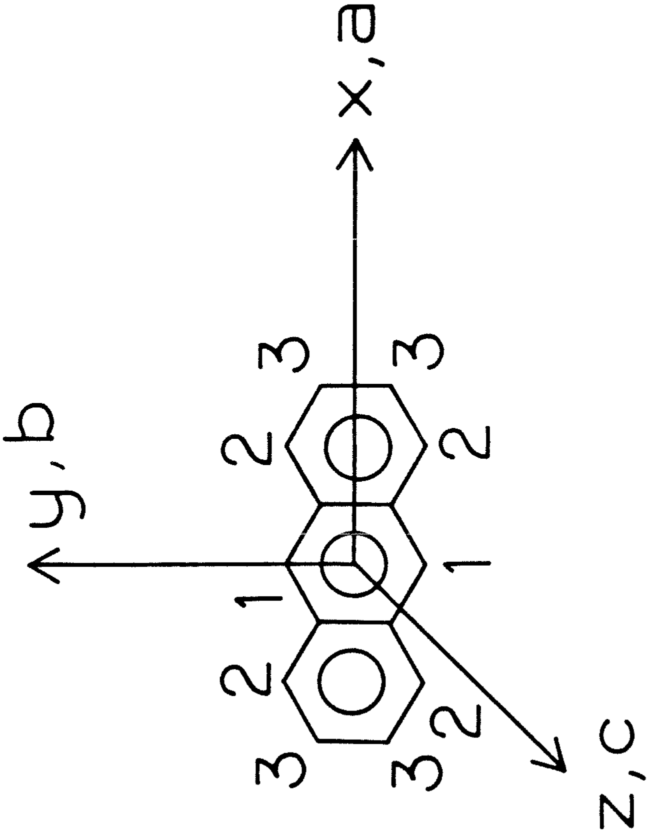

Figure 9

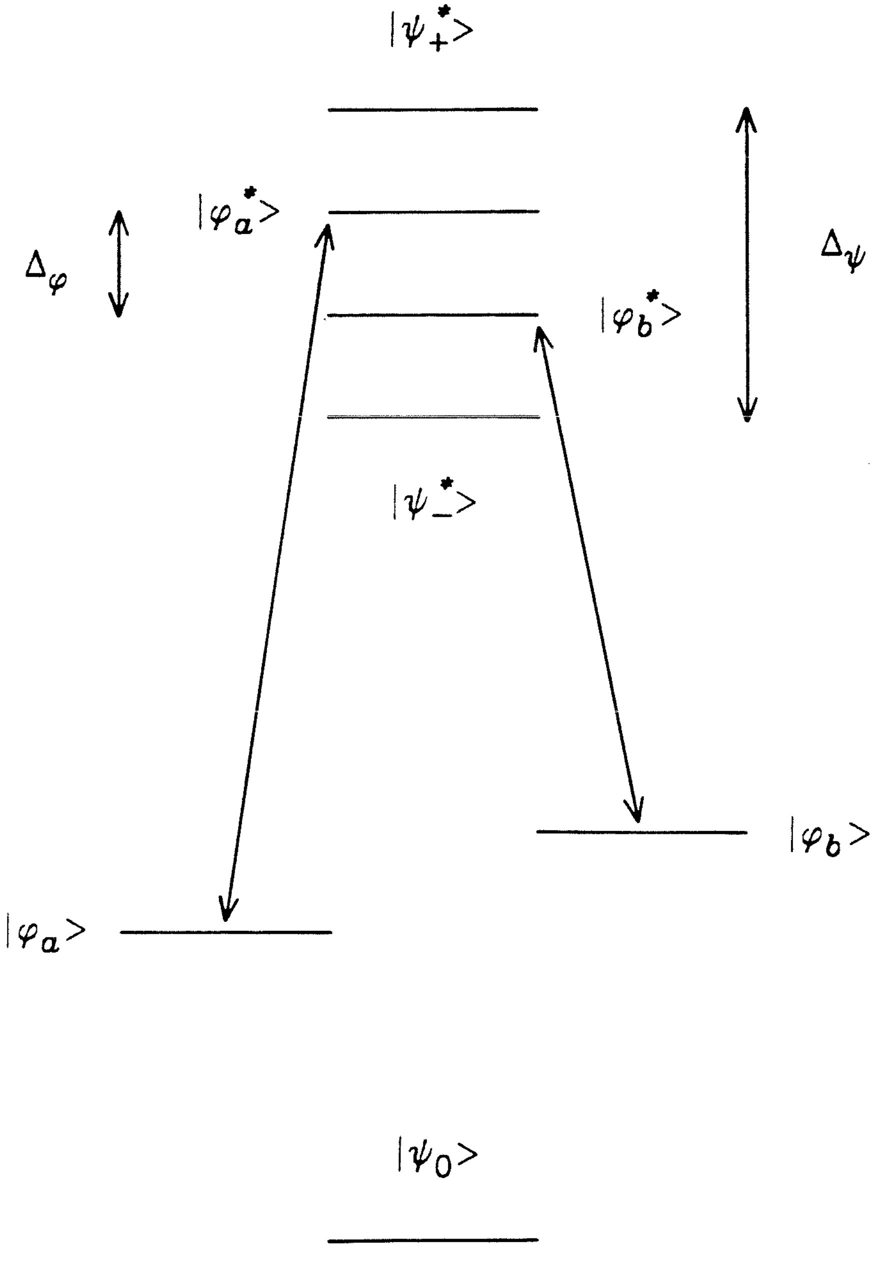
$|\psi_+^*\rangle$
$|\varphi_a^*\rangle$
Δ_φ
Δ_ψ
$|\varphi_b^*\rangle$
$|\psi_-^*\rangle$
$|\varphi_b\rangle$
$|\varphi_a\rangle$
$|\psi_0\rangle$

Figure 10

Rotational Band Contour Analysis of S_1 Vibrational Levels in Jet-cooled Anthracene-9d_1 and Anthracene-d_{10}

Chapter 8

Rotational Band Contour Analysis of S_1 Vibrational Levels in Jet-cooled Anthracene–9d$_1$ and Anthracene–d$_{10}$

ABSTRACT

The power-normalized S_1 fluorescence excitation spectra (resolution 0.5 cm^{-1}) of free jet-cooled anthracene–9d$_1$ and anthracene–d$_{10}$ (0 - 2000 cm^{-1}) have been obtained and compared to that of anthracene–h$_{10}$. Rotational band contours (resolution 0.1 cm^{-1}) were obtained for 65 levels in anthracene–9d$_1$ and 71 levels in anthracene–d$_{10}$, and were compared with 61 levels in anthracene–h$_{10}$. Detailed analysis of position, intensity, and vibrational symmetry allowed correlation of most of the ≈ 200 levels studied in the three isotopic anthracenes. The similarity of the excitation spectra and rotational band contour shapes, and the excellent correlation of vibrational levels, documents the highly analogous rovibronic nature of these three analogs. The spectral purity of rotational band contours, which reflects the number of strongly coupled levels involved, was found to correlate nicely with spectral emission character (relaxed *vs.* unrelaxed emission) and temporal behavior (single, modulated, or double exponential). The energy at which spectral impurity became great enough that rotational P-(Q)-R structure was completely obscured was found to be several hundred cm^{-1} less in the deuterated anthracenes than in anthracene–h$_{10}$. This supports the importance of density of states (anthracene–h$_{10}$ *vs.* anthracene–d$_{10}$) and molecular symmetry (anthracene–h$_{10}$ *vs.* anthracene–9d$_1$) in determining spectral purity, and, by analogy, in determining IVR rates.

I. INTRODUCTION

In a previous paper [1], we reported an exhaustive rotational band contour analysis of over fifty vibrational levels in anthracene$-h_{10}$ S_1 below 2000 cm^{-1} vibrational energy. From this analysis it was possible to assign the vibrational symmetries (fully-allowed a_g or vibronically-allowed b_{1g}) of all levels below 1100 cm^{-1} and many higher energy levels. In addition, the distinctiveness of the P-(Q)-R structure of contours and their relatively invariant full-widths at half-maxima (FWHM) served as bases for evaluating the spectral purity of levels, i.e. whether a level had major contributions from one (spectrally pure) or more than one (spectrally impure) vibronic state. In some cases it was possible to probe the nature and extent of coupling of overlapping vibronic levels using selective (energy-resolved) detection techniques.

Although the fluorescence excitation spectra of anthracene$-9d_1$ (point group symmetry C_{2v}) and anthracene$-d_{10}$ (D_{2h}) in supersonic molecular beams have been reported previously [2], these spectra were not normalized with respect to laser intensity (hence the relative intensities of different levels were subject to considerable error), nor were they analyzed in any detail. The isotopic analogs anthracene$-h_{10}$, anthracene$-9d_1$, and anthracene$-d_{10}$ can potentially provide a well-characterized series with which to study the roles of symmetry and density of states in intramolecular dynamics.

The density of states in anthracene$-9d_1$ is only slightly greater than in anthracene$-h_{10}$ (≈ 10 % in the S_1 C-C stretching region) [3], but the lower symmetry reduces the restrictions on which levels can anharmonically couple. There are four one-dimensional irreducible representations in C_{2v} *vs.* eight in D_{2h}. Thus, on the average, a given level is allowed by symmetry to couple anharmonically to twice as many levels in anthracene$-9d_1$ as in anthracene$-h_{10}$. Comparison of the behavior of these two isotopic analogs may isolate the influence of symmetry on intramolecular dynamics.

In contrast, comparison of anthracene-h_{10} and anthracene-d_{10} should isolate the influence of the density of states on these same dynamics. These analogs both have D_{2h} symmetry, but due to mass-effect reduction of vibrational frequencies, the density of states is considerably larger in anthracene-d_{10} than in anthracene-h_{10} (≈ 3 x as large in the C-C stretching region) [3].

Before such comparisons can be made, however, the vibrational levels in the deuterated anthracenes need to be characterized as thoroughly as those in anthracene-h_{10}. In this paper we present power-normalized fluorescence excitation spectra of both deuterated anthracenes and compare these spectra with that of anthracene-h_{10}. We then analyze the rotational band contours of 65 levels in anthracene-9d_1 and 71 levels in anthracene-d_{10} and correlate these with 61 levels in anthracene-h_{10}. The similarity of the spectra of the three analogs indicates that there are no substantial differences in their rovibronic nature which would invalidate comparison of the isotopes. Accordingly, the roles of molecular symmetry and density of states in anthracene spectroscopy and dynamics are investigated in this paper and a companion study [3].

II. EXPERIMENTAL

Our experimental system, except for the pressure-tuning apparatus, has previously been described in detail [4]; a full description may be found in Ch. 4. The dyes used in this study were 25% normal concentration LDS 750 in normal concentration methanolic LDS 698 (lower energies) and normal concentration ethanolic LDS 698 (higher energies). Spectra were all taken at 443 K with 50 psi of carrier gas. A nozzle diameter of 0.5 mm and a laser-to-nozzle distance of 10 mm (X/D = 20) were used thoughout the study. Doubling the laser-to-nozzle distance had no effect on the excitation spectrum near the origin, indicating optimal cooling at 10 mm. When the emission was not resolved with the monochromator, it was passed through a UV bandpass filter (Schott UG-11) to remove stray visible light and through a cutoff filter (Schott GG-395) to remove scattered laser light. Pressure-tuning was done with nitrogen, which gives a full scan range of 20 cm^{-1} at 360 nm. The pulsed dye laser was frequency calibrated using an iron-neon lamp and the optogalvanic method [5]. Vibrational frequencies are reproducible to $\pm 1 cm^{-1}$ below 1000 cm^{-1} and $\pm 2 cm^{-1}$ above 1000 cm^{-1}. Reported intensities are corrected for background, and are reproducible to ± 5 %.

Anthracene–h_{10} (Aldrich 99.9+ %) and anthracene–d_{10} (Aldrich 98+ %) were used without further purification. Anthracene–9d_1 was synthesized from 9-bromoanthracene (Aldrich 98 %) by lithiation with n-butyllithium followed by hydrolysis in D_2O [6]. Following recrystallization in benzene, the purity of the product was found to be > 99 % chemically by gas chromatography, and > 95 % isotopically by mass spectrometry (the balance being anthracene–h_{10}). The excitation spectrum of anthracene–9d_1 showed minor anthracene–h_{10} impurity lines; these were readily identified by absolute frequency and relative intensity, allowing unambiguous analysis of the anthracene–9d_1 transitions.

III. RESULTS AND DISCUSSION

A. Fluorescence Excitation Spectra

The power-normalized S_1 fluorescence excitation spectra of anthracene-$9d_1$ and anthracene-d_{10} are compared with that of anthracene-h_{10} in Fig. 1. Each spectrum is plotted against vibrational (= relative) energy, i.e. energy above the electronic origin. By obtaining the spectrum of a mixture of all three analogs, the relative positions of the anthracene-$9d_1$ and anthracene-d_{10} origins were accurately determined to be 12.2 and 71 cm^{-1}, respectively, to the blue of the anthracene-h_{10} origin (at 27,695 cm^{-1} [2]). Origin blue-shifts upon deuteration are expected since excited-state vibrational frequencies are usually lower than ground-state frequencies, and so have smaller *absolute* deuterium shifts. Thus the sum of the zero-point vibrational frequencies is reduced less (in an absolute sense) in an excited state than in the ground state, resulting in a greater origin transition energy.

The vibrational energies (cm^{-1}) and relative intensities (origin = 100 %) of 65 ± of the more intense levels in each isotopic species are listed in Table I. The intensities above which the table is complete for each species are: anthracene-h_{10}, 0.05 %; anthracene-$9d_1$, 0.1 %; anthracene-d_{10}, 1 %. Analagous levels in the different isotopic species are placed on the same line of the table.

Analogy was inferred by considering the following criteria: (1) the assignment must be consistent with the vibrational symmetry found by rotational band contour analysis; (2) isotopic shifts should be small (a few %) for most vibrations; large shifts, possibly up to the harmonic oscillator limit of $2^{-1/2}$, may be observed in the C-C-H bending region (900 - 1200 cm^{-1}); (3) the observed intensities, relative to nearby levels (= local relative intensities), should usually be similar in the different isotopic species, though the intensity of C-C-H bends may change anomalously upon deuteration; (4) the position and local relative intensity of anthracene–9d$_1$ levels should usually be intermediate between those of anthracene–h$_{10}$ and anthracene–d$_{10}$, and usually closer to the former; and (5) combination band frequencies and intensities should be consistent with the fundamental frequencies and intensities (i.e. the frequency will usually be slightly less than the sum of the fundamental frequencies, and the intensity will usually be on the order of the product of the fundamental intensities). As an example of the last criterion, consider the anthracene–h$_{10}$ 1801 cm^{-1} level with intensity 0.14 %: 385 + 1420 = 1805 cm^{-1}, and 13.5 % x 0.73 % = 0.10 %.

It is shown in § IIIB that symmetric (a_g) and antisymmetric (b_{1g}) modes can easily be distinguished by contour shapes. The small number of antisymmetric modes simplified determination of analogy, and thus provided a check on the isotopic shifts and intensity changes of nearby symmetric levels. Levels of different isotopes were not considered analogous and placed on the same line of Table I unless this assignment was consistent with most or all of the above criteria.

The excitation spectra of these three analogs are qualitatively very similar, but they differ quantitatively in the variation of average intensity with vibrational energy. In anthracene–h$_{10}$, the intensity of levels drops precipitously with increasing vibrational energy; e.g. the strongest level in the C-C stretching region (1380 cm^{-1}) is only 1.4 % as strong as the origin. The average level intensity drops off less rapidly in anthracene–9d$_1$; the strongest C-C stretch at 1409 cm^{-1} is 5.3 % as intense as the origin. In anthracene–d$_{10}$, average intensity decreases slowly with E_{vib}; the 1382 cm^{-1} C-C stretch is 40.8 % as strong as the origin. The trend is especially obvious when one considers the multipliers in Fig. 1 (1, 10, 100 in anthracene–h$_{10}$; 1, 10, 20 in anthracene–9d$_1$; and 1, 1, 3 in anthracene–d$_{10}$). In an electronic transition involving little geometry change, most of the intensity is concentrated in the origin; increasing geometry change results in a spread of intensity over more transitions. It would thus appear that more highly deuterated anthracenes experience larger geometry changes upon excitation to S_1.

One other difference was noted in the excitation behavior of the three analogs: while anthracene–h_{10} was efficiently vibrationally cooled by neon carrier gas (the spectrum in Fig. 1 was obtained with 50 psi Ne), anthracene–9d_1 and anthracene–d_{10} showed slight and severe apparent sequence congestion, respectively, in neon. Both deuterated anthracenes cooled well with 50 psi N_2 (see Fig. 1). The origin of this difference in cooling behavior between the isotopic analogs is not clear.

B. Rotational Band Contour Analysis

At lower vibrational energies (< 1100 cm^{-1}) in both deuterated anthracenes, nearly all of the rotational band contours conformed to one of two distinct types. The much commoner contour type, exemplified by the electronic origins, exhibited well-separated P and R branches, but no Q-branch, and had FWHM near 3.2 cm^{-1}. The rarer contour type (e.g. $\bar{\nu}_{11}$) showed a sharp Q-branch, and was narrower than the prevalent contour type (FWHM ≈ 2.5 cm^{-1}). This situation is identical with that found in anthracene–h_{10} (prevalent contour type: FWHM ≈ 4.0 cm^{-1}; rarer contour type: FWHM ≈ 2.3 cm^{-1}) [1]. The two types of contours of each of the three isotopic species are compared in Fig. 2 (commoner labelled a_g, rarer labelled b_{1g}); the similarity of each contour type for the different analogs is striking. In the previous anthracene–h_{10} study, it was convincingly argued that the prevalent contour type was associated with symmetric (a_g) vibrations, while the rarer type was due to antisymmetric (b_{1g}) vibrations. Although the same conclusion can be reached for the deuterated compounds strictly by analogy, the arguments of the previous study, suitably modified, are given below.

Assuming anthracene to be planar, anthracene$-d_{10}$ belongs to the point group D_{2h}. The similarity of the contours of anthracene$-9d_1$ suggests that it is reasonable to use D_{2h} nomenclature to describe this species, despite the fact that it belongs to point group C_{2v}. We shall follow this convention in this paper so that the symmetry descriptors are consistent throughout. As C_{2v} is a subgroup of D_{2h}, this does not result in the loss of useful information, and C_{2v} nomenclature can be recovered from the D_{2h} designations. In D_{2h}, the x, y, and z axes transform like B_{3u}, B_{2u}, and B_{1u}, respectively. Using the convention $I_x < I_y < I_z$ (so that x is the a rotational axis, y the b, and z the c, where $A > B > C$), the S_1 state is B_{2u} in symmetry.

Using lower-case letters to denote vibrational symmetries and capital letters for electronic symmetries, the ground vibronic state (which is the only one appreciably populated in the free jet with nitrogen carrier gas) is $|A_g a_g>$. Hence one may specify the symmetry of a vibronic transition to S_1 simply by specifying the symmetry of the vibrational level in S_1. An a_g transition will be fully (electric dipole- and Franck-Condon-) allowed and will be y-polarized, since $<B_{2u}|y|A_g>$ $<a_g|a_g>$ $\neq 0$. Although there are no known low-lying B_{1u} states with considerable oscillator strength from S_0, there is such a B_{3u} state [7]. Thus x-polarized b_{1g} transitions will be vibronically (Herzberg-Teller-) allowed [8] since $<B_{2u}b_{1g}|x|A_g a_g>$ $\neq 0$. We expect the fully-allowed a_g transitions to predominate over the vibronically-allowed b_{1g} transitions, and so can associate the prevalent contour type with a_g vibrations and the rarer type with b_{1g} vibrations. This conclusion is substantiated by the fact that the true electronic origin, being vibrationless, must be totally symmetric (a_g), as observed experimentally in the three anthracenes (i.e. the assigned origin contours are of the prevalent type).

In the following section, our assignment of transition symmetries is confirmed by computer simulation of contour shapes as a function of transition moment orientation. Anticipating this, a brief description of higher energy behavior and an explanation of the symmetry assignments in Table I is appropriate. At higher vibrational energies, there is a tendency for contours to be broader and less clearly structured; above ≈ 1700 cm^{-1} virtually no contours are noticeably structured. Such contours are termed "spectrally impure", meaning that more than one vibronic level contributes significantly to the contour. This phenomenon is discussed in greater detail in § IIIE. Contours which are identifiable as a_g or b_{1g} but which show evidence of more than one contributing level are denoted by a_g+ or b_{1g}+; contours which are not identifiable due to overlap of several vibronic levels are simply denoted by +. In some cases, contributing levels are separated sufficiently that each can be identified, e.g., $2a_g$. For a complete explanation of the notation in the Symmetry columns in Table I, see footnote d of that table. Assigned a_g, a_g+, and + contours are compared in § IIIE and Fig. 6.

C. Computer Simulation of Contours

As indicated above, the association of the commoner contour type with a_g vibrational levels in S_1, and the rarer contour type with b_{1g} levels, can be rigorously substantiated by computer simulation of rotational band contour shapes as a function of transition moment orientation (x, y, or z). Computer simulations were generated by a Fortran program developed by Schlag's group in Munich [9]. Distortion in S_0 and S_1 was assumed to be negligible. Sufficiently large J-values were included in the calculations so that a doubling of the maximum included J-value had insignificant effect on the calculated contour shape (typically J_{max} = 30 was satisfactory). The resolution was taken to be 0.1 cm^{-1}, the upper bound on the UV laser bandwidth, as in the anthracene–h_{10} study.

The rotational constants of the deuterated anthracenes in S_0 were calculated using the same structural data [10] as was used in the anthracene–h_{10} study. The results (in cm^{-1}) for anthracene–9d_1 are A = 0.06824, B = 0.01520, and C = 0.01243; for anthracene–d_{10}, A = 0.05915, B = 0.01385, and C = 0.01122. For comparison, in anthracene–h_{10}, A = 0.0700, B = 0.01520, and C = 0.01249. All three molecules are close to being prolate symmetric tops, with asymmetry parameters of κ = -0.9007 (anthracene–9d_1), -0.8903 (anthracene–d_{10}), and -0.9058 (anthracene–h_{10}). All three molecules are close to "Case 7" in Ueda and Shimanouchi's study of rotational band contour shapes in asymmetric tops [11], as all are planar (thus 1 - C/A - C/B = 0, since $C^{-1} = A^{-1} + B^{-1}$) and all have 2C/B ≈ 1.6 (anthracene–9d_1, 1.636; anthracene–d_{10}, 1.620; anthracene–h_{10}, 1.643).

Anthracene–d_{10} has no fermions, so the statistical weights of each of the rotational symmetries are equal. In anthracene–9d_1, there are four pairs of equivalent protons which transform similarly. Character analysis yields Γ_{pair} = $3A + B$ (using C_{2v} rotational subgroup nomenclature), so $\Gamma_{tot} = (3A + B)^4 = 136A + 120B$. Note that 136 + 120 = 256 = 2^8 as expected for eight fermions with two possible spin states each. The variation in statistical weights in this molecule is comparable to that found in anthracene–h_{10} ($\Gamma_{tot} = 288A + 240(B_1 + B_3) + 256B_2$) [1].

Two parameters were fit by hand to reproduce the experimental contours: rotational temperature and excited state rotational constants. As rotational temperature is increased, simulations become broader and the P-R branch gap increases. The dependence is weak, and the temperatures can be estimated from previous studies, so fitting to the nearest K (as evaluated by the P-R branch gap values) is straightforward. Rotational temperatures are not expected to depend on vibrational symmetry, so the differences in the temperatures for a_g and b_{1g} vibrations provides a measure of the uncertainty in the fitted temperature. The temperatures in nitrogen carrier gas were found to be a_g = 23 K, b_{1g} = 23 K for anthracene–9d$_1$; and a_g = 21 K, b_{1g} = 26 K for anthracene–d$_{10}$; compare to a_g = 15 K, b_{1g} = 8 K for anthracene–h$_{10}$. This increase in rotational temperatures upon deuteration may be significant as it parallels the poorer vibrational cooling of these compounds in neon, as discussed in § IIIA.

Variation of the excited-state rotational constants affects the relative intensities of the P, Q, and R-branches. Since rotational constants are not expected to change appreciably upon excitation (they usually decrease slightly due to slightly increased bond lengths), fitting them to the nearest 1/4 % is feasible if one assumes that the three constants change by the same amount upon excitation, i.e. $A^*/A = B^*/B = C^*/C$. Although this assumption is not necessarily correct, it greatly simplifies the fitting procedure. The reductions of rotational constants upon excitation to S_1 were found to be 1/2 % for anthracene–9d$_1$, and 3/4 % for anthracene–d$_{10}$, compared to 1 % for anthracene–h$_{10}$.

It should be emphasized that neither of the two fitted parameters had a profound influence on the contour shapes of the simulations, e.g. a_g contours always lacked Q-branches while b_{1g} contours always exhibited them. This is important as polarization (symmetry) assignments might otherwise be ambiguous. The excellent agreement of the simulations and experimental contours, depicted in Figs. 3 (anthracene–9d$_1$) and 4 (anthracene–d$_{10}$), provides definitive evidence that the commoner and rarer contour types correspond to a_g and b_{1g} levels in S_1, respectively. One minor point of disagreement is the failure to observe the structure on the R-branch in the anthracene$-d_{10}$ a_g simulation. As the simulations also predict greater modulation in the low J-region than is observed experimentally, it is not surprising that the R-branch structure is obscured. Assuming a larger effective resolution would modify the simulations appropriately, but does not seem warranted given the narrowness of the experimental Q-branches.

Simulations of z-polarized b_{3g} vibrational contours, using the derived average temperatures and S_1 rotational constants found above, are extremely broad, with exceptionally intense Q-branches. As in the case of anthracene$-h_{10}$, *no* such contours were observed for the deuterated anthracences. We conclude that vibronic coupling to B_{1u} states is negligible in the first excited states of the three anthracenes studied.

Finally, it should be noted that the relative insensitivity of the contour shapes to the indeterminant parameters (rotational temperature and excited-state rotational constants), coupled with the ease of *a priori* estimation of these parameters, results in the feasibility of *predicting* contour shapes of molecules for which ground state structural data is available. By comparing the simulation shapes for transition moments lying along the three rotational axes of a molecule, the distinguishability of the different polarizations may be ascertained. Thus, the effectiveness of this technique in determining vibrational symmetries can be evaluated before undertaking an experimental study. The asymmetric top contour study of Ueda and Shimanouchi [11] can also be used for this purpose, but the discrete resolution values and higher temperatures in that study make evaluation of the technique's usefulness more difficult.

D. A Resolved Detection Study

Following excitation to S_1 + 1380 cm^{-1} in anthracene–h$_{10}$, quantum beat modulations have been observed in the fluorescence decays under certain detection conditions [12,13]. Detection in the region of the Franck-Condon maximum in the emission (e.g. to S_0 + 1460 cm^{-1}) yields a typical single exponential decay without modulation. In contrast, detection of emission to the S_0 + 389 cm^{-1} level results in a distinctively modulated decay (389 cm^{-1} is ν_{12}, the most prominent a_g fundamental in the S_1 excitation spectrum). In order to probe the coupling mechanism responsible for these quantum beats (and hence implicated in the process of restricted vibrational redistribution), the frequency analogs of the temporal experiments have been performed [1,12]. The rotational band contour of S_1 + 1380 cm^{-1} is normal (i.e. similar to other a_g contours observed in S_1) when emission to the S_0 + 1460 cm^{-1} region is detected. In contrast, detection of emission to S_0 + 389 cm^{-1} yields a unique contour, which differs from other a_g contours in having the R branch much more intense than the P branch, in having a greater FWHM, and in having a wider, deeper P-R branch gap. This corresponds to an enhancement of large J-valued transitions and $\Delta J = +1$ transitions. The most likely coupling mechanism in this case is Coriolis coupling, which increases as the molecule rotates more quickly (larger J) due to increased centripetal forces. These tend to stretch bonds in a manner which resembles a vibration, thus vibrational and rotational motions are coupled.

In anthracene–9d$_1$, the S_1 + 1411 cm^{-1} level is suitable for a similar study, since (1) it is an intense, spectrally pure level, exhibiting distinct P-R structure; and (2) two types of quantum beat modulations (in- and out-of-phase) are observed in the fluorescence decays under certain detection conditions [3]. Specifically, detection of emission to S_0 + 389 cm^{-1} yields in-phase quantum beats due to emission from a state which is initially populated by the laser pulse (as in the case of the previously discussed anthracene–h_{10} quantum beats). In contrast, detection of emission from a state populated indirectly through coupling to a laser-populated state, e.g., emission to S_0 + 1499 cm^{-1}, yields out-of-phase quantum beats. These two types of quantum beats differ in phase by 180°, since population oscillates between the states producing the two types of modulation. Total detection of emission (i.e. detection of all emission except that absorbed by a laser cutoff filter) yields a typical single exponential decay with no quantum beat modulations.

The frequency analogs of these temporal experiments are depicted in Fig. 5. The resolved emission (= dispersed fluorescence) spectrum is shown in the upper half of the figure, trace A. The rotational band contour obtained with total detection, corresponding to a single exponential decay, is shown in trace B in the lower half of the figure. Detection of emission to the range S_0 + 389 ± 100 cm^{-1}, shown by the interval labelled 1 in trace A, yields the contour in trace C, corresponding to in-phase quantum beats. Contour D, corresponding to out-of-phase quantum beats, was obtained through detection of interval 2 in trace A (S_0 + 1499 ± 25 cm^{-1}). These three contours are very similar in appearance, the differences being within the range of experimental uncertainty (as judged by spectral reproducibility). Certainly there are no dramatic differences in contour shapes as in anthracene–h_{10} S_1 + 1380 cm^{-1}. It would therefore appear that a different coupling mechanism (presumably anharmonic coupling), which is at most mildly J-dependent, is responsible for the quantum beats in this system. This is not surprising given the extent of anharmonic coupling elsewhere in anthracene S_1, and suggests that the apparent Coriolis coupling in anthracene–h_{10} S_1 + 1380 cm^{-1} may be the exception, rather than the rule.

E. Spectral Purity of Rotational Band Contours

In recent years, vibrational redistribution has been characterized in both energy-resolved and time-resolved emission experiments. At low vibrational energies, where vibrational redistribution is slow compared to fluorescence, emission spectra are composed of sharp, discrete lines, and structurally resemble excitation spectra. In the time domain, single exponential fluorescence decay curves are observed. At intermediate vibrational energies, the fluorescence is a combination of sharp lines and broad, unstructured emission. At these energies, intramolecular quantum beat modulation of fluorescence decays is sometimes evident. Quantum beats arise from the interaction of a small number of levels, and so characterize the region of restricted vibrational redistribution. In-phase quantum beats and sharp emission may be associated with those states initially populated by the laser pulse, while out-of-phase quantum beats and continuum emission are due to states populated indirectly through vibrational redistribution. At high vibrational energies, only continnum emission is observed, and biexponential fluorescence decays are observed. The fast component of a biexponential decay reflects dissipative (= statistical = irreversible) vibrational redistribution to a large number of states, while the slow component reflects the subsequent decay of the states populated by vibrational redistribution.

Vibrational density of states appears to be one of the most important parameters in determining redistribution rates. It is reasonable to expect that the density of states will influence the static nature of a molecule as well as its dynamical behavior. As an example, the 'spectral purity' of an excitation contour should depend upon the density of states in a manner analogous to the emission characteristics, since, as the density of states increases, the probability of anharmonic coupling (Fermi resonance) should also increase. This hypothesis is supported by the results of this study. At low vibrational energies, contours are spectrally pure, i.e. involve only one vibronic level with appreciable transition probability from the ground vibronic state. Spectrally pure contours exhibit distinct P-(Q)-R structure and have well-defined FWHM; an example (anthracene–d_{10} S_1 + 1039 cm^{-1}, assignment: a_g) is shown in Fig. 6, trace A. At intermediate vibrational energies, contours are somewhat spectrally impure, i.e. consist of two or more overlapping vibronic levels with similar or dissimilar transition probabilities. In this region, the P-(Q)-R structure is typically discernable (at least on the stronger transitions) but may be partially obscured. The different levels are usually at least partially resolvable; an example is shown in Fig. 6, trace B (anthracene–d_{10} S_1 + 1450 cm^{-1}, assignment: a_g+). At high vibrational energies, contours are very impure spectrally, consisting of a number of overlapping levels usually of comparable intensity. The P-(Q)-R structure is rarely discernable, and individual vibronic levels cannot normally be resolved. An example is given in Fig. 6, trace C (anthracene–d_{10} S_1 + 1751 cm^{-1}, assignment +). The comparison afforded in Fig. 6 demonstrates the decrease in P-(Q)-R structure, and increase in FWHM, of rotational contours as vibrational energy is increased.

The distribution in energy of the three classes of spectral purity for each of the anthracenes is depicted in Fig. 7. In order to emphasize the correlation between spectral purity, spectral emission character, and temporal behavior, results from energy- and time-resolved emission experiments are also included in the figure. Definitions of the three regimes (low, intermediate, and high energies) for each type of experiment are given in the figure caption. Several conclusions can be reached following examination of this figure. (1) There is a general correlation between each of the three regimes in each of the three types of experiments, as hypothesized above. (2) The individual regimes tend to be broader as defined by spectral purity than as defined by the two emission criteria. This leads to significant overlap of the regimes. (3) The deuterated anthracenes show high-energy regime spectral purity at significantly lower energies (hundreds of cm^{-1} less) than anthracene$-h_{10}$.

These observations are consistent with what would be expected intuitively. As mentioned earlier, Fermi resonance occurs between nearby levels of the same symmetry; the probability of finding one or more levels of the appropriate symmetry close to an optically active level increases as the vibrational density of states increases. Thus, allowing for a random element (which includes both coupling strength and randomness of level arrangement), the abundance of Fermi resonances should increase with increasing energy. Fermi resonances produce overlapping optically active levels either with or without discernable P-(Q)-R structure, depending upon the number of interactng levels and their separations. The overall correlation of the three types of experiments indicates that vibrational energy influences spectral emission character and temporal behavior in a fashion similar to that of spectral purity.

The overlap of the three regimes of spectral purity is a result of the random element of resonance. The apparent lack of overlap of the three regimes as deduced from the emission experiments is probably a result of two factors: (1) the much smaller number of data points from the emission studies; and (2) a reduced randomness of coupling strengths due to a sampling of smaller coupling matrix elements and coupling ranges (see Ch. 2).

The reduction of the lower limit of the high-energy regime of spectral purity upon deuteration is consistent with the dependence of coupling on density of states and symmetry. The magnitude of the anticipated shifts can be estimated from calculated density of states curves [3]. The density of states is approximately the same in anthracene$-d_{10}$ near 1175 cm^{-1} as it is in anthracene$-h_{10}$ at 1400 cm^{-1} (the lowest energy structureless contour in anthracene$-h_{10}$ is at

1417 cm^{-1}). Excluding the two lowest data points (845 and 937 cm^{-1}), which are rather isolated, the lower limit for the high-energy spectral purity regime in anthracene–d_{10} is 1136 cm^{-1}, which is comparable to the estimated value. This substantiates the influence of density of states on spectral purity. As mentioned in the introduction, strictly on the basis of molecular symmetry, we would expect twice as many states to anharmonically couple to a given level in anthracene–$9d_1$ as in anthracene–h_{10}. The density of states of anthracene–$9d_1$ at 1250 cm^{-1} is approximately one-half that of anthracene–h_{10} at 1400 cm^{-1}, which is not too different from the lower limit of the high-energy spectral purity regime in anthracene–$9d_1$ at 1135 cm^{-1} (excluding an isolated point at 899 cm^{-1}). This substantiates the influence of molecular symmetry on spectral purity.

Correlations of this type are not apparent for the low and intermediate energy regimes of spectral purity; in fact, the upper limit of the low energy regime increases slightly upon deuteration. This is not too surprising, as the distinction of the low and intermediate energy regimes is somewhat arbitrary (levels were considered to be overlapping if their centers were within 4 cm^{-1} of each other), and the distribution of the intermediate regime may be particularly subject to random element effects. If the low and intermediate energy regimes are combined into a structured regime (meaning that P-(Q)-R structure is discernable), then a somewhat more consistent picture emerges. The upper limit of the structured regime is then 1635, 1582, and 1690 cm^{-1} for anthracene–h_{10}, anthracene–$9d_1$, and anthracene–d_{10}, respectively. Given the discrete, unevenly distributed nature of the data points, and the random element involved, this probably is statistically equivalent to an approximate invariance of the upper limit of the structured regime with respect to extent of deuteration.

It is not completely clear why a significant decrease in this limit is not observed upon deuteration, although it might be argued that this regime is subject to greater random element effects than the unstructured regime, where a greater number of states are interacting, more effectively averaging the random elements. Perhaps the least biased way of testing the deuteration trend is to average the upper limits of the structured regime and lower limits of the structureless regimes, excluding no data points. This yields 1526, 1240, and 1268 cm^{-1} for anthracene–h_{10}, anthracene–$9d_1$, and anthracene–d_{10}, respectively, in reasonable agreement with the expected shifts for anthracene–$9d_1$ ($\approx$ 150 cm^{-1}) and anthracene–d_{10} ($\approx$ 225 cm^{-1}).

Similar analyses are not possible for spectral emission character and temporal behavior due to the lesser data point densities. The observation of a high-energy regime dispersed fluorescence spectrum at 1509 cm^{-1} in anthracene–$9d_1$ (compared to 1635 cm^{-1} in anthracene–h_{10}) may well be a reflection of the reduced molecular symmetry of anthracene–$9d_1$.

In conclusion, although quantitative analysis is hampered by random element effects, the spectral purity data are qualitatively consistent with the hypotheses that increased vibrational density of states and decreased molecular symmetry decrease the energy of the transition from structured to unstructured rotational contour profiles. The correspondence between spectral purity, spectral emission character, and temporal behavior suggests that an analogous conclusion may be reached concerning IVR, specifically, that IVR rates are increased by higher densities of states and lower molecular symmetries.

REFERENCES

[1] B. W. Keelan and A. H. Zewail, *J. Chem. Phys. 82*, 3011 (1985).

[2] W. R. Lambert, P. M. Felker, J. A. Syage, and A. H. Zewail, *J. Chem. Phys. 81*, 2195 (1984).

[3] D. H. Semmes and A. H. Zewail, to be published.

[4] B. W. Keelan, J. A. Syage, J. F. Shepanski, and A. H. Zewail, in *Proceedings of the International Conference on Lasers 1983*, ed. R. C. Powell (STS Press, McLean, Virginia, 1985), p. 718.

[5] E. F. Zalewski, R. A. Kellar, and R. Engleman, Jr., *J. Chem. Phys. 70*, 1015 (1979), and references therein.

[6] J. L. Charlton and R. Agagnier, *Can. J. Chem. 51*, 1852 (1973).

[7] See, e.g., S. Fischer and E. Lim, *Chem. Phys. Letts. 26*, 312 (1974), and references therein.

[8] G. Herzberg, *Electronic Spectra and Electronic Structure of Polyatomic Molecules*, (Van Nostrand Reinhold, New York, 1966), pp. 66 - 8, 137 - 41.

[9] H. Selzle, W. E. Howard, and E. W. Schlag, *Rotational Band Contour Program*, from Technische Universitat Munchen.

[10] B. N. Cyvin and S. J. Cyvin, *J. Phys. Chem. 73*, 1430 (1969).

[11] T. Ueda and T. Shimanouchi, *J. Mol. Spectrosc. 28*, 350 (1968).

[12] W. R. Lambert, P. M. Felker, and A. H. Zewail, *J. Chem. Phys. 81*, 2217 (1984).

[13] P. M. Felker and A. H. Zewail, *Phys. Rev. Letts.* *53*, 501 (1984).

Table I: Comparison of S_1 Vibrational Levels in Anthracene-h_{10}, -9d_1, and -d_{10}

Anthracene-h_{10}			Anthracene-9d_1			Anthracene-d_{10}		
Energy[a]	Intensity[b]	Assignment[c]	Energy	Intensity	Symmetry[d]	Energy	Intensity	Symmetry
0	100.00	0_0^0	0	100.0	a_g	0	100.0	a_g
209	0.17	a_g	210	0.1	a_g	---	--	--
232	0.74	$\overline{11}{}_0^1$	231	1.4	b_{1g}	229	11.2	b_{1g}
385	13.51	12_0^1	385	11.8	a_g^+	370	58.9	a_g
390	0.45	2x209?	396	0.2	==	--	--	--
--	--	--	--	--	--	392	1.1	b_{1g}
--	--	--	421	0.2	a_g	--	--	--
444	0.08	a_g	449	0.3	a_g	430	1.6	a_g
473	0.19	a_g	460	0.7	a_g	418	4.5	a_g
541	0.71	$\overline{11}{}_0^2$	542	1.6	a_g	525	10.2	a_g
583	0.24	11_0^1	583	0.8	a_g	567	3.5	a_g
623	0.06	a_g	614	0.6	a_g	561	2.1	a_g
630	0.05	b_{1g}	634	0.2	b_{1g}	619	1.4	b_{1g}
678	0.03	a_g	673	0.1	a_g	649	5.7	a_g
--	--	--	694	0.1	a_g	--	--	--
748	0.19	a_g	742	0.5	a_g	690	2.6	a_g
755	0.45	$10_0^1, a_g$	751	1.5	a_g	720	11.8	a_g
766	0.91	12_0^2	769	2.3	a_g	743	14.5	a_g
775	0.04	a_g	778	0.1	a_g	--	--	--
--	--	--	832	0.2	$2a_g$	--	--	--
--	--	418+370	--	--	--	788	1.7	a_g
889	0.22	$\bar{9}_0^1$	880	0.5	b_{1g}	791	6.7	$2b_{1g}$
895	0.08	b_{1g}	864	0.2	b_{1g}	764	1.1	b_{1g}
--	--	--	884	0.5	b_{1g}	--	--	--
905	0.09	a_g	899	0.1	+	804	1.7	a_g
910	0.05	a_g	904	0.2	a_g	809	2.4	a_g
--	--	--	913	0.1	a_g	--	--	--
--	--	--	948	0.1	a_g?	917	2.1	a_g
961	0.04	a_g	959	0.1	a_g	928	0.7	==
966	0.03	a_g	966	0.2	a_g	937	1.5	+
--	--	--	995	0.1	a_g^+	--	--	--

Table I (cont.)

Anthracene-h_{10}			Anthracene-$9d_1$			Anthracene-d_{10}		
Energy	Intensity	Assignment	Energy	Intensity	Symmetry	Energy	Intensity	Symmetry
1019	0.24	9^1_0	1012	0.2	a_g	--	--	--
--	--	--	1028	0.1	a_g	--	--	--
1042	0.21	a_g	1037	0.6	a_g	829	16.5	a_g
--	--	--	1073	0.1	$3b_{1g}$	--	--	--
1094	0.14	a_g	1089	0.5	a_g	845	3.4	+
--	--	--	1101	0.1	b_{1g}+	--	--	--
1142	0.07	$10^1_0 12^1_0$	1135	0.3	+	1092	2.9	a_g
1146	0.19	12^3_0				1114	1.6	a_g
1158	0.08	a_g	--	--	--	--	--	--
--	--	--	1160	0.7	b_{1g}	864	1.0	b_{1g}
1168	0.56	$7^1_0, 8^1_0$	1167	1.1	a_g	874	5.4	a_g
			1173	1.3	+	882	8.8	a_g
--	--	--	1183	0.3	+	--	--	--
1184	0.15	$\bar{7}^1_0$	1189	0.4	b_{1g}+	--	--	--
--	--	--	1269	0.1	+	--	--	--
--	--	--	1278	0.1	+	--	--	--
--	--	--	1297	0.2	+	--	--	--
--	--	--	1304	0.2	a_g	--	--	--
--	--	--	1319	0.2	a_g	--	--	--
1291	0.19	a_g	--	--	--	--	--	--
--	--	--	--	--	--	1039	1.9	a_g
--	--	--	--	--	--	1136	1.0	+
--	--	--	--	--	--	1162	1.2	+
--	--	829+370	--	--	--	1197	3.8	a_g
--	--	--	--	--	--	1235	1.5	a_g
--	--	--	--	--	--	1307	3.5	a_g
--	--	--	--	--	--	1339	8.6	+
--	--	--	--	--	--	1359	1.7	a_g
--	--	--	--	--	--	1364	3.5	+
1380	1.39	$6^1_0, a_g$	1375	3.0	a_g+	1382	40.8	a_g
1389	0.27	a_g	--	--	--	--	--	--

Table I (cont.)

Anthracene-h_{10}			Anthracene-$9d_1$			Anthracene-d_{10}		
Energy	Intensity	Assignment	Energy	Intensity	Symmetry	Energy	Intensity	Symmetry
1409	0.80	$2a_g$?	1409	5.3	a_g	1450	33.2	a_g+
1414	0.13	+	1418	0.3	+	1419	2.4	a_g
1418	0.35	+				1425	2.4	a_g+
1420	0.73	5^1_0	1435	1.5	a_g	1440	15.2	+
--	--	--	1454	0.3	a_g+	--	--	--
1469	0.09	1094+385	1469	0.2	+	1215	1.1	+
--	--	--	1480	0.2	$2b_{1g}$	1465	2.5	b_{1g}?
1501	1.03	4^1_0	1499	3.4	a_g+	1484	17.7	+
1506	0.20	b_{1g}	--	--	--	--	--	--
1508	0.24	b_{1g}	--	--	--	--	--	--
1514	0.56	$\bar{4}^1_0$+	1509	2.2	+	1475	9.6	+
1516	0.24	b_{1g}	1520	0.3	b_{1g}	1497	3.9	$b_{1g}+b_{1g}$?
1543	0.06	+	1532	0.2	+	1510	2.5	+
1545	0.08	+	1540	0.5	+			
1548	0.09	a_g				1241	2.7	a_g
1550	0.14	$7/8^1_0 12^1_0$	1550	0.2	+	1249	1.6	a_g
1577	0.06	==	1573	0.3	+	1546	4.6	a_g
1590	0.07	==	1582	0.3	a_g+	1554	4.8	+
1635	0.25	a_g+	1629	0.4	+	1592	6.5	a_g+
1640	0.09	+	--	--	--	1587	3.7	a_g
--	--	--	--	--	--	1608	1.9	a_g+
1715	0.07	==	1705	0.1	+	1641	6.3	a_g+
--	--	2x829	--	--	--	1658	2.8	a_g+
--	--	1307+370	--	--	--	1679	1.0	a_g
--	--	--	--	--	--	1690	2.0	a_g+
--	--	1339+370	--	--	--	1712	2.5	+
--	--	1359+370	--	--	--	1729	1.4	+
1767	0.23	$6^1_0 12^1_0$	1765	0.7	+	1751	7.6	+
1771	0.11	+	--	--	--	--	--	--
1773	0.13	1389+385	--	--	--	--	--	--
--	--	--	--	--	--	1778	4.2	+

Table I (cont.)

Anthracene-h_{10}			Anthracene-$9d_1$			Anthracene-d_{10}		
Energy	Intensity	Assignment	Energy	Intensity	Symmetry	Energy	Intensity	Symmetry
1792	0.28	1409+385	1792	1.2	+	1811	8.9	+
1795	0.05	1414+385	1803	0.1	==	1793	1.1	+
1798	0.05	1418+385						
1801	0.14	$5^1_0 12^1_0$	1820	0.1	==	1821	6.4	+
1883	0.04	+	--	--	--	--	--	--
1885	0.12	$4^1_0 12^1_0$	1886	0.6	+	1852	3.6	+
1890	0.04	1506+385	--	--	--	--	--	--
1895	0.04	$\bar{4}^1_0 12^1_0$	--	--	--	1846	3.6	+
1897	0.04	1516+385	--	--	--	1866	0.6	==
--	--	--	1926	0.1	==	1920	1.5	+
--	--	--	--	--	--	1952	1.7	+
--	--	1592+370	--	--	--	1961	1.7	+

---

[a] Vibrational energy in cm^{-1}. The $-h_{10}$ data are primarily from Refs. 1 and 2. The $-h_{10}$ origin is 27695 cm^{-1} (from Ref. 2); in this study the $-9d_1$ and $-d_{10}$ origins were found to be shifted 12.2 and 71 cm^{-1} respectively to higher energy.

[b] Percent intensity relative to the origin of each molecule (100 %), which is the most intense transition in each molecule. The $-h_{10}$ data is primarily from Refs. 1 and 2.

[c] A^m_n denotes the transition of mode number A from n quanta in the ground electronic state to m quanta in the excited state S_1; combination bands are $A^m_n B^i_j$... A bar over a mode number indicates a non-totally symmetric (i.e. b_{1g}) vibration. Where mode numbers have not been assigned in Ref. 2, combination bands are denoted by a+b, where a and b are the $-h_{10}$ vibrational frequencies in cm^{-1} (in a few cases, combination bands in $-d_{10}$ have no observed $-h_{10}$ analog; the $-d_{10}$ frequencies are then given in this column). For levels not assigned in Ref. 2, vibrational symmetries from Ref. 1 are given (see note d for designations; superpositions of levels are also denoted with a comma, e.g. $10^1_0, a_g$ indicates that mode number 10 and another a_g vibration overlap).

[d] Vibrational symmetries found in this study from rotational band contour analysis. Superpositions of levels are denoted variously, e.g. $2a_g$ (two a_g vibrations overlap), a_g+ (one or more vibrations of indeterminate symmetry overlap with an a_g vibration), or just + (two or more vibrations of indeterminate symmetry overlap). The designation == indicates that no symmetry analysis has been performed for that level.

FIGURE CAPTIONS

Figure 1: S_1 fluorescence excitation spectra of anthracene–h_{10} (50 psi Ne, 415 K, X/D = 24), anthracene–$9d_1$, and anthracene–d_{10} (both 50 psi N_2, 443 K, X/D = 20). Energy references are the electronic origins (anthracene–h_{10} = 27,695 cm^{-1}, anthracene–$9d_1$ = 27,707 cm^{-1}, anthracene–d_{10} = 27,766 cm^{-1}). Note that the multiplicative factors for the intensities differ in the three spectra, e.g. in anthracene–h_{10} the strong transition near 1400 cm^{-1} is only a little over 1 % as intense as the origin, while in anthracene–d_{10} the corresponding transition is more than 1/3 as intense as the origin. For a discussion of these spectra see § IIIA.

Figure 2: Comparison of experimental rotational band contours for the origin (a_g symmetry) and $\bar{\nu}_{11}$ (b_{1g} symmetry) for each of the three isotopic species studied. Experimental conditions were 50 psi N_2, 443 K, X/D = 20. The contours are identical except for very slight differences in P-(Q)-R branch relative intensities and FWHM, indicating that the three isotopic analogs are very similar vibronically. See § IIIB.

Figure 3: Comparison of experimental rotational band contours (EXP) and computer simulations (SIM) for anthracene–$9d_1$. Experimental conditions as in Fig. 2. The contours were best reproduced by using excited-state rotational constants reduced 1/2 % from the ground state values, and taking the rotational temperature to be 23 K. The excellent agreement between the experimental contours and simulations, which are relatively independent of the fitted parameters, unambiguously confirms the symmetry assignments (a_g and b_{1g}) made by spectral considerations. This also demonstrates the usefulness of simulations for predicting contour shapes of molecules for which ground-state structural data is available. See § IIIC.

Figure 4: Comparison of experimental contours (EXP, conditions as in Fig. 2) and computer simulations (SIM) for anthracene$-d_{10}$. The experimental contours were best reproduced by using excited state rotational constants reduced 3/4 % from S_0 values, and taking the rotational temperature to be 21 K (a_g) or 26 K (b_{1g}). The agreement between the simulations and the experimental contours is very good, although the structure in the R-branch of the simulation was not observed in experimental contours. See § IIIC.

Figure 5: Selective detection study of the S_1 + 1411 cm^{-1} level in anthracene$-9d_1$. The resolved emission (= dispersed fluorescence) spectrum is shown in trace A, above. Total detection (i.e. detection of all emission except that absorbed by a laser cutoff filter) yields the typical rotational band contour B, below. In the temporal domain, these detection conditions result in typical single exponential fluorescence decay. Detection of emission to S_0 + 389 (± 100) cm^{-1} (this interval being labelled 1 in trace A) gives contour C; in the corresponding fluorescence decay, in-phase quantum beat modulations are observed. Detection in the interval labelled 2 in trace A (S_0 + 1499 (± 25) cm^{-1}), which exhibits out-of-phase quantum beat modulation of the fluorescence decay curve, produces contour D. The similarity of these three contours indicates that the coupling between the quantum-beating states is insensitive to the rotational quantum number J, suggesting anharmonic coupling. See § IIID for a detailed discussion.

Figure 6: Variation of spectral purity of rotational contours with vibrational energy in anthracene$-d_{10}$. As energy (and the vibrational density of states) increases, the spectral purity of contours decreases. The three contours shown are S_1 + 1039, 1450, and 1751 cm^{-1}, which are assigned as a_g, a_g+, and +, respectively. Note the decrease of the distinctiveness of the P-R rotational

structure, and increase in FWHM, as vibrational energy increases. Spectral purity provides a qualitative measure of the variation of 'effective' density of states with energy, and correlates nicely with spectral emission character (relaxed *vs.* unrelaxed emission) and temporal behavior (single, modulated, and double exponential decays). See § IIIE.

Figure 7: Low (▽), intermediate (◇), and high (△) energy regimes as deduced by spectral purity of rotational band contours (RBC), amounts of unrelaxed *vs.* relaxed emission in dispersed fluorescence spectra (DFS), and temporal behavior of fluorescence decay curves (FDC) in anthracene–h_{10} (H10), anthracene–9d_1 (9D1), and anthracene–d_{10} (D10) [1-3]. The three regimes for each type of spectrum are defined as follows. Rotational band contour: low = no overlapping levels to ± 4 cm^{-1}; intermediate = overlapping levels but P-(Q)-R structure still discernable; high = overlapping levels with with no distinct P-(Q)-R structure. Dispersed fluorescence spectra: low = sharp structure only; intermediate = both sharp structure and broad continuum; high = broad continuum only. Fluorescence decay curves: low = single exponential; intermediate = quantum beat modulations; high = biexponential. Note overall correlation of the regimes for the three different types of spectra. The reduction of the lower limit of the spectral purity high energy regime upon deuteration reflects the increase in density of states (anthracene–d_{10}) or decrease of molecular symmetry (anthracene–9d_1) which occurs upon deuteration. For a much more detailed discussion see § IIIE.

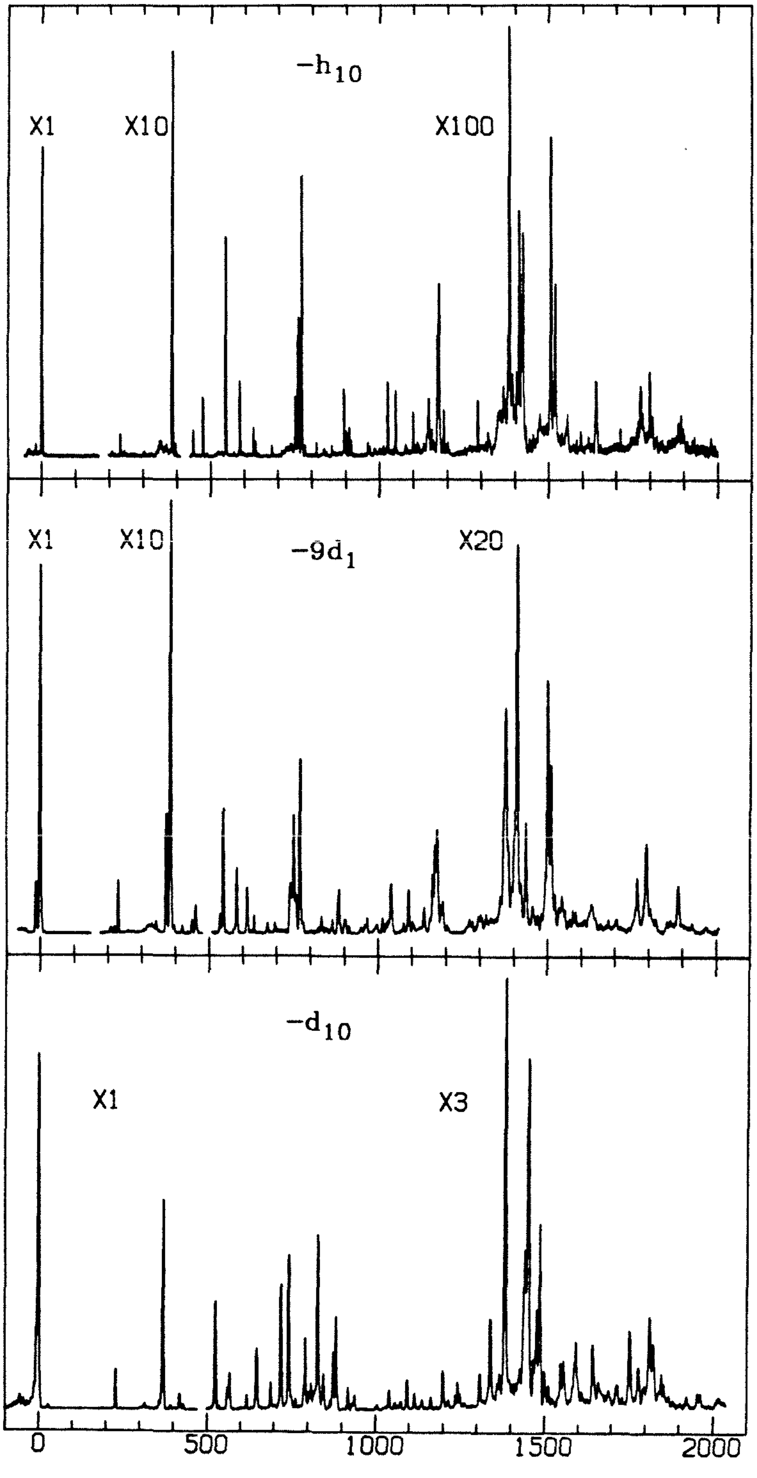
-h$_{10}$
X1
X10
X100
X1
X10
-9d$_1$
X20
-d$_{10}$
X1
X3
0
500
1000
1500
2000
RELATIVE ENERGY (CM^{-1})

Fig. 1

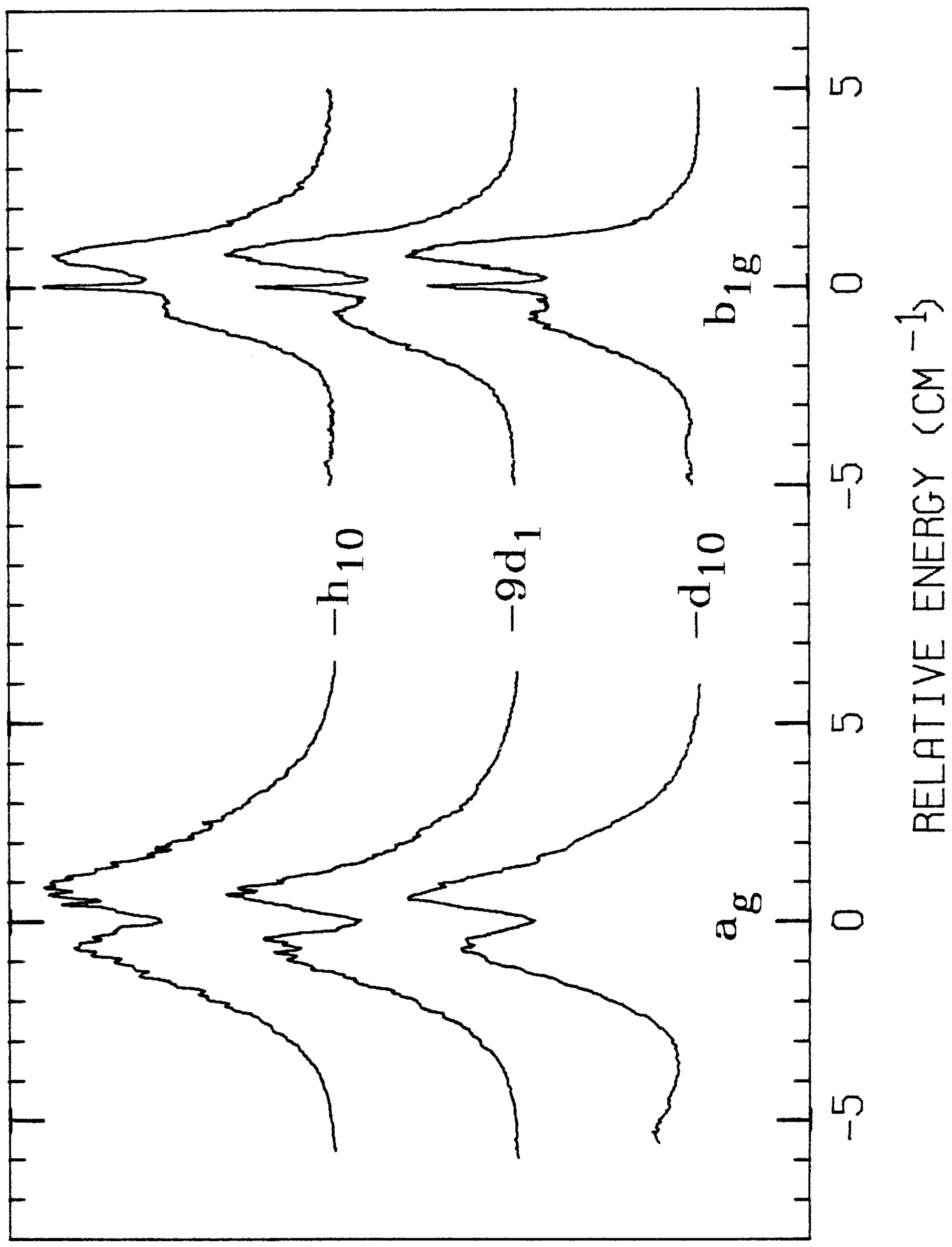

Fig. 2

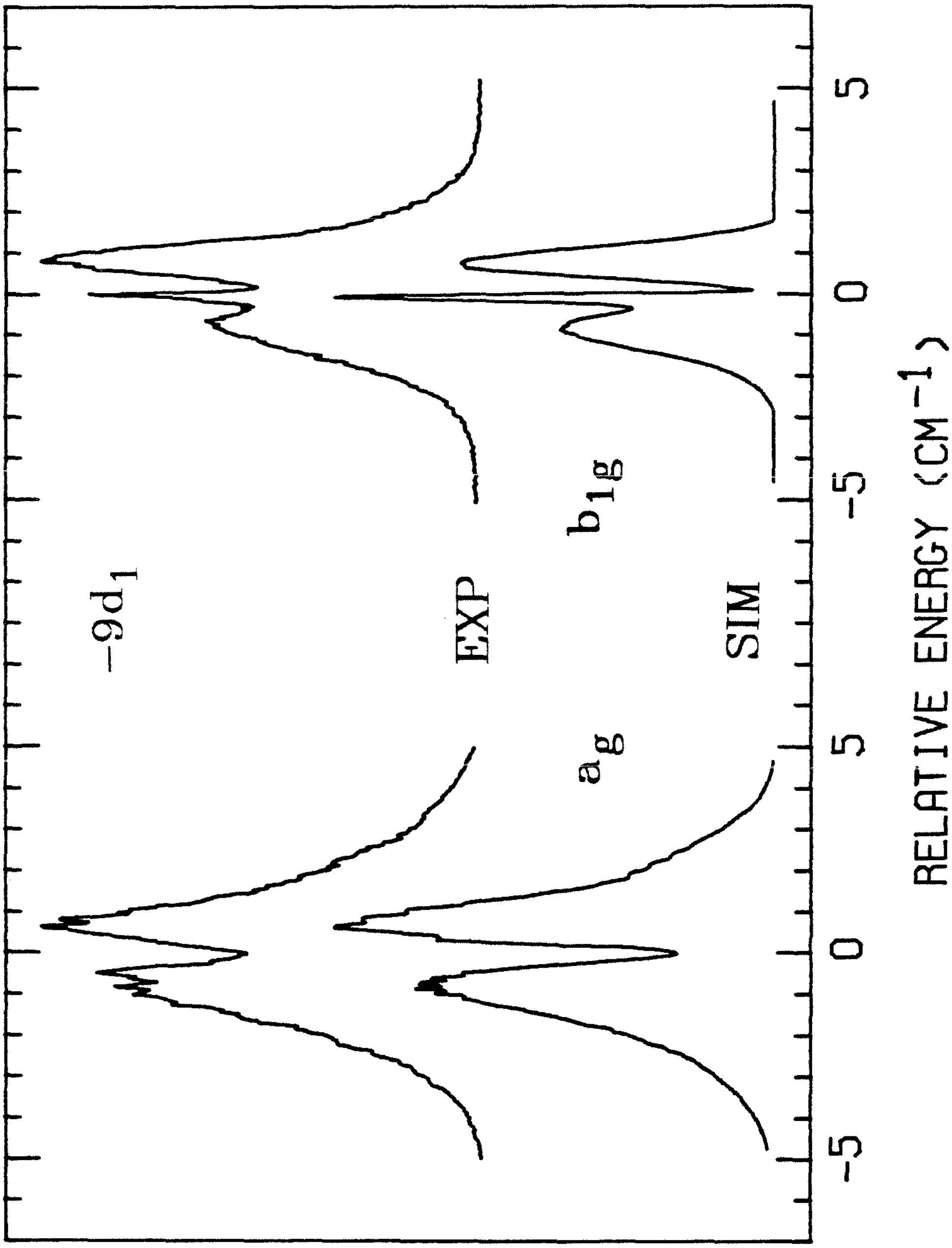

Fig. 3

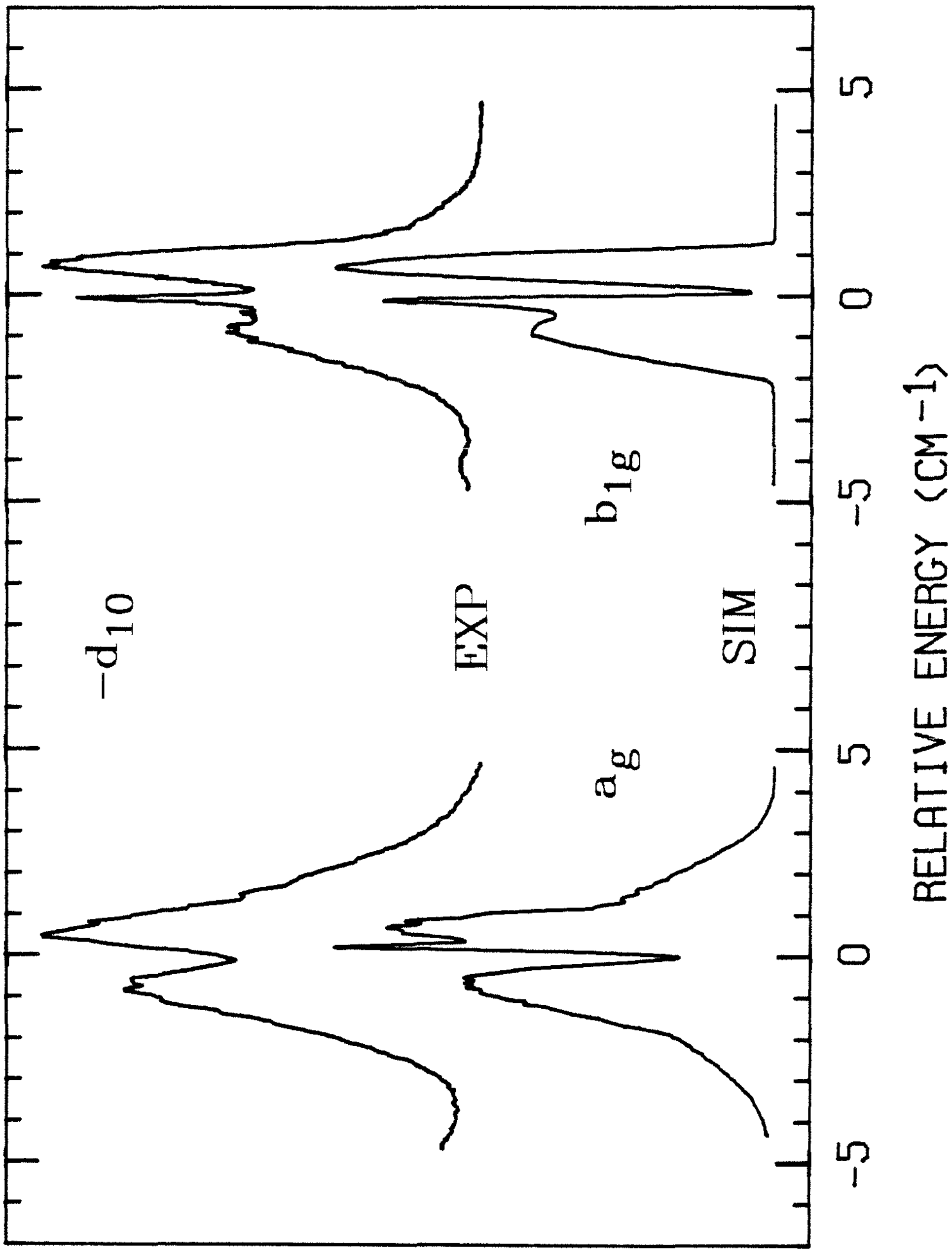

Fig. 4

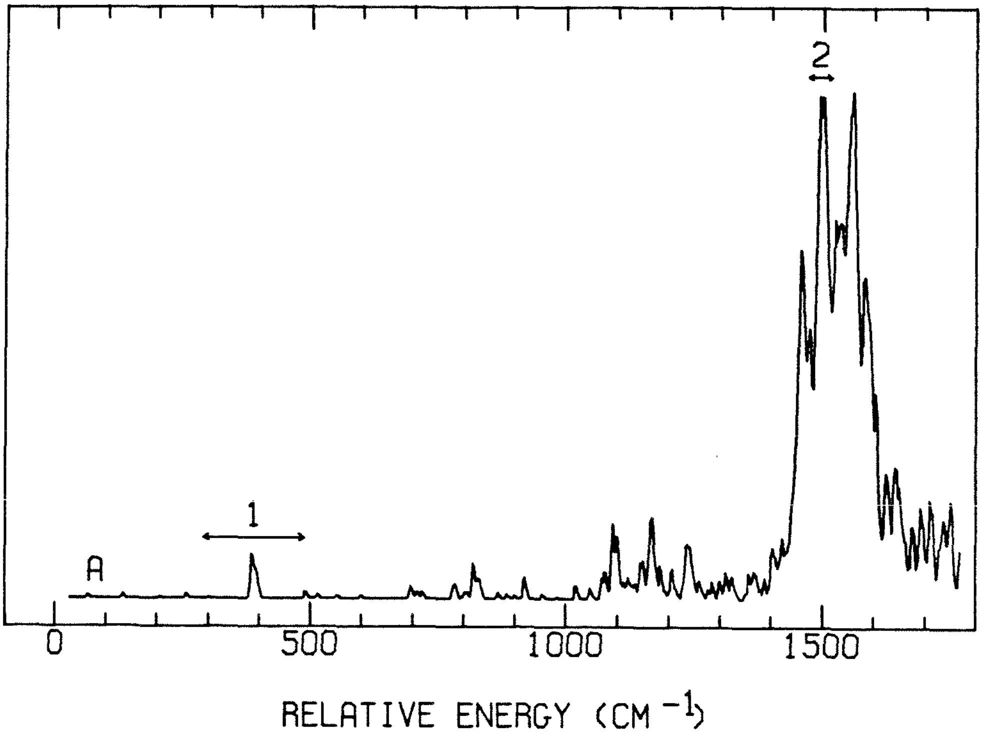
2
1
A
0
500
1000
1500
RELATIVE ENERGY (CM $^{-1}$)

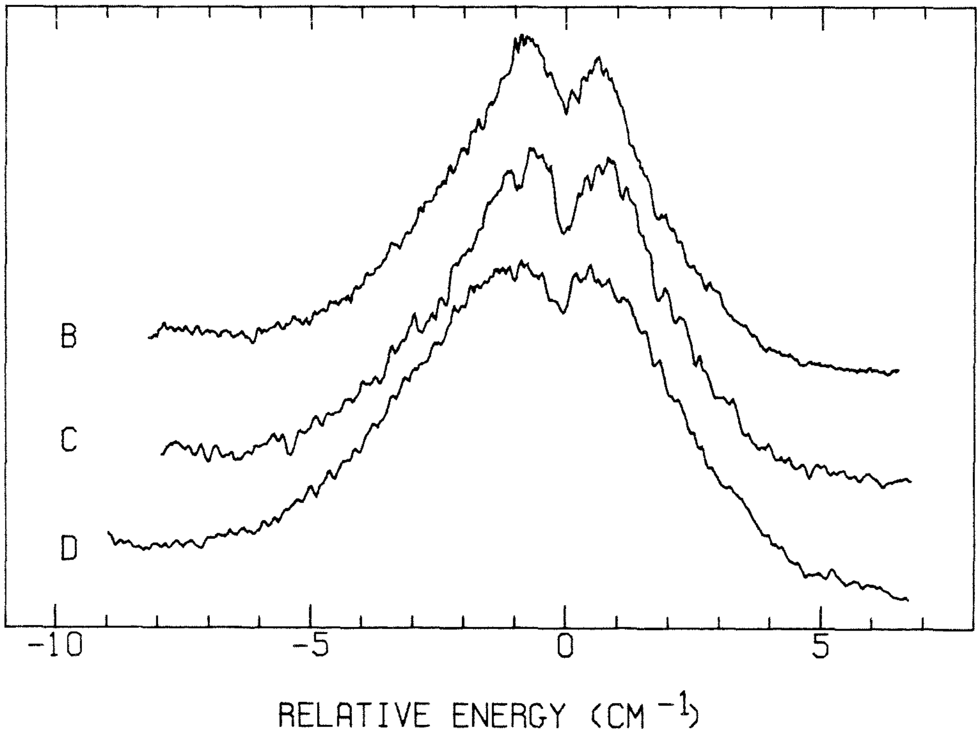
B
C
D
-10
-5
0
5
RELATIVE ENERGY (CM $^{-1}$)

Fig. 5

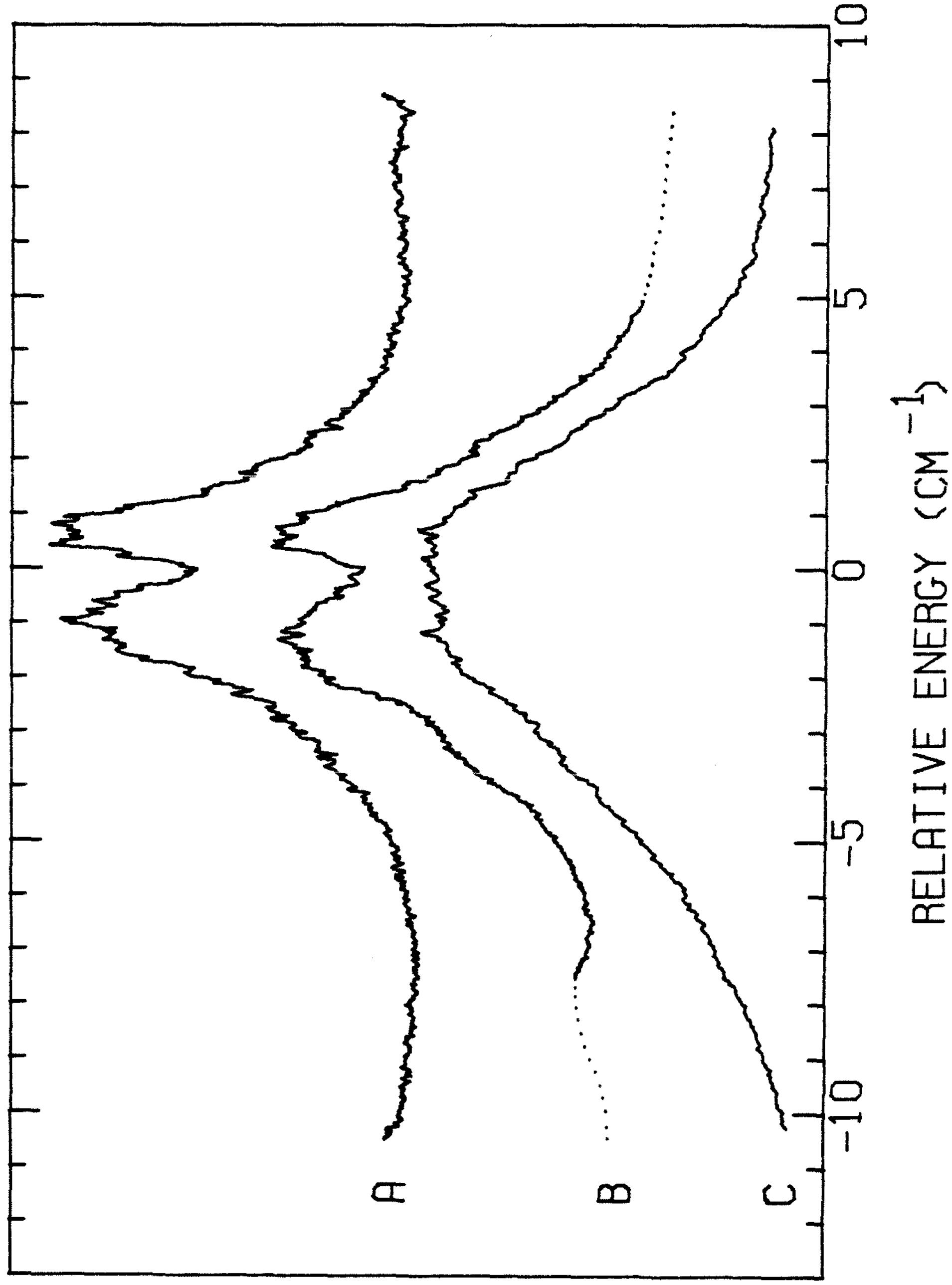

Fig. 6

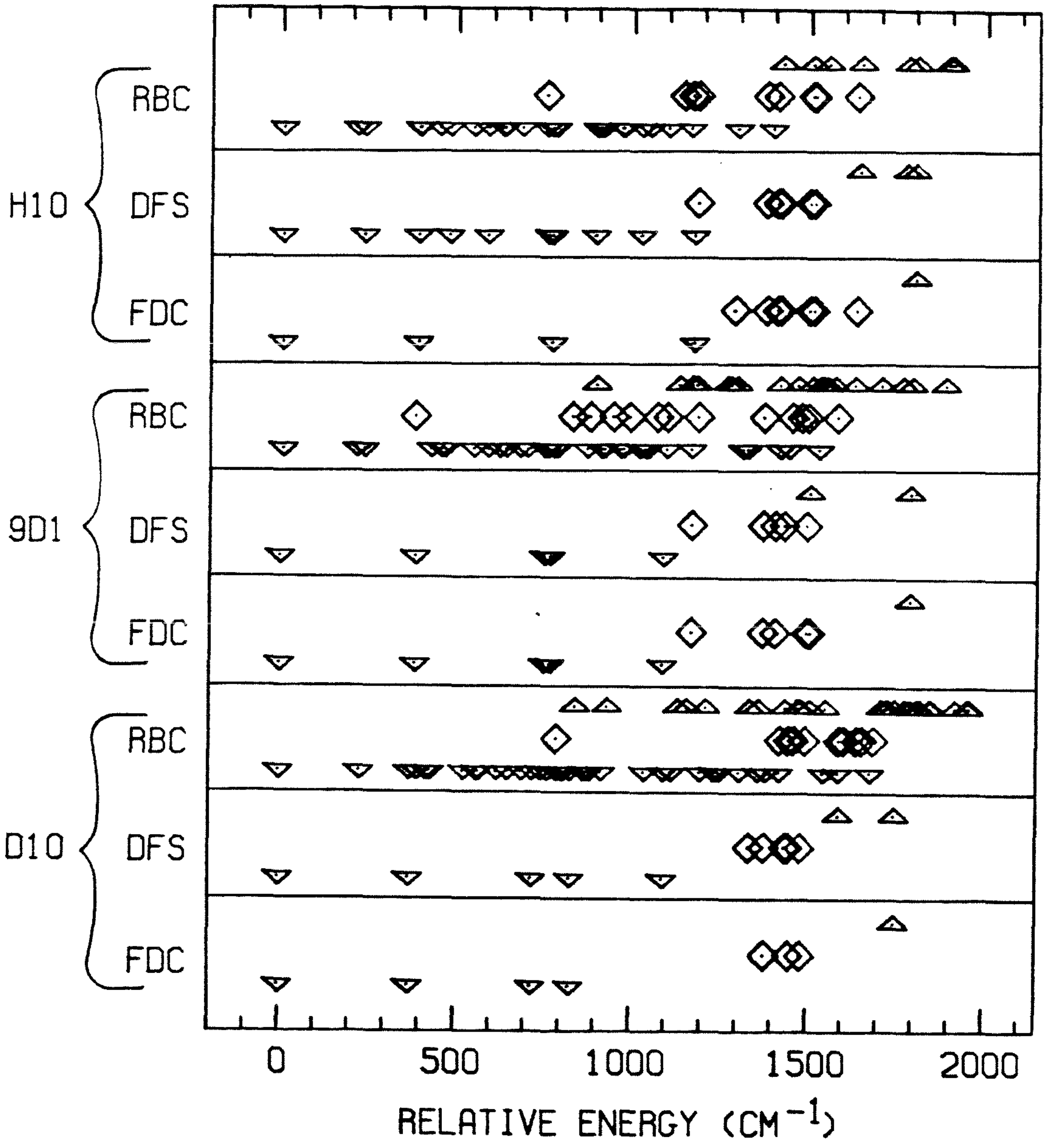
H10
RBC
DFS
FDC
9D1
RBC
DFS
FDC
D10
RBC
DFS
FDC
0
500
1000
1500
2000
RELATIVE ENERGY (CM^{-1})

Fig. 7

Summary and Conclusions

Chapter 9

In Chs. 1 - 2 of this thesis, the phenomenon of intramolecular vibrational redistribution (IVR) was introduced by discussing its theoretical and practical interest, presenting a simple theoretical description thereof, and reviewing several very recent experimental studies which exemplify the current approaches to, and understanding of, IVR. Consideration of the simple IVR model presented raised several questions which were suggested to best be addressed using complimentary high resolution spectral and temporal experimental techniques. Given this motivation, a high-resolution tunable laser - free jet apparatus was constructed to compliment an extant single-photon counting apparatus capable of high-resolution temporal experiments. Three types of high-resolution spectra can be obtained using the new apparatus.

(I) Fluorescence excitation spectra (resolution 0.5 cm^{-1}) yield excited-state vibrational frequencies and Franck-Condon overlap factors. These, in conjunction with other spectral data (see below), allow the assignment of vibronic levels through comparison with computational normal mode analyses. A good example of the utility of these spectra (as well as a demonstration of some of the advantages of free jet experiments) is found in Ch. 5. Gas-phase and condensed-phase experiments had failed to unequivocally establish the ordering of the A_g^* and B_u^* excited electronic states, which was of considerable theoretical interest due to the effect of excited-state ordering on the spectroscopy and isomerization of diphenylpolyenes. One- and two-photon free jet excitation spectra unambiguously proved that the A_g^* state lies at least 1050 cm^{-1} below the B_u^* state in diphenylbutadiene (above which energy a nonradiative process, probably isomerization, occurs), and that the one-photon spectrum below 1050 cm^{-1} was due to vibronic coupling within the forbidden A_g^* manifold. Another important example may be found in Ch. 8, where the vibronic natures of three isotopic anthracenes were compared in detail by analyzing their excitation spectra. Only minor differences were found; increased deuteration led to slightly increased geometry change upon excitation and poorer vibrational and rotational cooling in nitrogen carrier gas. This justified the comparison of these three isotopic species to deduce the effects of molecular symmetry and vibrational density of states on IVR.

(II) Dispersed fluorescence spectra yield ground state vibrational frequencies and Franck-Condon overlap factors, which compliment the information in excitation spectra, and thus aid in the assignment of vibrational modes. The degree of similarity of dispersed fluorescence spectra of excited-state levels may be used to estimate the extent of coupling between the levels, as exemplified by studies of several sets of overlapping levels in stilbene . In Ch. 6 the technique of selective (resolved) detection is discussed in detail, and it is shown that completely equivalent information may be obtained by recording rotational band contours under differing detection conditions, as was done in the study of S_1 + 754 / 756 cm^{-1} in anthracene$-h_{10}$. When used in conjunction with resolved detection, rotational band contour analysis can even be used to determine the nature (J-dependence) of levels which are not spectrally resolvable (as in the case of quantum beats). Two such studies, on S_1 + 1380 cm^{-1} in anthracene$-h_{10}$ and S_1 + 1411 cm^{-1} in anthracene$-9d_1$, are referred to below. This latter approach, however, is somewhat more convoluted; dispersed fluorescence spectra still provide the simplest assay of coupling strengths on the order of cm^{-1}.

(III) Rotational band contour spectra are very high resolution (0.1 cm^{-1}) fluorescence excitation maps of single or overlapping vibronic levels, which can yield vibrational symmetries and spectral purities for excited-state levels. Methods of predicting, fitting, and analyzing rotational band contours using computer simulations are documented in Ch. 4. The usefulness of rotational band contour analysis in assigning vibrational symmetries is best demonstrated in Ch. 8, where it is shown that the three isotopic anthracenes are highly analogous rovibronically, agreeing with and extending the conclusions of the excitation analysis mentioned earlier. Deduction of the vibrational symmetries of numerous levels in the three anthracenes also reveals that their S_1 state (B_{2u}^{*} in D_{2h}) vibronically couples to a nearby B_{3u}^{*} state but not to any B_{1u}^{*} states. Contours may also be used to evaluate spectral purity, which is a measure of the number of strongly interacting levels contributing to a contour, and thus reflects the effective vibrational density of states at that energy. Spectral purity is defined and discussed in detail in Ch. 8, where it is shown to correlate with spectral emission character and temporal behavior; results of analyses based on these characteristics are discussed below.

By analyzing the three types of spectra described above for five different molecules, it has been possible to provide tentative answers (subject to further study of a wider variety of molecules) to each of the four questions posed in Ch. 1. These are addressed in turn below:

(1) What type of coupling is responsible for IVR in specific cases? Several cases of Fermi resonance (anharmonic coupling) have been fully documented in anthracene–h$_{10}$ (S_1 + 754 / 756 cm^{-1} and S_1 + 1379 / 1380 cm^{-1}), meaning that coupling was demonstrated from dispersed fluorescence spectra, and that the interacting levels were shown to be of the same symmetry by rotational band contour analysis. The presence of four of the eight b_{1g} levels detected anywhere in anthracene–h$_{10}$ in a single 10 cm^{-1} interval is undoubtedly due to a strong Fermi resonance. In addition, there are numerous clusters of levels in the excitation spectra of the other anthracenes and stilbene which are very likely to be in Fermi resonance, but were not investigated in detail. The resolved detection study of the quantum-beating S_1 + 1411 cm^{-1} level in anthracene–d$_{10}$ indicates that the coupling mechanism responsible for the modulations is essentially J-

independent, indicating anharmonic coupling. In contrast, a similar study of S_1 + 1380 cm^{-1} in anthracene–h_{10} revealed a J-dependent coupling mechanism, presumably Coriolis coupling. Thus, this level is anharmonically coupled to a level ≈ 1 cm^{-1} away, but apparently interacts with closer lying states *via* Coriolis coupling. Although anharmonic coupling appears to dominate interactions spanning cm^{-1}, short-range Coriolis interactions may also contribute to IVR in the molecules studied.

(2) What are the magnitudes of the strengths and ranges of these coupling mechanisms? As discussed above, strengths and ranges of anharmonic coupling as deduced from spectral experiments vary from approximately one to ten cm^{-1} in the molecules studied herein. It should be noted, however, that detection of Fermi resonances with strengths / ranges much below 1 cm^{-1} is not usually possible in these experiments since the rotational bandwidths preclude resolution of the individual levels. As discussed in Ch. 2, shorter range interactions are undoubtedly present and may be especially important in determining IVR dynamics.

(3) Does molecular symmetry influence coupling efficiency? Comparison of the onset of structureless rotational band contours (due to strong coupling among several close lying levels) in anthracene–h_{10} and anthracene–9d_1 suggests that the reduction of symmetry in the latter enhances coupling relative to the former. In anthracene–9d_1, twice as many states are allowed to couple anharmonically to a given level as in anthracene–h_{10}; this is expected to shift the 'effective' density of states curve ≈ 150 cm^{-1} to the red. The observed shift of the structureless contour onset is ≈ 300 cm^{-1} to the red, supporting the applicability of symmetry-weighted density of states. Thus, molecular symmetry appears to affect coupling efficiency by limiting the number of nearby levels which can couple to a given level; decreased molecular symmetry results in

enhanced coupling.

(4) Does the vibrational density of states influence coupling efficiency? There is quite a bit of support for the influence of density of states on IVR rates from data on the variation of spectral emission character and temporal behavior with vibrational energy. Further substantiation arises from the comparison of stilbene and diphenylbutadiene dynamics (see Ch. 5). Above the nonradiative decay thresholds, the derivative of the decay rate logarithm with respect to energy is nearly five times as large in diphenylbutadiene as in stilbene. Since the nonradiative decay (presumably isomerization) is probably preceeded by IVR, decay rates likely reflect IVR rates. If this is the case, this result is consistent with an increase in IVR rates resulting from the substantially larger density of states in diphenylbutadiene (due to the presence of very low frequency torsional modes introduced by the additional ethylenic unit). Comparison of structureless contour onsets in anthracene–h_{10} and anthracene–d_{10} provides further support for the effect of density of states on coupling. Due to mass effect reduction of vibrational frequencies in anthracene–d_{10}, a ≈ 225 cm^{-1} red-shift would be expected in the onset relative to anthracene–h_{10}, and a ≈ 275 cm^{-1} shift is observed experimentally. While this agreement is probably fortuitously good, this result and those described above certainly substantiate the enhancement of coupling and IVR that results from an increase in vibrational density of states.

In conclusion, the complimentary high-resolution spectral and temporal experiments described herein have improved our understanding of the fascinating phenomenon of IVR by probing the coupling mechanisms responsible for its occurrence.

PROPOSITIONS

A Study of the Mechanism of Enzymatic Photoreactivation Repair of Pyrimidine Dimers in DNA

Proposition 1

Exposure of DNA to UV radiation results in lethal pyrimidine dimerization. The enzyme photolyase repairs this damage by a poorly understood mechanism involving absorption of visible light. Advanced biosynthetic techniques, irradiate-probe experiments, and resonant magnetic measurements designed to study the dynamics and intermediate structures of this unusual reaction are described, and their interpretations discussed.

I. INTRODUCTION

For over two decades the importance of enzymatic repair of damaged DNA has been recognized. One important natural cause of damage is UV radiation, which in some cases may be lethal (i. e. prevent replication).

Below the ionization threshold of DNA, UV radiation has been shown to produce two types of damage: hydration of the olefinic bond in cytosine [1,2], and dimerization of pyrimidines (thymine and cytosine) [3,4]. The former is believed to be relatively harmless due to the existence of an equilibrium between hydrated and unhydrated cytosine which, under typical biological conditions, strongly favors the unhydrated form [5]. Pyrimidine dimers may be formed from two bases on the same strand (hereafter SS-dimers, for single-strand) or two bases on complementary strands (hereafter CL-dimers, for cross-linked). This is shown for the case of thymine, the dimers of which were studied first, in the accompanying figure.

Several enzymatic repair mechanisms have been documented for the repair of pyrimidine dimers. SS-dimers are repaired by deletion of the dimer nucleotides and replication using the intact complementary strand as a template [6]. CL-dimers are repaired by deletion of the dimer nucleotides in both strands and replication after recombination with an intact homologous DNA molecule [7]. Finally, either type of dimer may be repaired *in situ* by a photoreactivating enzyme, photolyase, which utilizes visible radiation to dissociate the dimer [8].

The final mechanism is of particular interest for a number of reasons, and is not well understood. In only one instance (Streptomyces griseus) has evidence for the existence of a chromophore in photolyase been presented [9]. In the remainder of the studied cases, the visible transparency of the separate enzyme and UV-damaged substrate (and mixed enzyme and undamaged substrate) suggets that a charge-transfer complex is involved in the photoreactivation process [10]. Since photolyase does not dissociate dimers in DNA substrates less than nine nucleotides long [11], it may be inferred that the additional nucleotides are necessary for recognition of the dimer or for formation of the charge-transfer complex. The observation that photolyase dissociates dimers containing the pyrimidines thymine (T), cytosine (C), and uracil (U) [12] suggests that binding in the complex occurs at the 1, 2, 5, or 6 positions in the pyrimidine ring, as the 3 and 4 positions are very different in character in these three bases (see figure for ring numbering). Very indirect evidence has been obtained which indicates that the most likely binding site is the 2-carbonyl functionality [13].

Other than noted above, essentially nothing is known about the mechanism of photoreactivation. Further study of this unusual phenomenon seems warranted. In this proposition, I describe a series of experiments designed to help answer the four following questions:

1/ Does the type (SS or CL) or composition (TT, TC, or CC; uracil is not considered as it occurs in RNA, not DNA) of dimer influence the efficiency of photoreactivation?

2/ On what time-scale are dimers located by the photolyase? When a dimer is recognized, is a stable complex formed, or do only those encounters accompanied by simultaneous photon absorption result in successful photoreactivation?

3/ On what time-scale does the charge-transfer complex decay subsequent to absorption of a visible photon?

4/ What is the nature (chemical, structural) of the charge-transfer complex?

II. ENZYME AND SUBSTRATE SELECTION

Photolyase from Escherichia coli may now be isolated in large quantities in relatively pure form [14]. It is the best-characterized photolyase, and so is chosen for use in this study. The molecular weight is 36.8 kg/mole; it is 13 % carbohydrate by mass. There is an RNA decamer associated with each molecule, the function of which is unknown. There are no unusual amino acids present in the enzyme, and no bases other than the four typical species are present in the associated RNA. The gene responsible for production of photolyase, termed phr, has been located at 15.7 minutes on the K-12 chromosome [15,16]. Although at this time little else is known about this enzyme, it will probably be sequenced sometime in the near future; knowledge of its structure will undoubtedly aid the understanding of photoreactivation.

In the last few years it has become feasible to synthesize small oligonucleotides (up to twenty bases in length) on a reasonable scale without undue investment of time or capital [17]; automated synthesizers are just now becoming commercially available and will further simplify the procedure. For this study the following oligonucleotides, susceptible to the indicated dimerizations, would be synthesized:

SS-TT	SS-CC	SS-CT	CL-TT	CL-CC	CL-CT
TTTTTTTTT	CCCCCCCCC	TCTCTCTCT	ATATATATA	GCGCGCGCG	ACACACACA
AAAAAAAAA	GGGGGGGGG	AGAGAGAGA	TATATATAT	CGCGCGCGC	TGTGTGTGT

III. IRRADIATE-PROBE EXPERIMENTS

There are two important phenomena in this enzyme-substrate system which may be induced by irradiation: formation of dimers (230 - 300 nm; peak 260 nm) and repair of dimers (300 - 600 nm; peak 375 nm). The repair of a dimer involves an increase in monomer concentration and a decrease in complex concentration. These phenomena occur most readily at the absorption maxima of the reactive species. Hence in addition to inducing these phenomena, 260 nm and 375 nm radiation may be used to probe the concentrations of monomer (and thus dimer) and complex respectively. The difference between irradiating and probing is perhaps somewhat arbitrary. Irradiation is very intense and substantially alters the relative concentrations of species present. A probe is much less intense and monitors the concentrations of species present but only negligibly changes the concentrations of these species.

These considerations suggest three irradiate-probe experiments addressing the first three questions posed earlier. They are described in sequence below.

In the first experiment, damaged substrate is prepared by irradiating an undamaged substrate and enzyme mixture. By probing the mixtures at 260 nm before and after irradiation, "boundary values" of absorbance can be determined, which allows the dimer concentration to be monitored indirectly. The enzyme is included initially so that its 260 nm absorption is included in the boundary values. Subsequently, while irradiating these mixtures at 375 nm to repair damage, a 260 nm probe would be employed to obtain the dimer concentration decay curve. Either the initial repair rate or total fraction of repair could be used to evaluate the relative efficiencies of repair of the six types of dimers.

In the second experiment, undamaged substrate and enzyme mixtures are flash-irradiated and immediately probed at 375 nm to monitor complex formation as a function of time. If only a transient complex is formed, as is the case in many gas phase reactions [18], the curve will be flat. If a stable complex is formed, the concentration should rise from zero and asymptotically approach a constant value. The information obtained in this experiment will depend on the time necessary for a flash-irradiation to effect significant dimerization, and the time required for enzyme recognition of a dimer.

If the formation of a stable complex is indicated, enzyme and damaged substrate mixtures should be prepared (by 260 nm irradiation of enzyme and undamaged substrate mixtures) to produce a large concentration of complex. The mixtures are flash-irradiated at 375 nm and immediately probed at 260 nm to monitor monomer appearance, which allows an estimate of the complex lifetime. The lower limit on time resolution will, as in the second experiment, be determined by the length of the flash-irradiation.

IV. MAGNETIC RESONANCE SPECTROSCOPY EXPERIMENTS

Charge-transfer complexes typically involve only minor electron density redistribution in the ground state, but in the excited state (usually formed by absorption of a UV or visible photon) may be properly termed electron transfer complexes [18]. Radical pair production may be involved. Radical intermediates can often be detected by magnetic resonance experiments; the extreme selectivity of these techniques makes them ideal for the study of biological samples, where a number of complicated species are often present. For example, photosynthetic electron-transfer reactions have been studied by EPR (electron paramagnetic resonance) [19], CIDNP (chemically induced dynamic nuclear polarization) [20], CIDEP (chemically induced dynamic electron polarization) [21], and ENDOR (electron nuclear double resonance) [22]. Of particular relevance to this proposal, EPR has been successfully employed to study enzyme-substrate reactions [23], and there has been a CIDNP study of (substituted) ethylene-cyclobutane interconversion [24]. Recall from the figure that dimerization is a [2+2] cycloaddition resulting in formation of a cyclobutyl ring, and hence the above reaction may provide a simple model for the photoreactivation process.

In order to study the mechanism of photoreactivation by these methods, it is helpful to be able to continuously generate the species of interest so that time-resolved techniques are unnecessary. If there is only a transient complex, this would be done by irradiating an enzyme and damaged substrate mixture continuously at 375 nm. If a stable complex is formed, the ground state could be studied in a mixture of enzyme and damaged substrate in the dark, whereas the excited state (formed by the absorption of a 375 nm photon) could be studied in the same manner as a transient complex.

An EPR experiment could yield values of the g-factor and hyperfine splittings; observation of a signal would establish the involvement of one or more free radicals in the mechanism. The value of g provides information about the chemical nature of the site of the unpaired electron. The hyperfine splittings help to identify nearby nuclei. A CIDNP experiment could yield values of the chemical shifts of protons near the unpaired electron and coupling constants to nearby protons. The spectrum might be especially simple as the dimers have only three types of protons (methyl, tertiary carbon, and amino) each of which should be distinguishable. The observation of a signal would imply that recombination of free radicals occurs in the photoreactivation mechanism.

With this information it will likely be possible to locate the site of the unpaired electron if it resides in the dimer. The g-factor would help distinguish between carbon, nitrogen, and oxygen sites; the chemical shift would allow differentiation between carbon and nitrogen sites. The hyperfine splittings and coupling constants would determine nearby structure and perhaps shed some light on the delocalization, if any, of the unpaired electron.

These experiments would help elucidate the mechanism (e. g. confirm radical or radical pair involvement) of the photoreactivation as well as provide data on the structure of the intermediates. From this information the binding site on the dimer might be ascertained, and some data on the structure of the photolyase at the binding site could be obtained. Hence these resonant magnetic measurements, possibly augmented by more sophisticated CIDEP and ENDOR studies, should help to answer the final question posed in this proposition.

REFERENCES

[1] R. Beukers and W. Berends, *Biochim. Biophys. Acta 38* (3), 573 (1960).

[2] R. Beukers and W. Berends, *Biochim. Biophys. Acta 41* (3), 550 (1960).

[3] R. Beukers and W. Berends, *Biochim. Biophys. Acta 49* (1), 181 (1960).

[4] J. Marmur and L. Grossman, *Proc. Nat. Acad. Sci. USA 47* (6), 778 (1961).

[5] R. A. Deering, *Sci. Am. 207*, 135 (1962).

[6] P. C. Hanawalt, *Endeavor 31*, 83 (1972).

[7] R. S. Cole, *Proc. Nat. Acad. Sci. USA 70*, 1064 (1973).

[8] C. S. Rupert, in *Photophysiology 2*, 283, A. C. Geise (ed.), Academic, New York (1964).

[9] A. P. M. Eker, in *DNA Repair Mechanisms*, 129, P. C. Hanawalt, E. C. Friedberg, and C. F. Fox (eds.), Academic, New York (1978).

[10] J. C. Sutherland, *Photophys. Photochem. 25*, 435 (1977).

[11] J. K. Setlow and F. J. Bollum, *Biochim. Biophys. Acta 157*, 233 (1968).

[12] R. B. Setlow, *Science 153*, 379 (1966).

[13] J. C. Sutherland, in *DNA Repair Mechanisms*, 137, P. C. Hanawalt, E. C. Friedberg, and C. F. Fox (eds.), Academic, New York (1978).

[14] R. M. Snapka and B. M. Sutherland, *Biochem. 19*, 4201 (1980).

[15] D. A. Youngs and K. C. Smith, *Mut. Res. 51*, 133 (1978).

[16] A. Sancar and C. S. Rupert, *Mut. Res. 51*, 139 (1978).

[17] E. g. DNA Synthesis Kit, New England Biolabs, Beverly, MA.

[18] J. B. Birks, *Photophysics of Aromatic Molecules*, 412, Wiley, New York (1970).

[19] J. Fajer, D. C. Borg, A. Forman, R. H. Felton, D. Dolphin, and L. Vegh, *Proc. Nat. Acad. Sci. USA 71*, 994 (1974).

[20] S. G. Boxer, Ph. D. Thesis, The University of Chicago (1976).

[21] P. L. Dutton, J. S. Leigh, and M. Siebert, *Biochim. Biophys. Acta 292*, 654 (1973).

[22] B. Ke, E. Dolan, V. A. Shuvalov, and V. V. Klimov, in *Biological Events Probed by Ultrafast Laser Spectroscopy*, Ch. 3, R. R. Alfano (ed.), Academic, New York (1982).

[23] I. Yamazaki, H. S. Meson, and L. H. Piette, *J. Biol. Chem. 235*, 2444 (1960).

[24] H. D. Roth, in *Chemically Induced Magnetic Polarization*, Ch. 4, L. T. Muus, P. W. Atkins, K. A. McLauchlan, and J. B. Pedersen (eds.), D. Reidel, Boston (1977).

β = Sugar-phosphate Chain

Protons are not shown.

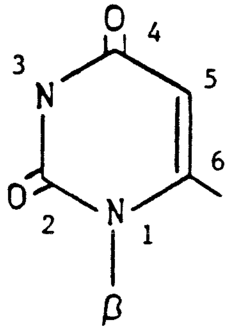

Thymine

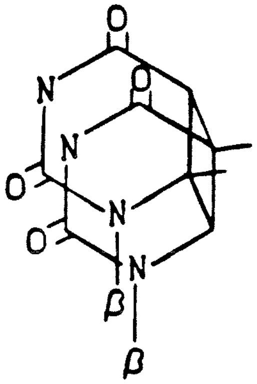

SS-Dimer

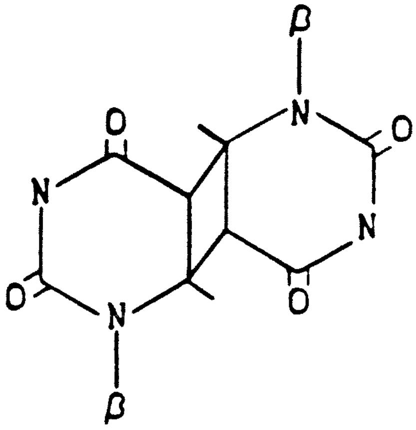

CL-Dimer

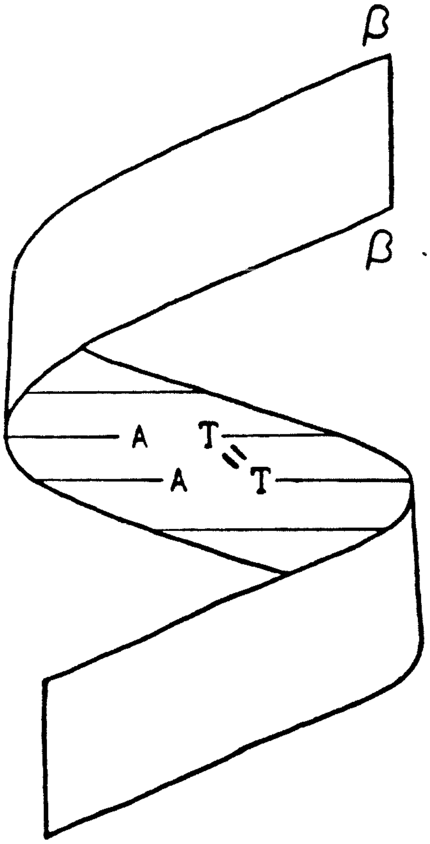

SS-Dimer in situ

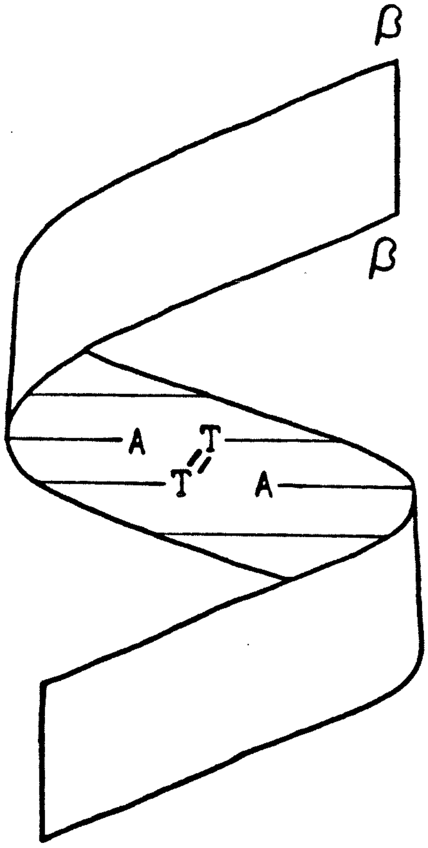

CL-Dimer in situ

Laser Magnetic Resonance Detection of Methyldiazenyl Radical

Proposition 2

ABSTRACT

Direct observation of methyldiazenyl radicals during the gas phase S_1 photolysis of azomethane would confirm one-bond scission in the homolytic loss of nitrogen from this species. Such an observation would be particularly important in resolving the controversy over the azo compound homolysis mechanism, as simple, symmetric azoalkanes have been thought to be the least likely of the diazenes to undergo one-bond scission. Methyldiazenyl radical can be probed at four fundamentals (ν_3, ν_4, ν_7, and ν_{10}) by mid-IR laser magnetic resonance, a sensitive high resolution method of detecting paramagnetic species. The calculated steady state concentration of methyldiazenyl radicals in a laser magnetic resonance spectrometer exceeds the detection threshold for this technique by up to three orders of magnitude, confirming the practicality of the proposed experiment.

I. INTRODUCTION

Diazenes, or azo compounds, are an interesting class of molecules containing a -N=N- linkage with *cis*– or *trans*– organic substituents (as with the structurally analogous alkenes, *trans*– isomers are stabler). As diazenes possess an excellent leaving group (N_2), their chemistry is suggestive of that of the peroxides. Their predominant reaction, other than isomerization, is homolytic elimination of molecular nitrogen, producing two free radicals (or a biradical in cyclic species). Homolysis may be effected through thermolysis, photolysis, or radiolysis; solution phase thermal decomposition has been studied most extensively.

There has been a great deal of controversy over the exact mechanism of homolysis; the two alternatives, one-bond and two-bond scission, are depicted in the accompanying figure. One-bond scission involves a diazenyl radical intermediate which is thought to undergo rapid vibrational predissociation; two-bond scission entails synchronous cleavage of both C-N bonds, with no intermediate formed. Engel, in a comprehensive 1980 review article, suggests that more symmetrical diazenes tend toward two-bond scission, while less symmetrical species undergo one-bond scission [1]. This issue continues to be highly controversial, with more recent thinking favoring one-bond scission in essentially all cases (see § II).

A definitive result, not obtained to date, would be the ***direct*** observation of diazenyl radicals during the decomposition of a diazene sample. Note that indirect (but convincing) evidence for diazenyl radicals has been obtained in CIDNP [2] and other (see § II) studies, but an EPR spectrum assigned to $C(CN)(CH_3)_2N_2$ [3] has been questioned by later workers [4]. A relatively new spectroscopic technique, laser magnetic resonance (see § III), is ideally suited for the observation of transients like diazenyl radicals for three principal reasons: (1) the technique is extremely sensitive; (2) it selectively probes paramagnetic species; and (3) it is a very high resolution technique, facilitating distinction of similar species.

I herein propose to study the gas phase S_1 photodecomposition of azomethane, $CH_3N_2CH_3$, using mid-IR laser magnetic resonance. Detection of up to four vibrational modes of the methyldiazenyl radical, CH_3N_2, should be possible using this technique (see § IV). The observation of this radical would be of particular significance since azomethane is a simple, symmetric azoalkane, the type formerly regarded as least likely to decompose *via* one-bond scission.

This report is organized as follows. In § II, I review recent theoretical and experimental work pertaining to the issue of one-bond *vs.* two-bond scission. In § III, I summarize the theory and development of laser magnetic resonance, and describe applications of the technique which are particularly relevant to the proposed experiment. In § IV, I explain the choice of azomethane as the precursor for laser magnetic resonance detection of a diazenyl radical. Finally, in § V, I calculate the expected steady state concentration of methyldiazenyl radical, assuming typical experimental parameters, and show that this exceeds the detection limits of mid-IR laser magnetic resonance by up to three orders of magnitude.

II. RECENT WORK ON ONE-BOND vs. TWO-BOND SCISSION

In his comprehensive 1980 review article, Engel concluded that the issue of one-bond *vs.* two-bond scission was still highly controversial, but that current evidence favored one-bond scission in less symmetric diazenes and two-bond scission in more symmetric species [1]. Since 1980, almost all experimental and theoretical work has favored one-bond scission in azo compounds, regardless of the degree of symmetry. These more recent studies are discussed below.

On the theoretical front, Dewar has argued that essentially all organic reactions are one-bond reactions, since *synchronous* N-bond reactions will normally have activation energies that are roughly N times as large as for analogous one-bond reactions [5]. Concerted N-bond reactions are claimed to be composed of N *sequential* one-bond reaction steps, the first of which is slow compared to subsequent steps. These considerations lead to the conclusion that diazene homolysis should proceed by one-bond scission, followed by rapid vibrational predissociation of the resultant diazenyl radical. The conclusions of this study are supported by Dannenberg and Rocklin's calculations on the homolysis of azoethane [6], and the calculations of Bigot *et al.* on the decomposition of the parent diazene HNNH [7]. In contrast, Hiberty and Jean [8] calculated one-bond scission to be favored for pyrazolines, but not nearly to the extent predicted by Dewar. A very recent reconsideration of the activation energies for a variety of azo compounds supports the one-bond cleavage mechanism in all but the most highly branched compounds [9].

Experimentally, a variety of techniques have been employed to probe the homolysis reaction. In 1969, Bauer [10] proposed that two-bond scission should result in the formation of highly excited nitrogen since the bond length in nitrogen is so much shorter than the N=N separation in diazenes. In contrast, one-bond scission was suggested to lead to highly excited *radicals*, since the excess energy in the N=N bond would be efficiently channeled to the incipient organic radical prior to the dissociation of the diazenyl radical. This criterion has been applied in two recent experimental studies, the results of which favor one-bond scission in each case. Dougherty *et al.* [11] found that homolysis of a symmetric bicyclic azoalkane resulted in a highly excited biradical (as demonstrated by the rearrangement of the ring closure product, bicyclobutane, to the linear conjugated polyene, butadiene). An energetics analysis revealed that the vibrational excitation of the nitrogen product was minimal (at most ≈ 11 % of the available energy). Engel *et al.* [12] used transient gas phase coherent anti-Raman spectroscopy (CARS) to monitor the formation of nitrogen and methyl radical in the 355 nm (S_1) photodissociation of azomethane, and to probe the vibrational energy distribution in the nitrogen product. They found that the appearence times for nitrogen and methyl were ≈ 2 and 4 nsec, respectively, suggesting that the lifetime of the methyldiazenyl radical is on the order of 2 nsec. The existence of the diazenyl radical intermediate was substantiated by the minimal vibrational energy in the nitrogen product (≈ 2 % of the available energy).

Neuman and Binegar have determined the activation volumes [13] for homolytic cleavage of two symmetric *cis*–azoalkanes through high pressure experiments [14]. The values obtained fall in the range previously shown to correspond to one-bond cleavage with possible recombination of the diazenyl and organic radicals before loss of nitrogen occurs from the diazenyl radical. In contrast, Crawford and Chang concluded from secondary kinetic isotope effects in allylic pyrazolines that one-bond cleavage occurs but is irreversible [15]. Engel and Gerth irradiated acyclic azoalkanes and subsequently isolated new azoalkanes in which the allylic group was attached to the azo group by the other end [16]. This proves that one-bond scission was sometimes followed by rotation of the allylic group and then recombination to form a new azoalkane molecule.

Engel *et al.* also examined steric interactions in pyrazolines and found that they were important in one case where a concerted reaction should have been relatively unaffected, supporting one-bond scission [17]. Liu found that the homolysis and isomerization reactions of an allylic diazirine had the same solvent dependences, suggesting a common transition state and thus one-bond scission [18]. Adam and coworkers have done product studies on a variety of diazene homolyses, using both 355 nm (S_1) and 185 nm (S_2) photolyses [19-22]. In each case they explained their findings in terms of diazenyl radical intermediates of differing electronic configurations and spin multiplicities. Finally, in contrast to the conclusions reached by all of the above researchers, Golden *et al.* interpreted the low preexponential factor for azoisopropane homolysis (as redetermined by their new laser pyrolysis technique) as indicating two-bond scission [23].

III. THE TECHNIQUE OF LASER MAGNETIC RESONANCE

Laser magnetic resonance, hereafter LMR, is analogous to EPR, the differences being that excitation occurs in the far IR (rotational + ΔM_J transitions) or mid-IR (vibrational + ΔM_J transitions) rather than in the microwave region (pure ΔM_J transitions), and that detection is likewise in the IR rather than microwave region. Like EPR, LMR probes paramagnetic species only, and so is ideal for selectively studying free radicals. The resolution of the technique is Doppler-limited (or sometimes pressure-limited in the far IR).

The theory, development, and applications of this technique are thoroughly detailed in six review articles which have appeared in the last six years. Evenson, who invented the technique in 1968, listed all the papers published on LMR and all the species studied by LMR through 1981 [24]; Davies presented an especially clear account of the theory of LMR that same year [25]. Reviews pertaining specifically to mid-IR LMR [26] and far IR LMR [27] were also published about this same time. More recent reviews appeared in 1983 [28] and 1985 [29]; the latter emphasizes recent studies of molecular ions. Very recent work on time-resolved LMR is mentioned below.

In a typical LMR experiment, a sample flow system is placed within the cavity of an IR laser, and the magnetic field strength at the sample is varied. When a Zeeman resonance is reached, intracavity absorption occurs, resulting in a change in laser gain, which is monitored with an IR detector. The signal amplification resulting from the intracavity arrangement makes this technique extremely sensitive. The lowest reported detection limit for far IR LMR is 10^6 cm^{-3} (averaging time = 1 sec, S/N = 1) [30]; mid-IR LMR is perhaps a factor of 6 - 10 less sensitive [25,26,28]. Earlier review articles list slightly higher detection limits; these, of course, depend upon the magnitude of the transition dipole moments. The sensitivity of LMR is much better than that of EPR [25], and may be comparable to that of laser-induced fluorescence (LIF) [29].

The principal limitation of LMR (excepting the applicability to paramagnetic species only) is the restricted number of IR lasers and IR laser lines. Mixed isotope CO and CO_2 lasers adequately cover the mid-IR ranges 1450 - 2000 cm^{-1} and 875 - 1110 cm^{-1}, respectively, when one accounts for the magnetic field tunability of about 2 cm^{-1} [26]. Considerable progress has been made recently with optically pumped far IR lasers, extending the tuning ranges substantially in that domain [28].

To date, LMR has only been applied to simple paramagnetic species; the largest radicals investigated thus far are CH_3O [31,32] and CH_2OH [33,34]. There is no reason to believe that LMR cannot be applied to larger species, but as the emphasis previously has been on detailed analysis of spectra rather than simply on detection of paramagnetic species, the tendency to study small species is not surprising [25]. A few kinetic LMR studies have been reported quite recently, suggesting that the research emphasis may be shifting. The production, reaction, and disappearence of Cl and SiH_3 were monitored by mid-IR LMR [35], while F atom reactions with NO and H_2O were followed using far IR LMR [36]. These laser photolysis studies had μsec temporal resolution; an earlier chlorine photolysis experiment was reported to have 70 nsec resolution [37]. Some of the practical aspects of these kinetic experiments have been discussed very recently [38].

The merits of mid-IR *vs.* far IR LMR are nicely summarized in McKellar's review [26]. For the purposes of this study, mid-IR LMR is preferable, since the vibrational frequencies of the relevant species have been calculated or are known experimentally (see § IV), simplifying the location, distinction, and identification of these species. If a diazenyl radical is observed in the mid-IR, the values of the rotational constants derived from its spectrum might allow an efficient search of the far IR if more sensitive detection were desired for better characterization.

IV. THE MOLECULAR SYSTEM

The simplest stable azoalkane, azomethane ($CH_3N_2CH_3$, hereafter AM) is chosen for the proposed experiment for the following eight reasons. (1) LMR has thus far only been used to analyze simple paramagnetic species, containing up to five atoms [31-34]. The only diazenyl radical which could be produced from AM is the hexatomic methyldiazenyl radical (CH_3N_2, hereafter MDAR). (2) The vibrational frequencies of MDAR have been calculated [39], and four vibrations are at appropriate energies for investigation by mid-IR LMR: three CH_3 bends (ν_3 = 1788 cm^{-1}, ν_4 = 1693 cm^{-1}, and ν_{10} = 1784 cm^{-1}) fall into the CO laser region, while a CH_3 'rock' (ν_7 = 1014 cm^{-1}) can be excited with a CO_2 laser [26]. (3) The other paramagnetic species directly produced upon photolysis of AM is the methyl radical [40], which has three IR active vibrations at 617 cm^{-1} (ν_2, out-of-plane bend), 1026 cm^{-1} (ν_4, in-plane bend) and 3162 cm^{-1} (ν_3, in-plane stretch) in solid neon [41]. The ν_2 mode (606 cm^{-1} in the gas phase) has been studied by tunable diode laser spectroscopy, yielding rotational, centrifugal distortion, and spin-rotation interaction constants, and the transition dipole moment, which is very large (0.28 D) [42,43]. The ν_3 mode (3161 cm^{-1} in the gas phase) has been studied by difference frequency laser spectroscopy, yielding vibration-rotation interaction, Coriolis coupling, and l-type doubling constants [44]. The data from these high resolution IR techniques should readily allow distinction of the ν_4 mode in methyl radical from the ν_7 mode in MDAR. (4) The CARS experimental data [12], though indirect, are consistent with the formation of MDAR from 355 nm (S_1) photolysis of AM. (5) The photochemistry and spectroscopy of AM have been studied in some detail previously [45]; of particular importance, the gas phase S_1 photochemical quantum yield of nitrogen is known to be unity below one atmosphere pressure [46], and the S_1 absorption spectrum is known (ε_{max} = 5 l/mole-cm; λ_{max} = 340 nm; $\varepsilon = \varepsilon_{max}/2$ at λ = 310 and

370 nm) [47a]. (6) Despite the low extinction coefficient, the location of the symmetry-forbidden S_1 transition is ideal for mercury arc photoloysis, which can lead to the dissociation of a significant fraction of the precursor molecules under typical flow tube conditions (see § V). (7) AM is a gas at room temperature (bp = 1.5 °C [48]), so vapor pressure is not a limiting factor in the production of MDAR. (8) Finally, AM is a simple, symmetric azoalkane, and so direct observation of a diazenyl radical would be especially significant, as such diazenes were formerly thought to be the least likely to undergo one-bond scission.

V. CALCULATION OF EXPECTED SIGNAL-TO-NOISE

The exceptional sensitivity of the LMR technique has already been discussed. Three facts especially lend credibility to the idea of detecting MDAR by LMR: (1) the sensitivity of LMR can be comparable to LIF [29], which is routinely used to investigate processes occurring on the picosecond time-scale [49]; (2) LMR is sufficiently sensitive that 70 nsec temporal resolution has been achieved in one study [37]; (3) LMR and other high resolution IR techniques are sensitive enough to study molecular ions [29]. A more convincing argument for the plausibility of the proposed experiment results from a comparison of the calculated steady state concentration of MDAR with the reported sensitivities of the LMR technique, as is done below.

First, we calculate the output (photons/sec) of a medium-pressure mercury arc in the range 310 - 370 nm, where the absorption of AM is a maximum. (There is also considerable output in the tails of the absorption, so ε_{max} is used in the following calculation, rather than an average ε.) Medium-pressure mercury arcs are available with a UV power (P) of 1066 W [47b], 51 % of which (544 W) is in the specified range [47c]. An excimer laser, by comparison, would produce only about 20 W [29], and would provide no real advantages. The useful arc output O is thus:

$$O\ (\text{photons/sec}) = P\ (\text{J/sec})/\varepsilon\ (\text{J/photon}) = P\lambda/hc =$$
$$(544\text{W})(340\text{x}10^{-9}\ \text{m})/(6.63\text{x}10^{-34}\ \text{J-sec})(3\text{x}10^{8}\ \text{m/sec}) = 9.3\text{x}10^{20}\ \text{sec}^{-1}$$

We now calculate the number of photons absorbed per second by AM; since the quantum yield for nitrogen is unity at low pressures [46], this will equal the number of MDAR produced per second (assuming, of course, that the one-bond scission mechanism is operative). Helpful in the following calculations are several experimental parameters taken from the Cl/SiH$_3$ μsec study [35]: sample pressure, 7.5 torr; excitation region, 12 cm path length by 1 cm diameter cross-section. At 7.5 torr, the molar concentration M of AM would be:

$$M = n/V = P/RT = (7.5\text{torr})/(62.4\ \text{torr}-\text{l/mole}-\text{K})(300\ \text{K}) = 4.0\text{x}10^{-4}\ \text{moles/l}$$

Now the number of photons absorbed per second is $O(1 - I/I_0)$, where I_0 and I are the intensities before and after absorption. The ratio is given by Beer's Law, $\log_{10}(I_0/I) = \varepsilon ML$, where L is the path length in cm. Since $\varepsilon = 5$ l/mole-cm [47a], the number of photons absorbed per second, ΔO, is:

$$\Delta O = O(1 - I/I_0) = O(1 - \text{antilog}[-\varepsilon ML]) =$$
$$(9.3\text{x}10^{20}\ \text{sec}^{-1})(1 - \text{antilog}[(5\ \text{l/mole}-\text{cm})(4.0\text{x}10^{-4}\ \text{M})(12\ \text{cm})]) = 5.0\text{x}10^{19}\ \text{sec}^{-1}$$

This, then, represents the production rate of MDAR [50].

The MDAR are decaying rapidly due to vibrational predissociation, at a rate which is the inverse of their lifetime. In accordance with the CARS study [12], the lifetime of MDAR is assumed to be 2 nsec in the gas phase following S_1 photolysis. At the steady state condition, the rate of production will balance the rate of decay, i.e. $\Delta O = \tau^{-1}$ x SSC, where SSC is the steady state concentration. Dividing by the excitation volume [35] so that SSC is a number density (and thus can be compared with LMR sensitivity estimates), we obtain:

$$\text{SSC}(\text{cm}^{-3}) = (5.0\text{x}10^{19}\ \text{sec}^{-1})(2\text{x}10^{-9}\ \text{sec})/(12\ \text{cm})(\pi/4)(1\ \text{cm})^2 = 1.1\text{x}10^{10}\ \text{cm}^{-3}$$

The best reported sensitivity for far-IR LMR is 10^6 cm^{-3} (1 sec averaging time, S/N = 1) [30]; this should probably be increased by a factor of 6 - 10 for mid-IR LMR [25,26,28]. Although the transition dipole moment of MDAR is unknown, there is no reason to believe that it is atypically small; the transition dipole moment is very large in methyl radical [43]. Thus the proposal of detection of MDAR by LMR is plausible, with the signal-to-noise potentially on the order of 10^3.

VI. CONCLUSION

The issue of one-bond *vs.* two-bond scission in the homolytic loss of nitrogen from azo compounds is still very controversial, although in the past five years there has been growing support for the predominance of the former. The one-bond cleavage mechanism could be confirmed for this important reaction by the direct observation of diazenyl radicals during decomposition of a diazene sample. The relatively new technique of laser magnetic resonance is ideal for such an observation, due to its extreme sensitivity, selective detection of paramagnetic species, and high resolution. Azomethane, the simplest stable azoalkane, presents a number of advantages for such an experiment: (1) azomethane homolysis has been studied extensively; (2) methyldiazenyl radical is fairly simple, facilitating spectral analysis; (3) the radical vibrational frequencies have been calculated and four fundamentals lie in the energy regions accessible to mid-IR laser magnetic resonance; (4) the results of a CARS study of gas phase azomethane photolysis are consistent with the formation of methyldiazenyl radical; (5) the other direct product of azomethane decomposition which is paramagnetic, methyl radical, has been characterized previously; and (6) the observation of a diazenyl radical intermediate in the decomposition of a simple, symmetric azoalkane would be especially significant, as these were formerly believed to be the least likely diazenes to undergo one-bond scission. The medium-pressure mercury arc photolysis of gas phase azomethane in a laser magnetic resonance spectrometer is calculated to yield a steady state concentration of methyldiazenyl radical up to three orders of magnitude larger than the detection threshold, confirming the plausibility of the proposed experiment.

REFERENCES

[1] P. S. Engel, *Chem. Rev. 80*, 99 (1980).

[2] J. G. Green, G. R. Dubay, and N. A. Porter, *J. Am. Chem. Soc. 99*, 1264 (1977), and references therein.

[3] P. B. Ayscough, B. R. Brooks, and H. E. Evans, *J. Phys. Chem. 68*, 3889 (1964).

[4] G. Koga and N. Koga, *The Chemistry of Hydrazo, Azo, and Azoxy Groups*, ed. S. Patai (New York: Wiley, 1975), Ch. 19.

[5] M. J. S. Dewar, *J. Am. Chem. Soc. 106*, 209 (1984).

[6] J. J. Dannenberg and D. Rocklin, *J. Org. Chem. 47*, 4529 (1982).

[7] B. Bigot, A. Sevin, and A. Devaquet, *J. Am. Chem. Soc. 100*, 2639 (1978).

[8] P. C. Hiberty and Y. Jean, *J. Am. Chem. Soc. 101*, 2538 (1979).

[9] G. D. Mendenhall and H. T. E. Chen, *J. Phys. Chem. 89*, 2849 (1985).

[10] S. H. Bauer, *J. Am. Chem. Soc. 91*, 3688 (1969).

[11] M. H. Chang, R. Jain, and D. A. Dougherty, *J. Am. Chem. Soc. 106*, 4211 (1984).

[12] P. L. Holt, K. E. McCurdy, J. S. Adams, K. A. Burton, R. B. Weisman, and P. S. Engel, *J. Am. Chem. Soc. 107*, 2180 (1985).

[13] R. C. Neuman, Jr., *Acc. Chem. Res. 5*, 381 (1972).

[14] R. C. Neuman, Jr. and G. A. Binegar, *J. Am. Chem. Soc. 105*, 134 (1983).

[15] R. J. Crawford and M. H. Chang, *Tetrahedron 38*, 837 (1982).

[16] P. S. Engel and D. B. Gerth, *J. Am. Chem. Soc. 105*, 6849 (1983).

[17] P. S. Engel, L. R. Soltero, S. A. Baughman; C. J. Nalepa, P. A. Cahill, and R. B. Weisman, *J. Am. Chem. Soc. 104*, 1698 (1982).

[18] M. T. H. Liu, *Chem. Soc. Rev. 11*, 127 (1982).

[19] W. Adam, T. Oppenlander, and G. Zang, *J. Org. Chem. 50*, 3303 (1985).

[20] W. Adam, O. Delucchi, K. Hill, E. M. Peters, K. Peters, and H. G. Vonschnering, *Chem. Ber. 118*, 3070 (1985).

[21] W. Adam, M. Dorr, K. Hill, E. M. Peters, K. Peters, and H. G. Vonscherning, *J. Org. Chem. 50*, 587 (1985).

[22] W. Adam, W. G. Gillaspey, E. M. Peters, K. Peters, R. J. Rosenthal, and H. G. Vonscherning, *J. Org. Chem. 50*, 580 (1985).

[23] D. F. McMillan, K. E. Lewis, G. P. Smith, and D. M. Golden, *J. Phys. Chem. 86*, 709 (1982).

[24] K. M. Evenson, *Faraday Disc. Chem. Soc. 71*, 7 (1981).

[25] P. B. Davies, *J. Phys. Chem. 85*, 2599 (1981).

[26] A. R. W. McKellar, *Faraday Disc. Chem. Soc. 71*, 63 (1981).

[27] K. M. Evenson, R. J. Saykally, and D. A. Jennings, in *Chemical and Biochemi-*

cal Applications of Lasers, ed. C. B. Moore, Vol. 5 (New York: Academic, 1980), pp. 95-138.

[28] D. K. Russell, *Electron Spin Resonance 8*, 1 (1983).

[29] E. Hirota and K. Kawaguchi, *Ann. Rev. Phys. Chem. 36*, 53 (1985).

[30] F. Temps and H. G. Wagner, *Ber. Buns. Phys. Chem 88*, 410 (1984).

[31] H. E. Radford and D. K. Russell, *J. Chem. Phys. 66*, 2222 (1977).

[32] D. K. Russell and H. E. Radford, *J. Chem. Phys. 72*, 2750 (1980).

[33] H. E. Radford, K. M. Evenson, and D. A. Jennings, *Chem. Phys. Letts. 78*, 589 (1981).

[34] H. E. Radford, *Chem. Phys. Letts. 71*, 195 (1980).

[35] L. Krasnoperov, E. N. Chesnokov, and V. N. Panfilov, *Chem. Phys. 89*, 297 (1984).

[36] J. S. Geiger, D. R. Smith, and J. D. Bonnett, *Chem. Phys. 74*, 239 (1983).

[37] L. N. Krasnoperov and V. N. Panfilov, *Kinet. Catal. 20*, 447 (1979), English translation.

[38] T. Bohland, F. Temps, and H. G. Wagner, *Z. Phys. Chem. Neue Folge 142*, 129 (1984).

[39] K. Yamashita, M. Kaminoyama, T. Yamabe, and K. Fukui, *Chem. Phys. Letts. 83*, 78 (1981).

[40] A potential secondary reaction product that is paramagnetic is $CH_3N_2CH_2$, formed by hydrogen abstraction of AM by methyl radical. It could be distinguished from MDAR by virtue of having two rotational constants which are significantly smaller than those of MDAR.

[41] A. Snelson, *J. Phys. Chem. 74*, 537 (1970).

[42] C. Yamada, E. Hirota, and K. Kawaguchi, *J. Chem. Phys. 75*, 5256 (1981).

[43] C. Yamada and E. Hirota, *J. Chem. Phys. 78*, 669 (1983).

[44] T. Amano, P. F. Bernath, C, Yamada, Y. Endo, and E. Hirota, *J. Chem. Phys. 77*, 5284 (1982).

[45] O. P. Strausz, J. W. Lown, and H. E. Gunning, *Compr. Chem. Kinet. 5*, 566 (1972).

[46] M. H. Jones and E. W. R. Steacie, *J. Chem. Phys. 21*, 1018 (1953).

[47] J. G. Calvert and J. N. Pitts, *Photochemistry* (New York: Wiley, 1967), (a) p. 453; (b) p. 691; (c) p. 696.

[48] *CRC Handbook of Chemistry and Physics*, 65th ed., ed. R. C. Weast (Boca Raton, Florida: CRC Press, 1984), p. C-118.

[49] See, e.g., W. R. Lambert, P. M. Felker, and A. H. Zewail, *J. Chem. Phys. 81*, 2217 (1984).

[50] If a flow rate of 2 l/sec is assumed, this corresponds to a 10 % dissociation of AM:

$$(5.0\text{x}10^{19}\ \text{sec}^{-1})/(4.0\text{x}10^{-4}\ \text{M})(6.02\text{x}10^{23}\ \text{mole}^{-1})(2\ \text{l/sec}) = 0.10$$

Thus Beer's Law will be approximate. The actual flow rate in the Cl/SiH_3 study was 0.5 l/sec, though there is no indication that this is a limiting value.

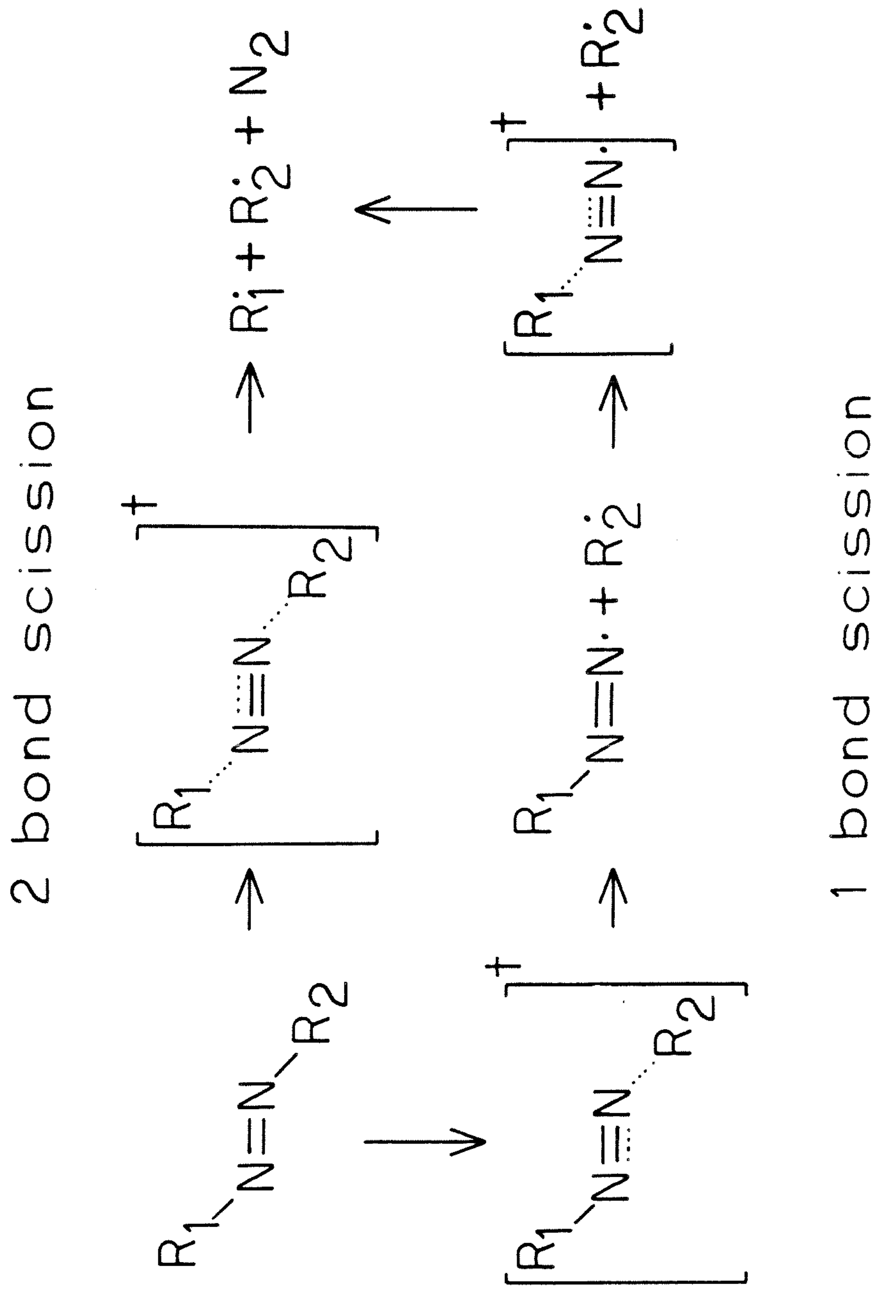
2 bond scission
1 bond scission
R1–N=N–R2
[R1···N≡N···R2]+
R1· + R2· + N2
R1–N=N· + R2·
[R1···N≡N·]+ + R2·

The Effect of Anharmonic Coupling and Vibrational Predissociation on the Excitation Profile of the O-H Stretching Fundamental in Supersonic Jet-Cooled Phenol-Benzene Complexes

Proposition 3

ABSTRACT

Anharmonic coupling and vibrational predissociation are believed to broaden the absorption profiles of hydrogen bond-perturbed stretching vibrations. Supersonic jet expansion laser spectroscopy of phenol-benzene complexes should elucidate the importance of these two phenomena in this prototype system. Combination band analysis of the fluorescence excitation spectrum near the O-H stretching fundamental will reveal the extent of anharmonic coupling and identify participating low frequency hydrogen bond modes. Fluorescence decay experiments will allow determination of upper bounds on vibrational dissociation rates so that resultant linewidths due to lifetime broadening may be calculated. The latter experiments also have the potential to demonstrate mode selectivity in the vibrational predissociation process.

I. INTRODUCTION

One of the most intriguing aspects of hydrogen-bonded systems (denoted A–H · · · B) is that infrared absorption profiles of A-H stretching fundamentals, when perturbed by hydrogen-bonding, are spectacularly broadened relative to those of the unperturbed stretches. This is true even in the gas phase, where the systems are simple enough that it should be possible to develop accurate theoretical descriptions of the systems. The first quantum theory to explain this phenomenon was proposed by Stepanov [1]. His theory relied upon two key hypotheses: (1) In hydrogen-bonded complexes, the A-H and H · · · B stretches are strongly anharmonically coupled, leading to a *progression* of the form $\Delta\nu(\text{A–H}) \pm n\Delta\nu(\text{H} \cdots \text{B})$, n = 0, 1, 2... in the absorption spectrum, in contrast to the *single* absorption line in uncomplexed A-H. (2) Vibrational predissociation is so fast in these systems that lifetime broadening of the individual lines of this progression cause it to coalesce into a continuous contour.

The anharmonic coupling (first) hypothesis is currently widely accepted, despite the paucity of direct experimental confirmation. In nearly all absorption profiles in which structure has been observed, it has been poorly resolved and irregular; a notable exception is the symmetric, very strongly bound HF_2^- [2]. The vibrational predissociation (second) hypothesis has met with considerable criticism, based partly on misleading calculational studies. A plausible alternative hypothesis (the extended anharmonic coupling hypothesis) is that one or both of the very low frequency ir active hydrogen bond *deformations* are strongly coupled to the A-H stretch [3]. Combined with Stepanov's anharmonic coupling hypothesis, this would lead to the prediction of a more complicated absorption progression with frequencies $\Delta\nu(\text{A–H}) \pm n\Delta\nu(\text{H} \cdots \text{B}) \pm m\Delta\nu(\delta_1) \pm l\Delta\nu(\delta_2)$, n, m, l = 0, 1, 2... ($\delta$ = deformation). The pump-probe technique used in the very recent phenol-benzene work [4], described in § III, provides the most direct observation of vibrational predissociation in gas phase hydrogen-bonded systems to date; additional studies of this type over extended energy intervals should clarify predissociation rates (and thresholds) in these systems.

The greatest difficulty in testing the anharmonic coupling hypotheses has been resolving absorption profiles to a sufficient degree to allow detailed vibrational analysis. In supersonic jet expansions, single vibronic level resolution is normally obtainable even for large molecules which have nearly structureless room temperature gas phase absorptions [5]. The simplicity of the jet spectra results from (1) the collisionless conditions; (2) the low vibrational temperatures (tens of K), which eliminate hot bands and sequence bands; and (3) the very low rotational temperatures (a few K) which reduce linewidths to only one to a few cm^{-1} [6]. Given these considerations, I herein propose to test the anharmonic coupling hypotheses by comparing the high resolution laser excitation profiles of A-H stretches in hydrogen-bonded complexes with those in uncomplexed A-H molecules. If Stepanov's anharmonic coupling hypothesis is correct, a simple progression of the form $\Delta\nu(\mathrm{A{-}H}) \pm n\Delta\nu(\mathrm{H}\cdots\mathrm{B})$ should be observed in the complex, while isolated A-H will exhibit a single line at higher energy. If the extended anharmonic coupling hypothesis is correct, then in the complex a complicated progression of the form $\Delta\nu(\mathrm{A{-}H}) \pm n\Delta\nu(\mathrm{H}\cdots\mathrm{B}) \pm m\Delta\nu(\delta_1) \pm l\Delta\nu(\delta_2)$ should be observed instead.

Complimentary time-resolved fluorescence experiments are also proposed to indirectly (but in real time) measure predissociation rates in hydrogen-bonded systems to determine if vibrational predissociation (or some other process) leads to significant line broadening, as hypothesized by Stepanov. Although less selective than the phenol-benzene pump-probe experiments, these simpler, one-color experiments should allow determination of predissociation rates (or upper bounds thereto) if these are comparable to fluorescence decay rates (ns^{-1}), as seems likely (see § III). In the event that predissociation is too fast to measure by this technique, more complicated pump-probe experiments (like those in the phenol-benzene work [4]) would directly yield dissociative lifetimes with superior temporal resolution. Additional benefits of time-resolved experiments are the measurement of predissociation thresholds in isolated complexes, and the potential for demonstrating mode selectivity in vibrational predissociation.

This report is organized as follows. In § II, I give a more detailed description of theoretical treatments of hydrogen-bonded systems, and review pertinent calculational literature. In § III, I discuss free jet and gas phase experiments from the literature which are relevant to the hypotheses being tested. The phenol-benzene work is emphasized as it exemplifies the use of jet expansions and laser spectroscopy in the study of hydrogen-bonded complexes and vibrational predissociation. Finally, in § IV, I describe my proposed experiments and their interpretations in detail.

II. THEORETICAL TREATMENTS

Let us consider the case of two nonlinear molecules forming a hydrogen-bonded complex A–H · · · B. In the uncomplexed state there are six translational and six rotational degrees of freedom. In the complexed state, there are only three translational and three rotational degrees of freedom. Hence the formation of a complex results in the creation of six new vibrational degrees of freedom, which are associated with the hydrogen bond. Those which correlate with the three lost translations are Raman-active, while those which correlate with the three lost rotations are infrared-active. The infrared-active vibrations may be thought of as a hydrogen bond stretch $\text{A–H}\overset{\longleftrightarrow}{\cdots}\text{B}$ and two deformations (bends) A–H · · · B. 

Stepanov [1] and later authors [3,7] reasoned that since the hydrogen is light compared to the substituents A and B, during a hydrogen stretch A and B are relatively stationary. Thus if the A-H bond is excited, it becomes longer, which effectively shortens and strengthens the H · · · B bond. Hence, the A-H and H · · · B stretches are strongly anharmonically coupled. Consequently, absorptions with frequencies $\Delta\nu(\text{A–H}) \pm n\Delta\nu(\text{H} \cdots \text{B})$, $n=0,1,2\ldots$ are expected in the infrared spectrum. Note that $\Delta\nu(\text{A–H}) \gg \Delta\nu(\text{H} \cdots \text{B})$, so the resultant absorption is a series of closely spaced lines arranged at approximately even intervals, as opposed to a single vibrational line. It has been suggested that further complication of the infrared absorption spectrum occurs due to anharmonic coupling of the A-H stretch and A–H · · · B *deformations*, and due to Fermi resonances, especially where A and B are large [3].

If one or both of the hydrogen bond deformations (δ_1 and δ_2) are strongly coupled to the A-H stretch, as in the extended anharmonic coupling hypothesis, then the progression due to H · · · B stretch coupling will be greatly complicated by the addition of the very low frequency intervals $\Delta\nu(\delta_1)$ and $\Delta\nu(\delta_2)$. Since

$\Delta\nu(\delta_{1,2}) << \Delta\nu(H \cdots B)$ (see § III), the individual lines of the $\Delta\nu(H \cdots B)$ progression will becomes complicated progressions themselves of $\Delta\nu(\delta_1)$ and $\Delta\nu(\delta_2)$, with the total frequency spectrum given by $\Delta\nu(A\text{–}H) \pm n\Delta\nu(H \cdots B) \pm m\Delta\nu(\delta_1) \pm l\Delta\nu(\delta_2)$. Stick diagrams of the absorption profiles for uncomplexed A-H and A–H $\cdots$ B, according to both Stepanov's and the extended anharmonic coupling hypotheses, are shown in Figure 1. Although both frequencies and intensities are qualitative in this diagram, the essential differences should be satisfactorily depicted.

Since Stepanov's vibrational predissociation proposal, a number of estimates of vibrational predissociation rates have been made. Using the general approach of Rosen [8], who studied unimolecular decomposition, Coulson and Robertson calculated predissociation rates assuming that excess energy is entirely converted to translational energy in the resultant fragments [9,10]. They found that predissociation rates were too small to sufficiently broaden the vibrational lines into a single smooth absorption. Further refinement of these calculations led to similar conclusions [11,12]. Agreement of quantum mechanical and classical calculations was demonstrated, lending credence to both calculation methods [13]. However, recognition of the greater efficiency of predissociation channels wherein the excess energy becomes *rotational* energy of the fragments invalidated the conclusions of these previous studies [14]. The best calculations available now [15] do not unequivocally disprove Stepanov's predissociation hypothesis.

III. RELEVANT EXPERIMENTS FROM THE LITERATURE

Several research groups have recently obtained spectra of hydrogen-bonded complexes in supersonic free jets. Ito *et al.* have obtained the excitation [16] and emission [17] spectra of phenol:base complexes. For example, in phenol:dioxane, low-frequency modes of 19/23 and 128/137 cm^{-1} (ground/excited-state) are attributed to hydrogen bond bending and stretching motions. Similar results were found for nine other bases, and for the indole analogs of the phenolic complexes [18]. Multiple conformers were usually observed, and some low-frequency intervals were not assignable. McVey *et al.* thoroughly characterized the benzoic acid dimer through its fluorescence excitation [19,20] and dispersed fluorescence [21] spectra. A low-frequency mode of 57/58 cm^{-1} (ground/excited state) was attributed to an out-of-plane bend or ring torsion. Transfer of energy between the two rings (one labelled by deuteration) on the time scale of emission was demonstrated. Since there is minimal electronic coupling between the rings, vibrational coupling through the hydrogen bonds was invoked to explain this phenomenon. Ito *et al.* extended this work [22] by studying the paratoluic acid:benzoic acid dimer. Several other spectral studies have focussed on *intra*molecular hydrogen-bonding. Jortner *et al.* [23] and Barbara *et al.* [24] have looked at anthraquinones, while Zewail *et al.* [25] and Kohler *et al.* [26] have studied methyl salicylate.

It is important to note that none of these spectral studies probed the A-H stretching fundamental region, and so provide no test of the anharmonic coupling hypotheses. The observation of low-frequency hydrogen bond fundamentals in a number of complexes is significant only insofar as it confirms that such vibrations exist, and provides frequencies thereof. The extent of anharmonic coupling between the A-H stretch and the hydrogen bond vibrations can only be ascertained through combination band analysis in the vicinity of the A-H stretching fundamental.

There have been several recent dynamical studies which are relevant to the vibrational predissociation hypothesis. In a very recent study [4], Knee, Khundkar, and Zewail measured predissociation rates in phenol-benzene 1:1 complexes up to 2500 cm^{-1} vibrational energy. This molecular system was chosen because (1) the S_1 vibrational levels are assigned, and the O-H stretching fundamental has significant transition probability in the $S_0 \rightarrow S_1$ excitation process [27]; (2) the phenol electronic transition energy is different enough from that of benzene that initial excitation is localized on the phenol moiety; and (3) the complex origin is red-shifted significantly (147 cm^{-1}) from the uncomplexed phenol origin. By heating phenol to 60 °C and cooling benzene to -15 °C, appropriate vapor pressures were obtained such that no complexes other than the 1:1 were present in the free jet, as determined by the mass spectrometric detection system. A pump pulse was used to excite complexes to specific vibrational levels in S_1, then a variable delay probe pulse ionized the excited complex. At low E_{vib}, the lifetimes observed were close to those of uncomplexed phenol; above the threshold of $\approx$ 1600 cm^{-1}, predissociation rates of several ns^{-1} were observed, corresponding to GHz linewidths.

Several other dynamical studies have not involved direct measurement of predissociation rates, but are of considerable relevance. Except for the phenol-benzene work, the most direct gas-phase observation of vibrational predissociation in a hydrogen-bonded system was Audibert and Palange's study [28] of diethylether-hydrogen fluoride. During a 10 ns laser pulse tuned to a complex absorption, an increase was observed in the uncomplexed HF signal during the laser pulse, placing an upper limit on the predissociation lifetime of 10 ns. During the laser pulse, the complexes experienced an average of five collisions; the role of these collisions in the predissociation process is not clear.

Auty *et al.* [29] have made lifetime measurements on water:dibenzofuran. They found that the hydrogen-bonded complex decays twice as rapidly as uncomplexed dibenzofuran. Zewail *et al.* performed extensive time-resolved studies on isoquinoline complexes with water and methanol [30,31]. Here the opposite trend was observed: lifetimes were increased by complexation. Above 1000 cm^{-1} of vibrational energy, a nonradiative decay channel in both methanol and water complexes was attributed to hydrogen bond cleavage [32]. Mass spectral studies of hydrogen fluoride complexes [33] and water complexes [34] indicated that predissociation lifetimes were less than a microsecond. Studies of hydrogen fluoride complexes have placed both lower [35] and upper [36] limits of 10 ns each on the predissociation lifetime. Finally, complexes of ethylene with hydrogen fluoride and chloride were found to have lifetimes of only a few picoseconds [37], as inferred from lineshape analyses.

IV. PROPOSED EXPERIMENTS

A. The Molecular System

The requirements for a suitable molecular system for the experiments proposed below are as follows: (1) A-H and B should preferentially form 1:1 complexes in a free jet expansion; (2) the $S_0 \rightarrow S_1$ transition in A-H should be isolated from electronic transitions in B so that there is no spectral overlap; (3) the A-H stretching fundamental in S_1 should have reasonable transition probability from the ground vibronic state (the only state appreciably populated in a free jet expansion); (4) the A-H vibrations in S_1 should ideally have been assigned previously; and (5) the complex electronic origin should be shifted far enough from the isolated A-H origin that the spectra can be analyzed separately. All five of these requirements are met by the phenol-benzene system discussed previously [4,16,17], which would be the prototype system for the experiments proposed herein. These experiments could be repeated using equally suitable but stronger bases like ethanol or dioxane [16,17] to test the effect of hydrogen-bond strength on anharmonic coupling and vibrational redistribution.

B. Fluorescence Excitation Experiments

Fluorescence excitation experiments have several advantages over ground-state absorption experiments [38]: (1) increased sensitivity due to emission detection; (2) the relative ease of continuous frequency tuning using dye lasers; and (3) the potential for temporally resolving the emission (see next section). The extent of anharmonic coupling between the low-frequency hydrogen-bond modes and the A-H stretching mode can be evaluated through combination band analysis of the excitation spectrum in the vicinity of the A-H stretching fundamental. Stronger anharmonic coupling will result in more numerous and intense combination bands between coupled modes. In several of the studies mentioned in § III, low frequency fundamentals and overtones were observed near the electronic origin in excitation (and emission) spectra, but combination bands were not observed since the A-H stretching region was not probed.

As shown in Figure 1 and discussed in § II, the predicted spectral profiles of the A-H stretching region differ for the cases of no coupling (trace 1), anharmonic coupling to the H · · · B stretch only (trace 2), and coupling to the low frequency A–H · · · B deformations as well (trace 3). The figure shows the red-shift of the complex origin and other A vibrations (which are nearly unaffected by complexation), and the reduction of the A-H stretching vibrational frequency upon complexation. The frequencies and intensities in this figure are strictly qualitative, but demonstrate the potential for proving or disproving the various anharmonic coupling hypotheses. The greatly simplified jet spectra should allow detailed vibrational analysis of any progressions observed, leading to assignment of the coupled modes through the determination of their S_1 vibrational frequencies.

Finally, it will be of considerable interest to compare the linewidth of the uncomplexed A-H stretch with those of individual lines in the predicted complex progression, and, in turn, to compare these linewidths with those calculated from the time-resolved experiments described below.

C. Time-Resolved Experiments

If an excited state decays by two mechanisms, one of which is emission of a photon (k_{fl}), and one of which is nonradiative vibrational predissociation (k_{vp}), then:

$$k_{fl} + k_{vp} = \tau_{fl}^{-1}$$
$$\varphi_{fl} = k_{fl} / (k_{fl} + k_{vp}) = k_{fl}\tau_{fl}$$

where τ_{fl} is the fluorescence lifetime and φ_{fl} is the fluorescence quantum yield. In order to accurately determine k_{vp}, it must be of comparable magnitude to k_{fl} [39]. If $k_{vp} \ll k_{fl}$, then most of the complexes will radiate before they can dissociate, so the dissociation rate will not be reflected in the observed decay. If instead $k_{vp} \gg k_{fl}$, then the quantum yield φ_{fl} will fall below the detection sensitivity threshold. We expect k_{fl} to be independent of E_{vib} as long as the electronic state being excited is isolated from other electronic states [5]. Vibrational predissociation is not possible until the vibrational energy exceeds a threshold depending upon the hydrogen bond strength. Thus k_{fl} can be taken to be the reciprocal of the fluorescence lifetime at the electronic origin ($E_{vib}=0$), yielding:

$$k_{vp}(E_{vib}) = \tau_{fl}^{-1}(E_{vib}) - \tau_{fl}^{-1}(0)$$

If there are additional decay mechanisms present, then k_{vp} will be overestimated; the calculated k_{vp} is thus an upper bound. The resultant estimated linewidths will also be upper bounds, as is desirable; the turning point in the k_{vp} *vs.* E_{vib} plot will provide a lower bound on the predissociation threshold. It is possible that the importance of additional decay channels might be clarified by comparing the dynamics of analogous vibrational levels in uncomplexed A-H and A–H · · · B. These measurements will allow evaluation of Stepanov's vibrational predissociation hypothesis; if true, the estimated linewidths must be at least on the order of the spacing between members of the excitation progression. The phenol-benzene work suggests that, at least near the threshold, k_{vp} should be measurable by this method. It is possible that predissociation will be so rapid higher above the threshold that rates cannot be accurately determined by the fluorescence lifetime technique. Then the more complicated pump-probe technique, used in the phenol-benzene work, would be employed to directly measure predissociation lifetimes with superior temporal resolution.

Finally, it should be noted that vibrational predissociation is not necessarily a nonradiative process; the molecular moiety excited may fluoresce following fragmentation. If the perturbation due to hydrogen-bonding is small, the emission of the complex may not be shifted appreciably from the emission of the uncomplexed molecular moiety. Although this is the case with some van der Waals complexes [40], the hydrogen bond perturbation is considerably larger. A shift of only 50 cm^{-1} or so is required to isolate the complex emission with a monochromator while still maintaining sufficient signal for time-resolved experiments.

D. Mode Selectivity

There is currently a great deal of interest in understanding whether reaction rates depend upon the symmetry and/or nuclear motions of the specific vibration excited, or whether they depend only upon E_{vib}. Dependence upon the specific level properties exclusive of E_{vib} is termed mode selectivity, which has thus far been demonstrated for only a few systems [41,42]. In addition to determining the time scale of vibrational predissociation in hydrogen-bonded complexes, the proposed time-resolved experiments would allow evaluation of the extent of mode selectivity in the predissociation process. If k_{vp} is plotted as a function of E_{vib}, fluctuations exceeding the uncertainty in k_{vp} may be attributed to mode selectivity. Observations of mode selectivity can contribute to our knowledge of factors affecting process rates.

V. CONCLUSION

The nature of the fluorescence excitation spectrum near the O-H stretching fundamental in the phenol-benzene complex should provide unambiguous evidence in substantiation or refutation of the various anharmonic coupling hypotheses proposed to explain the broad absorption profiles of hydrogen bond-perturbed stretches. Fluorescence decay measurements will allow calculation of the contribution of lifetime broadening to observed linewidths in the excitation profiles, and will probe mode selectivity in the vibrational predissociation process. Studies of other analogous complexes could elucidate the effect of hydrogen-bond strength on anharmonic coupling and vibrational predissociation in hydrogen-bonded systems.

REFERENCES

[1] B. I. Stepanov, *Nature 157*, 808 (1946).

[2] G. L. Cote and H. W. Thompson, *Proc. Roy. Soc. A 210*, 206 (1951).

[3] N. Sheppard, *Hydrogen Bonding*, ed. D. Hazdi (Pergamon, London, 1959), pp. 85-105

[4] J. L. Knee, L. R. Khundkar, and A. H. Zewail, *J. Chem. Phys. 82*, 4715 (1985).

[5] J. F. Shepanski, B. W. Keelan, and A. H. Zewail, *Chem. Phys. Letts. 103*, 9 (1983).

[6] B. W. Keelan and A. H. Zewail, *J. Chem. Phys. 82*, 3011 (1985).

[7] S. Bratoz and D. Hazdi, *J. Chem. Phys. 27*, 991 (1957).

[8] N. Rosen, *J. Chem. Phys. 1*, 319 (1933).

[9] C. A. Coulson and G. N. Robertson, *Proc. Roy. Soc. Lond. A 337*, 167 (1974).

[10] C. A. Coulson and G. N. Robertson, *Proc. Roy. Soc. Lond. A 342*, 289 (1975).

[11] G. N. Robertson, *J. Chem. Soc. Faraday Trans. II, 72*, 1153 (1976).

[12] G. N. Robertson, *Phil. Trans. R. Soc. Lond. A 286*, 25 (1977).

[13] J. Lascombe and J. C. Lassegues, *Mol. Phys. 40*, 969 (1980).

[14] M. S. Child, *Faraday Disc. Chem. Soc. 62*, 307 (1977)

[15] G. E. Ewing, *J. Chem. Phys. 72*, 2096 (1980).

[16] H. Abe, N. Mikami, and M. Ito, *J. Phys. Chem. 86*, 1768 (1982).

[17] H. Abe, N. Mikami, M. Ito, and Y. Udagawa, *J. Phys. Chem. 86*, 2567 (1982).

[18] Y. Nibu, H. Abe, N. Mikami, and M. Ito, *J. Phys. Chem. 87*, 3898 (1983).

[19] D. E. Poeltl and J. K. McVey, *Laser Chem. 3*, 189 (1983).

[20] D. E. Poeltl and J. K. McVey, *J. Chem. Phys. 78*, 4349 (1983).

[21] D. E. Poeltl and J. K. McVey, *J. Chem. Phys. 80*, 1801 (1984).

[22] Y. Tomioka, H. Abe, N. Mikami, and M. Ito, *J. Phys. Chem. 88*, 5186 (1984).

[23] G. Smulevich, A. Amirav, U. Even, and J. Jortner, *Chem. Phys. 73*, 1 (1982).

[24] S. R. Flom and P. F. Barbara, *J. Phys. Chem. 89*, 4489 (1985).

[25] P. M. Felker, W. R. Lambert, and A. H. Zewail, *J. Chem. Phys. 77*, 1603 (1982).

[26] L. Heimbrook, J. E. Kenny, B. E. Kohler, and G. W. Scott, *J. Phys. Chem. 87*, 280 (1983).

[27] H. D. Bist, J. C. D. Brand, and D. R. Williams, *J. Mol. Spectrosc. 21*, 76 (1966) and *24*, 413 (1967).

[28] M.-M. Audibert and E. Palange, *Chem. Phys. Letts. 101*, 407 (1983).

[29] A. R. Auty, A. C. Jones, and D. Phillips, *Chem. Phys. Letts. 112*, 529 (1984).

[30] P. M. Felker and A. H. Zewail, *Chem. Phys. Letts. 94*, 448 (1983).

[31] P. M. Felker and A. H. Zewail, *Chem. Phys. Letts. 94*, 454 (1983).

[32] P. M. Felker and A. H. Zewail, *J. Chem. Phys.* *78*, 5266 (1983).

[33] J. M. Lisy, A. Tramer, M. F. Vernon, and Y. T. Lee, *J. Chem. Phys.* *75*, 4733 (1981).

[34] M. F. Vernon, D. J. Krajnovich, H. S. Kwok, J. M. Lisy, Y. R. Shen, and Y. T. Lee, *J. Chem. Phys.* *77*, 47 (1982).

[35] A. S. Pine and W. J. Lafferty, *J. Chem. Phys.* *78*, 2154 (1983).

[36] K. J. Rensberger, R. A. Copeland, J. M. Robinson, and F. F. Crim, *J. Chem. Phys.* *83*, 1132 (1985).

[37] M. P. Casassa, C. M. Western, F. G. Celii, D. E. Brinza, and K. C. Janda, *J. Chem. Phys.* *79*, 3277 (1983).

[38] B. W. Keelan, J. A. Syage, J. F. Shepanski, and A. H. Zewail, *Proceedings of the International Conference on Lasers 1983*, San Francisco, CA, Society for Optical and Quantum Electronics (STS, McLean, VA, 1985), p. 718.

[39] W. R. Lambert, P. M. Felker, and A. H. Zewail, *J. Chem. Phys.* *81*, 2217 (1984).

[40] R. E. Smalley, D. H. Levy, and L. Wharton, *J. Chem. Phys.* *64*, 3266 (1976).

[41] M. Fujii, T. Ebata, N. Mikami, M. Ito, S. H. Kable, W. D. Lawrance, T. B. Parsons, and A. E. W. Knight, *J. Phys. Chem.* *88*, 2937 (1984).

[42] P. M. Felker and A. H. Zewail, *J. Phys. Chem.* *88*, 6106 (1984).

FIGURE CAPTION

Diagrammatic representations of two regions of the fluorescence excitation spectra of A-H (trace 1), and A–H · · · B (traces 2 and 3). Both frequencies and intensities are strictly qualitative. On the left is the electronic origin and a vibration localized on A; note that the origin is red-shifted upon complexation, but the vibrational interval is nearly unchanged. On the right is the A-H stretching fundamental region. In uncomplexed A-H, this is a single line. Upon complexation, the vibrational frequency is reduced, and anharmonic coupling to low frequency hydrogen bond modes produces a progression. In trace 2, only the H · · · B stretch ($\Delta\nu \approx 100$ cm^{-1}) is coupled to the A-H stretch; in trace 3, there is additional coupling to a deformation ($\Delta\nu \approx 20$ cm^{-1}).

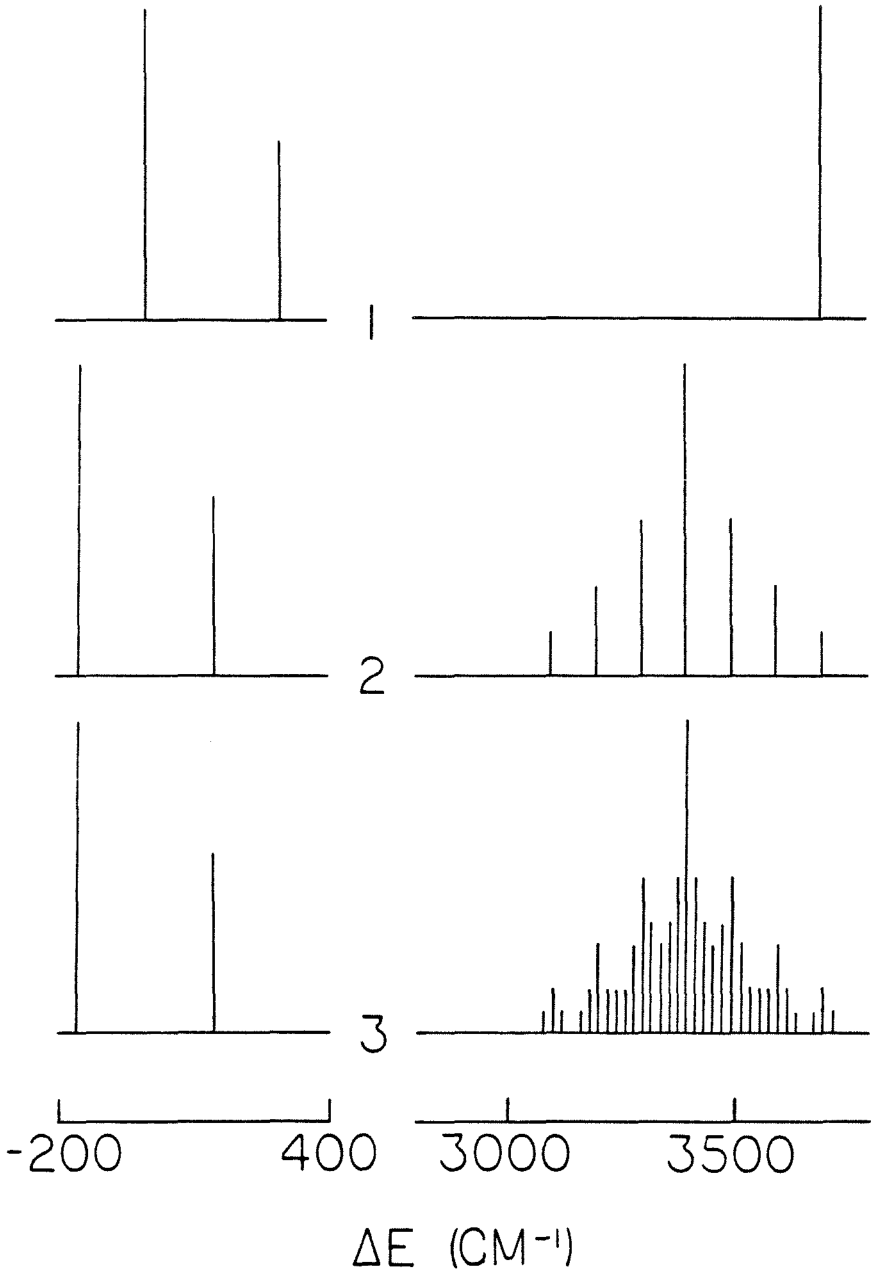

Figure 1